

On-Chip Compensation of Stress, Temperature, and Nonlinearity in a MEMS Gyroscope

Submitted in partial fulfillment of the requirements for the degree of

Doctor of Philosophy

in

Electrical and Computer Engineering

Erdinc Tatar

B.S., Electrical and Electronics Engineering, Middle East Technical University (2008)

M.S., Electrical and Electronics Engineering, Middle East Technical University (2010)

Carnegie Mellon University
Pittsburgh, PA

February, 2016

© Erdinc Tatar 2016
All Rights Reserved

To my grandmother, and my wife Ruba

Abstract

The micro-gyroscope performance has improved throughout the years as a result of extensive research, and advancements in fabrication technologies and readout electronics. Today the performance has reached to a point where the environmental effects play a significant role on the gyroscope drift. This thesis proposes on-chip stress, temperature and nonlinearity compensation techniques for high performance MEMS gyroscopes to further improve the gyroscope stability without sacrificing the noise performance.

Long term drift limits the performance of the micro-gyroscopes. Temperature has been found to be one of the important sources of long term drift. But constant temperature testing of one of the state of the art gyroscopes still exhibits long term drift. The main motivation of this thesis is solving the long term gyroscope drift problem by measuring the stress of the mechanical structure with on-chip stress sensors. Towards that end, a methodology that couples finite element analysis and circuit simulation has been developed to understand the stress zero rate output (ZRO) relation. To validate the trends in the simulations, stress tests have been performed on a silicon-on-insulator (SOI) MEMS gyroscope that is in-house fabricated, vacuum packaged, and ovenized. This thesis successfully demonstrates that stress compensation significantly suppresses long-term drift resulting in $9^\circ/\text{hr}/\sqrt{\text{Hz}}$ angle random walk (resolution) and $1^\circ/\text{hr}$ bias instability at 10,000 s (around 3 hr) averaging time, which is a seven times improvement over the uncompensated gyroscope output.

While stress compensation improves the long term stability, the noise performance of the gyroscope directly depends on the drive displacement. High drive displacement improves the gyroscope signal to noise ratio but also leads to a nonlinear force displacement behavior that is

observable as a hysteresis in the frequency-phase and frequency-amplitude relations. These nonlinearities lead to an amplitude-frequency effect where resonance frequency depends on the displacement. This affects the gyroscope long term stability. This thesis proposes a cubically shaped nonlinearity tuning comb finger design that cancels the inherent softening nonlinearity of the gyroscope by introducing a dc voltage controlled hardening nonlinearity. The functionality of the fingers is demonstrated and, furthermore, cancelling drive nonlinearities at high displacement leads to a better bias instability compared to the same displacement with uncompensated, nonlinear characteristics.

Acknowledgements

Coming to this point has required tremendous amount of support from my environment. Using words to express my appreciation is probably not enough for some but I will try my best. It has been a very long journey since my BS graduation and I apologize if I forgot to list some of the people's contributions on my career.

My journey in Carnegie Mellon University (CMU) started with a very lucky coincidence by meeting Prof. Gary Fedder in TRANSDUCERS 2011 conference in China. Looking back I realize that it turned out to be quite positive on my side. I developed critical thinking skills and I was educated throughout my PhD. I would like to thank my advisors Prof. Gary Fedder and Prof. Tamal Mukherjee for all the skill sets they taught me. I think the main skill I learnt from them is always keeping the brain in the loop which is very important and will be a guideline for the rest of my life. It was my pleasure to work with Prof. Fedder and Prof. Mukherjee. I would like to also thank my PhD committee members Prof. Koushil Sreenath and Prof. Maarten P. de Boer for their useful suggestions to improve the quality of my thesis.

I met a lot of friends in CMU. I would like to start with thanking Ekin Yagmur Gonen, working with him on the endless CMOS tapeouts will remain in my memories. I want to thank Metin Gokhan Guney for being my office mate and for the useful discussions on a broad range of topics. Dr. Congzhong Guo has provided good friendship and help on the research and social life. I would like to thank Dr. Dylan Fang for training on the Si-CMOS-MEMS process. Mary Beth Galanko has been a friendly colleague, I enjoyed working with her. I would like to thank Suresh Santhanam for his help in the cleanroom and vacuum packaging system. Previous and current Nanofab staff Chris Bowman, Carsen Kline, Dr. Matthew Moneck, James Rosvanis, and Norman Gottron have

provided help for my cleanroom work. I would like to thank ECE machine shop staff Steve Hoffman and Dave Belotti for machining the pieces for the vacuum packaging system. Chatting with Dr. Jason Gao and Dr. Pengfei Li was always joyful. Special thanks to Omer Ozdemir, Ozan Iskilibli, Yunus Emre Kesim, Enes Calayir, Metin Gokhan Guney, and Ekin Yagmur Gonen for spending their social life with me and my wife. Those times provided us a relaxing break. I would like to also thank the MEMS lab members Sean Yen, Lionel Wong, Ashwati Krishnan, Mats Forssell, Xiao Chuan Ong, Dr. Kristen Dorsey, and Dr. Nathan Lazarus. Also thanks to Mohamed Darwish for the spiritual support.

I would like to thank my funding sources. This work was supported by the Defense Advanced Research Projects Agency (DARPA) under agreement number FA8650-08-1-7824. The work was also partially supported by the National Science Foundation (NSF) Grant #CNS 0941497 as part of the Cyber-enabled Discovery and Innovation (CDI) program.

I would like to thank my mother Havva Tatar, father Adnan Tatar, brother Fikret Tatar, and sister Seyma Tatar for their lifetime support. Coming this far would not be possible without their emotional support. I would like to also thank my grandmother, she always wanted to see these days.

I was saving the biggest thanks for my wife, Ruba Tatar. I think the words are not sufficient to acknowledge her part in my life. She has always taken care of me emotionally and with her delicious food. I feel so lucky to have a wife who sacrificed her life to be with me. Hopefully good days are waiting for us and our kids in the future.

Table of Contents

Abstract.....	iv
Acknowledgements.....	vi
Table of Contents.....	viii
List of Figures.....	xii
List of Tables.....	xxv
Chapter 1 Introduction.....	1
1.1 Thesis Goal.....	1
1.2 Thesis Motivation.....	2
1.3 Gyroscope Operation and Different Gyroscope Structures.....	6
1.4 SOI-MEMS Gyroscope.....	11
1.5 Gyroscope equations.....	17
1.6 Gyroscope Equations with the Cubic Nonlinearity.....	23
1.7 SOI-MEMS Gyroscope with the Front-end and Biasing.....	29
1.8 Thesis Contributions.....	32
1.9 Thesis Outline.....	33
Chapter 2 Simulation Methodology and Gyroscope Control.....	35
2.1 Simulations.....	36
2.1.1 COMSOL Simulations of Environmental Effects on Resonance Frequency.....	36
2.1.2 Gyroscope Theory Including Anchor Displacements.....	39

2.1.3	Simulation Methodology	42
2.1.4	Simulation Results	47
2.1.5	Simulation Results with the Parasitics	50
2.2	Gyroscope Control Loops and Frequency Control	54
2.2.1	Gyroscope Control Loops for Drive and Sense	54
2.2.2	Frequency Control	59
2.3	Gyroscope Noise Analysis	67
2.3.1	Noise Analysis of the Closed-Loop System	76
2.4	Summary	79
Chapter 3	Fabrication and Vacuum Packaging	80
3.1	SOI-MEMS Fabrication Process	80
3.2	Discrete Vacuum Packaging System.....	83
3.2.1	Die Mounting for Vacuum Packaging	85
3.2.2	Getter.....	88
3.2.3	Temperature Planning and Vacuum Packaging System	90
3.2.4	Vacuum Packaging Results.....	96
3.3	Summary	98
Chapter 4	Nonlinearity and Frequency Tuning	99
4.1	Shaped Comb Finger Design	99
4.1.1	Shaped frequency tuning combs	101

4.1.2	Frequency tuning by changing overlap.....	105
4.2	Shaped combs for nonlinearity tuning	107
4.2.1	1 st generation Nonlinearity Tuning Fingers	110
4.2.2	2 nd generation Nonlinearity Tuning Fingers [87].....	112
4.2.3	Simulink Simulations with Nonlinearity Tuning	117
4.2.4	Allan Deviation Results with and without Nonlinearity Tuning	119
4.3	Test Results on Quality Factor and Proof Mass Potential Relation	121
4.3.1	Electrical Model of a Resonator	121
4.3.2	Test Results on Q	123
4.4	Summary	127
Chapter 5	On-chip Compensation Approach and Measurement Results	129
5.1	Temperature Driven Stress Effects on Frequency.....	129
5.2	Pure Stress Effects on Frequency.....	134
5.2.1	Test Results with Three-Point Bending Testbed	134
5.2.2	Test Results with Four-Point Bending Testbed	139
5.3	Environmental Sensors in the SOI-MEMS Gyroscope.....	143
5.4	Stress Effects on ZRO and SF for Open-Loop Sense Mode	147
5.5	Test Results on Stress and Temperature Compensation at Ambient Temperature	152
5.6	Gyroscope Test Results with the Ovenized Testbed.....	154
5.6.1	Test Results with External Stress.....	157

5.6.2	Allan Deviation Results without External Stress.....	165
5.7	Discussion on Die Bonding and Stress Sensors.....	171
5.8	Summary	179
Chapter 6	Conclusions and Future Work	181
6.1	Conclusions	181
6.2	Future Work	188
Appendices.....		192
A.	Details of the SOI-MEMS Process.....	192
SOI-MEMS Process.....		192
Die Release Process		196
B.	Details of Vacuum Packaging.....	198
Getter Deposition Process.....		198
Vacuum Packaging Process		200
C.	Integrated Gyroscope Designs in TSMC MEMS and Tower Jazz Process	207
Integrated Gyroscope Design in TSMC MEMS Process.....		207
Integrated Gyroscope Design in Tower Jazz Process		212
D.	Details of the Gyroscope PCB	222
References.....		226

List of Figures

Figure 1.1: Description of Coriolis force, as the ball moves from point 1 to 2 it follows a straight line in inertial frame (b) and a curved path in rotating reference frame (c)..... 6

Figure 1.2: Concept of an ideal MEMS vibratory rate gyroscope. 8

Figure 1.3: Whole angle gyroscope operation, the drive axis follows the applied rotation with a very stable, geometrically defined angle coefficient. 8

Figure 1.4: Implementation of a rectangular MEMS gyroscope, image is taken from [31]..... 10

Figure 1.5: Stanford disc resonating gyroscope, image is taken from [35]. 10

Figure 1.6: Michigan μ HRG [21] (a), and UC Irvine μ HRG [22] (b)..... 11

Figure 1.7: Layout with the anchor locations marked with black (a), and modal shapes (b and c) of the three-fold symmetric SOI-MEMS gyroscope 12

Figure 1.8: SEM of the three-fold symmetric third generation SOI-MEMS gyroscope (a) with the location of the stress sensors highlighted and with the zoomed SEM images of the shaped frequency tuning combs (b), shaped nonlinearity tuning combs (c), and straight drive and sense combs (d). 13

Figure 1.9: Cartoon summarizing the design of the SOI-MEMS gyroscope..... 14

Figure 1.10: The first generation SOI-MEMS gyroscope, the zoomed image on the right shows the mode decoupling springs. 16

Figure 1.11: SEM of the (a) second generation SOI-MEMS gyroscope, (b) first generation shaped nonlinearity tuning fingers, and (c) shaped frequency tuning fingers. 17

Figure 1.12: Schematic of a 2-DoF spring-mass-damper system. 18

Figure 1.13: (a) Mechanical spring hardening force, and (b) electrostatic spring softening force 24

Figure 1.14: Amplitude (A) solutions with frequency for different β for increasing drive. 26

Figure 1.15: Phase (ϕ) solutions with frequency for different β for increasing drive.....	27
Figure 1.16: Practical up and down frequency sweeps on (a) the theoretical amplitude and (b) phase solutions.....	28
Figure 1.17: Drive and sense configuration for the SOI-MEMS gyroscope.	29
Figure 1.18: An equivalent configuration to Figure 1.17 that solves the stiction problem for the stress sensors by connecting the substrate to ground.....	31
Figure 2.1: FEA simulation results for 500 mW of heater power applied to one of the heaters, first Joule heating simulation to get the temperature map (a), and then thermal expansion simulation gives the anchor displacements (b).....	38
Figure 2.2: Three states of the device for different stress levels. Position 0 shows the initial state, Position + shows when an outwards directed stress is applied, and Position – shows when an inwards directed stress is applied to the device.	39
Figure 2.3: A comb drive with non-equal gaps due to external stress.....	41
Figure 2.4: The general simulation methodology.....	44
Figure 2.5: Simulation flow chart for NODAS simulations.	45
Figure 2.6: SEM of the SOI-MEMS gyroscope showing the separate sections.	46
Figure 2.7: NODAS schematic of the SOI-MEMS gyroscope with the detailed spring and side plate schematics.	46
Figure 2.8: AC magnitude and phase plots for drive displacement with gap mismatch $\Delta g = 10$ nm in drive combs before and after quadrature error cancellation.	48
Figure 2.9: AC magnitude and phase plots for sense displacement with gap mismatch $\Delta g = 10$ nm in drive combs before and after quadrature error cancellation.	48
Figure 2.10: ZRO and quadrature error vs. drive comb gap mismatch.	49

Figure 2.11: SF and drive displacement vs. drive comb gap mismatch.	50
Figure 2.12: Real world model of the transimpedance amplifier.	51
Figure 2.13: Measurement and NODAS simulation for the parasitic extractions with $V_{PM} = 0$ V.	51
Figure 2.14: Measurement and NODAS simulation with feedthrough and parasitics for the drive sweep.....	52
Figure 2.15: NODAS simulation results for a stress level of 1MPa including capacitive feedthrough and parasitics to ground.....	53
Figure 2.16: Test setup with the PCB and digital lock-in amplifier.	55
Figure 2.17: Gyroscope control architecture adapted from the IEEE standards [62].	56
Figure 2.18: Simulink model of the drive mode for PLL including the nonlinearities.	57
Figure 2.19: Simulink simulation result showing the drive PLL and amplitude control loop.....	59
Figure 2.20: Drive frequency vs. the frequency tuning voltage on the sense mode.	60
Figure 2.21: Mode matching by monitoring the quadrature amplitude.	61
Figure 2.22: Tuning voltage and measured quadrature signal amplitude during extremum seeking.	62
Figure 2.23: Simulink simulation results (a) and experimental measurements (b) for the drive displacement for different tuning voltages on the sense mode.	62
Figure 2.24: Mode matching with pilot tones around the drive frequency.....	64
Figure 2.25: Simulink simulation for the mode matching voltage (up) and the phase of the mode match (down) signals.	65
Figure 2.26: Tuning voltage on the sense (a) and drive resonance frequency drift (b) during the pilot tone mode matching experiment.....	67

Figure 2.27: Gyroscope front end and the circuits.....	69
Figure 2.28: Gyroscope front end with the noise sources.....	70
Figure 2.29: Power spectral density of the open-loop sense mode on the air table with and without the air connection.....	74
Figure 2.30: Allan deviation plots for the circuit noise when the instrumentation amplifier gain is 1 and 20.....	75
Figure 2.31: Block diagram of the force-feedback controller for the sense mode.	77
Figure 3.1: SOI-MEMS process fabrication steps.	81
Figure 3.2: SEMs of the SOI device backside for the standard recipe with excessive undercut (a) and the custom recipe with less undercut (b).....	83
Figure 3.3: Different approaches for vacuum testing the gyroscope, (a) vacuum chamber, (b) and (c) using a tubular vacuum packaged system, and (d) using hermetic epoxy to glue a lid in vacuum.	84
Figure 3.4: (a) Cartoon for the die mount tool, (b) the photo of the die mount tool, and (c) an activated nanofoil.....	87
Figure 3.5: A MEMS gyroscope mounted on ceramic DIP40 with nanofoil.	87
Figure 3.6: Shadow mask for getter deposition (a), and the metal lid with Ti/Au getter.	88
Figure 3.7: Metal lid with the getter before and after activation at different temperatures.....	91
Figure 3.8: Temperature profile used during vacuum packaging.	92
Figure 3.9: Vacuum packaging system.	93
Figure 3.10: Inside of the vacuum chamber showing (a) the details, (b) the top piece for sample movement and shutter, and (c) the cartridge heater.	94
Figure 3.11: Cross sectional schematic of the vacuum packaging system.	95

Figure 3.12: Schematic for the hermetic seal of the cartridge heater.	95
Figure 3.13: A vacuum packaged ceramic DIP40.	96
Figure 3.14: Frequency sweeps before vacuum packaging with $Q=20$ (a), and after vacuum packaging with $Q=23,000$ (b).	96
Figure 4.1: A MEMS capacitor with an arbitrary gap profile.....	99
Figure 4.2: Symmetrically placed shaped comb fingers on the layout.	100
Figure 4.3: A gap profile for the shaped frequency tuning (a), and an SEM of the fingers (b).	102
Figure 4.4: Calculated and simulated total capacitance for the shaped frequency tuning fingers shown in Figure 4.3.....	102
Figure 4.5: Derivative (dC/dx) of the simulated capacitance for shaped frequency tuning combs.	103
Figure 4.6: Measured tuning curve for the shaped frequency tuning combs.....	103
Figure 4.7: Frequency tuning by changing the overlap.	105
Figure 4.8: Simulated total capacitance for a finger tapering of $c=0.4\mu\text{m}$	106
Figure 4.9: Derivative (dC/dx) of the simulated capacitance for the total capacitance shown in Figure 4.8.	106
Figure 4.10: Up and down frequency sweeps in Simulink including the tip capacitances for 35 V dc on the proof mass, 23 V frequency tune and various ac drive amplitudes.....	108
Figure 4.11: Experimental frequency sweeps for the two modes for a straight mounted device (a.1-3), and for a 45° mounted device (b.1-3).....	109
Figure 4.12: SEM image of the first generation nonlinearity tuning fingers, the finer shape includes frequency and nonlinearity tuning at the same time.	110

Figure 4.13: Experimental frequency sweeps for different dc tuning potentials on the first generation nonlinearity tuning fingers.....	111
Figure 4.14: Total double sided simulated capacitance for the finger profile in 4.14 for $g_0 = 6.5 \mu\text{m}$, $x_{01} = 6 \mu\text{m}$, and $x_{03} = 7500 \mu\text{m}^3$	111
Figure 4.15: dC/dx for the total double sided capacitance shown above in Figure 4.14.....	112
Figure 4.16: (a) The cubic nonlinearity tuning finger gap profile and (b) SEM of the fingers..	113
Figure 4.17: Simulated total double sided capacitance for the 2 nd generation nonlinearity finger in Figure 4.16 with $g_0 = 2 \mu\text{m}$, and $x_{03} = 2500 \mu\text{m}^3$	113
Figure 4.18: dC/dx for the total capacitance shown above in Figure 4.17.	114
Figure 4.19: Measured up and down sweeps with increasing cubic tune potential for 600 mV ac for 15 μm finger-tip to anchor spacing.	114
Figure 4.20: Extracted cubic nonlinearity coefficient vs. applied voltage, the coefficients are derived using the curves in Figure 4.19.....	114
Figure 4.21: Measured up and down sweeps with increasing cubic tune potential for 900 mV ac for 15 μm finger-tip to anchor spacing.	116
Figure 4.22: Measured up and down frequency sweeps for 10.7 μm drive displacement with and without nonlinearity tuning for 20 μm finger-tip to anchor spacing for 40 V dc proof mass, 600 mV ac drive, and 0 V frequency tuning potential. The nonlinearity is set for 10.5 V dc potential to tune the cubic nonlinearity.....	116
Figure 4.23: Simulink simulations for PLL settling point vs PLL output voltage for various hardening levels.	118

Figure 4.24: Theoretical amplitude and phase solutions for the up (solid) and down (dashed) sweeps (a), PLL frequency when the quiescent frequency is higher than the resonance (upper figure), and lower than the resonance (lower figure) (b).	119
Figure 4.25: Measured Allan deviation test results with varying drive displacements with and without nonlinearity tuning.	120
Figure 4.26: Equivalent electrical model for one mode of the gyroscope.	122
Figure 4.27: Cartoon showing the locations of the fingers in the gyroscope.	124
Figure 4.28: Resonance test-bench schematic: dc voltage V_{PM} is applied to the rotor and V_{AC} is applied through the stator fingers.	125
Figure 4.29: Q of one mode of the gyroscope when tested from outer and inner combs for different V_{PM} .	126
Figure 4.30: Q- V_{PM} curves for three different devices, exhibiting similar behavior.	126
Figure 4.31: Proposed design for the gyroscope, drive and sense fingers are located side by side so no current flows on the proof mass.	127
Figure 5.1: Cross section (a) and top view (b) of the test setup to observe the temperature induced stress effects on frequency. Glass thermally isolates the die.	130
Figure 5.2: Measured frequency sweeps for different power levels for Mode 1.	131
Figure 5.3: Measured frequency sweeps for different power levels for Mode 2.	131
Figure 5.4: Comparison of simulated and measured frequency shifts for Mode 1 (a) and Mode 2 (b).	132
Figure 5.5: Location of the Mode 1 and Mode 2 spring with respect to the DIP40 (a), expected frequency shifts with and without temperature under compressive and tensile stress (b), measurement with increased heater power on Mode 1 (c).	133

Figure 5.6: Measurement and simulation results for a 45° mounted gyroscope (a). Cartoon of a 45° mounted gyroscope with respect to DIP40 (b)..... 133

Figure 5.7: Three-point bending stress testbed, metal block between the PCB and hardwood acts as a pivot. 134

Figure 5.8: Actual implementation of the three-point bending testbed. A tubular vacuum system is used..... 135

Figure 5.9: Simulated shape of the package with stress applied to the package edges (a). Simulated and measured frequency shifts with respect to the package edge displacement for mode x (b), and mode y (c). The gyroscope is mounted straight with respect to the package. 136

Figure 5.10: Simulated shape of the package with external stress applied to the package edges (a). Simulated and measured frequency shifts with respect to package edge displacement for mode x and mode y (b). The gyroscope is mounted 45° with respect to package recess..... 137

Figure 5.11: The displacement map (a) and y-axis stress map (b) of the folded flexures for a +y longitudinal anchor displacement. 138

Figure 5.12: The displacement map (a) and y-axis stress map (b) of the folded flexures for a +z transverse anchor displacement. 138

Figure 5.13: Four-point bending testbed, applying a load on the top Al fixture creates almost a uniform stress on the MEMS gyroscope..... 139

Figure 5.14: $\Delta R/R$ for the four silicon piezoresistors located on each side of the gyroscope during the calibration run. 140

Figure 5.15: Actual implementation of the four-point bending test (a), and the measurement and simulation results for mode x and y (b). 141

Figure 5.16: Simulated frequency shifts for the two modes of the gyroscope for different angles between the package recess and the MEMS gyroscope.....	142
Figure 5.17: SEM image of the third generation SOI-MEMS gyroscope with stress sensor locations highlighted	143
Figure 5.18: Wheatstone bridge stress sensor configuration to cancel temperature effects (a), stress and temperature sensitive released SOI piezoresistor, R_{stress} (b), temperature sensitive released SOI resistor, R_{nostress} (c).....	145
Figure 5.19: $\Delta R/R$ for R_{nostress} and R_{stress} over temperature.....	146
Figure 5.20: $\Delta R/R$ for R_{nostress} and R_{stress} under a four-point compressive bending test.	146
Figure 5.21: Wheatstone bridge outputs for S_3 and S_4 showing different sensitivities due to the die mount.	147
Figure 5.22: Four-point bending stress testbed used to test the vacuum packaged gyroscope on the rate table. Adding weights on the setup creates compressive bending stress.	148
Figure 5.23: 45° die mount (a). Transformation matrix between stress and gyroscope parameters (b), each parameter is dominated by a single stress component.	149
Figure 5.24: Drive mode frequency shift vs. stress sensor S_2 (a), and sense mode frequency shift vs. stress sensor S_1 (b), both of the shifts are linear with stress.....	150
Figure 5.25: Scale factor test results for different stress levels on sense mode stress sensor (S_1).	150
Figure 5.26: Zero rate output (ZRO) vs sense-axis stress (S_1).	151
Figure 5.27: Uncompensated Allan deviation test results of a SOI-MEMS gyroscope.	152
Figure 5.28: x axis stress (a), y axis stress (b), temperature (c), and uncompensated ZRO with just temperature fitting and stress and temperature fitting (d).....	153

Figure 5.29: Allan deviation test results for the uncompensated, temperature compensated, and stress and temperature compensated ZRO.....	154
Figure 5.30: Ovenized gyroscope stress testbed. Adding weight creates compressive stress on the die.....	155
Figure 5.31: External stress test results. Changes in uncompensated and compensated gyroscope ZRO (a), drive frequency and on-chip resistive temperature sensor (b), drive-axis stress sensor S_2 (c), and sense-axis stress sensors S_1 and S_3 (d).....	158
Figure 5.32: Allan deviation of the gyroscope ZRO for uncompensated, temperature compensated, stress compensated, and stress and temperature compensated cases.....	160
Figure 5.33: Second external stress test where a copper weight is moved from left to right for stress modulation. Temperature control not shown.	161
Figure 5.34: Result of second external stress test. Changes in uncompensated and compensated gyroscope ZRO (a), and outputs from the drive frequency and on-chip resistive temperature sensor (b), drive-axis stress sensor S_2 (c), and sense-axis stress sensors S_1 and S_3 (d).....	162
Figure 5.35: Allan deviation plots for uncompensated and stress, temperature, and stress and temperature compensated data.....	163
Figure 5.36: Open-loop frequency sweeps for the drive mode when the copper weight is on the right and left.....	164
Figure 5.37: Open-loop frequency sweep for the intentionally detuned sense mode when the copper weight is on the right and left.	164
Figure 5.38: ZRO of the ovenized gyroscope for different values of frequency mismatch between the drive and sense modes.....	165

Figure 5.39: Long term measurement data for a test without external stress. Changes in uncompensated and compensated ZRO (a), and outputs from the drive frequency and on-chip resistive temperature sensor (b), from the drive-axis stress sensor S_2 (c), and from the sense-axis stress sensors S_1 and S_3 (d).	166
Figure 5.40: Allan deviation of the gyroscope ZRO for the uncompensated, temperature compensated, and stress and temperature compensated cases.....	168
Figure 5.41: Allan deviation results for uncompensated and compensated ZRO for test #1.	169
Figure 5.42: Allan deviation for uncompensated ZRO and compensated ZRO for test #2.....	170
Figure 5.43: Allan deviation for uncompensated ZRO and compensated ZRO for test #3.....	170
Figure 5.44: Uncompensated and compensated raw ZRO for the three Allan deviation tests in Figure 5.41 through Figure 5.43. The average compensation coefficients in Table 5.1 is used.	171
Figure 5.45: Response of the environmental sensors when copper weight is added on top the gyroscope in Figure 5.33.....	172
Figure 5.46: Environmental sensor outputs of a different gyroscope at fixed temperature when the copper weight is moved from left to right and vice versa.....	173
Figure 5.47: Environmental sensor outputs of a different gyroscope in response to a temperature change.	174
Figure 5.48: Backside view of the gyroscope after it is demounted from the DIP40.....	174
Figure 5.49: (a) Manual nanofoil activation from one side, and (b) balanced nanofoil activation from corners using wirebonding.	176
Figure 5.50: Backside images of the manual activated and wirebond activated samples.	176

Figure 5.51: The simulated temperature distribution of the stress sensors in vacuum for 5 V V_{DD} .	178
Figure 5.52: Zoomed view of Figure 5.51 to show the temperature difference between $R_{nostress}$ and R_{stress} .	178
Figure 6.1: The current design for R_{stress} (a) and $R_{nostress}$ (a).	188
Figure 6.2: The proposed design for R_{stress} for thermal matching to $R_{nostress}$.	188
Figure 0.1: Tools needed to cut the solder preform.	201
Figure 0.2: Standalone cut solder preform and solder preform on the dummy package.	202
Figure 0.3: Inside of the vacuum chamber (a), and the top piece that houses the package holder and shutter.	204
Figure 0.4: Layout of the integrated TSMC MEMS gyroscope.	208
Figure 0.5: Pad map of the NO_CKT TSMC MEMS gyroscope.	209
Figure 0.6: 1/8 th of the TSMC-MEMS gyroscope layout with the fingers labeled.	210
Figure 0.7: Measured resonance curves from one of the TSMC MEMS gyroscopes, the device is mounted 45° with respect to the package recess.	211
Figure 0.8: Proposed vacuum packaging approach to solve the low quality factor problem of the TSMC MEMS gyroscopes.	212
Figure 0.9: Layout of the integrated Tower Jazz gyroscope.	213
Figure 0.10: Pad distribution of the Tower Jazz gyroscope.	214
Figure 0.11: Layout image of the Tower Jazz gyroscope with the finger labels.	215
Figure 0.12: ESD protection bridges for the input of the charge amplifiers.	216
Figure 0.13: Optical image of the 1/4 th of the Tower Jazz gyroscope.	216
Figure 0.14: Optical image of the 1/8 th of the Tower Jazz gyroscope.	217

Figure 0.15: Testbed for the Tower Jazz gyroscope.	217
Figure 0.16: Scope screen shot for scan chain testing.	218
Figure 0.17: Comparison between the SOI temperature resistor and CMOS temperature sensor, both of them are measuring the ambient temperature.....	219
Figure 0.18: Temperature sensor measurement results from three different sensors.	220
Figure 0.19: Test results from one of the normal stress sensors in a stress testbed.....	221
Figure 0.20: Photograph of the gyroscope PCB.	223
Figure 0.21: Photograph of the Gyro PCB and the Connection PCB.....	225

List of Tables

Table 2.1: Phase summary of the gyroscope signals.	40
Table 2.2: Extracted parasitic values	52
Table 2.3: Mode matching voltages for different modulation frequencies.....	66
Table 2.4: The constants and SOI-MEMS gyroscope parameters.....	68
Table 2.5: Circuit components and corresponding noise values.....	70
Table 2.6: Summary of the noise sources at V_{out}	71
Table 4.1: Total capacitance for different gap profiles.....	101
Table 4.2: Electrostatic forces for different gap profiles.....	101
Table 4.3: Comparison of shaped and linearly tapered fingers in the same layout area.....	107
Table 4.4: Typical values of the equivalent circuit parameters for the gyroscope tested in this thesis.	123
Table 5.1: Individual compensation coefficients of the three individual coefficients and their average.....	168
Table 6.1: Comparison of the state of the art commercial and research gyroscopes with the gyroscope studied in this work.	187
Table 0.1: Summary of the components.	224
Table 0.2: The pin map of the connection PCB.....	225

Chapter 1 Introduction

The first MEMS gyroscope was introduced by the Draper Laboratory in the early 90's [1]. Over the past twenty five years, micro-gyroscope performance has improved as a result of extensive research, and advancements in fabrication technologies and readout electronics. Today MEMS inertial sensors are widely used in various fields such as consumer electronics, automotive, medical, defense and aerospace industries for orientation detection, stabilization, and navigation. The consumer electronics segment of the inertial sensors market was over \$2B in 2013 according to a Yole Développement report [2] and the high performance MEMS gyroscope market was estimated around \$200M for 2014 [3]. MEMS is expected to continuously increase its share in the high performance gyroscope market by replacing the conventional bulky and expensive counterparts by offering a competitive or better performance at small size and low cost. This thesis proposes stress, temperature, and nonlinearity compensation techniques for high performance MEMS gyroscopes to further improve their performance.

1.1 Thesis Goal

The main goal of this thesis is solving the long term gyroscope drift problem by measuring the stress and temperature of the mechanical structure with on-chip stress sensors. Towards that end, this thesis first presents a simulation methodology that couples finite element analysis and circuit solver to understand the relation between stress and zero rate output (ZRO). This simulation methodology is then validated with stress tests on an in-house fabricated and vacuum packaged SOI-MEMS gyroscope. Our validation studies first focused on understanding the effects of stress and temperature on MEMS gyroscope resonance frequencies. Subsequently, after the

development of a vacuum packaging system, and of gyroscope control loops, the effect of stress on ZRO was validated with the use of on-chip stress sensors. The stress sensors consist of released fixed-fixed and folded SOI resistors connected in a Wheatstone bridge configuration.

This chapter starts with providing a literature review of the MEMS gyroscopes with the current research trends and the motivation for stress compensation. Next the gyroscope operation and different MEMS gyroscope types are explained. The chapter continues with solving the gyroscope equations with and without the cubic nonlinearity. Then the details of the gyroscope biasing and front end are provided. The chapter ends with the thesis contributions and thesis outline.

1.2 Thesis Motivation

Performance of micro-gyroscopes is determined by resolution, drift, scale factor, and zero rate output (ZRO) [4]. Scale factor has the unit of $V/^\circ/s$, and is the change of the output voltage per unit applied rotational rate. ZRO is the output of the gyroscope without any applied rotational rate due to the imbalances in the device. In the absence of rotation, the gyroscope ZRO is the sum of white noise and other noise that more slowly varies with time. White noise defines the resolution of the sensor and is also known as angle random walk (ARW). ARW is specified for 1 Hz bandwidth in the units of $^\circ/hr/\sqrt{Hz}$ or $^\circ/\sqrt{hr}$. The peak-to-peak value of more slowly varying “pink” noise determines the bias (offset) instability that is expressed in $^\circ/hr$. The bias instability represents a limit on resolution that cannot be improved upon by time averaging the signal. The noise and drift of a gyroscope is measured with an Allan variance test. The Allan variance is a method of representing the root mean square (rms) random drift error as a function of averaging time [5]. The gyroscope ZRO is recorded while the gyroscope is standing still and the Allan variance method is applied to the ZRO data to extract the noise and drift.

Temperature has been found to be one of the important sources of long term drift, and current state of the art gyroscopes use temperature compensation [6], [7]. Temperature compensated high performance commercial MEMS gyroscopes are already available. The Sensoror STIM210 gyroscope offers temperature compensated $0.5^\circ/\text{hr}$ bias instability and $0.15^\circ/\sqrt{\text{hr}}$ angle random walk (ARW) [8], and the Analog Devices ADIS16136 gyroscope offers temperature compensated $4^\circ/\text{hr}$ bias instability and $0.167^\circ/\sqrt{\text{hr}}$ ARW [9]. Temperature affects gyroscope operation by affecting the material properties, and by causing different amounts of expansion in the different materials comprising a gyroscope, thus inducing stress. Along with temperature and temperature-induced stress variations that can be captured by temperature sensing, environmental stress variations are a second significant source of long-term drift in well-designed micro-gyroscopes. However, to our knowledge, stress compensation is not employed in the literature nor in commercial MEMS gyroscopes.

Although not compensated actively, stress effects on MEMS inertial sensors have been studied previously. The effect of temperature induced die warpage on an anodically vacuum packaged gyroscope was measured by Moiré interferometry in [10]. Temperature induced stress changes the gyroscope resonance frequencies and the sensitivity to stress was reduced by switching from a fixed-fixed to a folded beam suspension [10], [11]. The thermal coefficient of expansion (TCE) mismatch between the packaging cap and sensor material is responsible for the die warpage. Analog Devices minimized the effect of stress on their MEMS accelerometers by carefully designing the anchor locations [12]. The anchor locations are the key components in understanding stress effects since the interaction between the MEMS and environment is established through the anchors. The interaction between the MEMS and package is also important; for example, thermally induced stress can be as high as 50 MPa, and the die-mount

adhesive has to be thick and very compliant for the least stress transferred to the die [13]. However, using a thick and compliant adhesive is generally not an option due to low outgassing and high quality factor (Q) requirements of vacuum packaged gyroscopes. A distributed system-level nodal modeling of the die bonding process has been studied and experimentally modeled on a microbridge in [14].

The die attachment area between the MEMS and package determines the amount of stress transferred to the MEMS from the package. A compliant metal interposer that isolates the MEMS structure from package stress has been shown in [15]. The metal interposers are compliant and mount the MEMS to the package from three points around the periphery. A similar approach involves fabricating a metallic suspension die attach tool that bonds to the package from the center and bonds to the MEMS around the periphery. The center to periphery connection is established by folded springs that relieve the stress [16]. Yet another approach to minimize the stress is mounting the MEMS die just from the center using elongated structures [17]. A simpler and more practical implementation of this method is simply mounting the MEMS to the package just from the center using a solder preform [18]. As die attach area is reduced, the stress effects on frequency is reduced. In addition to optimizing the die attach to minimize the stress effects, stress relief structures can be formed around the periphery of the MEMS die by etching cavities [19].

The Hemispherical Resonator Gyroscope (HRG) is an example of a topology that suppresses stress propagation from the substrate to the gyroscope structure [20]. The HRG is a 3D wine glass gyroscope with one central anchor that minimizes the stress effects on the actual vibrating structure. HRG is machined from quartz and hermetically sealed in high vacuum environment. Due to the low loss of the quartz material, high vacuum and its design, the HRG quality factor is 26 million, leading to its superior performance with $0.06 \text{ milli}^\circ/\sqrt{\text{hr}}$ ARW and $0.005^\circ/\text{hr}$ bias

instability. The major drawbacks of the HRG is its size (30 mm in diameter) and high cost (~\$100k). There is research being conducted to manufacture miniaturized MEMS versions of the HRG at lower cost and smaller size. MEMS HRG fabrication requires new 3D fabrication technologies and low loss materials for high Q. The current research uses micro-scale blow torching where high heat is used to shape fused silica into a 3D graphite mold [21] or micro glass blowing where fused silica is bonded to a titania silica glass substrate and heated up to 1700°C [22]. Q factor values over 1 million are obtained with these processes. Operating these 3D wine glass structures as a gyroscope is still an ongoing research topic. The central anchor in the HRG design approach has also been applied to planar MEMS gyroscopes [6], [23].

Although stress effects can be reduced by exploiting these above approaches, a finite residual stress on the die will exist due to the inevitable TCE difference between the MEMS device and its surroundings. In addition, even constant temperature testing of a state-of-the-art MEMS gyroscope in an oven exhibits long term drift [24]. While a central anchor point on the gyroscope rotor can relieve stress, the stator electrodes in an electrostatic gyroscope may still displace relative to the rotor due to stress effects. All of these issues motivates the implementation and study of a gyroscope with on-chip stress compensation.

This thesis focuses on ZRO compensation; however, there are also studies in the literature focusing on scale factor compensation. Scale factor drifts are also as important since they lead to inaccurate rotation rate measurements. The current state-of-the-art techniques include fabricating on-chip calibration stages and running the scale factor calibration continuously. The calibration stage is fabricated from a piezoelectric (PZT) material, the gyroscope is mounted on the stage, and the reference calibration rotational rate is obtained by a diffractive optics metrology in [25]. A two-

axis PZT calibration stage is proposed in [26] with capacitive threshold detection to obtain the reference calibration rate.

1.3 Gyroscope Operation and Different Gyroscope Structures

The operation of a MEMS gyroscope relies on the Coriolis force [27]. The Coriolis force was first published by the French scientist Gaspard-Gustave de Coriolis. Figure 1.1 describes the Coriolis force. Assume the blue circle is a spinning disk and there is an observer (red dot) on the edge and a ball (black dot) on the center. Once the ball is pushed towards the observer, the ball follows a straight line according to an observer in the non-rotating inertial frame of reference as shown in Figure 1.1.b. However, for an observer in the same rotating reference frame with the ball, the ball follows a curved path due to the Coriolis force as shown in Figure 1.1.c.

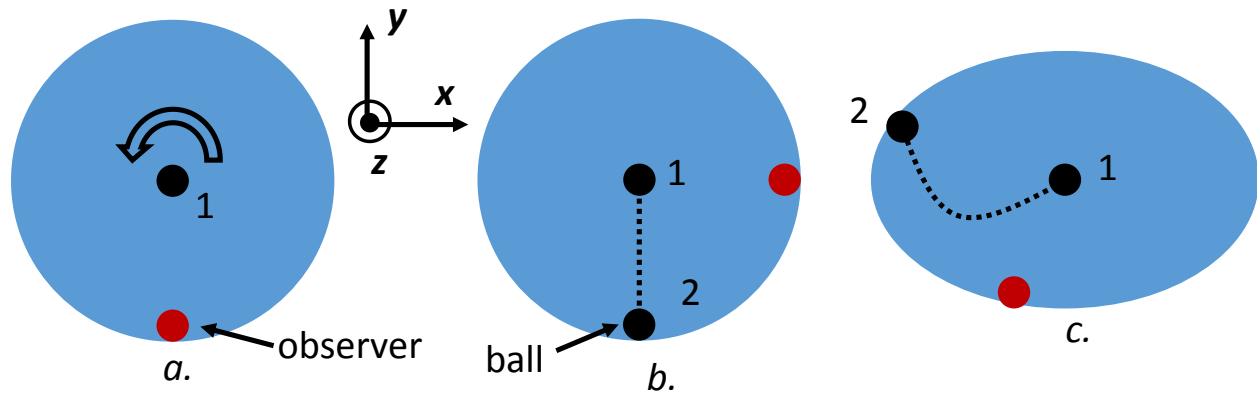


Figure 1.1: Description of Coriolis force, as the ball moves from point 1 to 2 it follows a straight line in inertial frame (b) and a curved path in rotating reference frame (c).

The Coriolis force occurs only in the rotational frame of reference and so is an apparent force that is proportional to the mass and velocity of the ball, and to the rotational rate of the spinning disc, and is orthogonal to both the velocity and rotation rate vectors. Coriolis force is expressed as:

$$F_{Coriolis} = ma_{Coriolis} = -2m\Omega \times v \quad 1.1$$

where m is the mass of the ball, Ω is the rotational speed of the disc, and v is the speed of the ball in the rotating inertial reference frame.

Figure 1.2 presents the concept of an ideal MEMS vibratory rate gyroscope that detects the Coriolis force and thus the rotational speed in the inertial frame of reference. A proof mass is vibrated at its resonance frequency using a feedback oscillator loop; this continuously vibrating mode is called the drive mode. The mass is moving back and forth along the x axis in the rotating reference frame for this case. When the proof mass is rotated about the z axis by an angular rotation Ω , then Coriolis force will be exerted on the proof mass in the y direction in the rotating reference frame. In the case of a perfect, ideal gyroscope, the proof mass will oscillate along a straight line inclined in the x - y plane, with the amount of inclination (θ) set by the rotational rate. As the general solution with non-idealities, the Coriolis force will cause the proof mass to follow an elliptical path in the rotating reference frame. The displacement in the x and y directions are detected by the sensing electrodes, and y displacement amplitude is a measure of rotational rate Ω . We look at the amplitude of the sense displacement to extract the rotational rate and for that reason this class of operation is called an amplitude modulated (AM) gyroscope.

If the drive axis of the proof mass is not constrained, and is free to rotate, then the drive axis rotates with the rotational rate as illustrated in Figure 1.3. The angle the drive axis shifts follows the applied angle by a geometry defined very stable coefficient [20]. This type of operation is called the whole angle operation that is identical to operation of a Foucault pendulum [28]. The output is directly proportional to the rotation angle and there is no bandwidth limitation in whole angle operation. However, tracking the drive-axis orientation in space requires complicated control electronics (the drive axis still vibrates but the axis of vibration shifts with the rotation), and whole

angle operation requires high Q and, at most, a very small frequency split between the degenerate modes of the gyroscope.

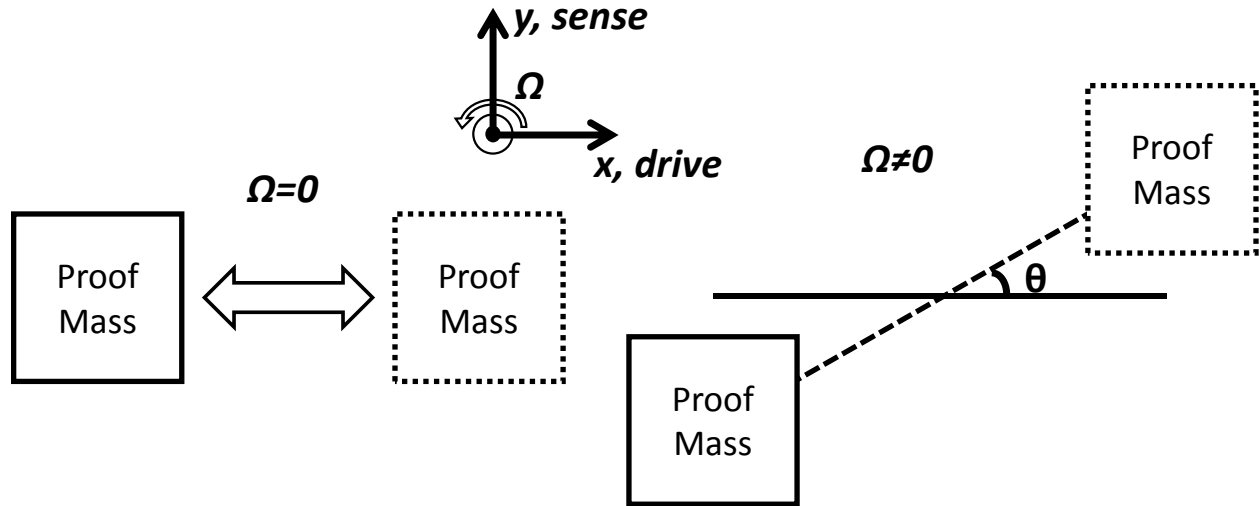


Figure 1.2: Concept of an ideal MEMS vibratory rate gyroscope.

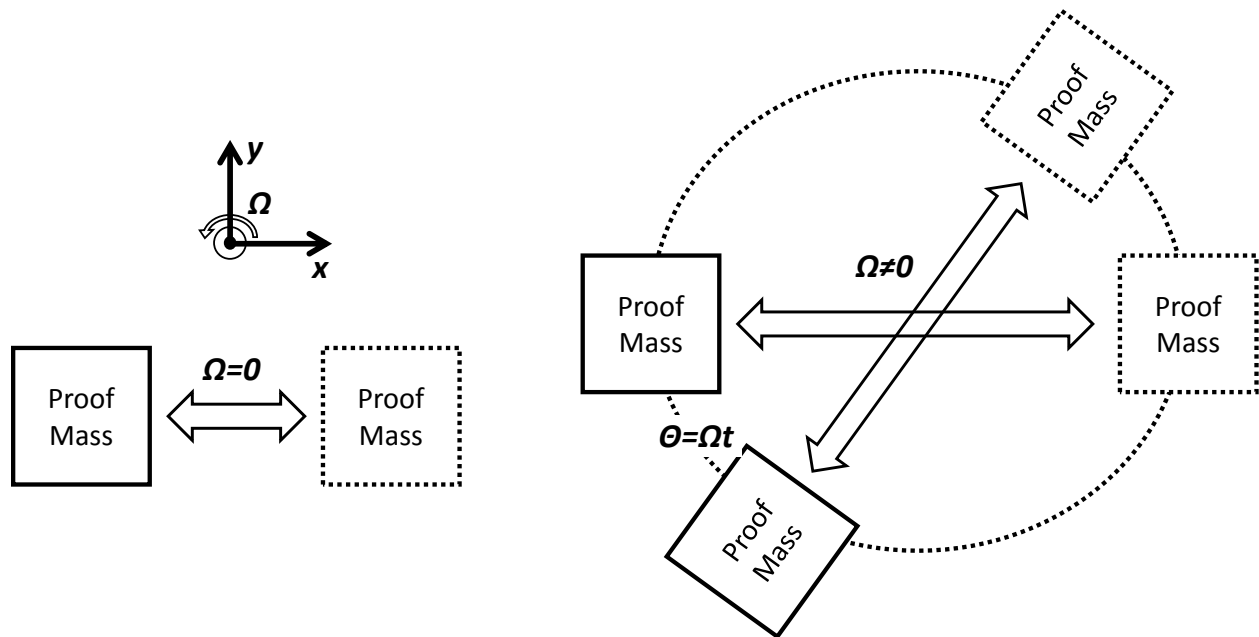


Figure 1.3: Whole angle gyroscope operation, the drive axis follows the applied rotation with a very stable, geometrically defined angle coefficient.

As an alternative to the AM operation, recently frequency modulated (FM) gyroscopes have been proposed by researchers [29], [30]. Both axes of the gyroscope are driven into resonance in FM operation, so the proof mass in Figure 1.2 moves on a circular path. In the presence of a non-zero

rotational rate (Ω), the proof mass rotation frequency increases or decreases leading to an increase or decrease in the resonance frequencies. This resonance frequency change is the applied rotation rate (Ω). Note that frequency and rotational rate has the same units. FM operation has very high range, very high bandwidth, and is more stable compared to AM operation since the output is directly frequency. But $1^\circ/\text{s}$ is $1/360$ Hz (~ 3 mHz) and detecting small rotational rates at a 10 kHz resonance frequency, typical of practical MEMS structures, requires sophisticated electronics.

A MEMS gyroscope can be classified in several different ways. Here, we classify them into two categories depending on their layout. The first category is the rectangular gyroscopes, and Figure 1.4 shows the implementation of a rectangular MEMS gyroscope [31]. The device has two identical modes; Figure 1.4.a shows the drive mode and Figure 1.4.b shows the sense mode. The central proof mass is free to move in the drive and sense directions, and couples the Coriolis force from drive to sense. The suspension decouples the drive and sense displacement for independent capacitive detection of each mode. The proof mass vibrates at its resonance frequency along the drive mode. In the presence of a rotation about the z -axis, the sense mode starts vibrating at the drive resonance frequency, which is detected by the sense comb interdigitated-finger capacitors. Various other rectangular MEMS gyroscope designs can be found in the literature, such as frame gyroscopes in which either the drive or sense proof mass is physically located within the other mode's proof mass. Examples of frame gyroscopes are the METU gyroscope [32] and Analog Devices gyroscope [33].

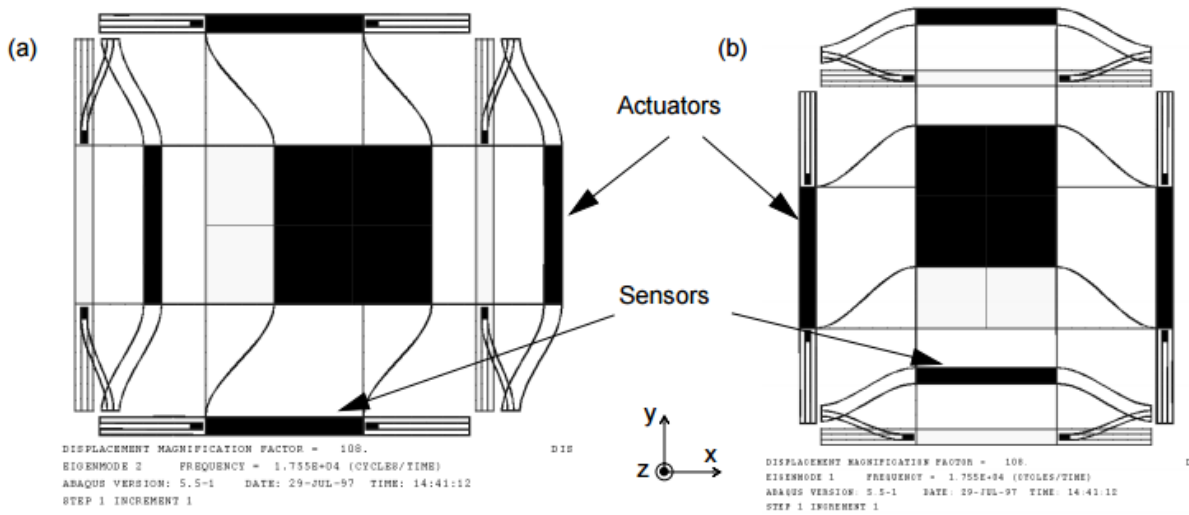


Figure 1.4: Implementation of a rectangular MEMS gyroscope, image is taken from [31].

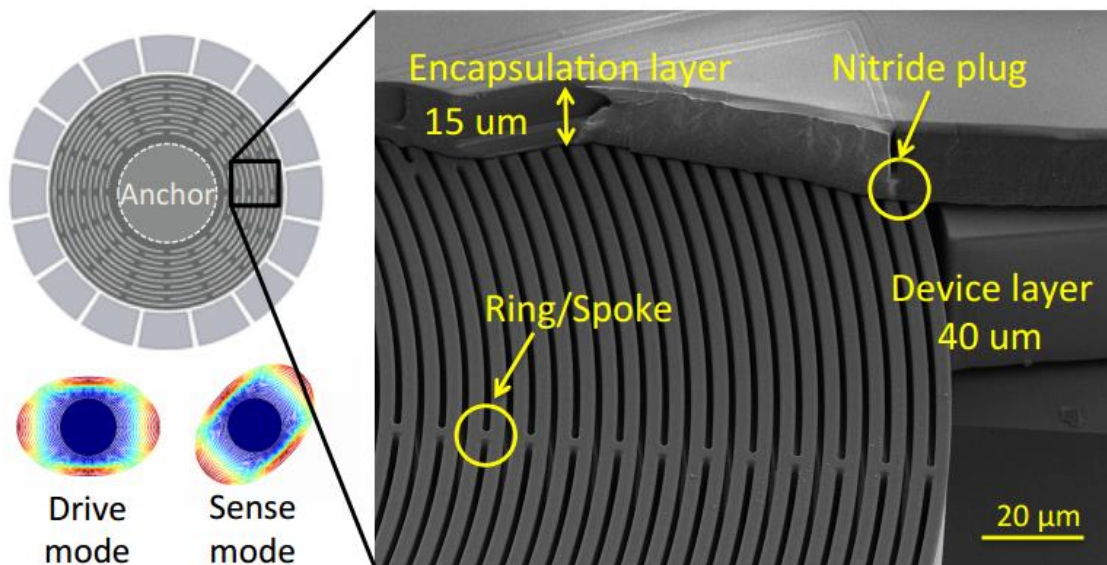


Figure 1.5: Stanford disc resonating gyroscope, image is taken from [35].

The second gyroscope category is the circular gyroscopes. Circular gyroscopes are either implemented in the form of a vibrating disc [6], [35], [36] or shell [34]. Instead of using dedicated flexures and rigid masses as in the rectangular gyroscopes, the modal shape of the circular gyroscopes includes distributed motion of a whole disc or bending of a shell structure. Figure 1.5 shows the disc resonating gyroscope (DRG) that is fabricated in the Stanford epi-seal silicon process [35]. The gyroscope has two degenerate modes. The operation is similar to the rectangular

gyroscopes; the drive mode is driven into resonance and sense mode is excited with the Coriolis force. The design includes slots on the mass to decrease the resonance frequency; otherwise a solid mass would have high resonance frequency in the order of MHz. One advantage of the circular design is the reduced frequency mismatch between the modes due to the inherent symmetry of the circular gyroscope structure. A further example of the DRG is the Boeing DRG [6]. μ HRGs can also be classified as the 3D version of the DRGs. These are the miniature versions of the classic HRG. Figure 1.6 shows the Michigan μ HRG [21] and UC Irvine μ HRG [22]. High resonance frequency disk gyroscopes also exist in the literature [36].

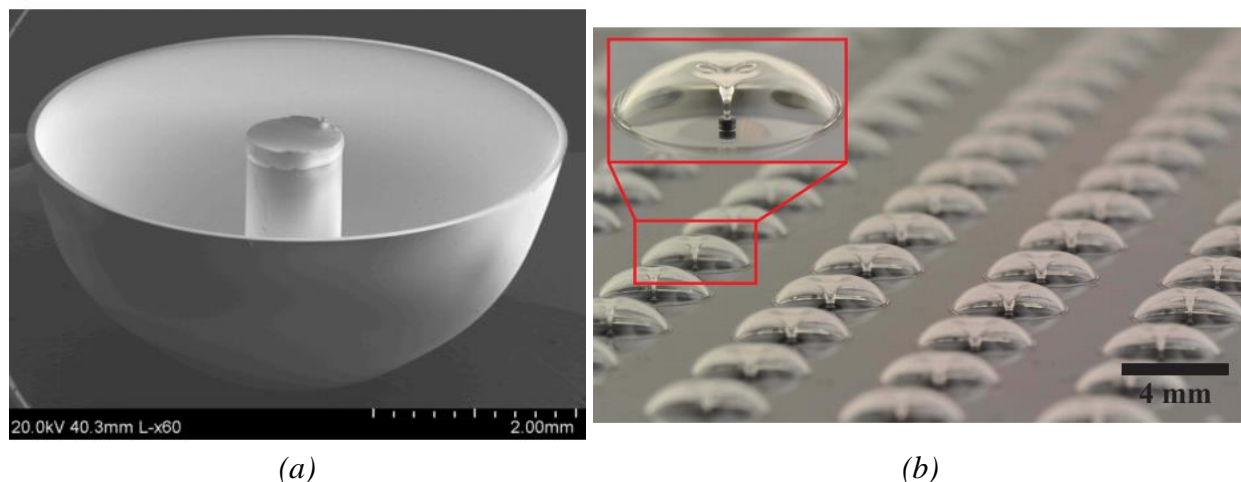


Figure 1.6: Michigan μ HRG [21] (a), and UC Irvine μ HRG [22] (b).

1.4 SOI-MEMS Gyroscope

This thesis focuses mainly on the three-fold symmetric, single mass, z-axis SOI-MEMS gyroscope. The gyroscope structure is similar to the designs of CMU [31], METU [37], and UC Irvine [38]. The SOI-MEMS gyroscope in this thesis extends the state of the art of three-fold symmetric designs by introducing three new features. The first involves using folded beams for suspension to improve the force-displacement linearity. The second are shaped combs for frequency and nonlinearity tuning. The third and the most important design feature is including stress sensors on

four sides to achieve stress compensation. Differential and quad-mass gyroscope structures are known to suppress the environmental vibration and shock [39], [40] and to improve the quality factor [41]. A single mass structure is chosen for the gyroscope used in this thesis since the main motivation of the thesis is to understand the environmental stress and temperature effects on the gyroscope, and having a single mass structure helps on fundamental understanding.

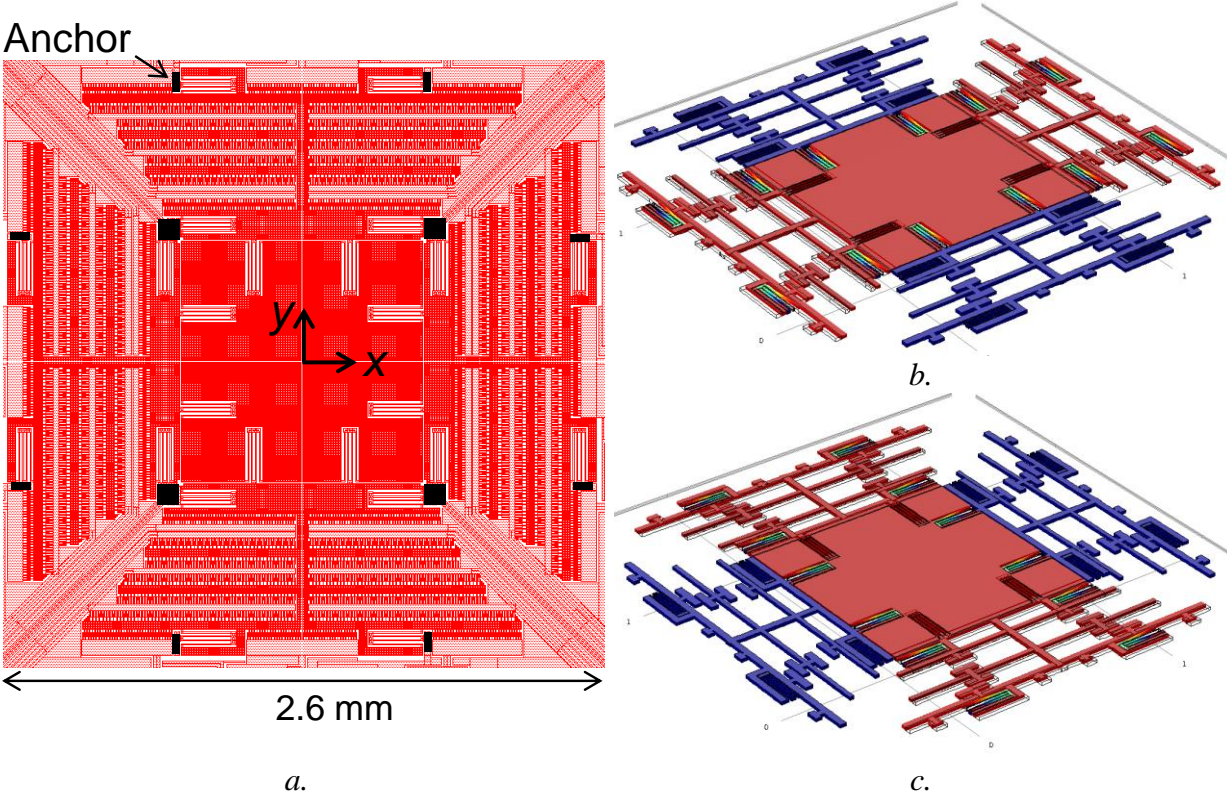


Figure 1.7: Layout with the anchor locations marked with black (a), and modal shapes (b and c) of the three-fold symmetric SOI-MEMS gyroscope

The gyroscope is designed to have two identical modes. Figure 1.7 shows the layout of the gyroscope with the anchor locations marked with black and first two modal shapes obtained with the eigenfrequency simulation in FEA. The gyroscope is three-fold symmetric, i.e., symmetric in the x , y , and diagonal axes. Either of the modes can be used as drive or sense due to the symmetry, and the design is suitable to switch in between the drive and sense modes to cancel offsets due to

mismatch in fabrication symmetry. The anchor regions for the springs are marked since the device interacts with its environment through the anchors. Both modes are designed identical with a resonance frequency of 10 kHz. As one of the modes is excited and moves, the other mode is kept stationary due to the design of the suspension system. The third mode is the out-of-plane mode that is around twice the frequency of the in-plane modes.

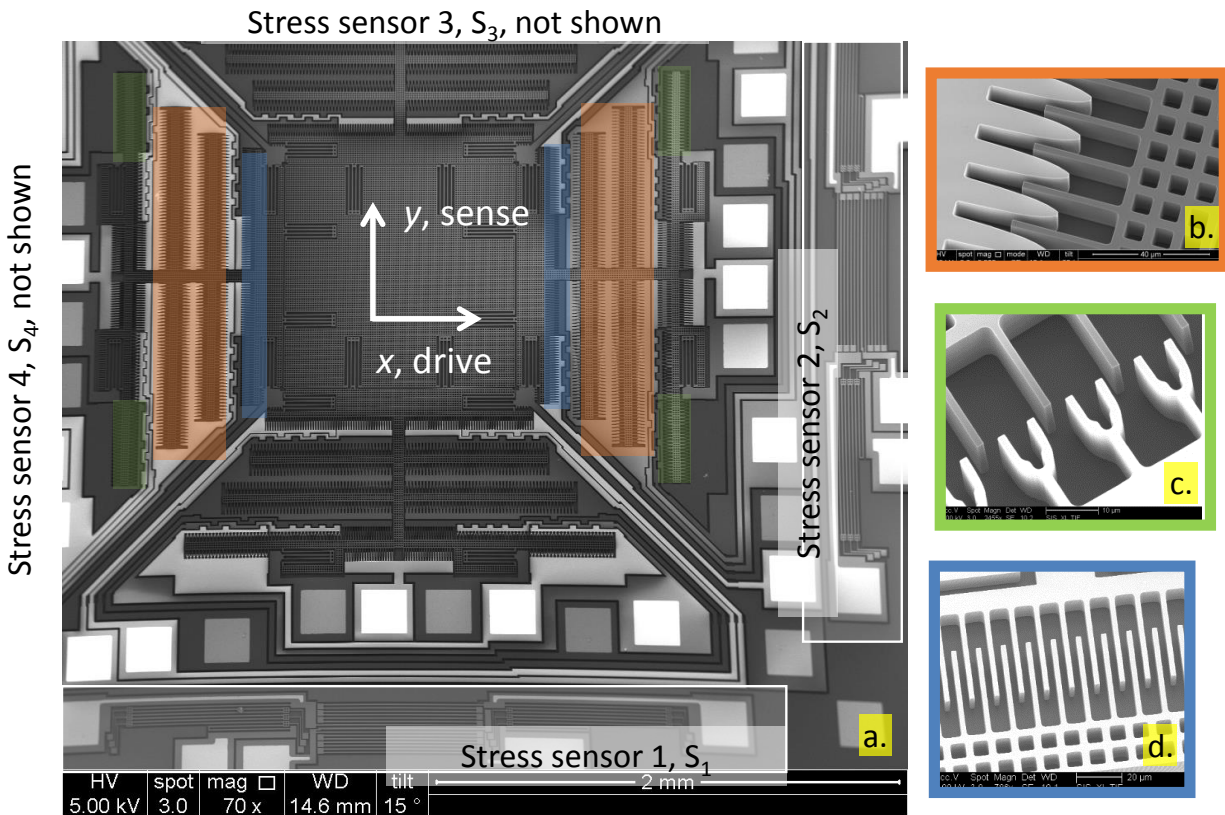


Figure 1.8: SEM of the three-fold symmetric third generation SOI-MEMS gyroscope (a) with the location of the stress sensors highlighted and with the zoomed SEM images of the shaped frequency tuning combs (b), shaped nonlinearity tuning combs (c), and straight drive and sense combs (d).

The design of the SOI-MEMS gyroscope has been updated throughout the course of this thesis study. Although the mechanical structure basically stayed the same there were updates on the types of fingers used and on the environmental sensors. There are three different types of designs referred as first generation, second generation, and third generation SOI-MEMS gyroscope in the

text of this thesis. The first and second generation designs are explained later in this section. Figure 1.8 presents a SEM of the third generation design. The third generation SOI-MEMS gyroscope includes stress sensors on four sides (highlighted white in Figure 1.8.a) and the different types of fingers (zoomed images of which are shown Figure 1.8.b-c). The details of the stress sensors will be explained in the following Chapter 5. The gyroscope includes three different types of fingers. The straight combs are used for driving the gyroscope and sensing the output current (Figure 1.8.d). The shaped frequency tuning combs are used to tune the frequency mismatches coming from the fabrication process (Figure 1.8.b). The shaped nonlinearity tuning combs are used to tune the softening nonlinearity at high drive displacements (Figure 1.8.c).

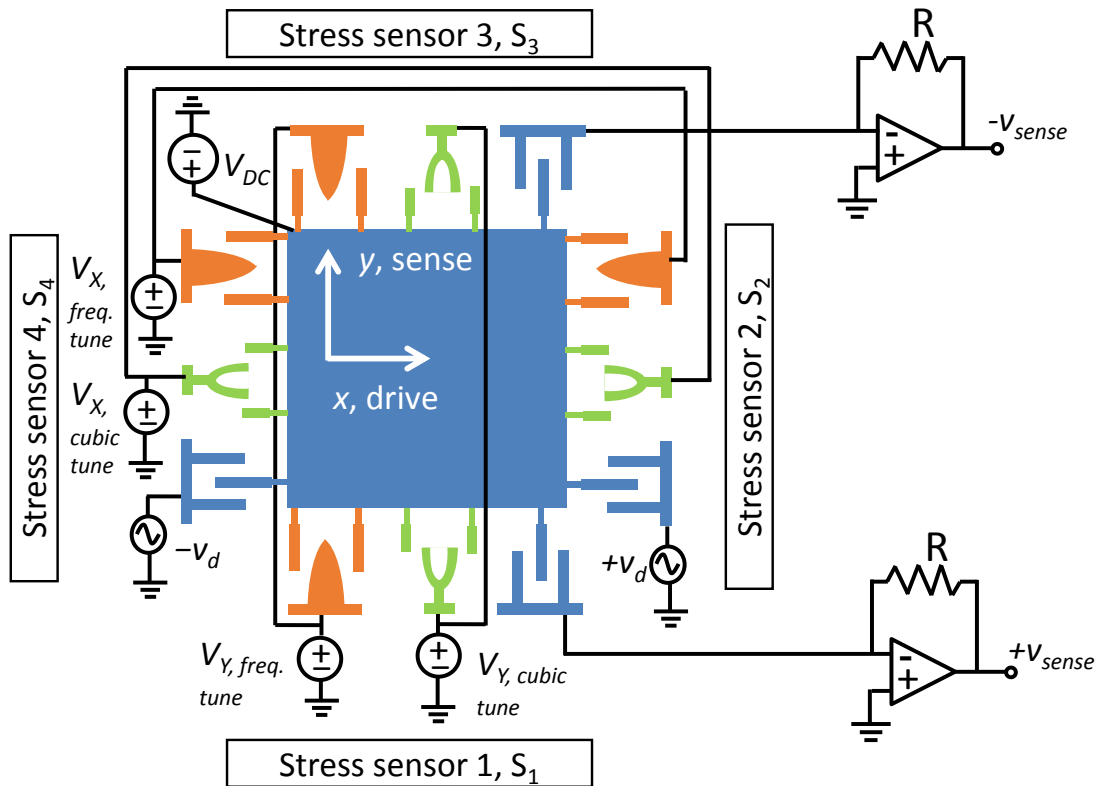


Figure 1.9: Cartoon summarizing the design of the SOI-MEMS gyroscope

In addition to the detailed SEM images in Figure 1.8, Figure 1.9 provides a cartoon that summarizes the design architecture of the SOI-MEMS gyroscope. The different types of combs

are placed on the layout symmetrically. The shaped frequency and nonlinearity tuning combs are controlled by a dc voltage. The gyroscope is activated by capacitive drive with the fingers connected to the $+v_d$ and $-v_d$ sources in Figure 1.9. The gyroscope is sensed by capacitive detection with the fingers connected to the input of the transimpedance amplifier in Figure 1.9. A high dc voltage on the proof mass amplifies the input ac electrostatic drive and the output ac motional currents. Stress sensors, located on each side of the gyroscope die, capture the normal stress in either x or y directions depending on its orientation. Stress sensors can also be configured to measure change in temperature. The overall idea is to match the modes using the frequency tuning combs, to increase the drive displacement and keep the frequency response still linear with the shaped nonlinearity combs, and to compensate the environmental stress and temperature effects with the use of stress sensors on each side.

Figure 1.10 shows the SEM of the first generation SOI-MEMS gyroscope and the zoomed view of the mode decoupling springs. The first generation gyroscope includes straight fingers for electrostatic drive and shaped linear frequency-tuning fingers. The design also includes on-chip silicon heaters marked with red as Heater 1-4 in Figure 1.10, and resistors to measure the on-chip temperature are made with gold deposited on top of the SOI silicon and marked with blue RTD 1-4 in Figure 1.10. The metal temperature sensing resistors (RTD 1-4) did not work in this design since the silicon underneath contributed a significant resistance and the equivalent resistance shifted due to both stress and temperature. The design comprises back-to-back located rotors and stators that form parallel-plate capacitors without any fingers ($C_{\text{back to back}}$ in Figure 1.10) and that lead to significant softening nonlinearity in the measurements.

Figure 1.11 presents the SEM image of the second generation SOI-MEMS gyroscope. The second generation design replaced the back-to-back capacitances with first generation nonlinearity tuning

fingers shown in Figure 1.11(b). Shaped linear frequency-tuning fingers were included and are shown in Figure 1.11(c). This gyroscope also includes on-chip silicon heaters and temperature sensing resistors made with gold deposited on top of the SOI silicon. The designed nonlinearity finger shape did not produce cubic hardening. In the final third generation design that is shown in Figure 1.8, the nonlinearity tuning fingers were redesigned with a new shape function and stress sensors were redesigned using released SOI resistors in the device layer.

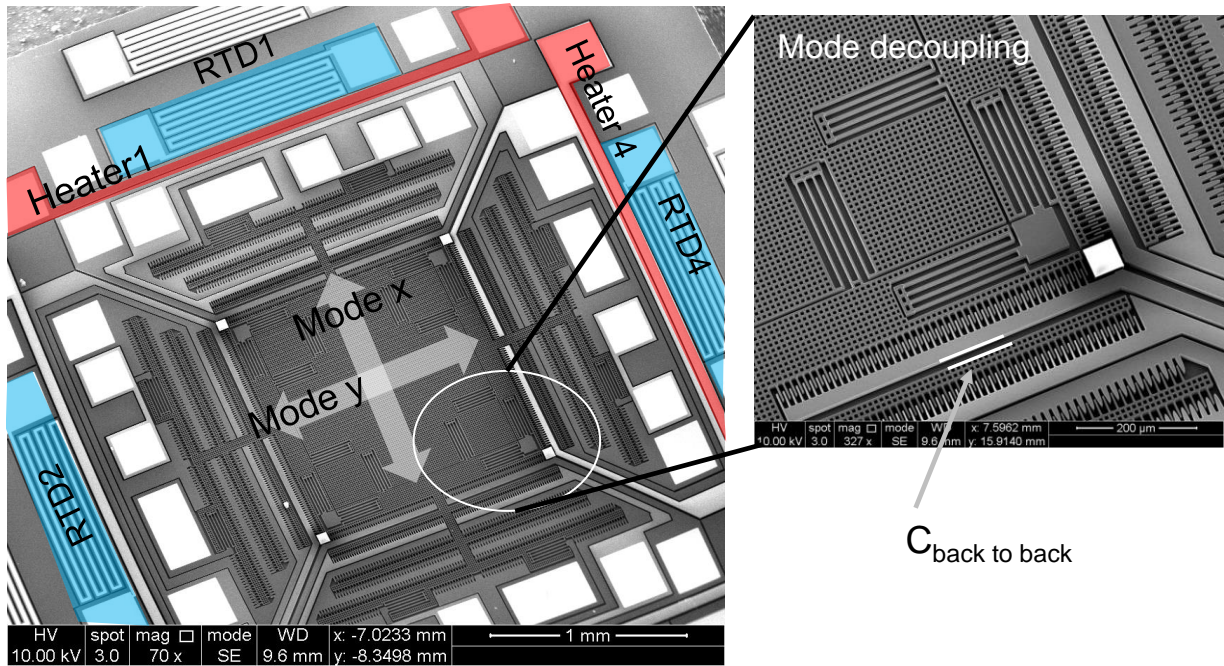


Figure 1.10: The first generation SOI-MEMS gyroscope, the zoomed image on the right shows the mode decoupling springs.

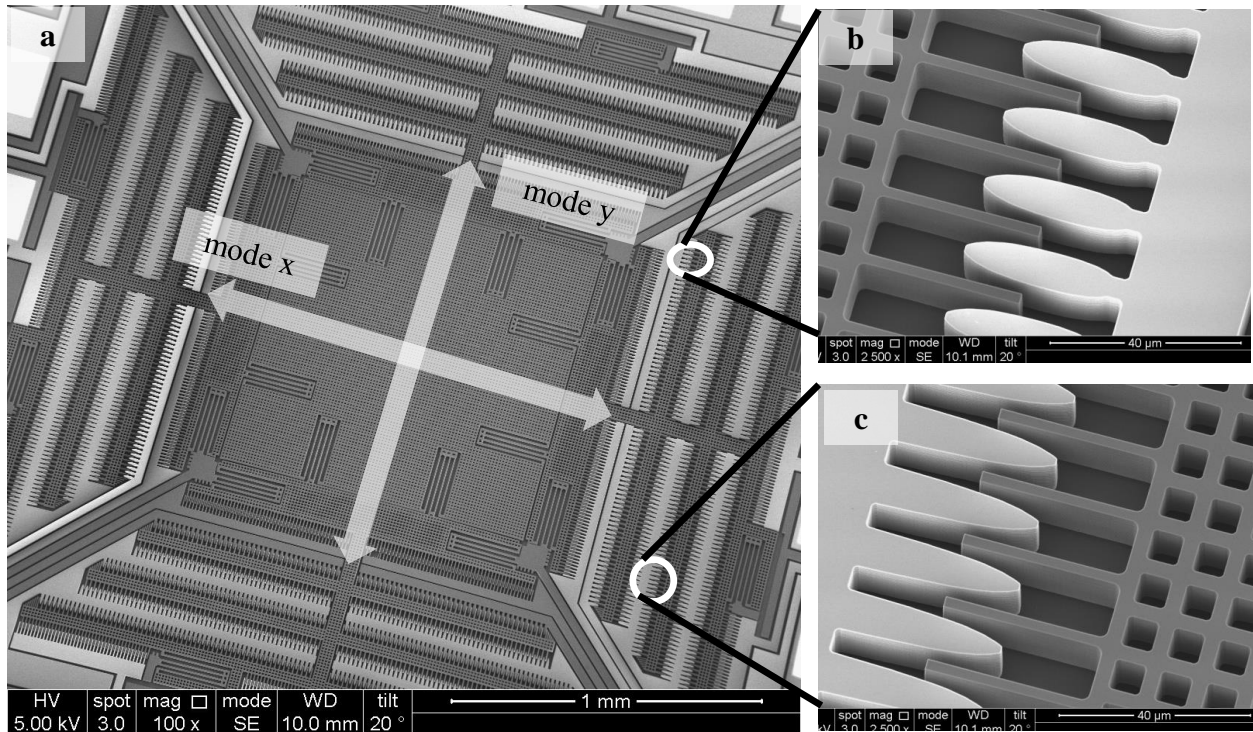


Figure 1.11: SEM of the (a) second generation SOI-MEMS gyroscope, (b) first generation shaped nonlinearity tuning fingers, and (c) shaped frequency tuning fingers.

1.5 Gyroscope equations

A gyroscope consists of drive and sense axes, and with the application of a rotation Coriolis force excites the sense mode through the coupling to the proof mass as explained in the previous section. The gyroscope with the drive and sense modes can be modeled as a two degree-of-freedom (DoF) system with 2nd order spring-mass-damper differential equations. Figure 1.12 shows the schematic of a 2-DoF spring-mass-damper system. The x and y axes are assumed to be drive and sense modes, respectively.

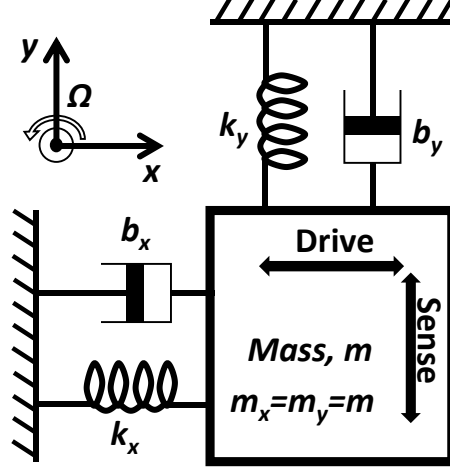


Figure 1.12: Schematic of a 2-DoF spring-mass-damper system.

Simplified equations of motion for a rate gyroscope are [42]:

$$m_x \ddot{x} + b_x \dot{x} + k_x x = F_d + \underbrace{2m_x \Omega \dot{y}}_{\text{Coriolis Force}} + \underbrace{m_x \Omega^2 x}_{\text{Centripetal Force}} + \underbrace{m_x \dot{\Omega} y}_{\text{Angular Acceleration}} \quad 1.2$$

$$m_y \ddot{y} + b_y \dot{y} + k_y y = -2m_y \Omega \dot{x} + m_y \Omega^2 y - m_y \dot{\Omega} x \quad 1.3$$

where m is the mass, b is damping, k is spring constant, x is the drive displacement, y is the sense displacement, Ω is the applied rotation rate, and F_d is the applied drive force. Subscripts x and y denote the drive and sense axes, respectively. Under typical operation conditions, drive displacement is in the order of micrometers, the sense displacement is in the order of nanometers, and sense displacement is zero for the closed-loop force-feedback operation. So, Coriolis force on the drive mode originating from the sense displacement can be neglected with respect to F_d . The gyroscope resonance frequency is typically 10 kHz. This frequency is orders of magnitude larger than the bandwidth of Ω that would make Coriolis and centripetal forces comparable on the drive mode; both of these inertial-based forces are much smaller than F_d . Centripetal force on the sense mode is also orders of magnitude smaller than the Coriolis force (assuming that the gyroscope is located at the center of rotation). However, if the gyroscope is located at a large offset from the

center of rotation, a considerable centripetal force may act on the gyroscope at high rotation rates which leads to a dc force that can offset the capacitive gaps. In a precision high-rotation application, mounting the gyroscope as close as the center of rotation is critical in terms of minimizing the effects of the centripetal force. For example, if the gyroscope is off center by 1 cm, the centripetal force at a rotational rate of 10 revolutions/s (3600°/s) creates a gap mismatch of 7.8 pm for the gyroscope studied in this thesis.

Angular acceleration on the drive mode can be neglected since the sense displacement is either small or zero. The angular acceleration on the sense mode can be comparable in magnitude to the Coriolis force, however since the bandwidth of the input rotation is assumed less than 100 Hz (which is 100 times less than the resonance frequency), the sense mode angular acceleration can also be ignored. So the simplified equations are

$$\ddot{x} + \frac{b_x}{m_x} \dot{x} + \omega_x^2 x = \frac{F_d}{m_x} \quad 1.4$$

$$\ddot{y} + \frac{b_y}{m_y} \dot{y} + \omega_y^2 y = -2\Omega \dot{x} \quad 1.5$$

$$\omega_x = \sqrt{k_x/m_x}, \quad 1.6$$

$$\omega_y = \sqrt{k_y/m_y}, \quad 1.7$$

Taking the Laplace transform of 1.4, and assuming the drive mode is driven at its resonance frequency, the drive displacement after some manipulations is

$$X(j\omega_x) = -j \frac{Q_x}{k_x} F_d(j\omega_x) \quad 1.8$$

where $Q_x = \sqrt{k_x m_x}/b_x$ is the quality factor of the drive mode. The sense displacement is found by combining 1.8 and 1.5 as

$$Y(j\omega_x) = -2\Omega \frac{Q_x}{k_x} \omega_x F_d(j\omega_x) \frac{1}{(\omega_y^2 - \omega_x^2) + \frac{\omega_y}{Q_y} j\omega_x} \quad 1.9$$

According to Eqn 1.9, maximum sensitivity (i.e., sense displacement in the y-axis due to an input rotation rate Ω) is obtained when the drive and the sense mode are matched, i.e. $\omega_x = \omega_y$. However, the bandwidth is reduced to ω_y/Q_y in open-loop sense mode for matched mode operation. In this thesis, the gyroscope is operated in a mode matched condition with a closed-loop sense mode to have appropriate sensing bandwidth (20 Hz). Equation 1.9 is rewritten in the time domain [43] by assuming a sinusoidal rotation with

$$\Omega(t) = \Omega \cos(\omega_\Omega t) \quad 1.10$$

$$F_d(t) = |F_d| \cos(\omega_x t) \quad 1.11$$

$$y(t) = -\frac{Q_x}{k_x} \omega_x \Omega |F_d| A_y \left\{ \cos((\omega_x - \omega_\Omega)t + \varphi_y) + \cos((\omega_x + \omega_\Omega)t + \varphi_y) \right\} \quad 1.12$$

where

$$A_y = \left[(\omega_y^2 - \omega_x^2)^2 + \left(\frac{\omega_x \omega_y}{Q_y} \right)^2 \right]^{-1/2} \quad 1.13$$

$$\varphi_y = -\tan^{-1} \left(\frac{\omega_x \omega_y}{Q_y (\omega_y^2 - \omega_x^2)} \right) \quad 1.14$$

As can be seen in Eqn. 1.12, the motion of the gyroscope in the sense axis is no longer at the drive resonance frequency (ω_x). Instead it consists of two parts that are equally separated from ω_x by the rate frequency (ω_Ω). The bandwidth of the gyroscope is the ω_Ω at which the gain drops by 3 dB from the peak gain, i.e., the gain when $\omega_\Omega = 0$. The sense mode output depends on the quality factor, spring constant, and drive and sense frequencies as seen in Eqn 1.12, and these parameters

have to be kept constant for robust gyroscope operation. Stress and temperature, the main source of variations considered in this thesis, affect these gyroscope parameters that in turn lead to a drift or zero rate output (ZRO) at the gyroscope output.

Further simplifications can be made to 1.9 depending on gyroscope operation conditions. By assuming drive and sense resonance frequencies are close to each other,

$$Y(j\omega_x) = -2\Omega j\omega_x X \frac{1}{2\omega_x(\omega_y - \omega_x) + jBW\omega_x} \quad 1.15$$

where X is the drive displacement at the drive resonant frequency of ω_x defined by 1.8 and $BW = \omega_y/Q_y$ is the open-loop bandwidth.

The drive displacement is kept as it is for simplicity. If the gyroscope is operating at mismatched conditions, i.e., $2\Delta\omega = 2(\omega_y - \omega_x) \gg BW$ then sense displacement is

$$Y(j\omega_x) \approx \frac{-2\Omega j\omega_x X}{2\omega_x \Delta\omega} = -\frac{jX\Omega}{\Delta\omega} \quad 1.16$$

If the gyroscope is operating at matched conditions i.e. $BW \gg 2\Delta\omega$ then sense displacement is

$$Y(j\omega_x) \approx \frac{-2\Omega j\omega_x X}{jBW\omega_x} = -\frac{2X\Omega}{BW} \quad 1.17$$

The sense displacement in response to the rate at matched conditions is multiplied by $2\Delta\omega/BW$ compared to the operation conditions with a mismatch of $\Delta\omega$. The sense mode response to rotational rate is directly proportional to $\Delta\omega$ in mismatch operation and directly proportional to Q in matched mode operation.

Thermal noise floor of the gyroscope determines the resolution. The rate equivalent noise can be found by dividing the Brownian noise force [44] to the unit Coriolis force:

$$\Omega_{noise} = \frac{\sqrt{4k_B T b_y}}{2m_y \omega_x X (\pi/180)} = \frac{180}{\pi} \sqrt{\frac{k_B T \omega_y}{m_y Q_y \omega_x^2 X^2}} \quad 1.18$$

where k_B is the Boltzmann's constant, T is the temperature and X is the drive displacement. So large mass, large quality factor, and large drive displacement are needed for a lower noise gyroscope. The drive displacement has the most dominant effect, and in general, once the gyroscope is vacuum packaged, mass and quality factor are fixed but the drive displacement can still be controlled. The increased drive displacement leads to nonlinearity and this thesis proposes a comb interdigitated-finger capacitive tuning structure to solve the nonlinearity problem that is addressed in Chapter 4. The gyroscopes are vacuum packaged to suppress the air damping and increase the quality factor and Chapter 3 explains the details of the developed vacuum packaging system.

Although it seems in 1.18 that a higher drive resonance frequency reduces the noise floor, the drive and sense resonance frequencies have to be increased at the same time for a gyroscope and Q also depends on the resonance frequency. The ring down time $\tau=Q/\pi f$, where f is the resonance frequency in Hz ($\omega=2\pi f$), an important metric for whole angle gyroscope operation [41], requires low resonance frequencies for longer ring down times. However, if the gyroscope resonance frequency is set to low frequencies (e.g., 1 to 2 kHz), then the gyroscope becomes vulnerable to environmental vibrations. So to make the gyroscope relatively robust with respect to the environmental vibrations, the resonance frequency is set around 10 kHz for the gyroscope in this thesis. Although rare, there are gyroscopes that have resonance in the MHz regime in the

literature [36], but they require nanogaps and special processing since the MHz resonance frequency leads to very stiff structures.

1.6 Gyroscope Equations with the Cubic Nonlinearity

High drive displacement improves the signal to noise ratio (SNR) of a gyroscope as seen in 1.18 but also leads to a nonlinear force displacement behavior that is observable as a hysteresis in the frequency-phase and frequency-amplitude relations [45]. The source of the nonlinearities is either due to springs which results in a hardening nonlinearity or due to electrostatic force which normally results in a softening nonlinearity. Figure 1.13 summarizes the hardening and softening forces that lead to nonlinearities. F is the force, x is the displacement, k_l is the linear spring coefficient, k_3 is the cubic spring coefficient, C_{tip} is the finger-tip to truss capacitance, ϵ is the permittivity, A is the area of C_{tip} and d is the gap between the finger tip and truss in Figure 1.13. Hardening occurs because of tension arising in the beams in the springs; as they bend more, the force displacement relation is no longer linear and force increases cubically as the displacement is larger. A design approach that minimizes the spring nonlinearity problem is given in [46]. The softening force occurs due to the fringe-field tip capacitances between the finger tips and anchors in the comb drives. When the comb finger tips (when d_{anchor} in Figure 1.13.b is large) are far from the anchor, these fringe fields can be neglected as they remain very small when the comb is displaced. However, at large displacements, the comb finger tips are displaced close to the anchor. In such a condition, the fringe fields change more with displacement. The electrostatic force depends on the displacement generating the nonlinearity. The fringe-field electrostatic force causes softening since the force has a positive spring coefficient while it is on the right hand side of the equation of motion in 1.4 or 1.5, the spring coefficient becomes negative once moved to the left hand side.

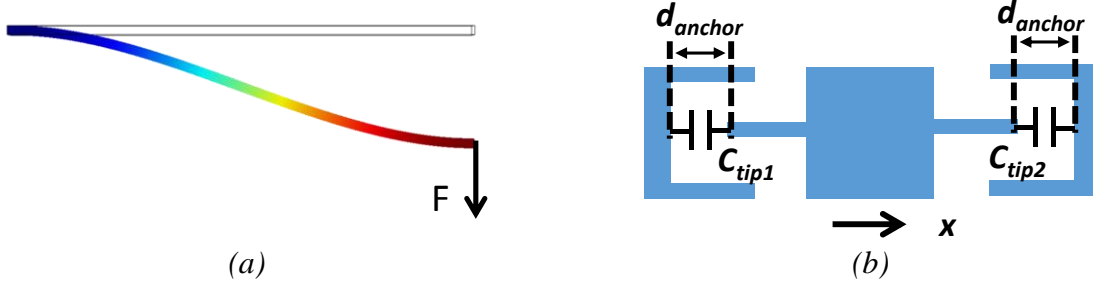


Figure 1.13: (a) Mechanical spring hardening force, and (b) electrostatic spring softening force

The hardening force arising from mechanical spring tension as in Figure 1.13.a is given by

$$F_{hardening}(x) = k_1x + k_3x^3 \quad 1.19$$

while the softening force arising from electrostatic spring effects as in Figure 1.13.b is given by

$$F_{softening}(x) = \frac{\partial(C_{tip1} + C_{tip2})}{\partial x} = \epsilon A \left(\frac{4x}{d^3} + \frac{8x^3}{d^5} \right) \quad 1.20$$

where k_1 and k_3 are the linear and cubic spring coefficients in 1.19. **Error! Reference source not found.** C_{tip} is the tip to truss capacitance, d is the tip to anchor distance (d_{anchor}), ϵ is the permittivity, and A is the area in 1.20. **Error! Reference source not found.** The device may exhibit either of the softening or hardening nonlinearities depending on its design and operating conditions. The gyroscope studied in this thesis uses folded beams and is mounted to the package in a stress-free way as will be explained in Chapter 3. Both of these design features suppresses the hardening nonlinearity. In addition, a relatively high dc voltage on the order of 25V to 35V is applied to the proof mass, which increases the electrostatic softening force. As a result of the design and biasing, the gyroscope in this thesis exhibits an overall softening nonlinearity. The thesis proposes a cubically shaped comb finger design that introduces a dc voltage controlled hardening force to cancel out the softening nonlinearity.

Softening and hardening nonlinearities have been simulated and measured in [45] and [47]. One major concern is the stability of closed-loop oscillations in the presence of nonlinearities with hysteresis, but it has been demonstrated that the closed-loop system is stable since the phase-amplitude relation is single valued [48]. Stable operation in a closed-loop drive mode under a softening nonlinearity on a MEMS disc resonator gyroscope has been shown in [49]. The effects of nonlinearity on bias instability and angle random walk (ARW) have been characterized. Although ARW decreases with increasing drive displacement in [49], a solid conclusion of the relationship between the drive displacement and bias instability cannot be drawn. This thesis shows that bias instability can be improved by cancelling the softening nonlinearity.

The nonlinearities in an oscillator are modeled by the Duffing equation [50] as:

$$\ddot{x} + \frac{\omega_0}{Q} \dot{x} + \omega_0^2 x + \beta x^3 = -\alpha \sin(\omega_f t) \quad 1.21$$

where β is the cubic nonlinearity coefficient, and the right hand side is the sinusoidal forcing function. Equation 1.21 is normalized with mass (m), and solved by assuming a sinusoidal steady state amplitude and phase at the forcing function frequency (ω_f), i.e. $x(t) = A \cos(\omega_f t + \phi)$. The derivatives are taken and then plugged into the equation, 3ω terms due to x^3 are ignored in the solution assuming the gyroscope has a high quality factor so they will be highly suppressed. The solution is obtained by matching the coefficients of the sines and cosines. The amplitude solution (A) is the roots of the equation:

$$\frac{9}{16} \beta^2 A^6 + \frac{3}{2} \omega^2 \beta A^4 + (\xi^2 + \omega^4) A^2 - \alpha^2 = 0 \quad 1.22$$

$$\omega^2 = \omega_0^2 - \omega_f^2 \quad 1.23$$

$$\xi = \frac{\omega_0 \omega_f}{Q} \quad 1.24$$

The phase solution (ϕ) is the roots of the equation:

$$\tan(\phi) = -\frac{\omega^2 + \frac{3}{4}A^2\beta}{\xi} \quad 1.25$$

Figure 1.14 and Figure 1.15 show the amplitude (A) and phase (ϕ) solutions with respect to the forcing function frequency ($\omega_f/2\pi$) for different β for increasing drive displacement. SOI-MEMS gyroscope parameters, i.e., $k = 94.3762$ N/m, $m = 3.08 \times 10^{-8}$ kg, $Q = 4750$, and $\beta = \pm 5.4 \times 10^9$ N/m³, were used in the solutions.

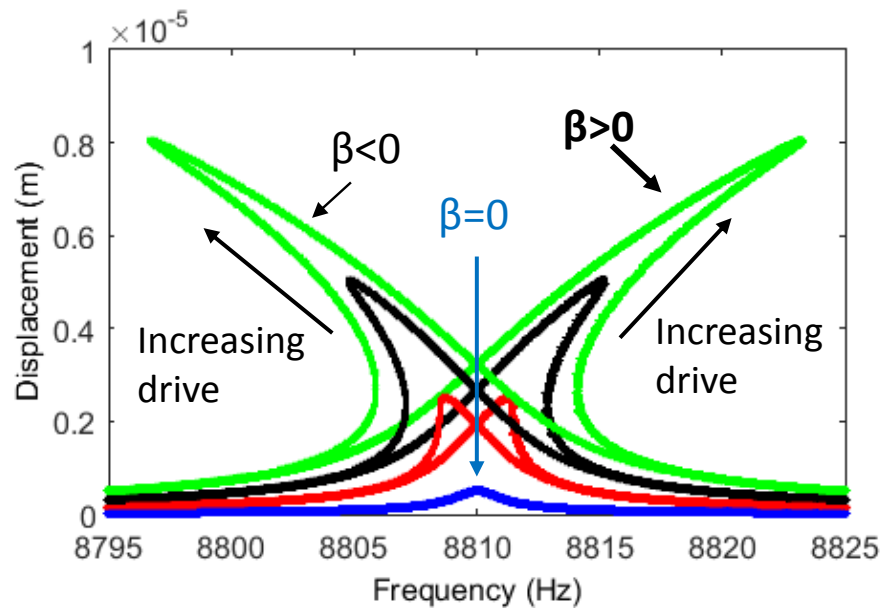


Figure 1.14: Amplitude (A) solutions with frequency for different β for increasing drive.

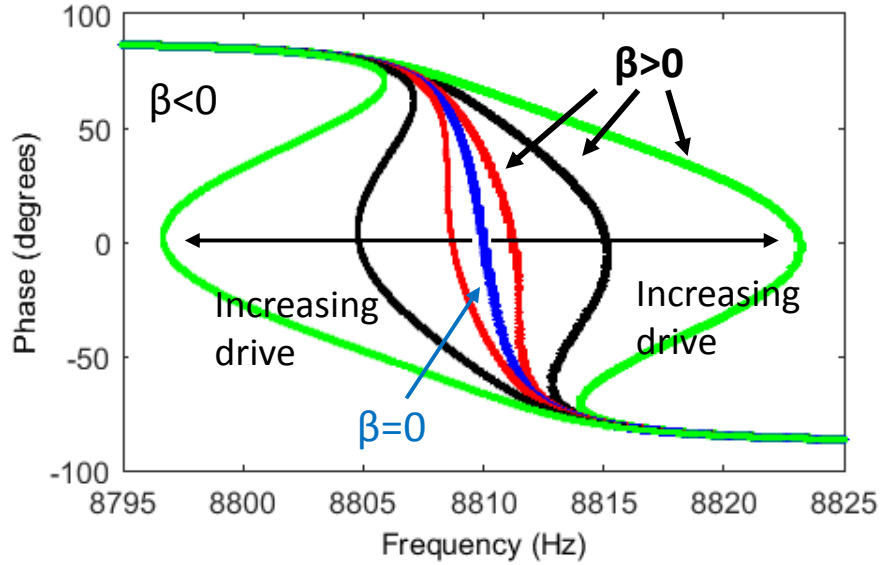


Figure 1.15: Phase (ϕ) solutions with frequency for different β for increasing drive.

The resonance curve is linear for $\beta = 0$. When the nonlinearity is hardening in nature ($\beta > 0$), the resonance curve bends towards the right implying the springs get stiffer as they bend more. On the other hand, when the nonlinearity is softening in nature ($\beta < 0$), the resonance curve bends towards the left implying the springs effectively get softer because of the electrostatic force as they bend more. The theoretical solutions show that the resonance frequency depends on the displacement. This is known as the amplitude-frequency ($A-f$) effect and has been well characterized for quartz oscillators in 1980's [51]. The resonance frequency is defined as the frequency at which the phase is 0° . There are also multiple amplitude and phase solutions for the frequencies around the resonance. Since there cannot be multiple amplitude points in practical resonance sweeps, different resonance curves are obtained during the experiments depending on the sweep direction. This phenomenon is known as hysteresis or Duffing effect. Figure 1.16 presents the practical up and down frequency sweeps on the theoretical amplitude and phase solutions for $\beta = 5.4 \times 10^9 \text{ N/m}^3$. Different responses are seen for up and down sweeps, and hysteresis can be observed.

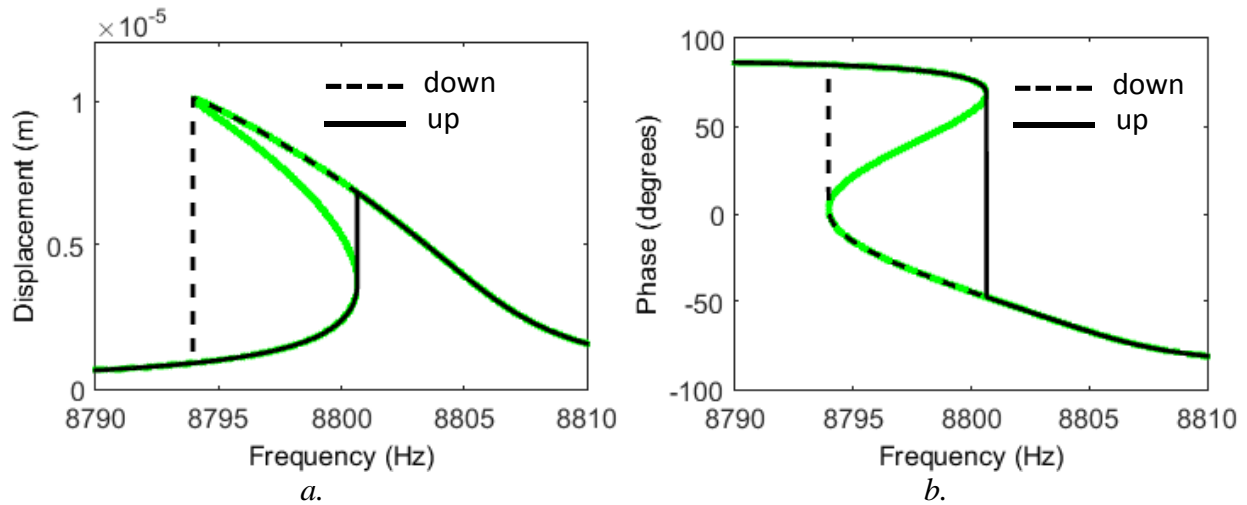


Figure 1.16: Practical up and down frequency sweeps on (a) the theoretical amplitude and (b) phase solutions.

Studies focusing on the A - f effect in MEMS oscillators have been performed and an optimum drive condition that balances the softening and hardening has been proposed in [52]. Although the drive displacement in a MEMS gyroscope is regulated by an amplitude control loop suppressing the A - f effect, there will always be amplitude disturbances around the set point. These amplitude fluctuations will lead to a drift in frequency in the drive mode if it is operated in the nonlinear regime. Since the sense mode operates at very small linear displacements, it does not experience these nonlinearity induced frequency drifts, and the gyroscope output may drift due to the change in the frequency mismatch between the drive and sense modes. The effect of this mismatch on the gyroscope performance depends on the gyroscope operation conditions. The A - f effect becomes more important as the mismatch decreases and the modes are matched. There isn't any compensation approach that considers this mismatch drift to the author's knowledge. Even though the drive loop is stable with the nonlinearities, a linear amplitude-frequency curve is still desired. Towards that end, this thesis proposes cubically shaped nonlinearity tuning fingers to cancel the softening nonlinearity.

1.7 SOI-MEMS Gyroscope with the Front-end and Biasing

The gyroscope is fabricated from a single layer of highly conductive silicon. So it is not possible to apply differential modulation voltages to capacitive sensing fingers on the movable mass and at the same time apply a dc polarization voltage to the movable mass to capacitive driving fingers as in [53]. Figure 1.17 provides the schematic that summarizes drive and sense configuration for the SOI-MEMS gyroscope. Given one conductive layer, the movable mass is biased with a dc voltage and an ac drive voltage is applied from one stator and the output current from another stator is converted into voltage by a transimpedance amplifier. Since a dc voltage is applied to the movable mass and the gap from the proof mass to the substrate is $2\ \mu\text{m}$, the same dc voltage is applied to the substrate to prevent pull-in. One problem of the MEMS devices with conductive substrates is the electrostatic levitation [54]. The electric field from the stator to the rotor is not balanced in the presence of the conductive substrate since it shorts the electric fields. This imbalance creates a net force on the rotor and levitates it. However, the SOI device layer is $15\ \mu\text{m}$ thick and the z axis spring constant is designed to be stiff, so levitation was not considered nor measured in the SOI-MEMS gyroscope.

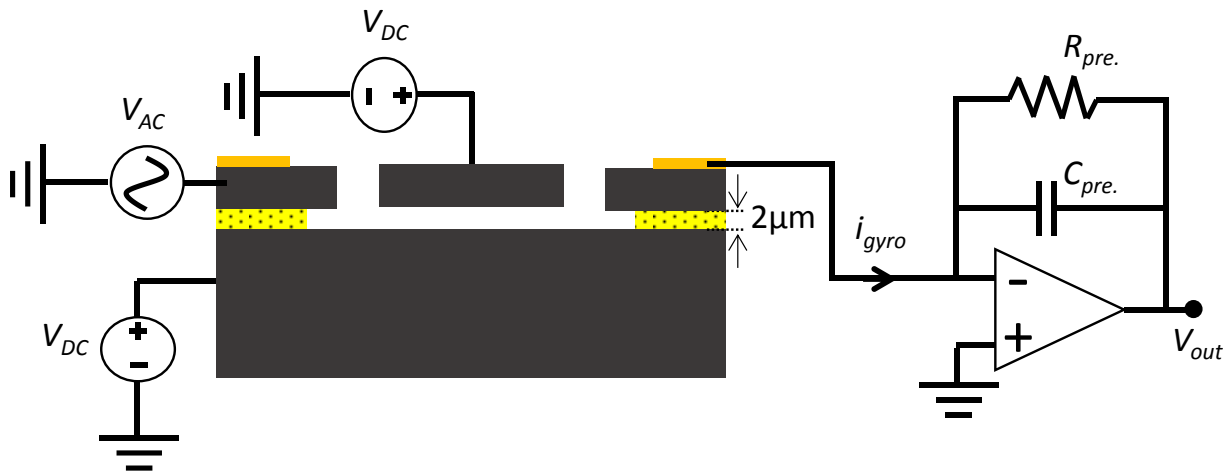


Figure 1.17: Drive and sense configuration for the SOI-MEMS gyroscope.

Capacitive driving and sensing are used during the operation of the gyroscope. The generated single-sided force that drives the gyroscope is

$$F_{drive} = \frac{1}{2} \frac{\partial C}{\partial x} (V_{DC} - V_{AC})^2 = \frac{1}{2} \frac{\partial C}{\partial x} (V_{DC}^2 - 2V_{DC}V_{AC} + V_{AC}^2) \quad 1.26$$

where $\partial C/\partial x$ is the drive capacitive sensitivity with displacement, V_{DC} is the dc polarization voltage, and V_{AC} is the amplitude of the ac driving voltage at the gyroscope resonance frequency. The squared terms in 1.26 are ignored because the gyroscope has a high quality factor around the resonance, and the dc and 2ω terms generated by the V_{DC}^2 and V_{AC}^2 terms are filtered by the high-Q bandpass property of a vacuum-packaged MEMS gyroscope. In addition, the gyroscope is driven differentially so the voltage-squared terms cancel out in operation. The resulting simplified differential drive force is

$$F_{drive} = \frac{\partial C}{\partial x} V_{DC} V_{AC} \quad 1.27$$

The output displacement current is

$$i_{gyro} = \frac{dQ}{dt} = \frac{d}{dt} (VC) = V_{PM} \frac{dC}{dt} \quad 1.28$$

$$i_{gyro} = V_{PM} \frac{\partial C}{\partial x} \frac{\partial x}{\partial t} \quad 1.29$$

where C in this case is the sense capacitance. The output current is converted into voltage with a transimpedance amplifier that has a very low input impedance. The high gain of the operational amplifier forces the input node to virtual ground so the voltage across the sense capacitor, C , in 1.28 can be considered as a constant, V_{PM} . The output current of the gyroscope depends on V_{PM} , on the capacitance change with position $\partial C/\partial x$, and on the velocity of the displacement.

The SOI-MEMS gyroscope design includes released SOI resistors for stress and temperature measurement. The high substrate voltage in Figure 1.17 causes stiction in the released resistors since they are biased at much lower voltages. Figure 1.18 presents an equivalent configuration to Figure 1.17 that solves the stiction problem by connecting the substrate and the proof mass to ground. An RC biasing circuit is connected to the stators, to couple the input (V_{AC}) through a coupling capacitor (C_{bias}) which also enables the dc polarization with a resistor (R_{bias}). R_{bias} needs to be a large for two reasons. First, a large resistor will have a lower current noise. Second, a large resistor presents a high impedance at the output, thus i_{gyro} flows into the transimpedance amplifier. The current noise of R_{bias} is converted into voltage by C_{bias} and excites the gyroscope; however, that contribution is negligibly small. C_{bias} should be selected to have a low impedance (relative to R_{bias} and the sense capacitance) at the gyroscope operation frequency. When the circuit is turned on, initially there will be a transient with $R_{bias}C_{bias}$ time constant for the dc voltage to settle on the stators. Since V_{DC} is constant and does not change with time after the initial transient, the voltage settling does not affect normal operation. R_{bias} and C_{bias} are selected as 500 M Ω and 5 nF, respectively. The time constant (τ) is 2.5 s, so it takes approximately 12.5 s (5τ) for the dc voltage to settle on the stators after the initial turn on event.

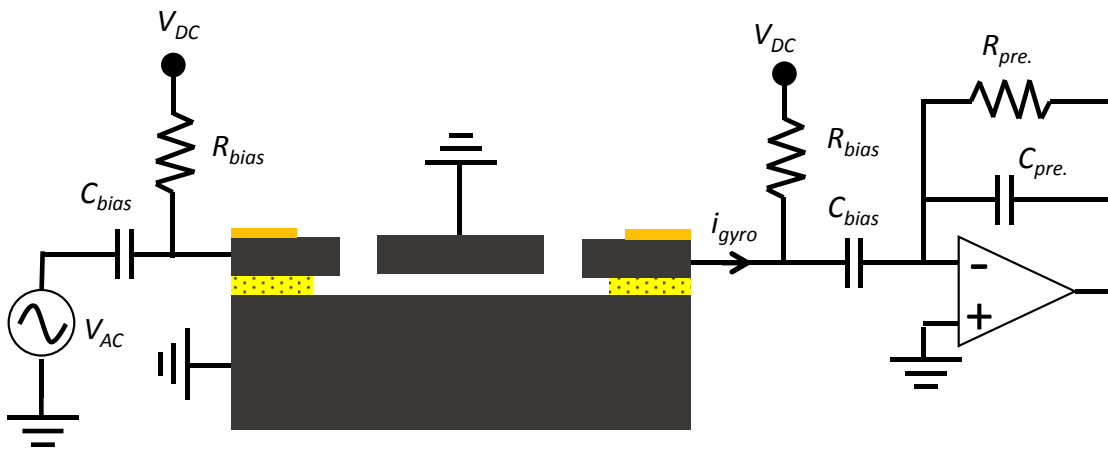


Figure 1.18: An equivalent configuration to Figure 1.17 that solves the stiction problem for the stress sensors by connecting the substrate to ground.

1.8 Thesis Contributions

The effect of stress, temperature, and nonlinearity on the gyroscope performance has been demonstrated both in simulations and experiments using a three-fold-symmetric SOI-MEMS gyroscope. On-chip stress and temperature is measured using released SOI-silicon resistors that consist of fixed-fixed and folded beams. The environmental compensation coefficients are obtained by using least squares fitting between the ZRO and environmental sensor outputs. The nonlinearity compensation is achieved by canceling the electrostatic softening nonlinearity in the gyroscope with the use of cubically shaped fingers that introduce a dc voltage controlled hardening force.

The main contribution of this thesis is the demonstration of stress compensation on gyroscope ZRO and improved long term stability with the stress compensation. The primary contributions towards achieving the stress and nonlinearity compensation are summarized below.

- A three-fold-symmetric mode-matched SOI-MEMS gyroscope with on-chip environmental sensors to study the effects of stress, temperature, and drive nonlinearity on gyroscope bias is designed and implemented. More detailed contributions in this gyroscope are:
 - on-chip stress and temperature sensors for compensation of the long term bias drift,
 - large stroke frequency tuning using shaped comb fingers,
 - large stroke gyroscope drive nonlinearity tuning using cubic-polynomial shaped comb fingers, and
 - a two mask SOI-MEMS fabrication process for the realization of the gyroscope.
- A simulation methodology is presented to predict the effect of stress and temperature on gyroscope ZRO and SF by coupling finite element analysis (FEA) (COMSOL) and circuit simulations using mixed MEMS-electronics models (Nodal Design of Actuators and Sensors

(NODAS), expressed in an analog hardware description language and run in Cadence), and a simulation methodology in FEA to understand the environmental effects on gyroscope resonance frequencies.

- An in-house discrete level vacuum packaging system using ceramic dual-in-line packages (DIP) and metal lids with in-house deposited getters is developed and characterized.
- Stress and temperature testbeds to extract the environmental effects on gyroscope performance are created, including
 - three-point and four-point bending stress testbeds based on ASTM standards, and
 - an ovenized stress testbed that servos on the on-chip temperature sensor and uses an external heater.
- Gyroscope control loops are implemented for the drive and sense modes to achieve fully closed-loop operation at mode matched condition.

1.9 Thesis Outline

The thesis organized as follows:

Chapter 2 provides the details of the simulation methodology and gyroscope control loops. The simulations start with applying a known temperature/stress/load to the gyroscope package and lead to solutions for the anchor displacements. These anchor displacements are then inserted into the NODAS model that contains the detailed mechanical model of the gyroscope and front-end circuits. ZRO and SF drifts are obtained in circuit simulation using NODAS behavioral models. Next, drive and sense mode closed-loop controllers are explained. Different control approaches for frequency matching are provided. Chapter 2 ends with documentation of the open-loop and closed-loop noise analysis and measurements of the gyroscope sense mode.

Chapter 3 presents the in-house developed SOI-MEMS fabrication process and in-house discrete level vacuum packaging system. The main contribution in processing is the optimized silicon etching recipe in deep reactive ion etcher. The vacuum packaging includes mounting the die to the 40-pin DIP (DIP40), activating the getter, and soldering the metal lid to the DIP40 in high vacuum. Successful packaging results are presented at the end of Chapter 3.

Chapter 4 demonstrates the frequency and nonlinearity tuning concept by engineering the electrostatic gap in special tuning capacitors. FEA analysis and measurement results on the frequency and nonlinearity tuning fingers are shown. The focus of Chapter 4 is tuning the electrostatic softening nonlinearity of the gyroscope with the introduced hardening from the shaped nonlinearity tuning fingers. Improvements on the long term stability of the gyroscope with nonlinearity tuning are also experimentally shown.

Chapter 5 presents the core experimental results for the stress effects on the gyroscope. The chapter starts with providing the results for temperature driven stress effects and pure stress effects on gyroscope resonance frequencies. Stress and temperature sensors in the SOI-MEMS gyroscope are explained. Stress effects on open-loop gyroscope SF and ZRO are shown next. Then test results in the ovenized stress testbed with and without application of external stress are given. The improvement with stress compensation on Allan deviation analysis is provided.

Chapter 6 provides the conclusions from the thesis and future work.

Chapter 2 Simulation Methodology and Gyroscope

Control

Two different simulation methodologies have been developed to understand the environmental stress and temperature effects on the gyroscope. The first technique uses finite element analysis (FEA; COMSOL Multiphysics, Burlington, MA) to simulate the environmental effects on the gyroscope resonance frequencies by coupling different solvers. The second simulation technique combines FEA and circuit simulation (Cadence Design Systems, Inc., San Jose, CA) to understand the effect of stress and temperature effects on gyroscope zero rate output (ZRO) and scale factor (SF). The second methodology uses COMSOL as the finite element modeling tool and the NODAS (Nodal Design of Actuators and Sensors) MEMS behavioral model library for use with the Cadence Spectre circuit simulator to implement the mixed MEMS-circuit level simulation. NODAS is a circuit library of composable and parameterized behavioral models for micro-machined devices, made in the Verilog-A analog hardware description language [55]. This first half of this chapter provides the details of both simulation methodologies.

The gyroscope drive mode requires a phase locked loop (PLL) and amplitude control to lock into the resonance and fix the drive amplitude respectively. In addition, having quadrature and force rebalance control on the sense mode improves the stability and robustness of the gyroscope ZRO and SF. After the drive and sense control loops are reviewed, different mode matching approaches and experimental results are provided although those techniques were not used during the operation. The chapter concludes with noise analysis of the sense mode under open-loop and closed-loop operation along with the noise measurements.

2.1 Simulations

There are mainly two types of simulation methodologies used to predict the environmental effects on gyroscope performance. Both type of methodologies start with FEA that takes the environmental stress/temperature disturbance as the input stimuli applied to a 3D solid model of the gyroscope chip and calculates the gyroscope anchor displacements on the chip. The anchor displacements are used as the boundary conditions for subsequent eigenfrequency simulations in COMSOL and for ZRO and SF simulations in the Cadence analog circuit simulator. The following sections cover the details of the FEA and Cadence simulations.

2.1.1 COMSOL Simulations of Environmental Effects on Resonance Frequency

The resonance frequencies of the drive and sense modes are significant for a gyroscope since the frequency mismatch determines the rate sensitivity. This thesis first focuses on the development of a FEA simulation method in COMSOL to understand the effects of stress and temperature on gyroscope resonance frequencies. COMSOL simulations in general consist of two parts. The first part includes the model of the gyroscope substrate with the anchors and the package. Excluding the actual gyroscope micromechanical structure still gives accurate results since the mechanical rigidity is dominated by the substrate. The source that creates the stress is applied to this model and anchor displacements are obtained. The source may be either mechanical or temperature induced stress. In the second part, anchor displacements are used as the boundary conditions for the eigenfrequency simulation of the 3D model of the gyroscope, giving its resonance frequencies. Separating the simulation into two steps highly reduces the burden on the simulator, since including the full gyroscope mechanical structure in the chip-level stress simulation causes

convergence problems, requires a huge number of elements and thus memory, and takes a very long time to simulate.

Temperature affects the gyroscope resonance frequencies through the negative temperature dependence of Young's Modulus (E) (-60 ppm/K) [56]. Temperature also induces a stress on the MEMS die because of the thermal coefficient of expansion (TCE) mismatches of the silicon die and package; this induced stress results in anchor displacements that modify the stiffness of the device springs. The change in the spring constant affects the resonance frequencies of the gyroscope. A testbed using heat to create temperature and stress changes on the MEMS die was designed and simulated in COMSOL. The 1st generation gyroscope has on-chip SOI silicon heaters located on each side of the SOI die and the die is thermally isolated from the environment with a glass substrate. Activating the heater creates a temperature change and TCE driven stress change. Figure 2.1.a and b show the simulation results when 500 mW of power is applied to one of the heaters. The FEA model consists of a glass, SOI handle layer, 2 μm thick SOI oxide, on-chip silicon heaters and the device spring anchors. The boundary conditions are the bottom of the glass is fixed for mechanical simulations and the bottom of the glass is room temperature for the thermal simulations. The glass to handle silicon attachment is modeled as perfectly rigid. Figure 2.1.a shows the temperature distribution, the glass layer thermally isolates the device layer from the package as expected. The thermal and mechanical characteristics of the die are dominated by the glass and the handle silicon since their combined thickness is 60 times that of the device layer. The output of the Joule heating simulation is coupled with a thermal expansion solver. Figure 2.1.b shows the displacement results due to the heater generated temperature distribution. Additional package stress can be added at this step. Anchor displacements are extracted from Figure 2.1.b and then used as boundary conditions for the modal simulations of the actual

mechanical structure. Modal simulations also take into account temperature dependence of Young's Modulus (E). Springs are assumed to have the same temperature as anchors. The mechanical system follows Hooke's law ($F=kx$), since the displacements are small enough. In other words, not only temperature differences but also anchor displacements vary linearly with respect to the heater power. These characteristics are then used to obtain frequency characteristics for different stress and temperature levels.

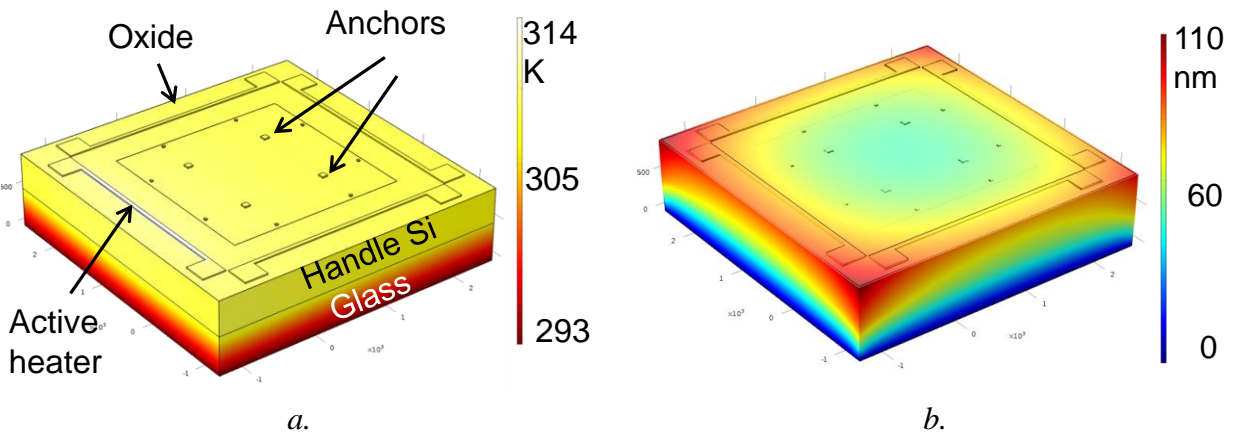


Figure 2.1: FEA simulation results for 500 mW of heater power applied to one of the heaters, first Joule heating simulation to get the temperature map (a), and then thermal expansion simulation gives the anchor displacements (b).

Temperature causes the resonance frequency to decrease linearly with -30 ppm slope since the resonance frequency is proportional to \sqrt{E} (E is the Young's Modulus). However, the stress effects on frequency are not straightforward. In order to understand how stress affects the gyroscope, one needs to examine how the anchors and springs are located on the device. Figure 2.2 shows gyroscope anchor positions for different stress levels. The dashed lines show the initial position of the gyroscope, red shows the expansion, and blue shows the contraction. The folded-flexure suspensions are anchored at the inner beams. When the heater is activated, the die expands as in Figure 2.1.b, and the anchors move from Position 0 to +. This movement induces a tensile stress on the inner beams increasing the y spring constant and creates a compressive stress on the outer

beams decreasing the y spring constant. Since inner and outer beams are connected in parallel, anchor displacement results in an overall decrease in the effective spring constant. The effective spring constant always decreases whether the anchor moves inwards or outwards because inner and outer beams will always see the stress in opposite directions as shown in the lower right graph in Figure 2.2. Temperature on the other hand contributes with a constant slope line. The transverse stress (y directed) is not taken into account since it has very little effect on spring constant compared to axial stress (x directed).

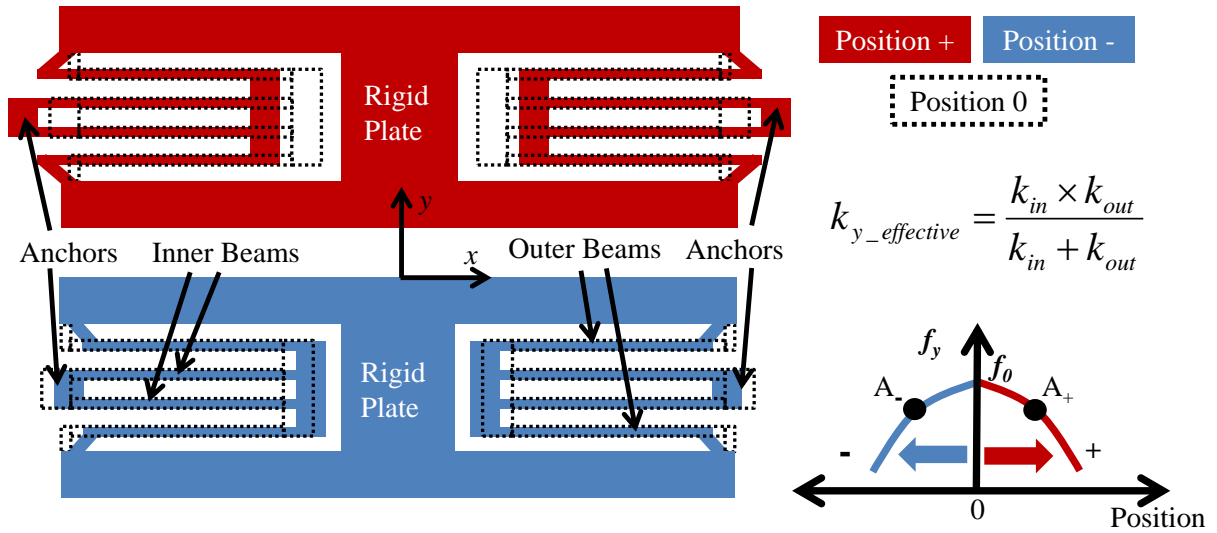


Figure 2.2: Three states of the device for different stress levels. Position 0 shows the initial state, Position + shows when an outwards directed stress is applied, and Position - shows when an inwards directed stress is applied to the device.

2.1.2 Gyroscope Theory Including Anchor Displacements

The equations of motion for a Coriolis vibratory rate gyroscope by neglecting the diagonal mass and damping terms, and ignoring centripetal and angular acceleration force terms, is:

$$\begin{bmatrix} m_{xx} & 0 \\ 0 & m_{yy} \end{bmatrix} \begin{bmatrix} \ddot{x} \\ \ddot{y} \end{bmatrix} + \begin{bmatrix} b_{xx} & 0 \\ 0 & b_{yy} \end{bmatrix} \begin{bmatrix} \dot{x} \\ \dot{y} \end{bmatrix} + \begin{bmatrix} k_{xx} & k_{xy} \\ k_{yx} & k_{yy} \end{bmatrix} \begin{bmatrix} x \\ y \end{bmatrix} = \begin{bmatrix} F_x \\ F_y \end{bmatrix} + \begin{bmatrix} 0 & 2\Omega m_{xx} \\ -2\Omega m_{yy} & 0 \end{bmatrix} \begin{bmatrix} \dot{x} \\ \dot{y} \end{bmatrix} \tag{2.1}$$

where m , b , k represents the mass, damping and stiffness respectively. Subscripts x and y denote the drive and sense axis, respectively. F is the externally applied force and Ω is the rotational rate in 2.1. k_{xy} and k_{yx} represent the direct coupling between the drive and sense modes and they are ideally zero. The only difference between 1.4, 1.5, and 2.1 is the inclusion of the diagonal stiffness terms (k_{xy} and k_{yx}). In a practical gyroscope, they are not zero and introduce quadrature error, which is one of the main error sources. The main focus of this section is an examination of the signals in terms their phases, as opposed to their amplitude analysis in section 1.5. The phase of each signal, summarized in Table 2.1, is exploited in gyroscope signal processing. The phases are derived by assigning x axis as the drive axis and driven at resonance, and y axis as the sense axis and perfectly matched to the drive frequency. F_y and diagonal stiffness terms are zero in 2.1. Drive force and Coriolis force has the same phase in a mode matched gyroscope and so does the drive displacement and Coriolis force induced sense displacement.

Table 2.1: Phase summary of the gyroscope signals.

Signal	Expression	Phase
Drive voltage	$V_d = V_{DC} \pm v_d \cos(\omega_0 t)$	0°
Drive force	$F_x = \frac{dC}{dx} V_{DC} v_d$	0°
Drive displacement	$X = -j \frac{1}{b_{xx} \omega_0} F_x$	-90°
Coriolis force	$F_{coriolis} = -2m_{yy} \Omega \dot{X}$	-180°
Sense displacement	$Y = -j \frac{1}{b_{yy} \omega_0} F_{coriolis}$	-270°

A MEMS gyroscope interacts with external stress from the environment through its anchors. Application of stress results in anchor displacements, and anchor displacements have two distinct effects on the gyroscope. The first effect is the spring constant change resulting in non-zero k_{xy} and k_{yx} , and shifts in k_{xx} and k_{yy} in 2.1. Non-zero k_{xy} and k_{yx} lead to quadrature error that has a 90°

phase difference with respect to the Coriolis induced sense signal, since Coriolis force is multiplied with the drive velocity; however, k_{xy} and k_{yx} are multiplied directly with the displacement. The main source of the quadrature error is the process imperfections, but anchor displacements change the amount of the quadrature error. Quadrature error can be as high as hundreds of $^{\circ}/s$, but it can be cancelled either by using special electrode structures [57] or with the use of lever type springs [33]. The principle axis stiffness (k_{xx} and k_{yy}) change as a result of anchor displacements and result in loading of the beams either with compressive or tensile stress. This leads to shifts in the resonance frequencies of the drive and sense modes. The frequency shift problem can be solved by using a closed-loop frequency control circuit. The frequency shifts can also be highly suppressed by operating mismatched or matched and closed-loop operation both of which provide enough bandwidth.

The second effect of the anchor displacements is the change in the electrostatic gaps of the drive and sense capacitances due to the non-equal displacement of the stator and drive electrodes.

Figure 2.3 shows a comb drive with non-equal gaps due to external stress.

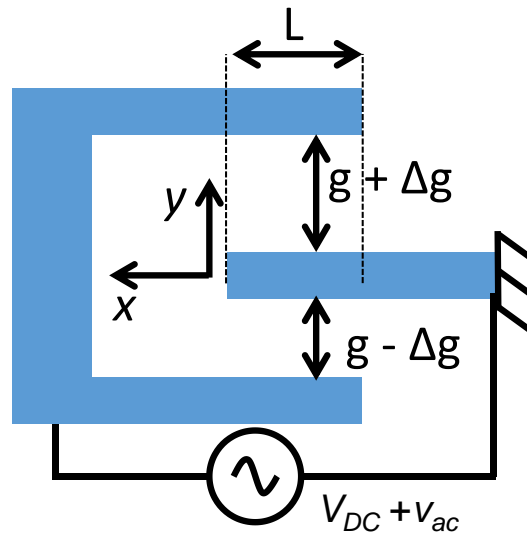


Figure 2.3: A comb drive with non-equal gaps due to external stress.

The lateral comb drives in the gyroscope are ideally designed to generate a force in the x (drive) direction but because of the gap mismatch they also create a force in the y (sense) direction. The force created in the sense direction is transferred into the sense displacement due to the finite sense-axis stiffness of the drive-axis springs. The ratio of the drive to sense forces for Δg is:

$$\frac{dC/dx}{dC/dy} = \frac{g^2}{2\Delta gL} \quad 2.2$$

where g is the nominal gap, Δg is the gap mismatch, and L is the finger overlap as shown in Figure 2.3. Then the ratio of the drive and sense displacements is

$$\frac{X}{Y} = \frac{k_a + k_{xx}}{k_{xx}} \frac{g^2}{2\Delta gL} \approx \frac{k_a}{k_{xx}} \frac{g^2}{2\Delta gL} \quad 2.3$$

where k_a is the sense-axis spring constant of the drive-axis springs. Assuming typical values of $k_a = 100 k_{xx}$, $g = 3 \mu\text{m}$, $\Delta g = 10 \text{ nm}$, $L = 15 \mu\text{m}$, and drive displacement $X = 1 \mu\text{m}$, the calculated sense displacement, Y , is 330 pm. A 330 pm gap offset corresponds to $130.3^\circ/\text{hr}$ bias shift for the gyroscope in this study. The phase of this sense directed force is the same as the drive-axis force, which is in phase with the Coriolis force according to Table 2.1. So, gap mismatch creates an output signal that cannot be distinguished from the Coriolis signal, and the simulations will focus on comb gap mismatches. The idea of drive comb mismatches leading to Coriolis in-phase sense displacements is also mentioned in [39].

2.1.3 Simulation Methodology

This section covers the details for the simulations that relate the environmental changes to gyroscope ZRO and SF. Obtaining ZRO and SF changes requires detailed modeling of the gyroscope mechanical structure with the front-end electronics. Both of them are modeled in a

circuit solver in Cadence Spectre using the NODAS MEMS model library. The anchor displacements, obtained through FEA are accepted as input to the NODAS models, and ZRO and SF changes are simulated with the developed simulation methodology.

2.1.3.1 NODAS

An analogy is readily formed between an electrical circuit having “through” variables of current and “across” variables of voltage and a mechanical circuit having through variables of force and across variables of displacement. Once this mapping of through and across variables is chosen, a self-consistent set of mechanical element models can be implemented using analog hardware description languages. The NODAS library is implemented in the language Verilog-A supported by Cadence. Since NODAS models are compatible with standard electrical circuit schematics in Cadence, electrical components such as preamplifiers can easily be included in the simulations providing a full system simulation advantage. Cadence Spectre is used as the solver in this study. A detailed description of the NODAS library is beyond the scope of this thesis; more information is found in [55], [58], and [59].

2.1.3.2 Simulation Procedure

Finite element analysis (FEA) and NODAS are used to obtain the stress-ZRO and stress-SF relations. FEA is very accurate but the complete gyroscope structure including the electronics cannot be modeled in FEA. However detailed simulations can be performed in the circuit solver. The goal is combining the detailed accuracy of the FEA with the system simulation capability of the circuit simulator. Figure 2.4 summarizes the general simulation methodology. COMSOL was used as the FEA software. The simulations start with applying a known stress to the gyroscope die in FEA to obtain the displacements of the spring anchors and stators of the combs. Then these displacements are inserted into the Cadence schematic, which interconnects the NODAS

behavioral beam and plate models of the gyroscope electromechanical structure. The front-end electronics, i.e., transimpedance amplifiers are also included in the Cadence Spectre schematic. Finally, drive and sense displacements are simulated by running an ac analysis to get the ZRO and SF.

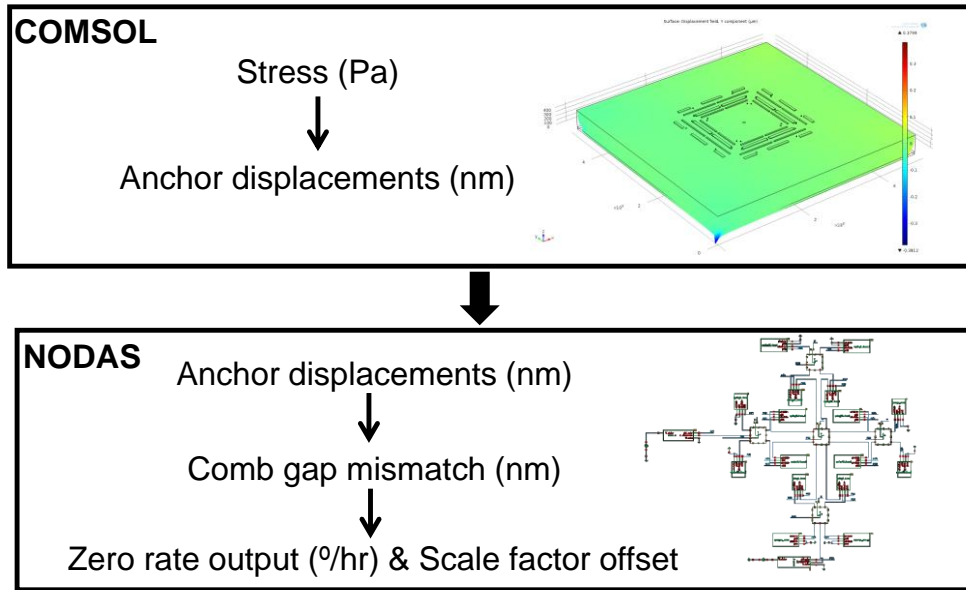


Figure 2.4: The general simulation methodology.

Figure 2.5 shows the simulation flowchart that accepts anchor displacements and/or comb gap mismatches as input and eventually calculates the ZRO. The first step is applying the anchor displacements or gap mismatches and obtaining the drive and sense resonance frequencies. The second step is the mode-matching, the real-life assumption is that the modes are always kept matched. So, the frequency mismatch caused by the anchor displacements and/or comb gap mismatches are tuned in the circuit simulation by parameters in the NODAS behavioral model of the frequency tuning combs. In addition to the frequency shift, the anchor displacements cause a quadrature signal (A_Q) that is three orders of magnitude larger than the in phase Coriolis in-phase signal (A_C). In step 3, the quadrature signal is tuned with open-loop simulation by applying a quadrature signal to the sense combs until the Coriolis phase is obtained. Finally, the remaining

signal that is in-phase with the Coriolis signal is converted into °/hr equivalent after obtaining the scale factor by applying a rotational rate in the simulations.

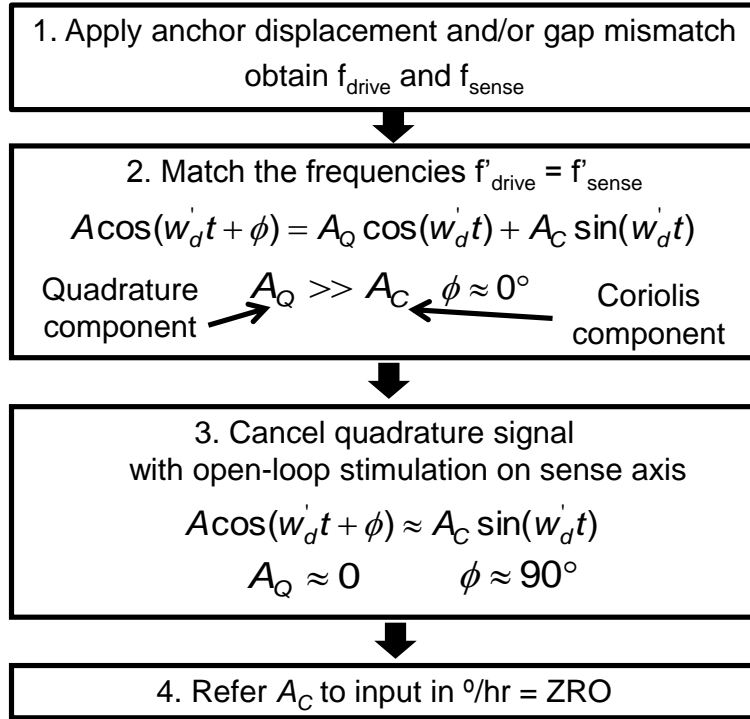


Figure 2.5: Simulation flow chart for NODAS simulations.

Figure 2.6 repeats the SEM image of the three-fold symmetric SOI-MEMS gyroscope to show how it is modelled in NODAS. The gyroscope consists of a central square proof mass and four mechanically decoupled side plates to detect the drive and sense displacements. Figure 2.7 presents the NODAS schematic of the gyroscope shown in Figure 2.6 with the detailed spring and side-plate schematics. The schematic comprises a central proof mass and four side-plates connected by springs made from composable interconnection of NODAS beam elements. Central proof mass and side plates are formed by connection of rigid plates and springs. Frequency tuning “shaped” combs on both axes allow independent tuning of the drive and sense frequencies. The schematic includes the electromechanical models of the drive and sense combs. The drive is connected to a small ac voltage source in series with a relatively large dc voltage in order to actuate

the drive axis. A separate small ac voltage drive in series with the large dc voltage is connected to the sense-axis comb to cancel the quadrature error. The output of the two main differential sense-axis combs is connected to transimpedance amplifiers allowing the observation of the voltage output in addition to the displacement.

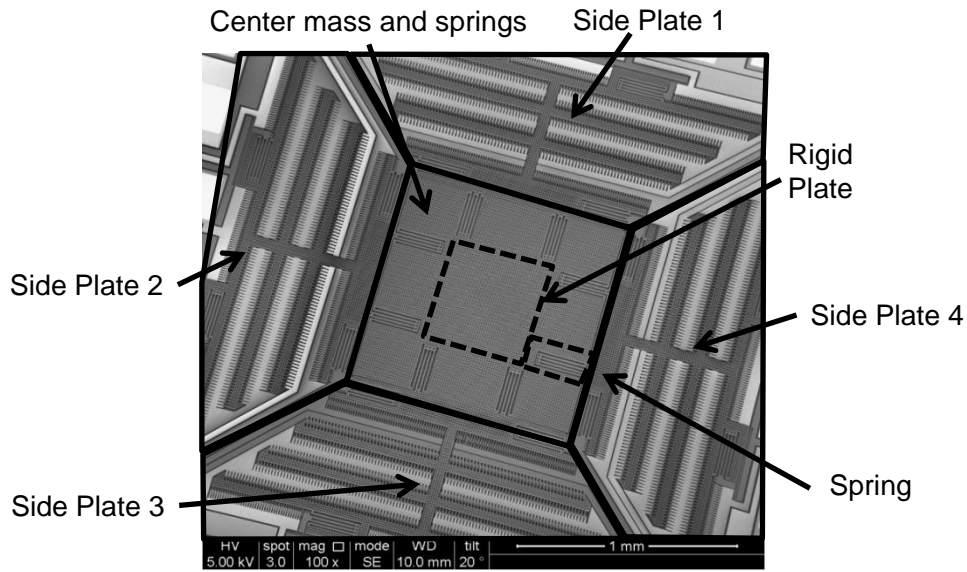


Figure 2.6: SEM of the SOI-MEMS gyroscope showing the separate sections.

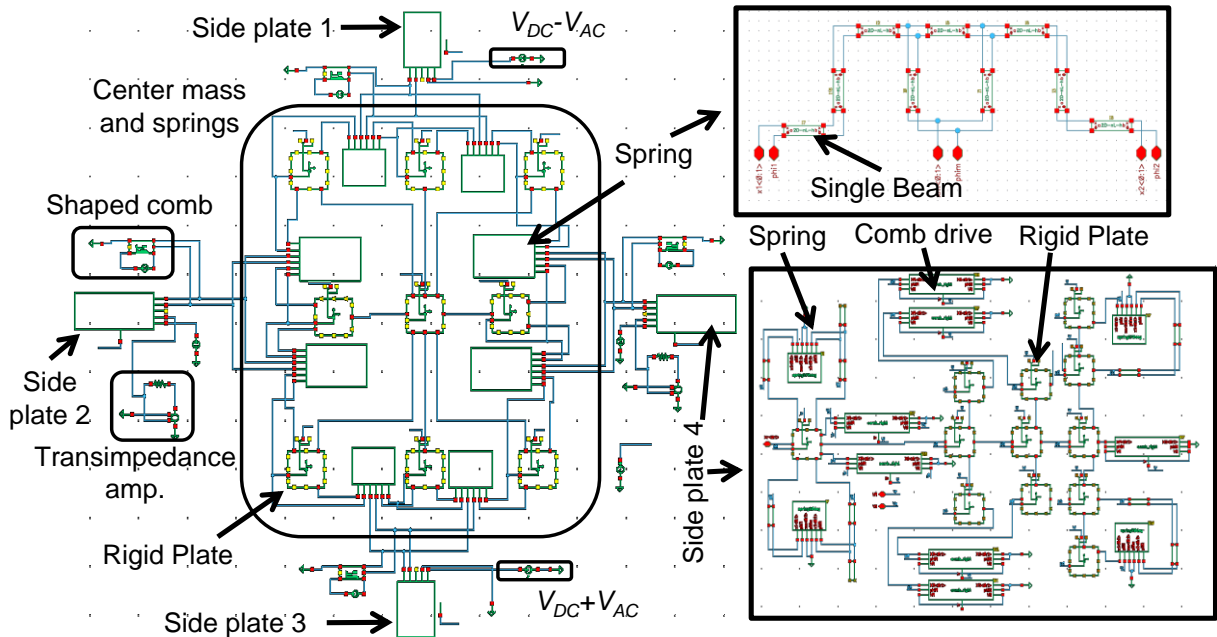


Figure 2.7: NODAS schematic of the SOI-MEMS gyroscope with the detailed spring and side plate schematics.

2.1.4 Simulation Results

AC analysis is used during the simulations. Figure 2.8 and Figure 2.9 show the typical ac sweep results for drive and sense displacements before and after quadrature cancellation for a gap mismatch of 10 nm ($\Delta g = 10$ nm) in drive combs after mode matching. Quadrature cancellation is achieved by applying an ac signal to the sense combs that has a 90° phase with respect to the drive signal. The simulations were run for a quality factor of 25,000, with 100 μ Hz resolution and 0.1 Hz span (the plots zoom into the resonance region). Such a resolution is needed to tune for the Coriolis in-phase signal that is orders of magnitude smaller than the quadrature signal.

The data points at the drive resonance frequency should be considered in ac analysis since the gyroscope operates at that point. Note that the plots are zoomed in images around the drive resonance. As shown in Figure 2.8, drive displacement is not affected from quadrature cancellation to the first order as expected, and the drive phase at resonance is -90° as calculated in Table 2.1. The sense displacement, on the other hand, has a phase of 0° before quadrature cancellation due to the large quadrature signal. The sense response looks like a regular second-order resonance curve before quadrature tuning is applied. The phase change is twice the drive phase change since the sense mode displacement is a result of 2nd order drive system acting on the 2nd order sense system. The transfer function of the driving voltage to the sense displacement is a 4th order system. The sense resonance curve changes its shape when the quadrature tuning voltage is applied. The amplitude response looks like a V shape because maximum tuning is obtained when the drive and sense resonance frequencies are the same. The phase also changes abruptly around the resonance because the quadrature signal changes its sign depending on whether it is higher or lower than the resonance frequency. The phase of the sense signal becomes 90° at the drive resonance frequency in Figure 2.9 after the quadrature cancellation.

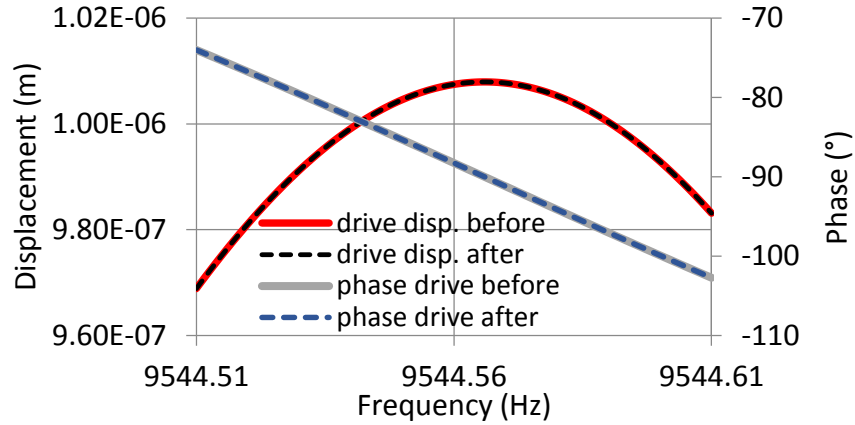


Figure 2.8: AC magnitude and phase plots for drive displacement with gap mismatch $\Delta g = 10 \text{ nm}$ in drive combs before and after quadrature error cancellation.

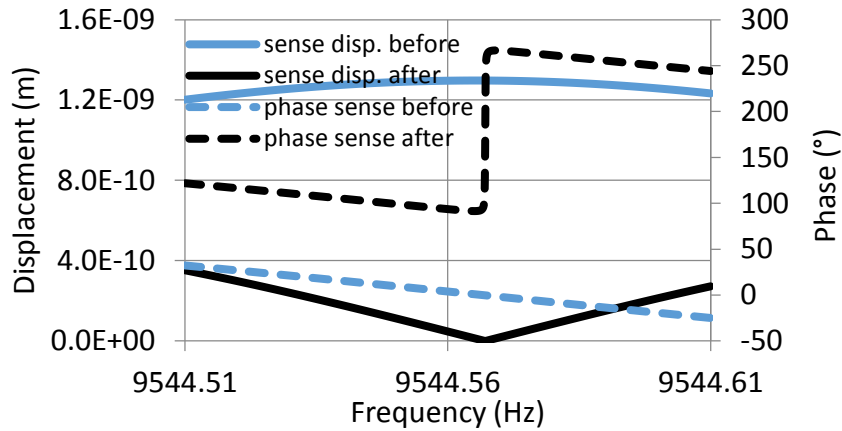


Figure 2.9: AC magnitude and phase plots for sense displacement with gap mismatch $\Delta g = 10 \text{ nm}$ in drive combs before and after quadrature error cancellation.

Note the three orders of magnitude difference between the quadrature and residual ZRO signal in Figure 2.9, which implies that the simulations require appropriate absolute numerical tolerance. The absolute tolerance used for the voltage and current are 10^{-6} and 10^{-12} , respectively with a relative tolerance of 10^{-3} . The SF is simulated by applying a $\pm 1^\circ/\text{s}$ rate and looking at the change in the sense displacement at the drive resonance after quadrature cancellation. The phase of the rate induced sense displacement is also $\pm 90^\circ$. Finally, input referred $^\circ/\text{hr}$ ZRO is obtained by dividing the residual Coriolis phase sense displacement by the SF.

A stress of 2 MPa — representative of levels seen in packaging — is applied to the gyroscope in FEA. The obtained anchor and stator displacements were applied to the NODAS model parameters, resulting in a simulated ZRO of $1.77^\circ/\text{hr}$ and quadrature error of $18.15^\circ/\text{s}$. Non-equal rotor and stator displacement is the source of ZRO. Temperature-induced packaging stress can be as high as 40 MPa [60], so stress may lead to hundreds of $^\circ/\text{s}$ quadrature error and tens of $^\circ/\text{hr}$ ZRO. The system-level simulation shows the overall effect of stress on gyroscope output; however, only gap mismatches are studied next to obtain the direct relation between ZRO (and SF) and the comb gap mismatch. A gap mismatch is applied only to one of the drive combs. Figure 2.10 shows the ZRO and quadrature signals with drive comb gap mismatch. The relation between the ZRO and quadrature error vs. gap mismatch is linear with $3.2^\circ/\text{hr}$ per 10 nm gap mismatch and $0.145^\circ/\text{s}$ per 10 nm gap mismatch, respectively. Figure 2.11 presents that SF and drive displacement follow the same trend with changing drive comb mismatch. No change in SF with drive comb gap mismatch is expected since the drive displacement kept constant by a feedback loop in a practical gyroscope.

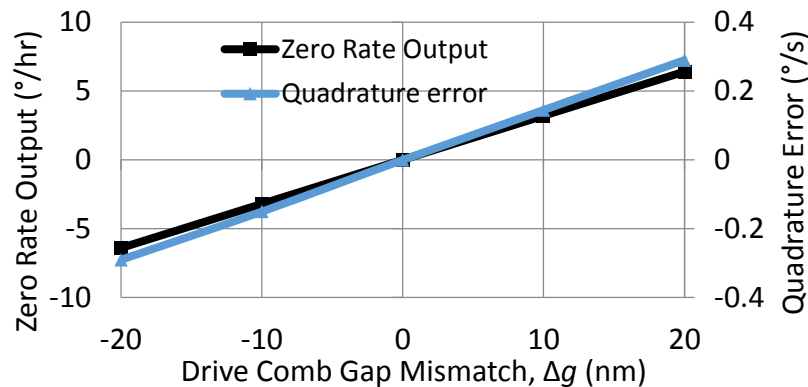


Figure 2.10: ZRO and quadrature error vs. drive comb gap mismatch.

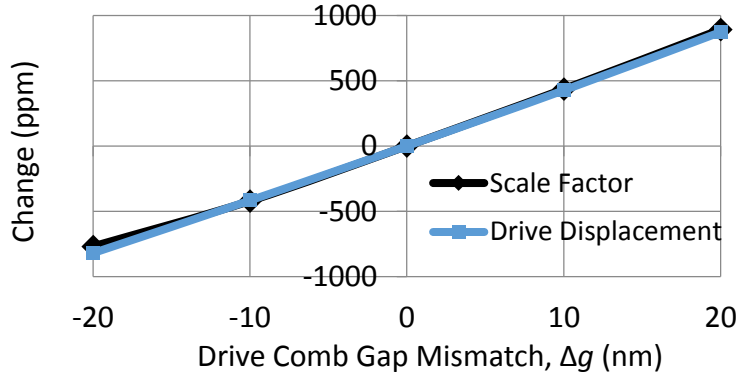


Figure 2.11: SF and drive displacement vs. drive comb gap mismatch.

The effect of single spring anchor displacements were also simulated, in addition to the drive comb gap mismatches. The single anchor displacements resulted in frequency shifts and output errors completely in quadrature, i.e., they didn't cause enough comb gap mismatch to create ZRO.

2.1.5 Simulation Results with the Parasitics

The simulation results presented in the previous section assumes ideal operation conditions. However, in the real world there will be parasitics and feedthrough capacitances that will modify the gyroscope characteristics. Figure 2.12 presents the real-world model of the transimpedance amplifier. C_p models the parasitic capacitance at the input node of the op-amp. C_f represents the feedthrough capacitance from the input of the gyroscope to the input of the transimpedance amplifier. C_f is originated from the device layout and external wirebonds and routing. C_{pre} and R_{pre} represent the resistance and capacitance of the preamplifier, respectively.

It is not possible to completely eliminate C_f and C_p ; however, they can be minimized by the design. C_p leads to amplification of the voltage noise of the op-amp, and increases the total noise. C_f effects the phase; the output current from the gyroscope (i_{gyro}) mixes with the current from V_{in} through C_f , which is equal to $V_{in}/j\omega C_f$. This current results in a shift of phases around resonance. C_f and C_p can be extracted experimentally by setting the dc proof mass potential to 0 V. $V_{PM} = 0$ V

makes sure that the MEMS structural motional current does not contribute and only electrical parasitic effects are observed. Figure 2.13 shows the measurement and NODAS simulation frequency sweep results for $V_{PM} = 0$ V for parasitic extraction.

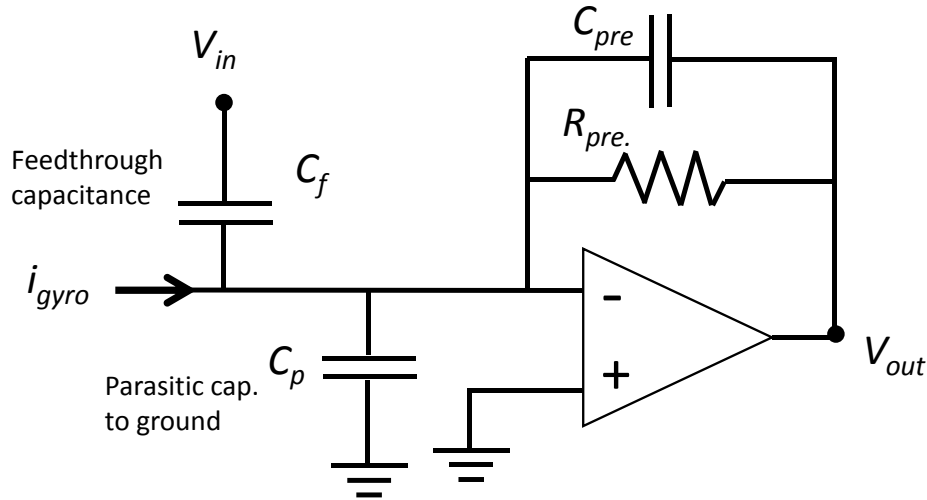


Figure 2.12: Real world model of the transimpedance amplifier.

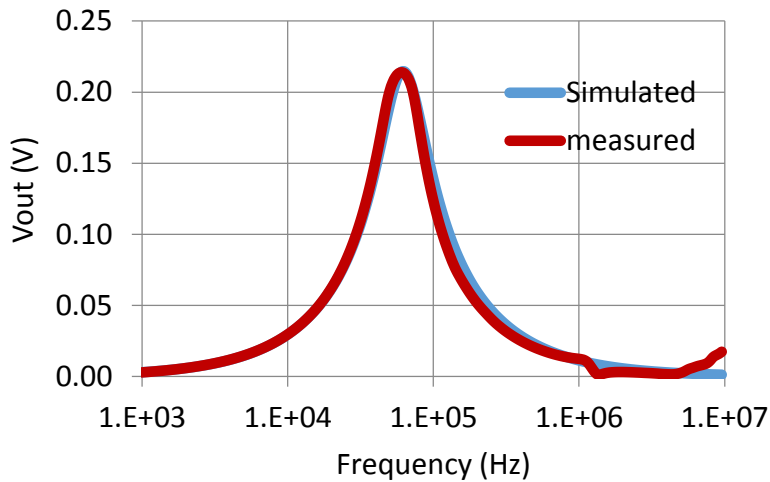


Figure 2.13: Measurement and NODAS simulation for the parasitic extractions with $V_{PM} = 0$ V. Referring to Figure 2.12 and assuming $C_p \gg C_f$, and $C_p \gg C_{pre}$, the dominant pole of the system will be at $\omega_{center} = 1/R_{pre}C_p$. The gain at ω_{center} is C_f/C_{pre} . The extracted parameters are provided in Table 2.2 for an experiment carried out using a 10 M Ω feedback resistance.

Table 2.2: Extracted parasitic values

C_f	230 fF	C_{pre}	210 fF
C_p	20 pF	R_{pre}	10 M Ω

Figure 2.14 shows the measurement and NODAS simulation results for the frequency response of the drive mode with feedthrough and parasitics. The resonance curve tilts towards the left because of the feedthrough current mixing with the motional current of the gyroscope.

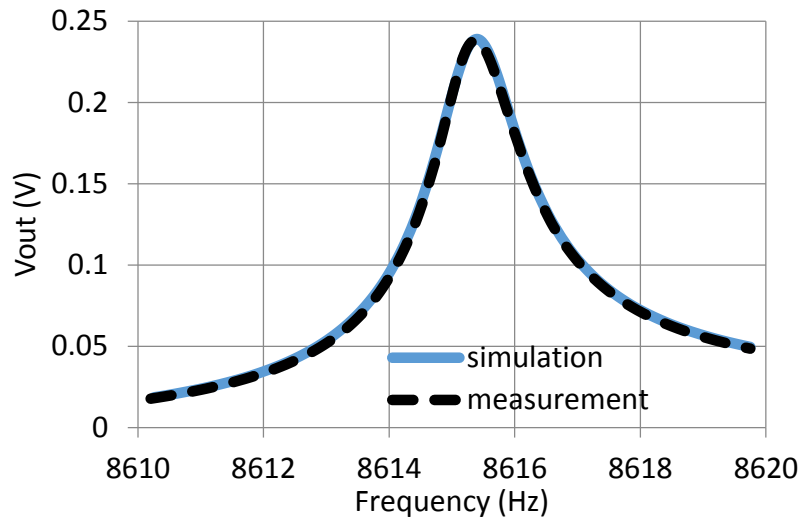


Figure 2.14: Measurement and NODAS simulation with feedthrough and parasitics for the drive sweep.

The ZRO simulations have been repeated with the feedthrough and parasitics to explore their effects on the final performance. Figure 2.15 presents the NODAS simulation results for ZRO. The anchor displacements were applied corresponding to a 1 MPa mechanical stress on the die. The main effect of the feedthrough capacitance is the shift in the peak of the voltage relative to the displacement. Since we can practically only monitor the voltage, we assume it is in phase with the displacement, but if there is feedthrough that is not the case. By looking at the displacement in Figure 2.15, 1 MPa stress results in 8 °/hr ZRO if the quadrature cancellation is performed. However, during testing only the voltages are available and either the 0° phase point or the point where the drive displacement is maximum may be chosen for the operation point. These operation

points lead to $2.8^\circ/\text{s}$ and $0.9^\circ/\text{s}$ ZROs respectively, that are much larger than $8^\circ/\text{hr}$. These simulations assume an open-loop sense operation, and feedthrough in the sense mode does not play an important role since there is no input voltage on the sense mode. The feedthrough from drive to sense is also measured to be negligible. So careful attention should be paid to the design of the both MEMS and PCB to minimize the feedthrough capacitance to suppress the phase errors.

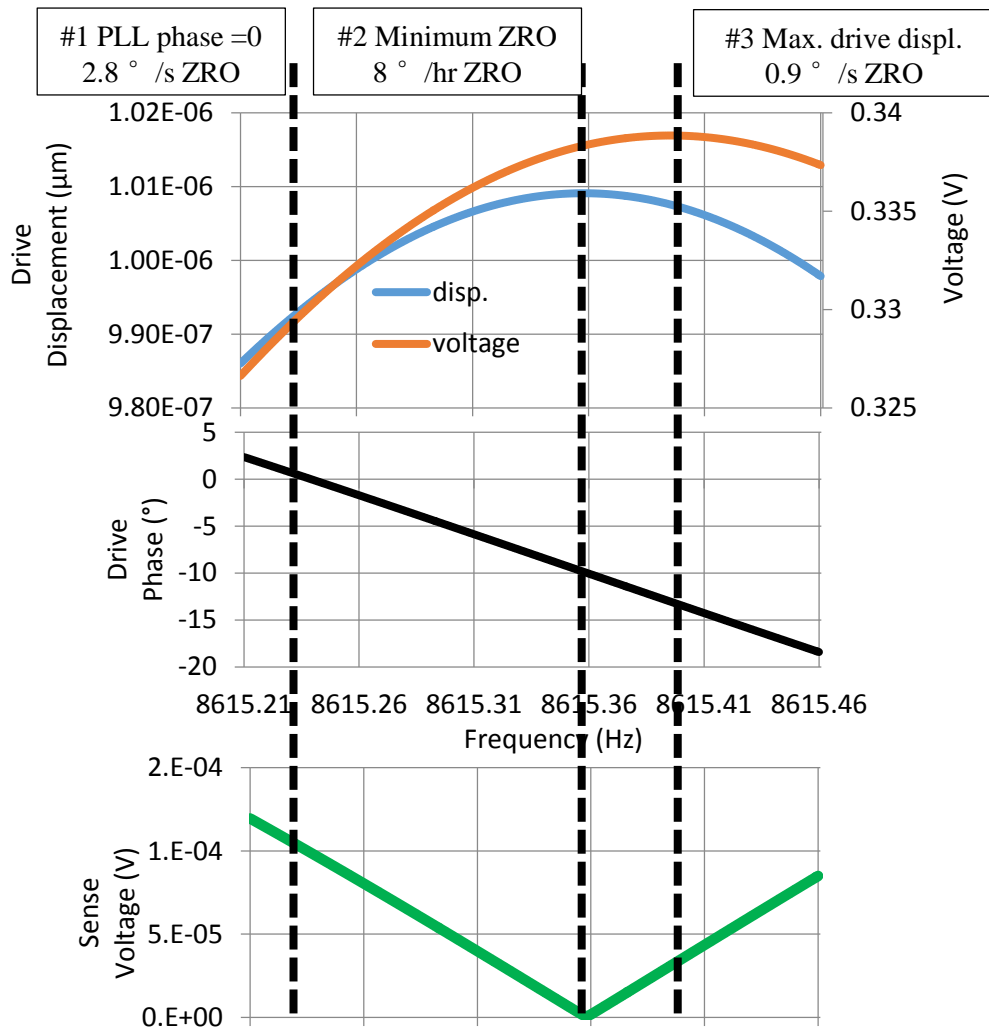


Figure 2.15: NODAS simulation results for a stress level of 1MPa including capacitive feedthrough and parasitics to ground.

2.2 Gyroscope Control Loops and Frequency Control

This section provides the details for the gyroscope control loops and different frequency control techniques that have been experimentally tried. The gyroscope control loops are first modeled in Simulink and proportional, integral, derivative (PID) parameters are obtained. The PID settings are then implemented in the physical gyroscope system. Although not implemented in the final gyroscope control, different approaches have been tried to build control loops to match the drive and sense resonance frequencies and to operate at a fixed frequency mismatch.

2.2.1 Gyroscope Control Loops for Drive and Sense

Gyroscope control is essential to ensure stable operation. At minimum frequency and amplitude control are necessary on the drive mode to lock into the resonance frequency and fix the drive displacement respectively. Sense mode can be operated in open loop with phase sensitive demodulation if the modes are mismatched. Open-loop sense mode operation is very vulnerable to drifts in matched mode since the bandwidth is limited with the quality factor. The gyroscope was operated in mismatched mode with open-loop sense in the initial phases of this study, but in the final phases the gyroscope operates in matched mode with closed-loop drive and sense modes.

The gyroscope output currents are converted into voltage through transimpedance amplifiers on a printed-circuit board (PCB). The test setup is shown in Figure 2.16. After some additional amplification and differential to single-end conversion, the drive and sense mode outputs are fed to a Zurich Instruments HF2LI digital lock-in amplifier [61]. The lock-in amplifier has two high speed inputs with 14 bit analog-to-digital converters (ADCs), two high speed analog outputs with 16 bit digital-to-analog converters (DACs) along with two independent phase locked loops (PLL), and four proportional-integral-derivative gain (PID) controllers.

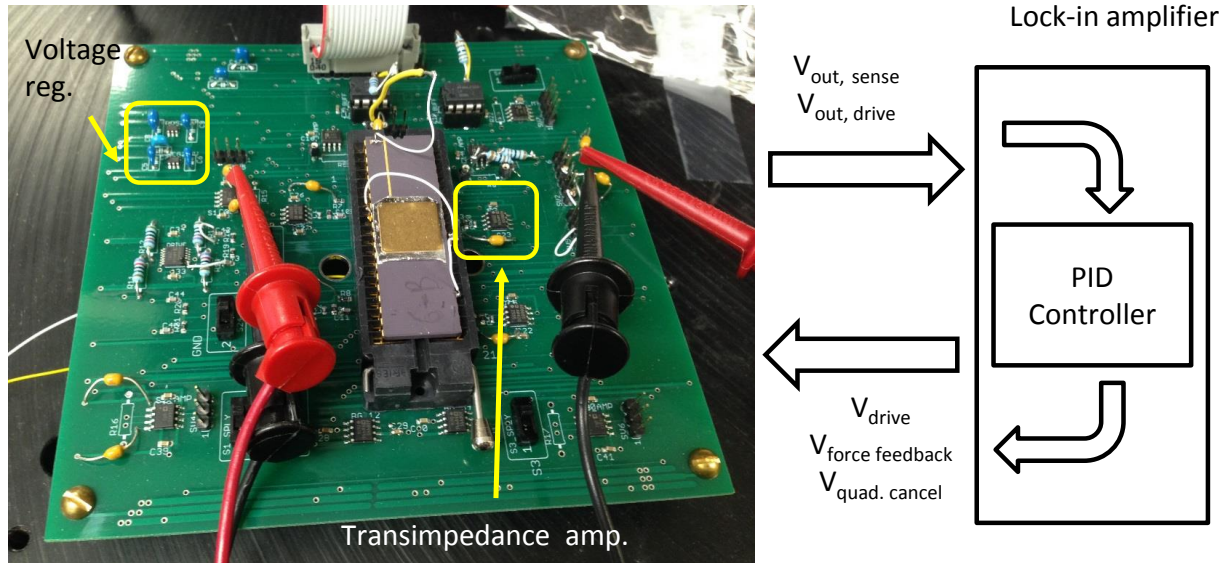


Figure 2.16: Test setup with the PCB and digital lock-in amplifier.

The gyroscope control architecture is adapted from the IEEE standards [62] which is shown in Figure 2.17. The x axis is assumed as the drive and y axis as the sense. Drive and sense mode outputs from the gyroscope are first digitized (ADC not shown in Figure 2.17) and demodulated into in-phase (I) and quadrature (Q) components. Although not shown, the demodulators include low pass filters. The various control loops are implemented by appropriately feeding back the I and Q components to the gyroscope electrostatic actuators. Next, one digital PLL is used to lock into the drive resonance, one PID controller is used to fix the drive displacement, and two PID controllers are used to cancel the quadrature and rate signals on the sense mode. One lock-in amplifier output is dedicated to drive and the other one is used for the sense mode. Both quadrature and rate cancellation are achieved by applying ac signals that are 90° out of phase, they are added in the lock-in amplifier and applied from a single output.

Modeling the gyroscope control system with the modulator and demodulator is not straightforward since the frequency in the system changes. The output of the PI controller is a control signal that is subsequently modulated to the drive resonance frequency and applied to the gyroscope actuator.

Then the output of the gyroscope is at the drive resonance frequency and once demodulated and low pass filtered it becomes a baseband signal. As a solution to the analysis complexity, the gyroscope, modulator, and demodulator are modeled as a single element, which captures the envelope of the gyroscope response.

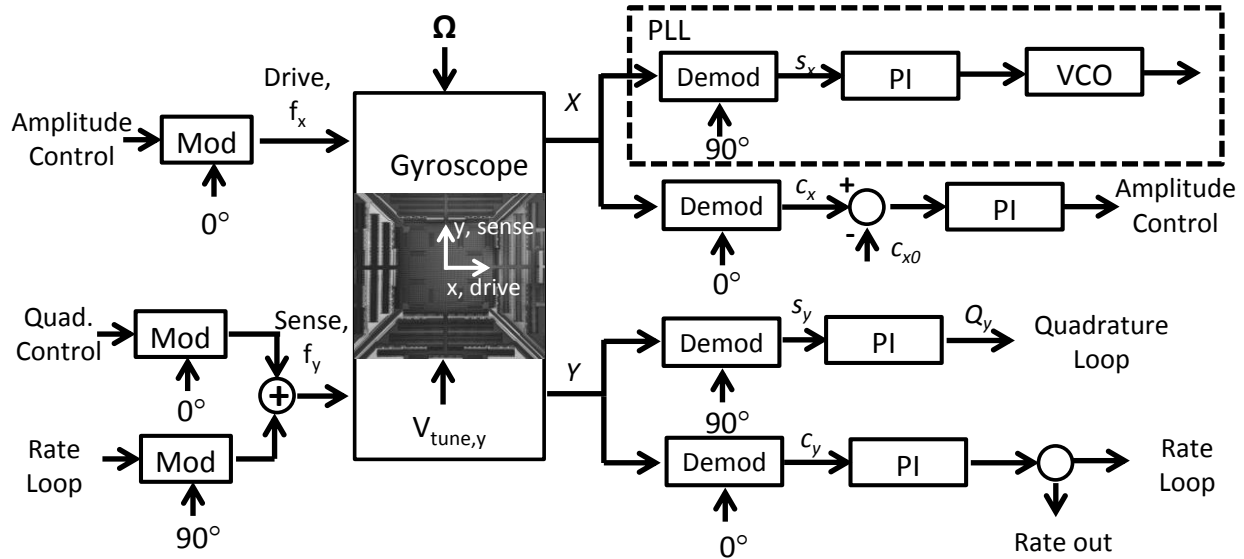


Figure 2.17: Gyroscope control architecture adapted from the IEEE standards [62].

The gyroscope drive mode is a resonant system that is modeled with the modulator and demodulator as a single pole system [62]:

$$H_{gyro} = \frac{A_0}{1 + s \frac{2Q_0}{\omega_0}} \quad 2.4$$

where A_0 is the resonance gain, Q_0 is the quality factor, and ω_0 is the resonance frequency. Equation 2.4 is the response of the drive mode to a slowly changing (the rate of the change is much smaller than the resonance frequency) input around the resonance frequency. The higher Q_0 , the slower the system response. The same equation can be used for the sense mode if the gyroscope is in matched mode operation.

A PID controller is modeled as:

$$H_{PID} = K_p + \frac{K_I}{s} + K_D s = \frac{K_I \left(1 + s \frac{K_P}{K_I} \right) + K_D s^2}{s} \quad 2.5$$

where K_P , K_I , and K_D are proportional gain, integral gain, and derivative gain, respectively. For a drive mode and matched sense mode controller setting $K_D=0$, and $K_P/K_I = 2Q_0/\omega_0$ cancels the pole of the gyroscope transfer function and results in the fastest settling time without any overshoot. The actual values of K_P and K_I is determined through MATLAB SIMULINK simulations.

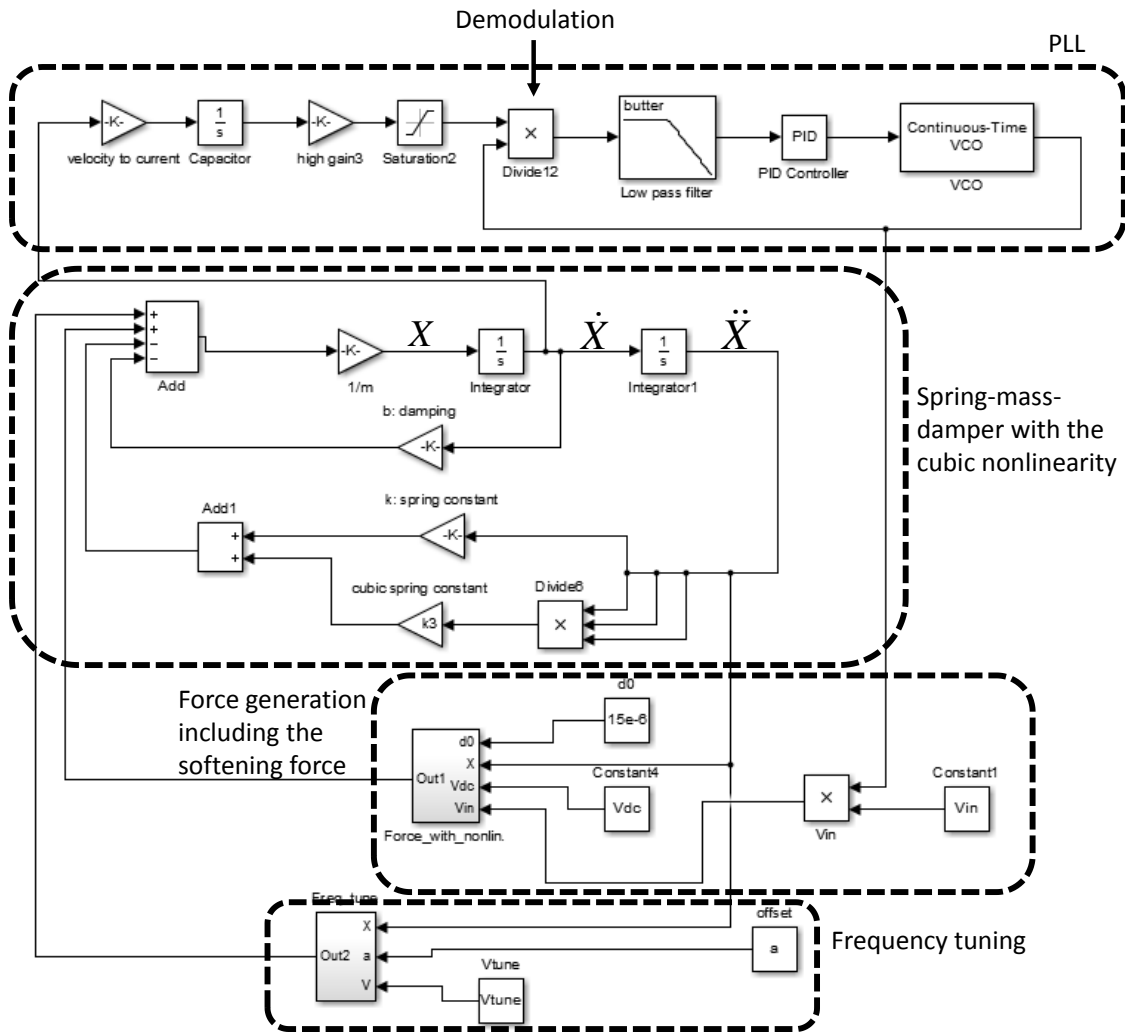


Figure 2.18: Simulink model of the drive mode for PLL including the nonlinearities.

Figure 2.18 presents the Simulink model of the drive mode for PLL with the nonlinearities. The spring-mass-damper system is modeled with each term represented separately instead of a transfer function to include the cubic hardening and softening force. The electrostatic force generation is modeled with the nonlinearities, i.e., with the nonlinear finger-tip to anchor capacitors. The frequency tuning combs are also modeled. The PLL model includes velocity to current conversion, demodulation, low pass filtering, and a voltage controlled oscillator (VCO). The velocity and input voltage are in-phase at resonance according to Table 2.1, but in this model a transcapacitive amplifier is used for current to voltage conversion which contributes another 90° of phase. The PID controller in Figure 2.18 tries to lock the frequency until the phase difference between VCO and gyroscope voltage output is 90° . The K_p/K_I ratio is known and the appropriate gain values are found by first increasing them until the instability point is reached and then setting them at half of those values. The amplitude control loop is not shown Figure 2.18 to keep the model simple but the structure similarly consists of phase sensitive demodulation, low pass filtering, and a PID controller. Figure 2.19 shows the simulation result for the model including drive amplitude control and PLL. The amplitude control and PLL work simultaneously in the simulation leading to an initial overshoot in the gyroscope driving voltage. The amplitude control loop is activated after the PLL during real implementation. The quadrature and rate controller are similar except for the fact that there is no need for a PLL and the displacements are set to zero rather than a certain amplitude.

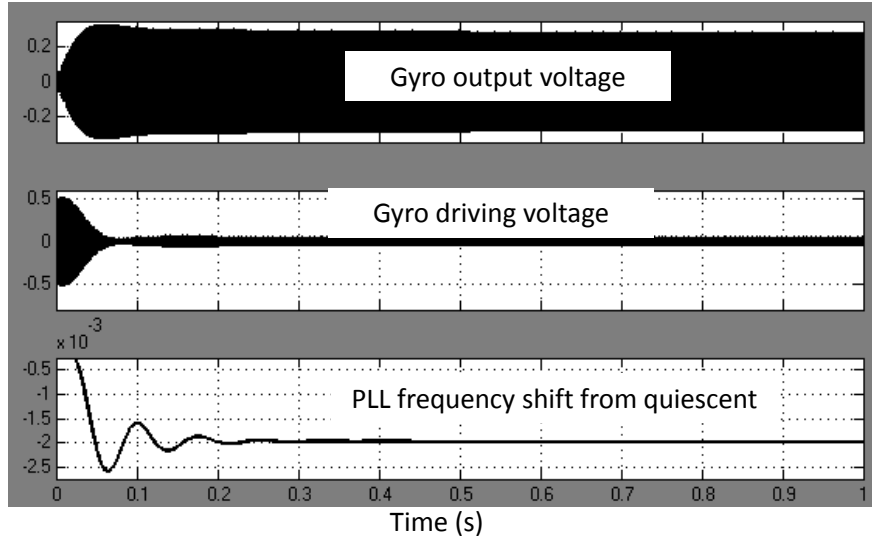


Figure 2.19: Simulink simulation result showing the drive PLL and amplitude control loop.

2.2.2 Frequency Control

In addition to the drive and sense controllers, a frequency control loop that matches the frequencies of the drive and sense modes is beneficial for maximum sensitivity and robust operation. Mode matching can be achieved by applying two pilot tones having an equal offset from the drive frequency to the sense mode and looking for the equal amplitude at the output [63]. The same idea can be implemented by injecting a perturbation signal to the dc quadrature cancellation electrodes and checking the phase of the sense output [64], [65]. Drive and sense modes can also be matched by searching for the maximum amplitude of the quadrature signal [66]. In this thesis, both ideas have been tried experimentally and in simulations as well as with an additional technique.

In all of the mode matching techniques the drive mode frequency is kept constant and the frequency tuning voltage on the sense mode is controlled by a loop. The control loop runs in MATLAB by reading the required data from the digital lock-in amplifier and controlling a dc power supply that is connected to the sense mode frequency tuning fingers.

2.2.2.1 Operating at a Fixed Mismatch

The first method targets a reduction of the resonant frequency mismatch in the two modes to 3 Hz to 4 Hz, hence increasing the sensitivity and keeping the mismatch constant at open-loop sense mode. Since the sense mode is open loop with quadrature cancellation, the rate controller is not needed for the sense mode. The idea is the voltage cancelling the quadrature error is a function of the mismatch between the drive and sense modes, assuming the quality factors do not drift. So if the controller tries to keep the quadrature cancellation voltage constant by modifying the frequency tuning voltage on the sense mode then the mismatch should be stabilized.

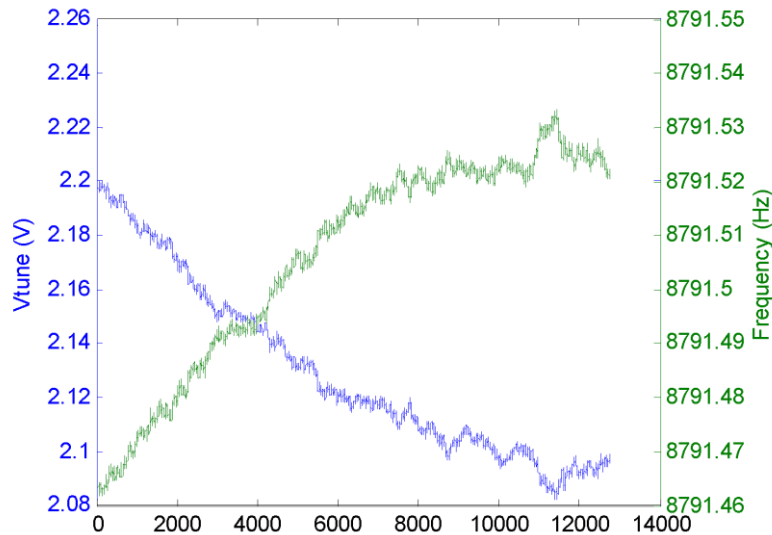


Figure 2.20: Drive frequency vs. the frequency tuning voltage on the sense mode.

Figure 2.20 presents the frequency tuning voltage vs. the drive frequency obtained from the experiment. The tuning voltage is on top of the 35 VDC needed to set an adequate electrostatic drive gain and motional current gain, so the voltage applied to the sense mode is around 37 V corresponding to an additional 2 V of tuning voltage. The curve trends look similar, i.e., the drive frequency is increasing and the sense frequency tuning voltage is decreased accordingly to increase the sense frequency. But the sensitivity of sense frequency to tuning voltage is 1 Hz/0.25 V, so the expected sense frequency change is 0.44 Hz, which is six times the drive frequency change.

Such a big difference between the frequency shifts is not expected. The idea of quadrature cancellation amplitude depending on mismatch independent of temperature is probably wrong. It is believed that temperature changes affect the quality factors which in turn changes the quadrature cancellation amplitude.

2.2.2.2 Mode Matching by Looking at Quadrature

The second technique implemented for the mode matching is similar to [66]. The amplitude of the quadrature signal should be maximized when the modes are matched. The sense mode operates open loop in this technique. Figure 2.21 presents the idea. Initially when the modes are mismatched the amplitude of the quadrature signal is relatively small, as the frequencies match the amplitude of the quadrature signal increases, peaking at the match point. Once the match point is passed the amplitude of the quadrature signal decreases again. So with an extremum seeking algorithm mode matching can be achieved.

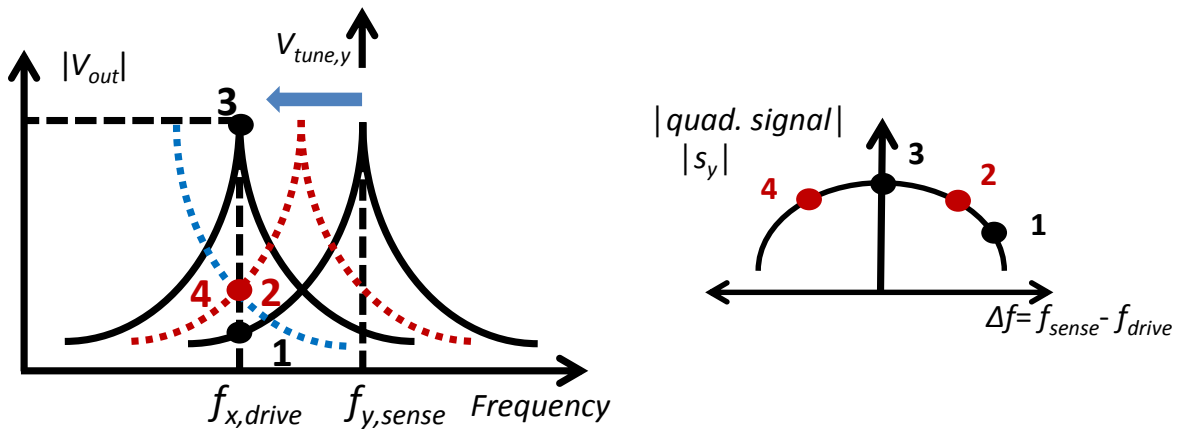


Figure 2.21: Mode matching by monitoring the quadrature amplitude.

An extremum seeking algorithm has been implemented in MATLAB that gets the quadrature amplitude from the lock-in amplifier and controls the dc power supply. Figure 2.22 presents the experimental results for the extremum seeking algorithm for the amplitude of the quadrature signal and tuning voltage. The algorithm works well initially but at some point the matching is

completely lost as seen from the jump in the quadrature cancellation voltage. A Simulink model has been formed to understand the source of the problem that includes the drive and sense mode together and the quadrature coupling in between them. The key in the Simulink model is that not only quadrature coupling from drive to sense is included but also the quadrature coupling from sense to drive is also included in the model. Initially the sense frequency is higher than the drive frequency and the frequency of the sense mode is tuned towards the drive mode while monitoring the drive displacement.

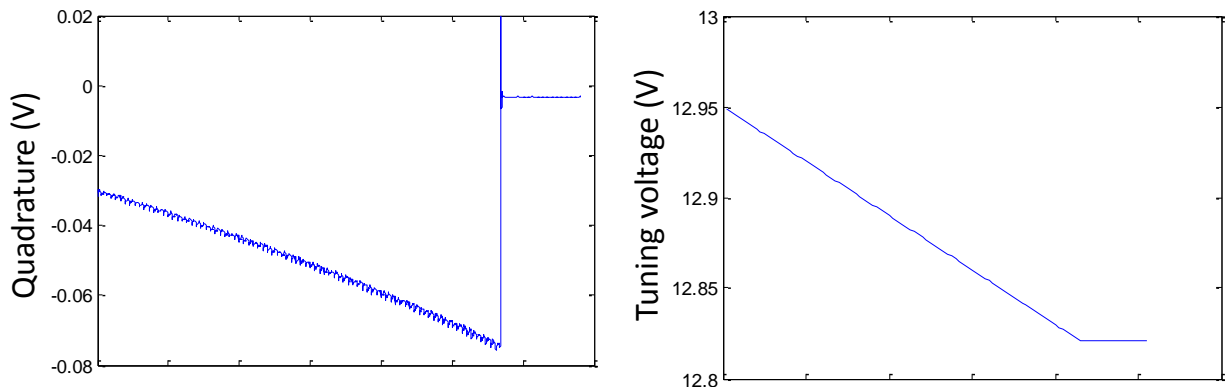


Figure 2.22: Tuning voltage and measured quadrature signal amplitude during extremum seeking.

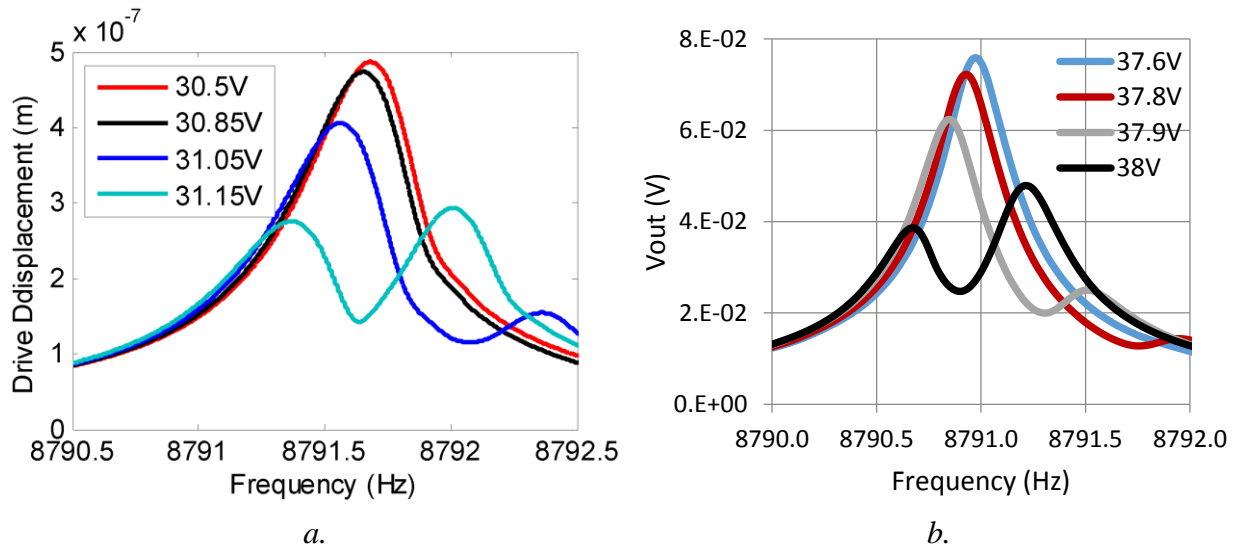


Figure 2.23: Simulink simulation results (a) and experimental measurements (b) for the drive displacement for different tuning voltages on the sense mode.

Figure 2.23 shows the Simulink simulation results and experimental measurements for the drive displacement for different tuning voltages on the sense mode. The tuning voltage difference between the experiments and Simulink model is due to the modeling of the frequency tuning fingers. Ideally drive displacement is not expected to be affected by the mode matching. Since the sense mode is open loop, the quadrature signal grows so high that it absorbs the energy of the drive mode. In other words, the energy from the drive mode leaks to the sense mode such that the drive resonance shape changes. The theoretical mode matching voltage is around 31.15 V and the drive resonance is highly changed at that voltage. The same argument is true for the experiments around 38 V. This change also reflects to the drive phase and the resonance frequency jumps leading to the graphs in Figure 2.22. So this set of experiments concludes that closed-loop quadrature cancellation is required for mode matching, and this is not a convenient way of mode-matching.

2.2.2.3 Mode Matching with Pilot Tones

The final and third technique that was implemented for mode matching injects two pilot tones around the drive resonance frequency to the sense mode and looks for the equal amplitude of these two tones at the sense mode output. This method has been implemented in different ways in the literature [63]-[65]. In this thesis, it has been implemented by amplitude modulating (AM) the quadrature cancellation signal with the amplitude modulator option in the digital lock-in amplifier. Equation 2.6 shows the mathematical formulation. A modulation frequency (ω_m) is added to the quadrature cancellation signal. This forms three frequency tones, one at the drive resonance frequency (ω_x) that cancels the quadrature signal, and two tones equally separated from the drive resonance frequency.

$$\begin{aligned}
s(t) &= [Q + M \sin(\omega_m t)] \sin(\omega_x t + \phi) \\
&= Q \sin(\omega_x t + \phi) + \frac{M}{2} \cos[(\omega_x - \omega_m)t + \phi] - \frac{M}{2} \cos[(\omega_x + \omega_m)t + \phi]
\end{aligned} \tag{2.6}$$

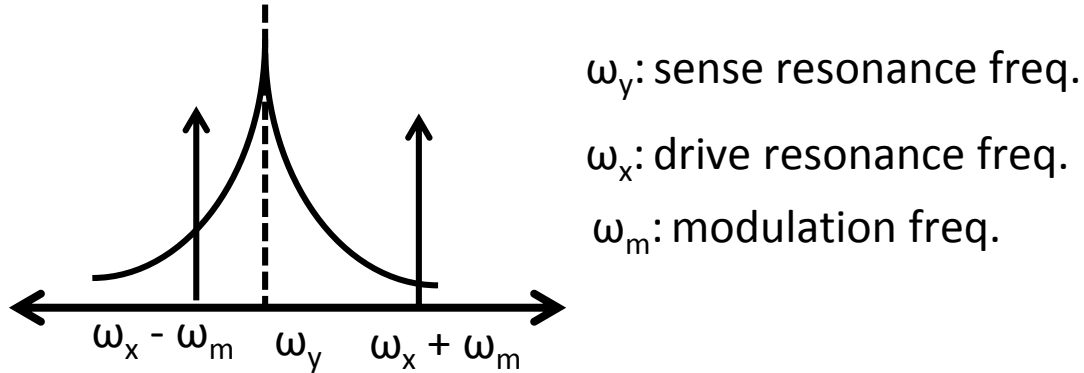


Figure 2.24: Mode matching with pilot tones around the drive frequency.

Since the two pilot tones are applied to the sense mode with the quadrature cancellation voltage, the response of the sense mode to these two symmetric tones is equal only when the drive and sense frequencies are the same. Figure 2.24 presents this idea. From the application point of view, three demodulations with sharp roll-off LPFs are required at frequencies $\omega_x - \omega_m$, ω_x , and $\omega_x + \omega_m$, and these are all done in the digital lock-in amplifier. The quadrature control is implemented in the lock-in amplifier, and the mode matching algorithm is implemented in MATLAB by reading the tone amplitudes at the sense mode output and trying to equalize them by changing the tuning voltage on the sense with PID control. Certain design criteria have to be met for this mode matching technique to work. Assuming the sense mode operates at closed loop if the tones fall in the bandwidth; then the sense mode controller will try to cancel them. If the sense mode operates in open loop and the tones are within the bandwidth, the tones will be visible at the output. On the other hand, if the tones are too far away from the sense mode then then we start to lose from the sensitivity since the sense mode response to these frequencies will be minimal. Based on this, the cut off frequencies of the demodulation low pass filters and the modulation frequency have to be selected properly.

A Simulink model including the closed-loop quadrature cancellation and rate control along with the drive mode have been formed to simulate the pilot tone mode matching algorithm. Figure 2.25 shows the simulation results for the tuning voltage and the phase of the modulation signal at the sense mode output. The simulation was run for a sense mode bandwidth of 30 Hz, modulation frequency of 25 Hz, and initial mismatch of 2 Hz. The mode matching loop is turned on after the quadrature and rate control loops have been activated. The loop tries to drive the phase of the modulation signal at the output to zero by making X_m/Y_m go to zero. The mode matching loop seems to work fine by applying 5.19 V to the sense mode frequency tuning combs.

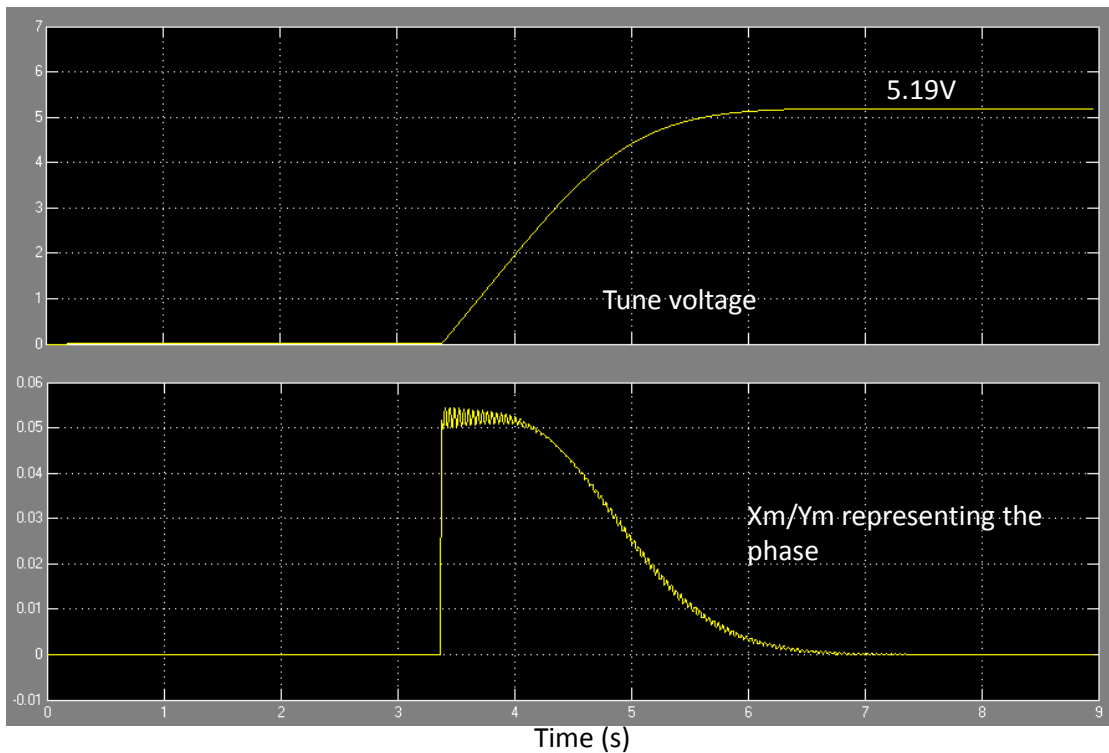


Figure 2.25: Simulink simulation for the mode matching voltage (up) and the phase of the mode match (down) signals.

Simulink mode matching simulations have been repeated with different modulation frequencies and Table 2.3 presents the tuning voltages for different modulation frequencies for an initial mismatch of 1 Hz. Everything else in the system is kept constant and ideally the mode matching

voltage should not depend on the modulation frequency. However, as the modulation frequency gets higher, the sensitivity decreases and the accuracy of the mode matching is reduced.

Table 2.3: Mode matching voltages for different modulation frequencies

Mismatch ($f_y - f_x$)	Modulation frequency (f_m)	Tuning Voltage
1 Hz	15 Hz	3.7 V
1 Hz	25 Hz	3.63 V
1 Hz	50 Hz	3.43 V
1 Hz	100 Hz	2.43 V

Simulink simulations show the trade-off between modulation voltage and matching accuracy, and as the modulation frequency is smaller it starts to interact with the rate controller. As a solution, an experiment has been conducted in which the modulation frequency is 10 Hz and the rate controller bandwidth is 20 Hz. To solve the coupling problem between the rate and frequency controllers, the mode matching loop turned on for 45 s and turned off for 3 minutes. The gyroscope output is blanked off during that 45 s period. Figure 2.26.a and b show the tuning voltage on the sense and the drive frequency drift during the pilot tone mode matching experiment. The drive frequency is increasing around 60 mHz, however the tuning voltage on the sense mode barely changes (~1 mV). So sense mode frequency can be assumed as constant, the change in frequency is 4 mHz. The experiment suggests that the modulation frequency needs to be further reduced to increase the sensitivity.

Some more additional experiments have been tried but without a solid conclusion. Very high demodulation low-pass-filter cutoff frequencies are needed to suppress the coupling between the rate and mode matching loops. Later, an experiment was run with the rate and quadrature loops closed and with ovenizing of the gyroscope. At that point, the closed-loop sense mode provided enough bandwidth such that the frequency drifts of the drive and sense modes were suppressed.

The best results were taken when the sense frequency tuning voltage was kept constant. It is believed that whenever the gyroscope is disturbed by changing the tuning voltage, the performance gets worse instead of better. So, finally the gyroscope was operated in closed-loop sense mode without any mode matching loop (i.e., open-loop mode matching through each experiment).

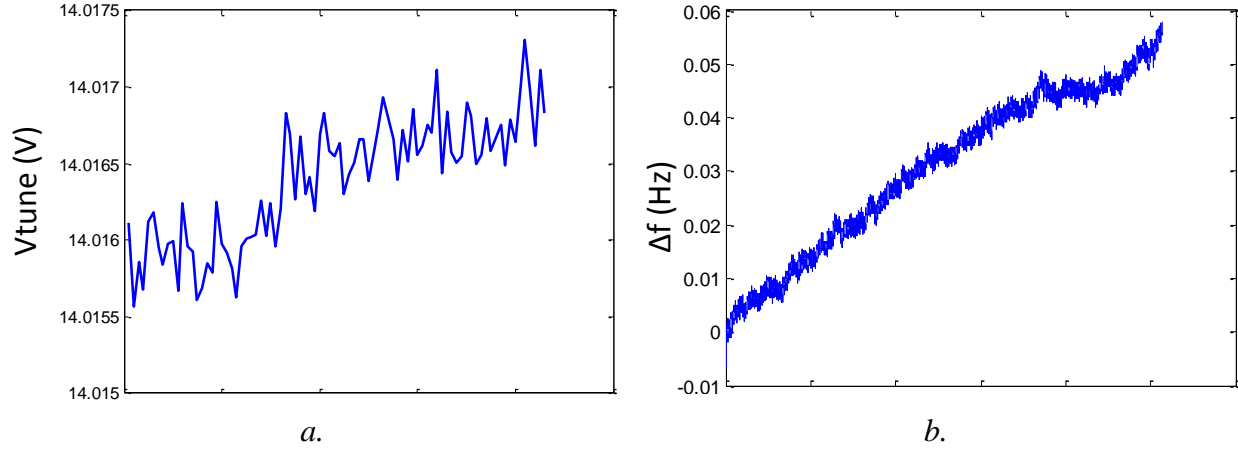


Figure 2.26: Tuning voltage on the sense (a) and drive resonance frequency drift (b) during the pilot tone mode matching experiment.

2.3 Gyroscope Noise Analysis

In this section, the Brownian (thermal) noise limit of the gyroscope is calculated. There are two contributors to the thermal noise: thermomechanical noise coming from the gyroscope and the thermal noise of the front end. The noise of the sense mode will be calculated since the drive displacement operates at high displacements and the thermal noise is not the dominant noise in the drive mode. The rate equivalent thermomechanical noise can be calculated by dividing the Brownian noise [44] by the unit Coriolis force:

$$\Omega_{rate_eqv_noise} = \frac{\sqrt{4k_B T b_y}}{2A m_y \omega_x X(\pi/180)} \quad 2.7$$

where k_B is the Boltzmann's constant, T is the absolute temperature, b_y is the damping constant of the sense mode, m_y is the mass of the sense mode, ω_x is the drive resonance frequency, X is the drive displacement, and A is the angle gain of the gyroscope. The Coriolis force exerted on the sense mode is directly proportional to the mass of the center proof mass. While it is translating into Coriolis acceleration in the sense mode, the Coriolis force acts on the mass of the overall sense mode, which is center mass and the side plates containing the capacitive electrodes. If we call the mass of the center mass as m_{PM} and the total mass of the side plates as $m_{sense\ side}$, then $A = m_{PM} / (m_{PM} + m_{sense\ side})$ and also $m_y = m_{PM} + m_{sense\ side}$. As an alternative, instead of m_y , m_{PM} can be used in 2.7. The x axis is assumed to be the drive axis and the y axis is assumed to be the sense axis. The denominator in 2.7 is multiplied with $\pi/180$ so that the unit of the rate equivalent noise will be $^{\circ}/s/\sqrt{Hz}$. The constants and SOI-MEMS gyroscope parameters are given in Table 2.4.

Table 2.4: The constants and SOI-MEMS gyroscope parameters.

Parameter	Value	Parameter	Value
k_B	$1.38 \times 10^{-23} \text{ m}^2\text{-kg-s}^{-2}\text{-K}^{-1}$	Q	18,000
T	300 K	A	0.56
$b_y = \sqrt{k_y m_y} / Q$	$9.45 \times 10^{-8} \text{ N-s-m}^{-1}$	ω_x	$2\pi \times 8800 \text{ rad/s}$
k_y	94 N/m	X	1 μm
m_y	$3.08 \times 10^{-8} \text{ kg}$		

Inserting the values in Table 2.4 in 2.7 yields a rate equivalent thermomechanical noise of 4.23 $^{\circ}/\text{hr}/\sqrt{Hz}$ for a 1 μm drive displacement amplitude.

The second noise contributor after the thermomechanical noise is the thermal noise of the gyroscope front-end circuit and the following circuits. Figure 2.27 presents the analog gyroscope front-end and signal conditioning circuits. The differential gyroscope output current is converted

into differential voltage output by transimpedance amplifiers. The differential voltage output is then converted into a single-ended output with a gain G by an instrumentation amplifier. The signal passes through a buffer before it goes to the digital lock-in amplifier.

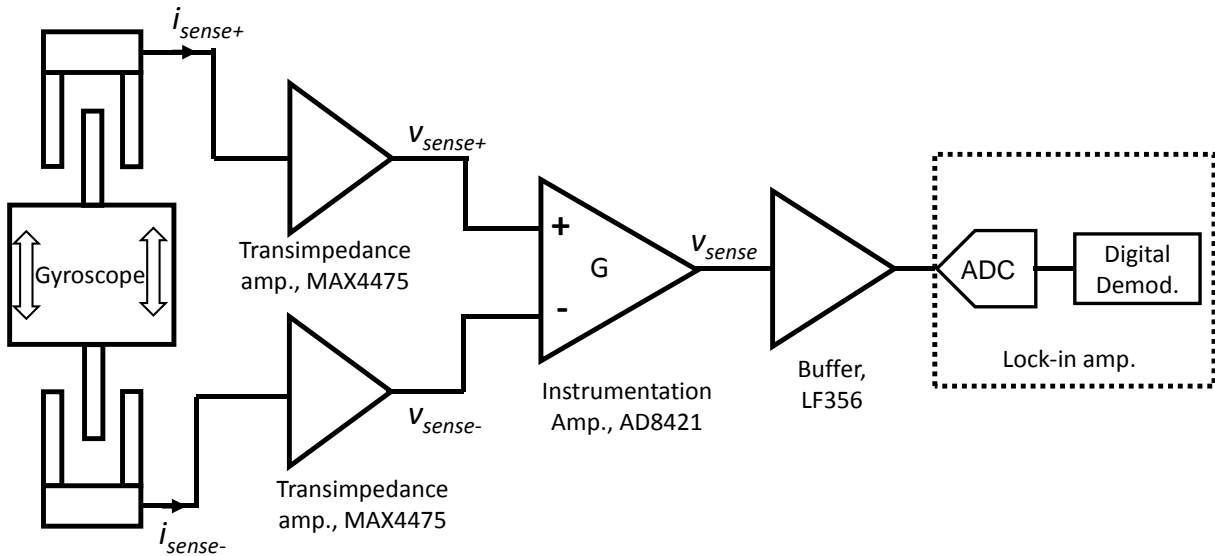


Figure 2.27: Gyroscope front end and the circuits.

We will examine the noise sources one by one starting with the transimpedance amplifier which dominates the overall circuit noise. Figure 2.28 shows the gyroscope front end with the noise sources. The gyroscope is biased with a RC network as explained in Section 1.7 and R_{bias} and C_{bias} are the biasing resistor and capacitor. The dc biasing point acts as a ground for the noise analysis.

Transimpedance amplifier converts the gyroscope output current into voltage with a capacitor instead of a resistor since the capacitor does not have thermal noise. C_{preamp} and R_{preamp} are the preamplifier capacitance and resistance. R_{preamp} is needed to provide dc discharge path for the input of the op-amp. C_p represents the undesired parasitic capacitance from the negative terminal of the op-amp to ground. The noise sources include the current noises for the resistors and op-amp voltage and current noise. The current noise components of the resistors are preferred since it is more convenient to deal with the current set up. Table 2.5 presents the circuit components

and corresponding noise values. The resistor noise values are calculated by using the thermal current noise equation $\sqrt{(4k_B T/R)}$. A low noise MAX4475 op-amp is used, and the noise values are obtained from the datasheet [67].

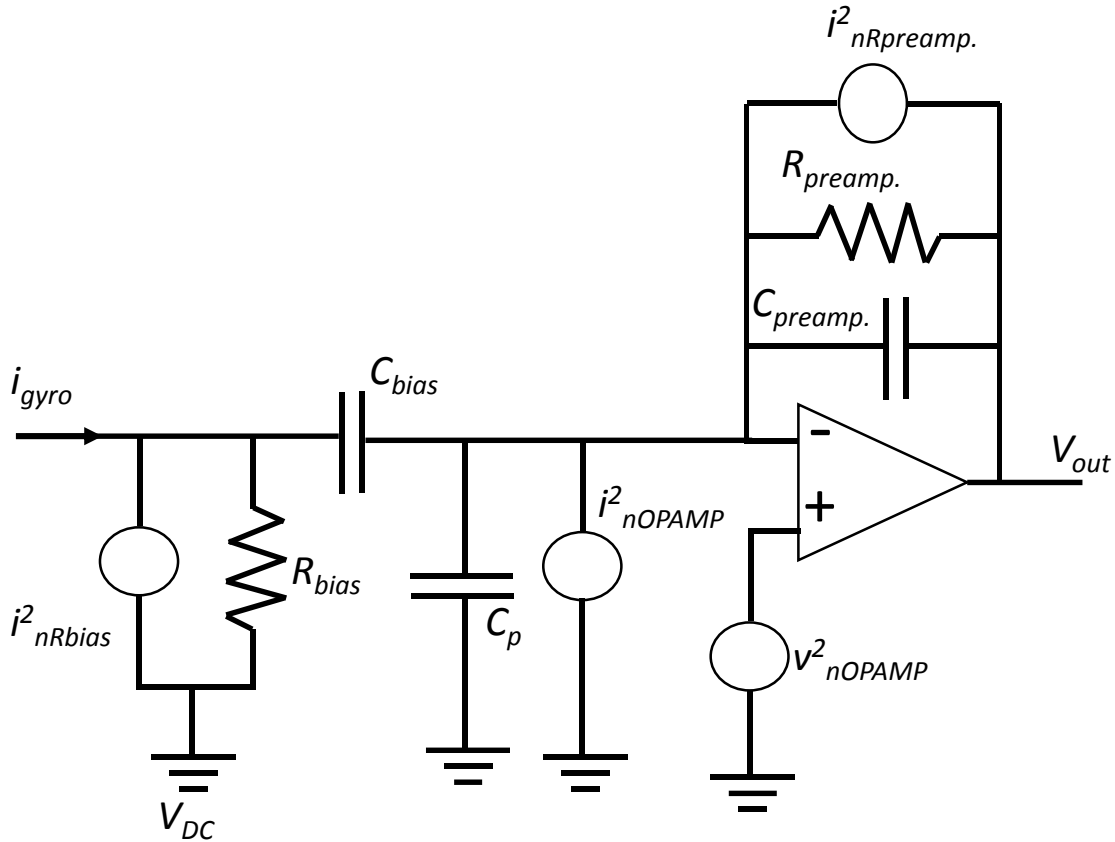


Figure 2.28: Gyroscope front end with the noise sources.

Table 2.5: Circuit components and corresponding noise values.

Component	Value	Noise Value
$R_{preamp.}$	470 M Ω	5.94 fA/ $\sqrt{\text{Hz}}$
$C_{preamp.}$	5 pF	-
R_{bias}	470 M Ω	5.94 fA/ $\sqrt{\text{Hz}}$
C_{bias}	5 nF	-
C_p	20 pF	-
i_{nOPAMP}	-	0.5 fA/ $\sqrt{\text{Hz}}$
v_{nOPAMP}	-	4.5 nV/ $\sqrt{\text{Hz}}$

Since the input impedance of the transimpedance amplifier is very small all the noise current sources, i_{nRbias} , i_{nOPAMP} , and $i_{nRpreamp}$ are converted into voltage by the impedance of the C_{preamp} at the drive resonance frequency. The negative feedback of the op-amp forces the negative terminal to follow the positive terminal leading to the amplification of the v_{nOPAMP} by $(1+C_p/C_{preamp})$.

Table 2.6: Summary of the noise sources at V_{out} .

Noise due to	Noise Contribution
$R_{preamp}, i_{nRpreamp} \times 1/(j\omega_x C_{preamp})$	21.5 nV \sqrt{Hz}
$R_{bias}, i_{nRbias} \times 1/(j\omega_x C_{preamp})$	21.5 nV/ \sqrt{Hz}
$i_{nOPAMP}, i_{nOPAMP} \times 1/(j\omega_x C_{preamp})$	1.8 nV/ \sqrt{Hz}
$v_{nOPAMP}, v_{nOPAMP} \times (1 + C_p / C_{preamp})$	22.5 nV/ \sqrt{Hz}

Then the total noise at the output of the transimpedance amplifier is found as

$$v_{nout} = \sqrt{21.5^2 + 21.5^2 + 1.8^2 + 22.5^2} = 37.9nV / \sqrt{Hz} \quad 2.8$$

The two differential transimpedance amplifier outputs are connected to the instrumentation amplifier for additional gain and differential to single-ended conversion. An AD8421 component is used as the instrumentation amplifier. The gain is set by connecting a resistor across gain terminals of the AD8421. The total input referred voltage noise of the AD8421 is given by [68]:

$$\begin{aligned} TotalVoltageNoise = \\ \sqrt{(OutputNoise / G)^2 + (InputNoise)^2 + (NoiseofGainResistor)} \end{aligned} \quad 2.9$$

The output and input voltage noise of the AD8421 is fixed at 60 nV/ \sqrt{Hz} and 3.2 nV/ \sqrt{Hz} , and the differential gain is fixed to 10 with a gain resistor of 1.1 k Ω . So, the total voltage noise at the input of the preamplifier is:

$$v_{n_inst.amp} = \sqrt{(60/10)^2 + 3.2^2 + (4.27)^2} = 8nV / \sqrt{Hz} \quad 2.10$$

The input current noise of AD8421 is 200 fA/ \sqrt{Hz} , and this will be converted into voltage by the output resistance of the transimpedance amplifier. However, the output impedance is in the order of ohms, so the noise contribution of the AD8421 input current noise is neglected. Then the total noise at the input of the instrumentation amplifier is:

$$v_{n_inst.amp} = \sqrt{37.9^2 + 37.9^2 + 8^2} = 54.2nV / \sqrt{Hz} \quad 2.11$$

The noise analysis has been done on a single-ended path up to this point; the transimpedance amplifier noise is repeated to account for the differential signal output. The noise at the output of the instrumentation amplifier is input noise (54.2 nV/ \sqrt{Hz}) times the gain (10) which is 542 nV/ \sqrt{Hz} . There is a buffer implemented with a LF356 op-amp in between the AD8421 and the lock-in amplifier. The voltage noise of the LF356 is 12 nV/ \sqrt{Hz} [69], which can safely be neglected compared to the total noise (542 nV/ \sqrt{Hz}). The input noise of the digital lock-in amplifier is 15 nV/ \sqrt{Hz} for the testing conditions [61] (at 8.9 kHz, 100 mV input range) that is also negligible compared to the total noise of the circuits.

The open-loop scale factor of the gyroscope is required to obtain the rate equivalent of the circuit noise. The scale factor of the gyroscope under matched mode operation conditions is calculated using 1.17:

$$|Y(j\omega_x)| = A \frac{2X\Omega}{BW} = 0.56 \frac{2 \times 1e-6 \times \pi / 180}{2\pi \times 8800 / 18000} = 6.36nm / ^\circ / s \quad 2.12$$

where A is the ratio of the center proof mass to the overall sense mode mass. The sense mode output current in 1.29 is converted into voltage by the transimpedance amplifier

$$v_{sense+} = V_{PM} \frac{\partial C}{\partial y} \frac{\partial y}{\partial t} \frac{1}{j\omega_x C_{Preamp.}} = V_{PM} \frac{\partial C}{\partial y} Y \frac{1}{C_{Preamp.}} \quad 2.13$$

The single-ended transimpedance amplifier output voltage v_{sense+} is 3.19×10^{-4} V/°/s ($\partial C/\partial y = 7.17 \times 10^{-9}$ F/m). The instrumentation amplifier has a gain (G) of 10, so the output is $2 \times 3.19 \times 10^{-4} \times 10 = 6.38$ mV/°/s. This is the peak voltage, so the root mean square (rms) scale factor is 4.5 mV/°/s. Then rate equivalent circuit noise is (542 nV/√Hz / 6.38 mV/°/s) = 0.43°/hr/√Hz, which is an order of magnitude smaller than the thermomechanical noise (4.23°/hr/√Hz). The gyroscope is limited by the thermomechanical noise under these conditions. Note that these calculations are valid only for the matched mode operation, the circuit noise will be more at the mismatched conditions. It will scale with $2\Delta\omega/BW$ where $\Delta\omega$ is the mismatch and BW is the open-loop bandwidth. For example, at 10 Hz mismatch the circuits noise increases by 40 times to 12°/hr/√Hz assuming a Q of 18,000. Thermomechanical noise does not change with mismatch, however the rate equivalent circuit noise decreases at the matched mode due to the increased current output of the sense mode.

The total voltage noise of the open-loop sense mode has been experimentally measured with a spectrum analyzer. Proof mass and frequency tuning voltage has been applied to the gyro without any ac driving voltage on the drive mode to keep the drive mode stationary. Then the only source causing the sense mode to vibrate is the thermomechanical noise. The spectrum analyzer was connected to the sense mode output buffer.

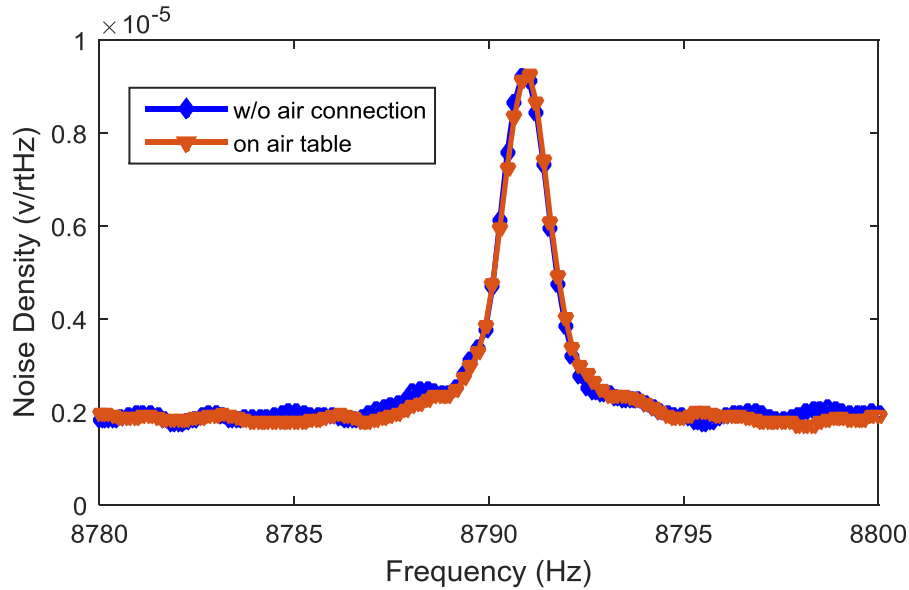


Figure 2.29: Power spectral density of the open-loop sense mode on the air table with and without the air connection.

Figure 2.29 shows the power spectral density of the sense mode output when the instrumentation amplifier gain is 10. A peak at the sense mode resonance frequency can be seen. Since the SOI-MEMS gyroscope is a single mass device it is vulnerable to environmental vibrations. In order to understand whether the noise peak is coming from environmental vibrations or the thermomechanical noise the measurements have been performed on the air table with and without the air connection. Both of the experiments resulted in identical results as shown in Figure 2.29 verifying that the source of the observed peak is thermomechanical noise. There is no external excitation on the sense mode; the peak is just due to the air molecules hitting to the sense mass, and high Q of the sense mode amplifies that motion at the sense resonance frequency. The circuit noise is not filtered since it is not passing through the sense mode. The flat region with $2 \mu\text{V}/\sqrt{\text{Hz}}$ noise level represents the circuit noise in Figure 2.29. Since we see a clear peak with almost five times the circuit noise, we can conclude that the system is thermomechanical noise limited.

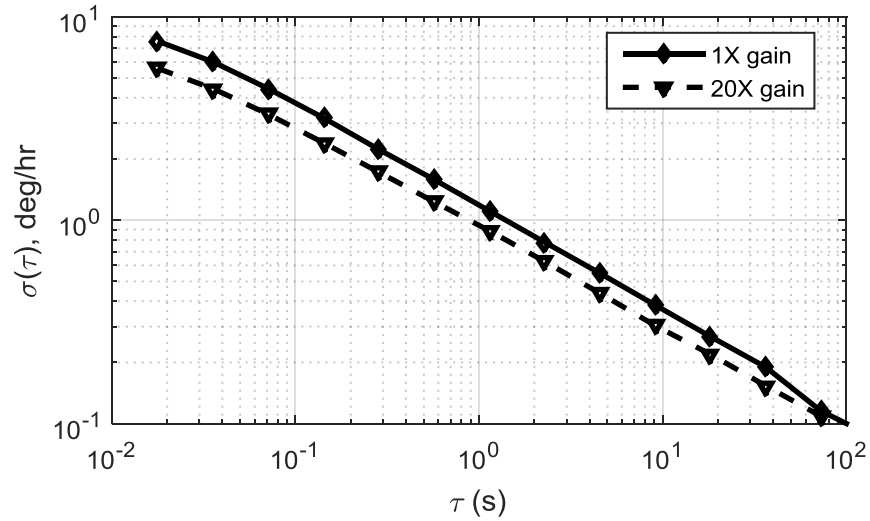


Figure 2.30: Allan deviation plots for the circuit noise when the instrumentation amplifier gain is 1 and 20.

We carried out an extra experiment to measure the circuit noise. Both sides of the sense mode capacitors are electrically grounded to eliminate the motional current contribution from the gyroscope. Then sense mode output is only due to the circuit noise, and the output noise is recorded with the digital lock-in amplifier when the instrumentation amplifier gain is set to 1 and to 20. Figure 2.30 presents the Allan deviation plots for the two cases. A $-1/2$ slope line is observed with the expected angle random walk (ARW) slope showing the noise is white. Increasing the gain of the instrumentation amplifier reduces the noise contribution of the amplifier and ARW is $1.15^\circ/\text{hr}/\sqrt{\text{Hz}}$ when the gain is 1 and $0.9^\circ/\text{hr}/\sqrt{\text{Hz}}$ when the gain is 20. The scale factors for $1\times$ and $20\times$ gain are calculated for $1.3\ \mu\text{m}$ drive displacement matched mode conditions as $0.585\ \text{mV}/^\circ/\text{s}$ and $11.7\ \text{mV}/^\circ/\text{s}$ respectively.

We can assume $1^\circ/\text{hr}/\sqrt{\text{Hz}}$ ARW when the instrumentation amplifier gain is 10 and calculate the voltage noise density as $2.3\ \mu\text{V}/\sqrt{\text{Hz}}$ that is consistent with the $2\ \mu\text{V}/\sqrt{\text{Hz}}$ density in Figure 2.29. Both of the measurements are four times larger than the $547\ \text{nV}/\sqrt{\text{Hz}}$ calculated circuit noise. Based on the measurements in Figure 2.29 and Figure 2.30 noise of the open-loop sense mode is

7.07 °/hr/√Hz. We assume a circuit ARW of 1°/hr/√Hz and multiply by $\sqrt{2}$ to convert it into thermal noise since the Allan deviation is performed on single sided spectrum. The total noise is five times the circuit noise yielding 7.07 °/hr/√Hz.

Equations 2.9 and 2.10 show that if the gain of the instrumentation amplifier is unity then the noise will be dominated by the 60 nV/√Hz output noise. Increasing the gain to 20 will highly suppress this noise. We can find the measured noise at the input of the instrumentation amplifier by using Figure 2.30 and look at their difference to check if it is around 60 nV/√Hz. The measured input referred noise of the instrumentation amplifier for 1× and 20× gain are 264.3 nV/√Hz and 206.8 nV/√Hz respectively. The difference between these is $\sqrt{(264.3^2 - 206.8^2)} = 164.6$ nV/√Hz which is 2.75 times the expected 60 nV/√Hz value. This difference is roughly consistent with the discrepancy between the measured and calculated total circuit noise. The measurements suggest the existence of a noise source that is not modeled.

2.3.1 Noise Analysis of the Closed-Loop System

Figure 2.31 shows the block diagram of the force-feedback controller for the sense mode. The gyroscope is driven by the electromechanical voltage (V) to force converter (F), K_d . The gyroscope sense mode (H_g) is modeled as a second order system that converts force (F) into displacement (X). The displacement (X) is converted into voltage by the gyroscope electrodes, transimpedance, and instrumentation amplifier represented by K_f . The Coriolis force is added as a force source at the input of H_g , and analog front end circuit noise and the input noise of the digital lock-in amplifier are included as v_{no} at the output of K_f . The overall gyroscope transfer function $K_d H_g K_f$ is represented as H_{gyro} to simplify the calculations. The output of H_{gyro} is digitized by an ADC and then demodulated ($K_{demod.}$) with a gain of 1. The low pass filter of the demodulator is not shown. The output of the demodulator goes to a PI controller (H_c) that tries to null the sense displacement.

The output of H_c passes through a modulator and DAC and applied to the gyroscope. The output of the system (V_{out}) is the amplitude of the voltage that nulls the sense displacement. The electromechanical noise of the mechanical structure is added as a voltage source ($v_{brownian}$) at the input of K_d .

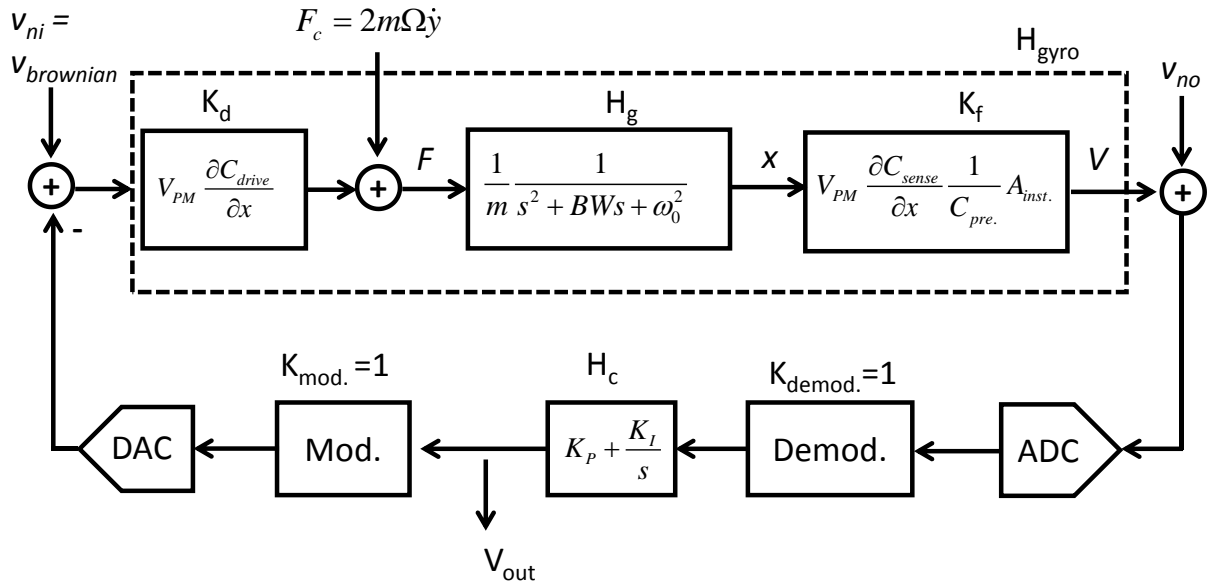


Figure 2.31: Block diagram of the force-feedback controller for the sense mode.

The gain of the desired signal that also represents the scale factor can be derived as:

$$\frac{V_{out}}{F_c \text{ closedloop}} = \frac{1}{K_d} \frac{H_c H_{gyro}}{1 + H_c H_{gyro}} \quad 2.14$$

The total noise power at the closed-loop output V_{out} is:

$$S_{nclosed} = \left| \frac{H_c}{1 + H_c H_{gyro}} \right|^2 (S_{no} + |H_{gyro}|^2 S_{ni}) \quad 2.15$$

where S_{ni} and S_{no} represent the power spectral density of $v_{brownian}$ and v_{no} , respectively with the unit of V^2/Hz . The loop at the V_{out} node is broken for the open-loop analysis and calculate the signal gain as:

$$\frac{V_{out}}{F_c}_{openloop} = \frac{1}{K_d} H_{gyro} H_c \quad 2.16$$

Similarly, the total noise power at the open-loop output is:

$$S_{nopen} = |H_c|^2 \left(S_{no} + |H_{gyro}|^2 S_{ni} \right) \quad 2.17$$

The noise equivalent rate (NER) to compare the open-loop and closed-loop cases is found by dividing 2.17 to 2.16 and 2.15 to 2.14.

$$S_{nopenNER} = S_{nclosedNER} = \frac{K_d^2}{|H_{gyro}|^2} \left(S_{no} + |H_{gyro}|^2 S_{ni} \right) \quad 2.18$$

We could have carried out the analysis by neglecting H_c in the open-loop analysis in 2.16 and 2.17 since there will not be a controller for the open-loop operation. That would also result in the same rate equivalent total noise. As shown in 2.18 open-loop and closed-loop systems result in the same NER. NER does not depend on H_c assuming that the digital or analog mechanism that is used to implement the closed-loop system introduces negligible noise. The closed-loop control is implemented digitally in the lock-in amplifier in this thesis that can be neglected. So the closed-loop NER of the gyroscope system is same as the open-loop NER, which is $7.07^\circ/\text{hr}/\sqrt{\text{Hz}}$, based on the measurements.

NER depends on H_{gyro} and H_{gyro} mainly suppresses the circuit noise S_{no} as shown in 2.18. A similar analysis for closed-loop gyroscope noise can be found in [70]. Closed-loop operation does not increase the noise but significantly improves the bandwidth for a high- Q mode matched gyroscope.

2.4 Summary

This chapter explained the simulation methodology, gyroscope control, and gyroscope noise analysis. The simulation methodology uses FEA software to obtain the anchor displacements, and anchor displacements are used in FEA eigenfrequency analysis to obtain the resonance frequencies with stress and temperature changes, and in mixed MEMS-electrical circuit simulation to obtain the ZRO and SF with stress. Simulations with feedthrough capacitance shows that stress originated quadrature signal may leak to the output underlying the importance of feedthrough minimization.

The PLL and amplitude control on the drive mode, and the quadrature and force rebalance on the sense mode constitute the gyroscope control loops. Different frequency control techniques were summarized; the closed-loop sense mode provided enough (20 Hz) bandwidth so frequency control was not needed for the gyroscope. The gyroscope noise analysis reveals the dominance of the thermal gyroscope noise. Closed-loop operation does not increase the noise if the mechanism that implements the control loop does not introduce considerable noise.

Chapter 3 Fabrication and Vacuum Packaging

This chapter explains the in-house developed SOI-MEMS fabrication process and discrete vacuum packaging system. The fabrication process consists of two masks and uses an SOI wafer to form the structures. The main effort on the fabrication process was spent on the deep reactive ion etching (DRIE) step, due to the fact that the DRIE tool (STS Multiplex ICP RIE) in the Carnegie Mellon Nanofabrication Facility does not have the SOI notching option [71]. The SOI fabrication process has been modified to be compatible with the developed vacuum packaging system. The vacuum packaging system uses ceramic packages and metal lids with getter material for long term stable vacuum. The chapter starts with the description of the fabrication process and of solved process problems and then moves to the details of the vacuum packaging system.

3.1 SOI-MEMS Fabrication Process

The gyroscope is fabricated by an in-house two mask SOI-MEMS process [72]. An SOI wafer with a p-type $\langle 111 \rangle$ highly conductive ($0.001\text{-}0.005 \Omega\text{-cm}$) $15 \mu\text{m}$ -thick device layer, $2 \mu\text{m}$ -thick buffered oxide layer (BOX), and $480 \mu\text{m}$ -thick handle layer is used. The reason for the choice of $\langle 111 \rangle$ silicon is its isotropic in-plane Young's modulus (E) [73], i.e. E does not depend on the orientation of the mechanical structures. The reason for the p-type choice is that p-type $\langle 111 \rangle$ wafers are more available in the market compared to the n-type $\langle 111 \rangle$ wafers. Although not specified by vendors, most commercial type $\langle 111 \rangle$ Si wafers are cut 5° off-axis leading to systemic Young's modulus mismatches between the two orthogonal directions. As a result of this issue, systematic frequency mismatches of 150 to 200 Hz were observed in the initial gyroscope designs, although the modes were exactly symmetric on the layout. The slight anisotropy in the mask making may also give rise to beam width mismatch between the two orthogonal

directions [74]. The frequency mismatch has been decreased down to 5 Hz by offsetting the beam width of the corresponding mode by 50 nm in the 3rd generation gyroscope design.

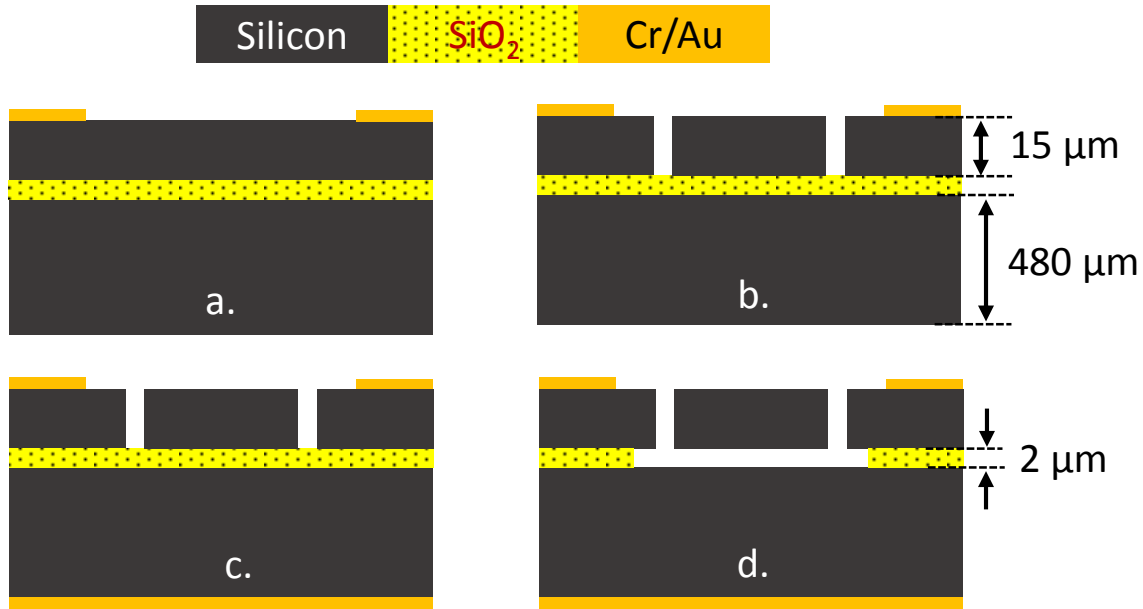


Figure 3.1: SOI-MEMS process fabrication steps.

Figure 3.1 summarizes the process flow. The process starts with 0.3 to 0.4 μm -thick Cr/Au metallization for the wirebonding pads (Figure 3.1.a). In the initial process (in the 1st and 2nd generation devices), the pads were defined by lift-off using a lift-off photoresist. In principle, the metallization never touches the silicon surface where the structures will be formed and this should yield better silicon etching. With time, it was realized that process constraint was not necessary and metal was blanket deposited and etched in the 3rd generation devices. Metal etching is easier since the bare silicon wafer is loaded into the sputtering chamber directly and heating during metal deposition is not an issue. In contrast, special attention is necessary not to overheat the lift-off photoresist during sputtering.

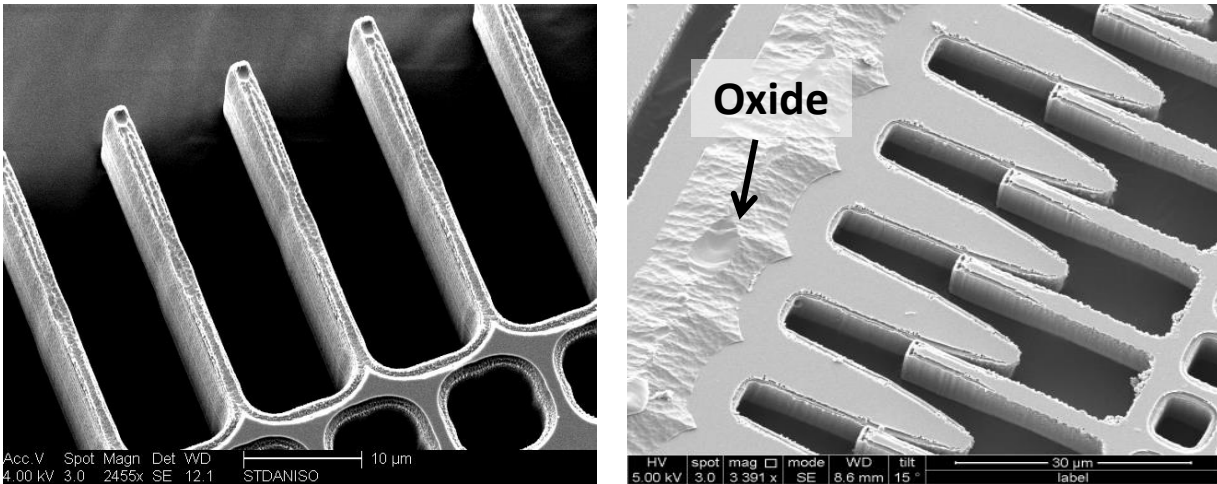
After the pad definition, structural layer etching is performed with silicon DRIE (Figure 3.1.b). Next an additional 0.3 to 0.4 μm -thick film of Cr/Au is deposited on the backside of the handle

layer to enable soldering of the die to a 40-pin dual-inline package (DIP40) before vacuum packaging (Figure 3.1.c). Then, the wafer is coated with a thick photoresist and diced. The dies are released in small batches in a timed buffered hydrofluoric acid (HF) etch, and the release process is completed with a critical point dryer (Figure 3.1.d). The Carnegie Mellon Nanofabrication Facility has a newly (as of 2015) obtained vapor HF tool that can also be used for the release of future runs.

Minimization of outgassing is critical since the gyroscopes are vacuum packaged before testing. Both the pad and backside metallization are sputtered in argon gas. The getter material is also sputtered as will be explained in vacuum packaging section. Argon is a noble gas and cannot be absorbed by the getter materials. Evaporated metal does not have the argon outgassing problem, but the evaporation tool in the Nanofabrication Facility has a very slow deposition rate (1 \AA/s). Because it would take a long time to evaporate the target thickness, sputtering is used. The argon is outgassed by vacuum baking the samples before vacuum packaging as will be explained in the following sections.

One major contribution on processing is the optimization of the DRIE recipe. Notching is a well-known phenomenon for DRIE of the SOI wafers and notching can be suppressed by pulsing the substrate bias power and plasma source power [75]-[76]. Unfortunately, the DRIE tool in the Nanofabrication Facility does not have the pulsed SOI-notch option. Notching creates silicon particles at the oxide interface and they form unwanted shorts between the stator electrodes and SOI handle layer after the release. The problem was noticed by measuring the resistances between the stators and substrate; normally they should be open, but megaohm resistances were measured. This residual finite resistance significantly reduces the yield. Some of the short problems can be solved by applying a current to these unwanted microbridges and “burning” them but this does not

solve the problem at its source. So a custom DRIE recipe was developed that reduces the notching by decreasing the etch rate and increasing the passivation. This effect is achieved by reducing the platen temperature to 15°C from 19°C, and increasing the passivation cycle time to 10 s from 8 s while keeping the etch cycle time constant at 12 s. The standard etch was 10 min 40 s (32 etch-passivation cycles), the custom etch time was 14 min 40 s (40 etch-passivation cycles). Figure 3.2 shows the backside SEMs for the standard and custom etch recipes. The standard recipe has excessive undercut, while the undercut is greatly reduced with the custom recipe.



(a) Backside SEM with 8 s passivation and 19°C platen temp., 10 min 40 s etch (b) Backside SEM with 10 s passivation and 15°C platen temperature, 14 min 40 s etch

Figure 3.2: SEMs of the SOI device backside for the standard recipe with excessive undercut (a) and the custom recipe with less undercut (b).

3.2 Discrete Vacuum Packaging System

Vacuum packaging of a MEMS gyroscope is crucial for a couple of key reasons. First and most important of all, vacuum packaging reduces the air damping suppressing the thermal noise significantly. Second, packaging protects the gyroscope from particles and humidity, providing a stable operation environment. And finally, as the goal of this thesis is to understand the stress effects on the gyroscope performance, having a vacuum packaged gyroscope (in contrast to testing

in a vacuum chamber) greatly simplifies the ability to perform external stress testing. Different vacuum packaging approaches were tried leading to development of the vacuum packaging system.

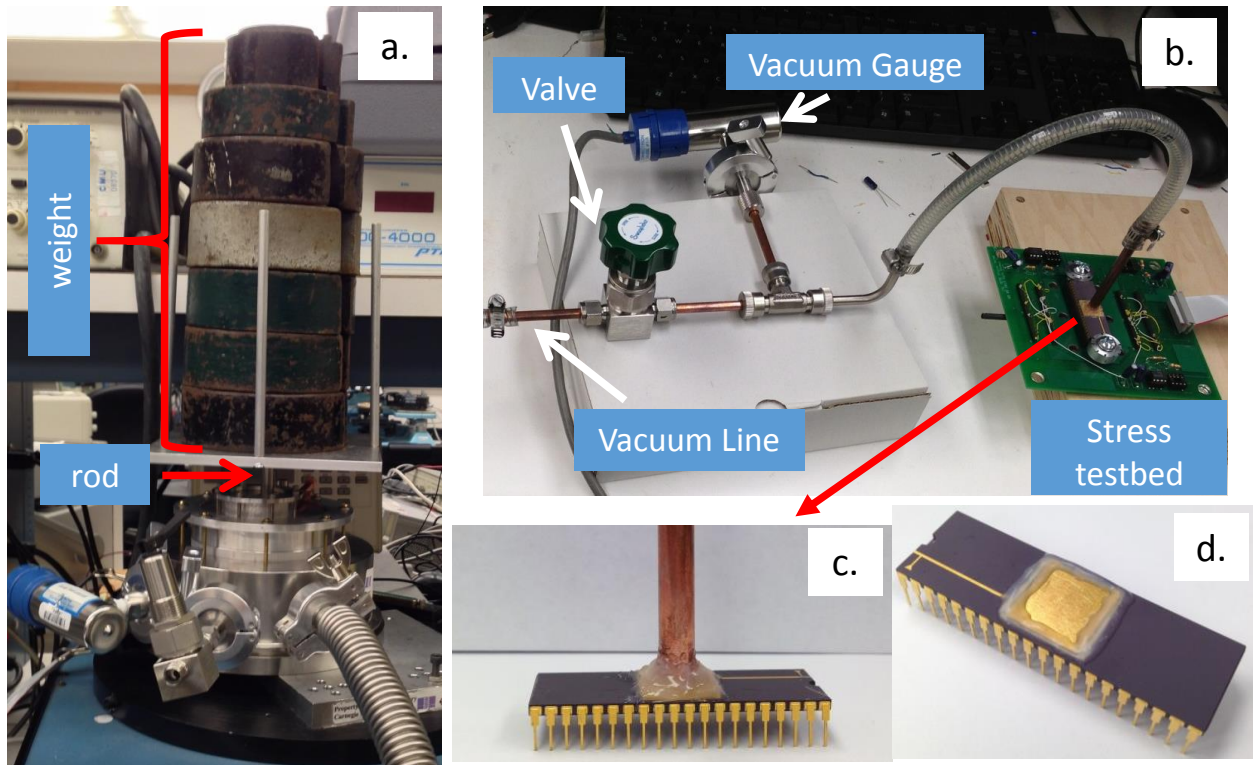


Figure 3.3: Different approaches for vacuum testing the gyroscope, (a) vacuum chamber, (b) and (c) using a tubular vacuum packaged system, and (d) using hermetic epoxy to glue a lid in vacuum.

Figure 3.3 summarizes the different approaches used for vacuum testing the gyroscope. Initially the gyroscope was placed in a vacuum chamber and stress was applied by adding weights through a rod (Figure 3.3.a). This set up was not flexible, difficult to rotate, and the sample cannot be seen. Next a hole drilled on a DIP40 lid and a copper tube was attached to it by hermetic epoxy (Henkel Hysol Trabond 2116), Figure 3.3.b shows the pumping system and Figure 3.3.c shows the DIP40 with the tube attached. The gyroscope sample is visible in this setup, but since a vacuum pump is still required, full rotation of the gyroscope on a rate table is not possible. In yet another approach, the device was sealed by gluing a metal lid to the DIP40 using a hermetic epoxy that cures at room

temperature in vacuum. Figure 3.3.d presents a sealed package with the hermetic epoxy. The pressure inside the cavity was at around a 1 Torr level and was not stable. The next sections explain the steps of the in-house developed vacuum packaging system.

3.2.1 Die Mounting for Vacuum Packaging

The vacuum packaging process starts with mounting the MEMS die to the package. Use of organic adhesives or epoxies is not allowed because of outgassing constraints. One common approach is using solder preforms such as gold tin (Au-Sn 80/20) [77]. A gold layer is deposited on the backside of the MEMS die during fabrication for the soldering to be successful. The eutectic point for the gold-tin solder is above 300°C. So both the sample and package is heated above 300°C, and gold-tin solder freezes at 270°C, attaching the MEMS to the package. Because of the thermal coefficient of expansion (TCE) mismatch ($TCE_{\text{package}} = 6 \text{ ppm}/^\circ\text{C}$, $TCE_{\text{Silicon}} = 3 \text{ ppm}/^\circ\text{C}$), this die attach method induces significant compressive stress on the MEMS die once cooled to room temperature.

This thesis proposes a stress-free die mounting technique using nanofoil [78]. Nanofoil from Indium Corporation is a reactive multi-layer foil that provides instantaneous heat once activated. This reactive multi-layer foil is fabricated by vapor depositing thousands of alternating nanoscale layers of aluminum and nickel. Once activated by a small pulse of energy, the local temperature rises up to 1500°C in milliseconds. The nanofoil has 10 μm -thick electroplated tin on both sides, and since the nanofoil is sandwiched in between two gold layers (gold on the package and gold on the bottom of the MEMS die), the 1500°C local temperature solders the MEMS die to the package. Neither the package nor the MEMS die is heated significantly in this process, leading to a relatively stress free mount at room temperature.

Nanofoil is composed of aluminum and nickel and $TCE_{\text{aluminum}} = 23.6 \text{ ppm}/^{\circ}\text{C}$, $TCE_{\text{nickel}} = 13 \text{ ppm}/^{\circ}\text{C}$. Once the exothermic reaction starts, the nanofoil will be free to relieve its stress until the tin freezes at 230°C . If aluminum and nickel are assumed to have equal volumes in the nanofoil, it can be treated as a single material with a TCE of $18 \text{ ppm}/^{\circ}\text{C}$. The package and the MEMS die will be at room temperature during the bonding process since the heat generated by the nanofoil is just large enough to melt the tin. Since only the nanofoil significantly rises in temperature, the packaging stress of the nanofoil will be directly related to its $40 \mu\text{m}$ thickness, the temperature difference between the room temperature and tin melting temperature ($230^{\circ}\text{C} - 20^{\circ}\text{C} = 210^{\circ}\text{C}$), and the TCE of the nanofoil ($18 \text{ ppm}/^{\circ}\text{C}$). If we compare this with Au/Sn solder that is $50 \mu\text{m}$ thick, has a TCE of $16 \text{ ppm}/^{\circ}\text{C}$, and has a melting point of 270°C , the packaging stress created just by the Au/Sn solder is almost the same as nanofoil packaging stress. But the main stress during the die mount process using Au/Sn will be coming from the ceramic package since both the MEMS die and package are heated. Packaging stress on silicon will be proportional to the TCE difference of silicon and ceramic ($6 \text{ ppm}/^{\circ}\text{C} - 3 \text{ ppm}/^{\circ}\text{C} = 3 \text{ ppm}/^{\circ}\text{C}$), along with the temperature difference of the Au/Sn melting temperature and room temperature ($270^{\circ}\text{C} - 20^{\circ}\text{C} = 250^{\circ}\text{C}$), and the package thickness of 1 mm . If we compare the TCE difference, thickness, and temperature difference multiplication of nanofoil and Au/Sn mounting by neglecting the Au/Sn solder preform stress, the nanofoil results in five times less stress.

A die mount tool has been designed to align the MEMS die to the package, and to apply pressure during nanofoil activation. Figure 3.4 shows the cartoon for the die mount tool (a), the photo of the die mount tool (b), and an activated nanofoil (c). The die mount tool with a vacuum hole in the middle is machined from aluminum. The die mount tool initially sits upside down and the MEMS die is placed into the middle cavity, and then the vacuum is turned on, holding the MEMS

die in its place. A copper weight with the vacuum hole is attached to the die mount tool before the MEMS die is placed into it. Next, the die mount tool is inserted into the die aligner aligning the position of the MEMS with respect to the package cavity. The outer shape of the die mount tool is an octagon, so the die can be mounted either 0° or 45° with respect to the package.

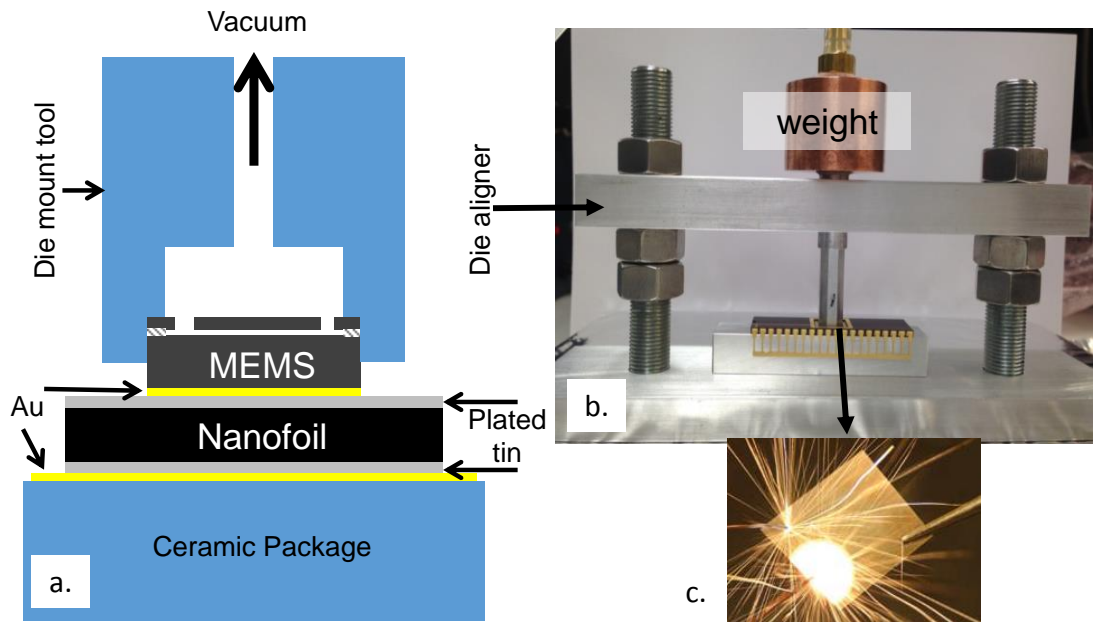


Figure 3.4: (a) Cartoon for the die mount tool, (b) the photo of the die mount tool, and (c) an activated nanofilm.

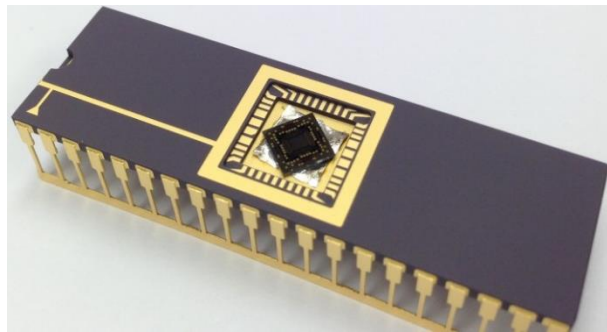


Figure 3.5: A MEMS gyroscope mounted on ceramic DIP40 with nanofilm.

After the alignment, the nanofilm is activated by shoring the leads of a dc voltage power supply on the nanofilm, and the stress free mounting is achieved within milliseconds. An activated nanofilm

is shown in Figure 3.4.c for reference. Figure 3.5 shows a MEMS gyroscope that is mounted on a ceramic DIP40 with nanofoil. The copper weight is necessary to achieve a uniform bond.

3.2.2 Getter

Getter is required for long term stable vacuum after hermetic seal. The proposed vacuum packaging system uses a titanium based getter [79]. Alternatively commercial getters are also available from SAES [80]. The getter consists of thin film sputtered titanium (Ti) gold (Au) with 1 μm and 30 nm thickness, respectively. Titanium is a reactive metal and keeps the vacuum constant by reacting with the outgassed gases in the vacuum cavity. Since exposure of titanium to atmosphere would directly saturate the gettering properties, a thin layer of gold is sputtered to protect the titanium. Ti/Au is sputtered on metal lids using a shadow mask. Figure 3.6 presents the aluminum shadow mask (a), and the metal lid with Ti/Au getter after deposition (b). Twenty five lids are deposited with getter at the same time. The gray Ti color can be noticed under the thin yellow Au color.

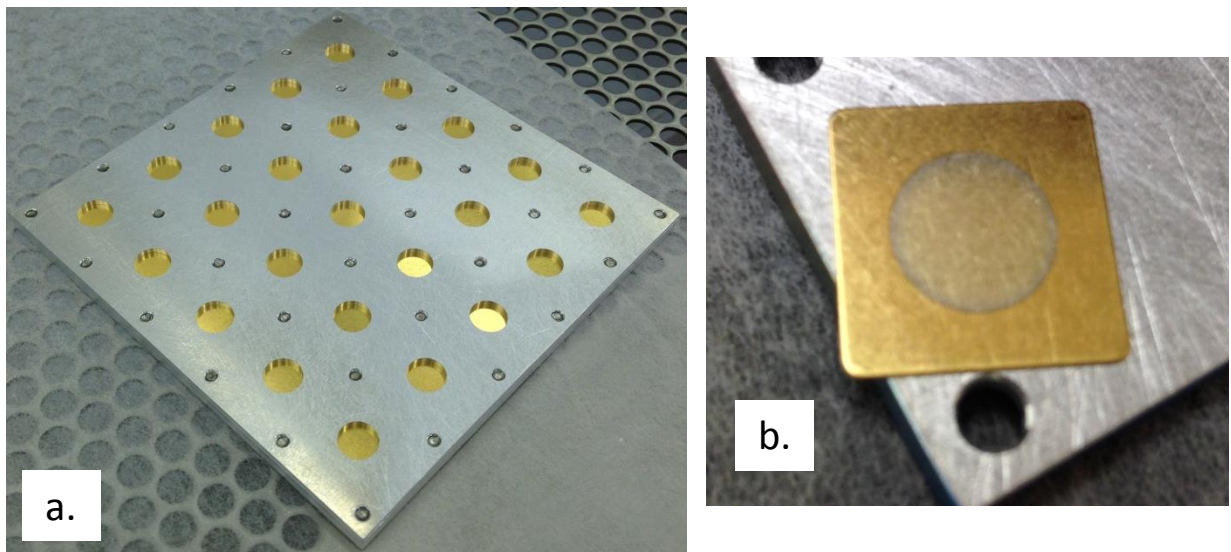


Figure 3.6: Shadow mask for getter deposition (a), and the metal lid with Ti/Au getter.

The getter is activated by heating the lid to a temperature above 300°C in high vacuum. The thin layer of Au diffuses into the Ti at this elevated temperature activating the getter. One fundamental question is how low of a pressure is needed not to saturate the Ti getter once activated. A rough estimate can be obtained with certain assumptions. The flux of air, i.e. the number of gas molecules passing through a unit surface per unit time is given by [81]:

$$J_N = P \sqrt{\frac{1}{2\pi k T m}} \quad 3.1$$

where P is the pressure in Pa, k is the ideal gas constant in $\text{J}\cdot\text{mol}^{-1}\text{K}^{-1}$, and m is the mass of the gas in kg/mol. It is assumed that a nitrogen flux of $J_N = 2.9 \times 10^{23} \text{ cm}^{-2}\text{s}^{-1}$ occurs at 760 Torr and 0°C. Then, if the pressure in the vacuum chamber is 100 μTorr and the temperature is 250°C, the flux is $J_N = 2.76 \times 10^{16} \text{ cm}^{-2}\text{s}^{-1}$. The getter area on the lid is 0.5 cm^2 so 1.38×10^{16} air molecules will be hitting to the getter surface per second.

The getter volume is $0.5 \text{ cm}^2 \times 1 \times 10^{-4} \text{ cm} = 5 \times 10^{-5} \text{ cm}^3$. Given the density of Ti is 4.5 g/cm^3 , the mass of the getter on the lid is $2.25 \times 10^{-4} \text{ g}$. The molar density of Ti is $2 \times 10^{-2} \text{ mole}/\text{g}$, so we have $4.5 \times 10^{-6} \text{ mole}$ of Ti on the lid. If we assume all the Ti molecules react with the gas molecules that hit to the getter surface then it takes $(4.5 \times 10^{-6} \times 6.02 \times 10^{23}) / 1.38 \times 10^{16} = 196 \text{ s}$ for the getter to saturate. This is a rough calculation that assumes the only gas is nitrogen and all the getter molecules react with the gases, but gives an idea of the pressure level. The getter is activated and exposed to vacuum around 40 minutes in the process, so below 2 μTorr level pressure, which provides 160 minutes of process time, is needed to be on the safe side so as not to saturate the getter during and after the getter activation.

3.2.3 Temperature Planning and Vacuum Packaging System

The MEMS gyroscope is mounted to the package in a stress-free way. The attachment is established with the plated tin on the nanofoil that has a melting temperature of 231.9°C. With a 50°C margin, the temperature during package-lid seal should not exceed 180°C for the die mount to remain stress free. Because if tin melts during the packaging then TCE mismatch leads to stress on the MEMS die. On the other side getter activation needs at least 300°C, and the higher the activation temperature the more the getter is activated. So the vacuum packaging system requires heating the lid separately in high vacuum for getter activation first and then merging the package and the lid for seal. Sample movement in the vacuum is needed. A pure indium solder preform with a melting temperature of 156.7°C is used for the lid package soldering that is within the temperature budget. In addition to pure indium, 80In/15Pb/5Ag solder with 154°C melting temperature has also been tried. The vacuum seal is obtained with the pure indium solder, we believe this is due to the fact that the oxidation of indium solder is slower compared to 80In/15Pb/5Ag solder.

Different activation temperatures and times have been tried for the getter. Figure 3.7 shows the lid with the getter before activation and after activation at 300°C for 15 minutes and at 350°C for 30 minutes. The yellow gold color still exists for 300°C temperature implying that the getter is not activated. However, a dark gray color can be observed for 350°C temperature activation confirming the getter activation. So, a temperature of larger than 350°C and close to 400°C is targeted for successful getter activation.

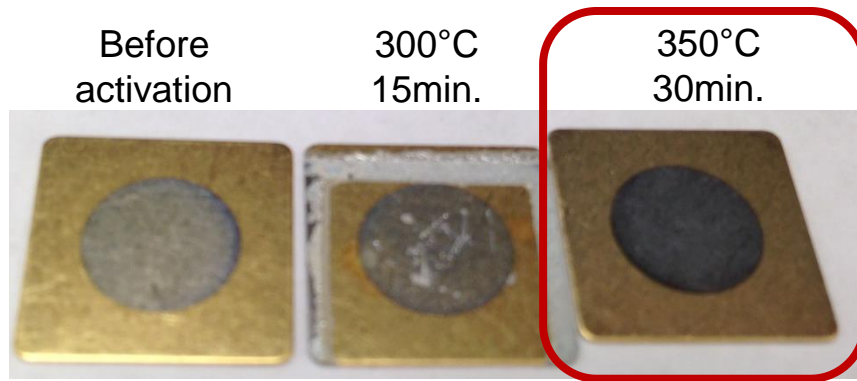


Figure 3.7: Metal lid with the getter before and after activation at different temperatures.

After the die mount using nanofilm, the gyroscope is wirebonded and characterized. The heights of the wirebonds are made sure to be low enough so that they are not shorted by the metal lid. If both of the gyroscope modes respond properly during the initial resonance tests, then the package is loaded into the vacuum chamber for outgassing. The gyroscope package is baked at 150°C in high vacuum for 12 to 24 hours. After the package outgassing, the chamber is vented and reloaded again with the lid as soon as possible to minimize reabsorption of the surfaces. The package outgassing and vacuum packaging cannot be done at once since once the indium solder preform is attached to the package that would decrease the maximum allowed temperature to less than 100°C. 100°C would be inefficient for outgassing, it should be higher than water boiling temperature to get rid of water vapor efficiently. In addition, experiments revealed that indium solder hardens once exposed to 100°C temperature for extended amount of time.

Figure 3.8 presents the temperature profile used during vacuum packaging based on the temperature requirements of the getter activation and lid-package seal. The process starts with slowly increasing the temperature to 150°C and waiting for 1 to 2 hours for the base pressure to be reached after the lid and ceramic package is loaded. Generally, a base pressure of 0.5 μ Torr is obtained. Then the temperature is increased to 250°C in half an hour with 15°C steps. The small step size in temperature keeps the pressure constant by preventing the overheating of the heater.

Next the lid is kept at 250°C for outgassing, and then heated to 400°C in half an hour with 15°C steps. The lid is kept above 380°C for 20 minutes for getter activation. Then the cooling water is turned on and the lid is cooled with the maximum cooling rate to 100°C. Once the getter is activated every step should be passed as fast as possible to minimize the getter saturation. The package is moved towards the lid and the temperature is increased to 200°C for hermetic seal. The temperature is kept at 200°C for 3 minutes. Finally, the package-lid pair is cooled with the highest cooling rate. The pressure inside the chamber is kept below 2 μTorr during the whole process.

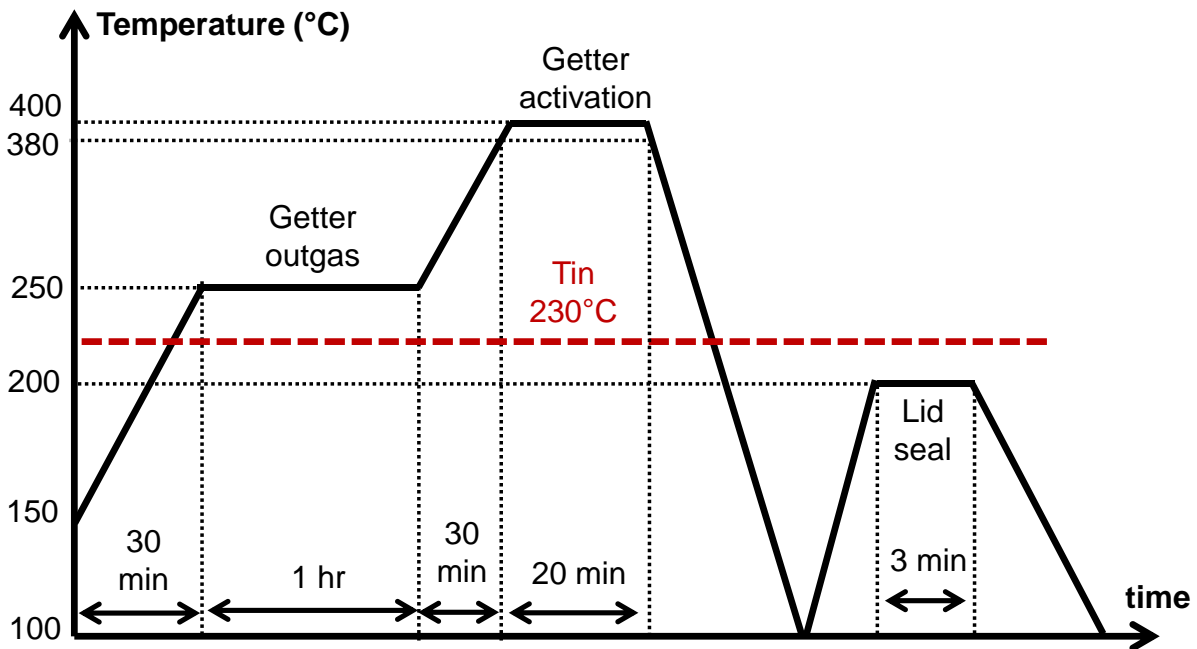


Figure 3.8: Temperature profile used during vacuum packaging.

Figure 3.9 shows the photo of the vacuum packaging system. A turbo pump is directly connected to the chamber to maximize the pumping rate. The temperature controller and vacuum gauges can also be seen. The vacuum gauge measures the pressure with a convectron and an ion gauge. The heater and thermocouple connections go inside the chamber through electrical feedthroughs. A chiller (not shown, under the table) cools and circulates the cooling water through the liquid feedthrough.

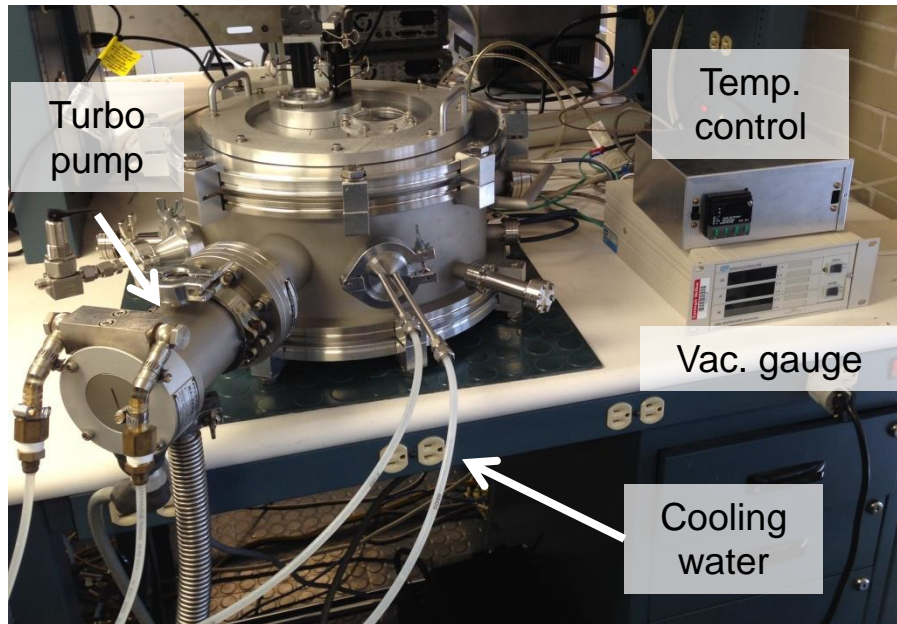


Figure 3.9: Vacuum packaging system.

Figure 3.10 presents the detailed view of the vacuum chamber, and Figure 3.11 shows the cross sectional schematic of the vacuum packaging system. The die aligner is a machined aluminum piece that houses the cartridge heater, cooling pipe, and thermocouple. The die aligner sits on another big aluminum block for mechanical support that is thermally isolated with ceramic spacers. The DIP40 is located on a mechanical fixture shown in Figure 3.10.b and Figure 3.11, and the die aligner is shaped as the complement of that mechanical fixture. The lid sits in the recess in the middle of the die aligner, and die aligner aligns the package to the lid for the hermetic seal. The shutter is a shiny aluminum piece and protects the package from overheating during the getter activation. The shutter and package pass through hermetic O-ring seals and can move vertically and rotate in vacuum. A 5 lb weight is applied on top of the package holder from outside during lid-package sealing. The solder preforms are bought in the form of 1 inch-wide 25 μm -thick metal tapes, and then cut into the frame shape with an aluminum mold. Two stacks of sheets (50 μm total thickness) are used to overcome the flatness of the overall system. Each layer of solder

preform with 25 μm thickness is first cut from the metal tape, and then stacked before they were cut into the frame shape.

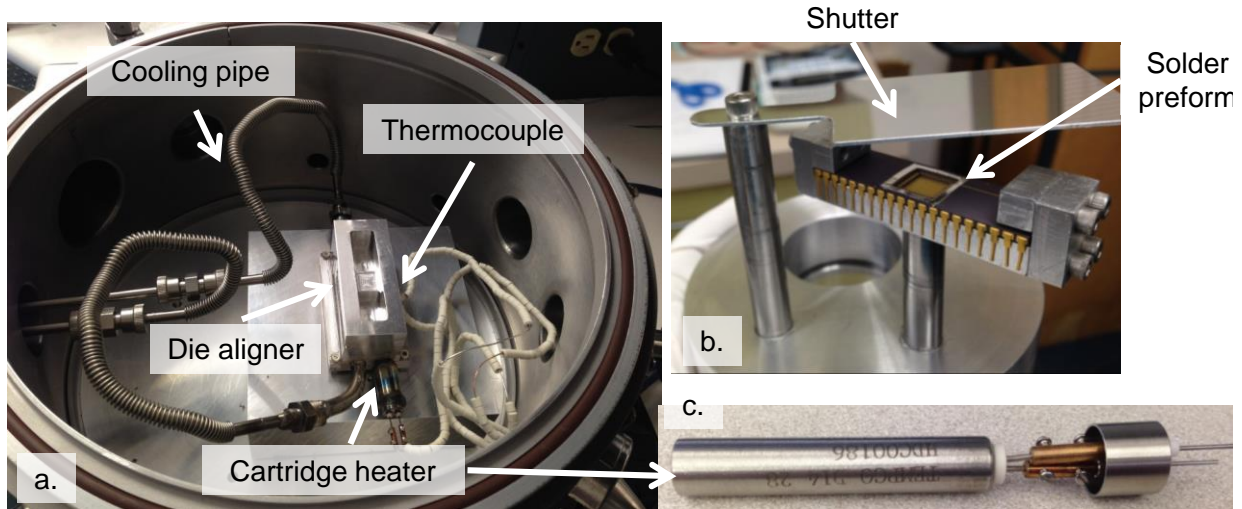


Figure 3.10: Inside of the vacuum chamber showing (a) the details, (b) the top piece for sample movement and shutter, and (c) the cartridge heater.

Thermal contact for the heater and cooling pipe is crucial for heating and cooling performance in vacuum. Since there is basically nothing except the radiation in vacuum to conduct heat, boron nitride is used as the fill material between the heater, cooling pipe, and the die mount tool. Boron nitride is known to survive at high temperatures without outgassing. As of heater, there are different heater options to use in high vacuum. These options include graphite and infrared (IR) heaters, both of them are vacuum compatible at high temperatures. Graphite heaters are low resistance, less than 10Ω , so they cannot be directly connected to the 120 V ac voltage. A transformer is needed to step down the voltage, and in general higher currents are needed. The IR heaters can be run from 120 V ac, but they are expensive (~\$1000) as are the graphite heaters. A low cost alternative uses regular cartridge heaters with modifications for vacuum operation. Cartridge heaters are not vacuum sealed on the electrical leads, resulting in outgassing in vacuum. Vacuum electrical feedthroughs were attached to the cartridge heater as shown in Figure 3.10.c. Figure 3.12 explains the hermetic sealing of the cartridge heater. After the electrical connection,

a stainless steel sleeve is welded to the cartridge heater and to the vacuum feedthrough in order to form a sealed heater. The sealed cartridge heater cost is less than \$100, and can be directly run from 120V AC. The only possible problem is durability of the heater in the long term. But no problems have been noticed so far after 20 packaging runs.

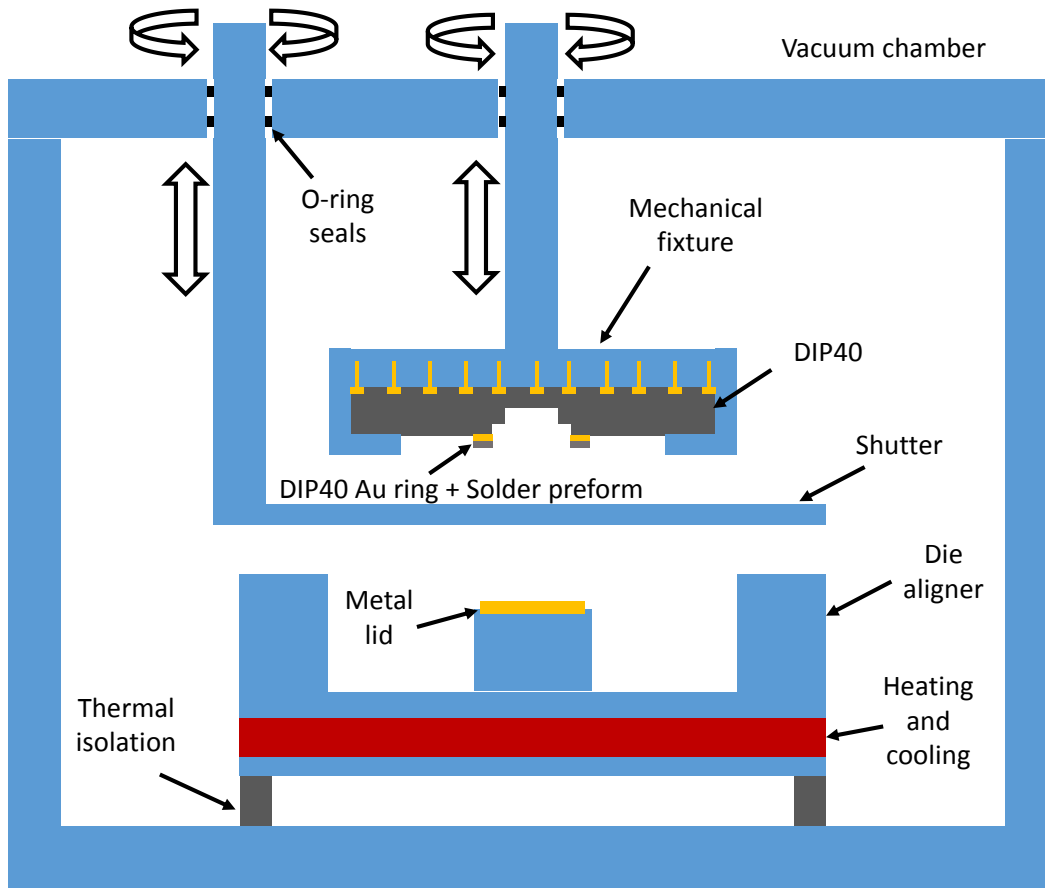


Figure 3.11: Cross sectional schematic of the vacuum packaging system.

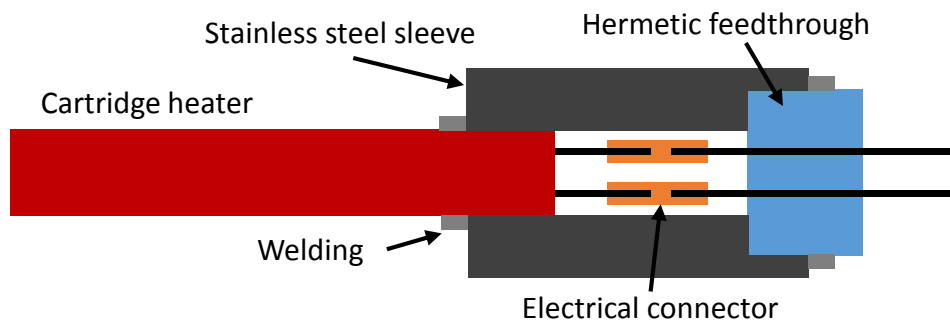


Figure 3.12: Schematic for the hermetic seal of the cartridge heater.

3.2.4 Vacuum Packaging Results

Figure 3.13 shows a vacuum packaged ceramic DIP40. Several MEMS gyroscopes have been vacuum packaged successfully. The pressure inside the package is characterized by monitoring the quality factor (Q) over time. Figure 3.14 presents the frequency sweep results before and after vacuum packaging. The Q of the device is 20 before vacuum packaging and 23,000 after the vacuum seal showing that the in-house developed vacuum packaging system is working.

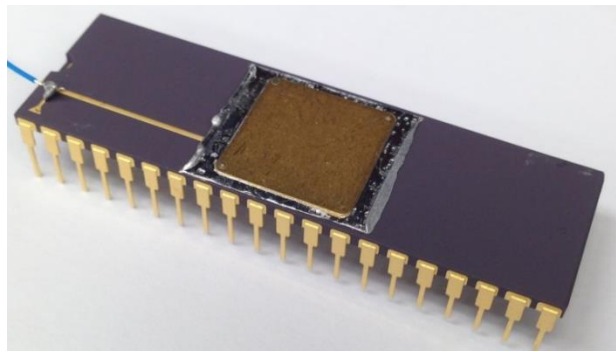


Figure 3.13: A vacuum packaged ceramic DIP40.

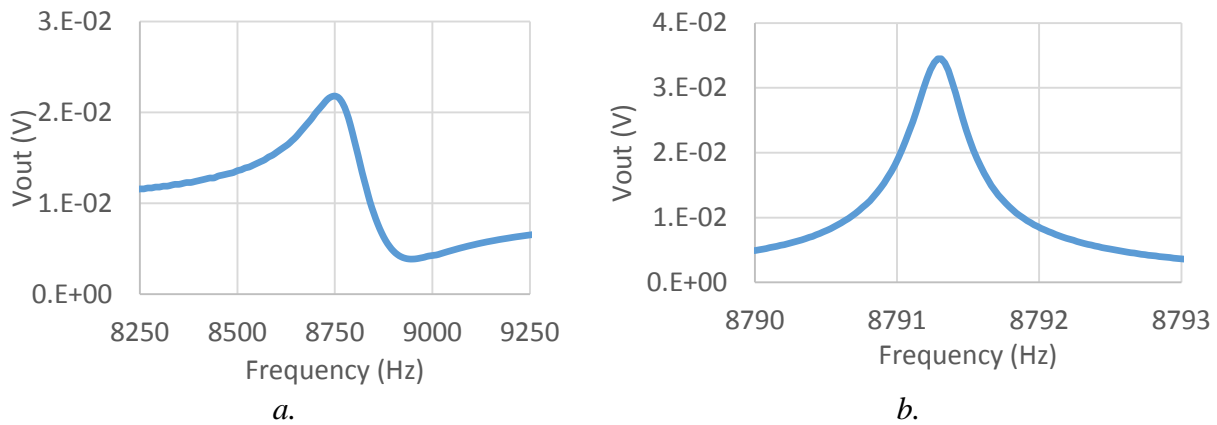


Figure 3.14: Frequency sweeps before vacuum packaging with $Q=20$ (a), and after vacuum packaging with $Q=23,000$ (b).

Five devices have been vacuum packaged successfully. The initial vacuum packaged devices had quality factors in between 4,000 to 6,000 corresponding to around 200 mTorr pressure. The Q increased with increasing the package outgassing temperature, but later a thermal contact problem was noticed in between the package and die aligner. Once that problem was corrected, the Q of

the devices increased to 20,000 range corresponding to around 50 mTorr pressure. The temperature is measured at the die aligner, not on the package. Since the initial package outgassing temperature was a lot lower than the measured temperature due to missing thermal contact, the outgassing step was not performed properly. This shows that the package outgassing temperature has a major effect on the final package pressure.

In all of the packaged gyroscopes, a 30% to 40% increase in Q was observed within the first 24 to 48 hours. The getter may be working slowly. The Q kept increasing once the stress sensors were activated. The stress sensors are basically suspended resistors in vacuum and with the application of a dc voltage they heat up. Increasing temperature is believed to increase the oxidation rate of silicon and result in a decrease in pressure in a small isolated cavity. A slow drop in Q with time was observed in the long term (> 3 months) in one of the samples, and the drop continued after applying hermetic epoxy on the bond ring. The Q dropped from 20,000 to 10,000 in 4 to 5 months. So, this issue is not believed to be a sealing problem, but rather a gettering problem that requires attention.

The vacuum sealing is done at μ Torr pressure, however the best obtained vacuum is 50 mTorr. This may be due to argon outgassing from the backside and pad metallization, or nanofoil may be outgassing. A detailed characterization on the in-house getter is also not performed, the getter may also be saturating. Additional studies can be performed such as replacing the nanofoil with a solder preform, and a packaging without any getter. Those studies could not be done due to time constraints. We continued with the testing once the gyroscope was packaged successfully since the main goal of this thesis is to study stress effects on the gyroscope.

3.3 Summary

This chapter explained the details of the in-house SOI-MEMS fabrication process and the in-house discrete level vacuum packaging approach. The fabrication process includes two masks for the pad metallization and structural layer definition. The main contribution is the optimized DRIE recipe due to the lacking notching option of the silicon etcher. Decreasing the etch rate solved the unwanted short problems.

Vacuum packaging starts with stress free die mounting with nanofoil. Tin melting temperature (231°C) puts the maximum temperature limit of 180°C on the package for the die mounting to remain stress free. The lid is heated to 400°C first for getter activation during vacuum packaging while the package is protected with a shutter. The package and lid are merged after the lid is cooled and hermetic sealing is achieved with low temperature indium solder preform. Cavity pressures as low as 50 mTorr was obtained with the in-house vacuum packaging approach.

Chapter 4 Nonlinearity and Frequency Tuning

A mode-matched gyroscope requires frequency tuning to keep the frequencies controlled against environmental changes and process imperfections. The gyroscope studied in this thesis achieves tuning of the frequencies through electrostatic shaped interdigitated combs [72]. The first concept of tailoring the electromechanical force by changing the gap profile was introduced in [82] and this thesis follows the same basic design methodology. The thesis not only uses shaped combs for frequency tuning but it also develops shaped combs to tune the softening nonlinearity. The more conventional way of frequency tuning uses the nonlinearity in parallel plate capacitors [83], which limits the maximum displacement. Shaped combs do not have any theoretical displacement limitation and allow the design of high displacement three-fold symmetric gyroscopes. This chapter also reports experimental results on the electrical tuning of the quality factor that was noticed during the experiments.

4.1 Shaped Comb Finger Design

Figure 4.1 shows a MEMS capacitor with an arbitrary gap profile. The rotor is assumed to move in the x direction. The rotor is straight shaped for simplicity but a random shape of the rotor does not change the analysis.

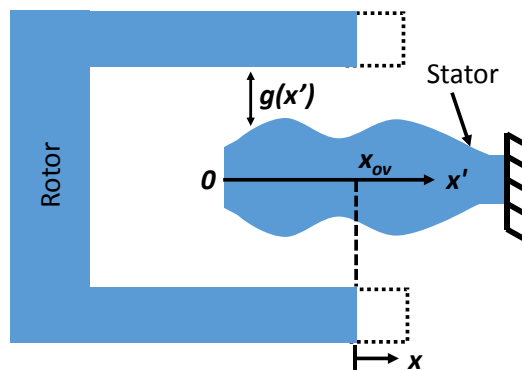


Figure 4.1: A MEMS capacitor with an arbitrary gap profile.

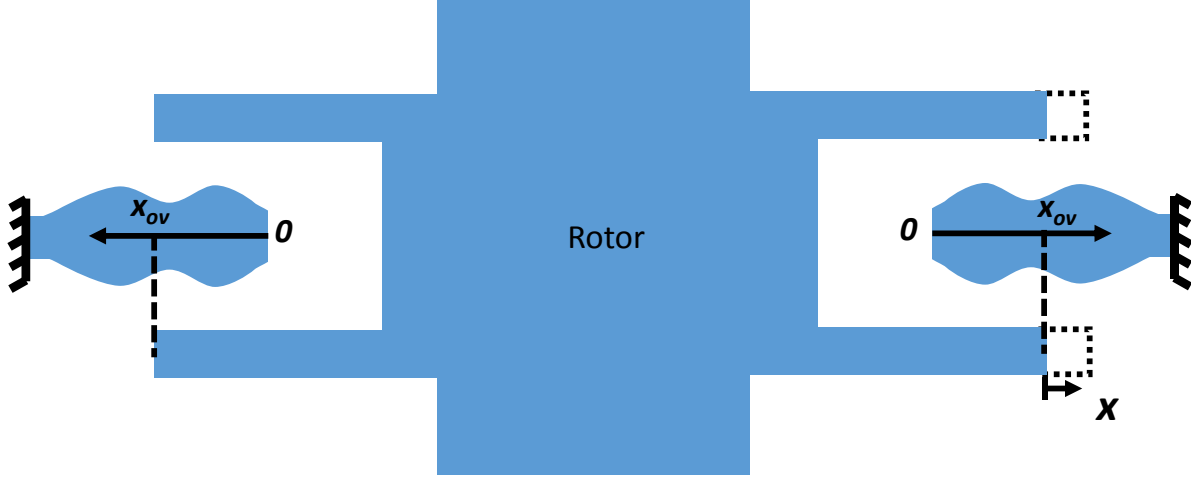


Figure 4.2: Symmetrically placed shaped comb fingers on the layout.

Assuming a parallel-plate capacitor model (i.e., neglecting the fringe fields) and the combs are placed symmetrically on the layout as shown in Figure 4.2, the total capacitance is:

$$C(x) = 2N\epsilon h \int_0^{x_{ov}+x} \frac{dx_1}{g(x_1)} + \epsilon h \int_0^{x_{ov}-x} \frac{dx_1}{g(x_1)} \quad 4.1$$

where ϵ is the permittivity of free space, h is the thickness of the structure, x_{ov} is the overlap of the electrodes at zero displacement, N is the number of fingers, and $g(x)$ is the gap profile. The electrostatic force is:

$$F(x) = N \frac{d}{dx} \left(\epsilon h \int_0^{x_{ov}+x} \frac{dx_1}{g(x_1)} + \epsilon h \int_0^{x_{ov}-x} \frac{dx_1}{g(x_1)} \right) V^2 \quad 4.2$$

$$F(x) = NV^2 \epsilon h \left\{ \frac{1}{g(x_{ov}+x)} - \frac{1}{g(x_{ov}-x)} \right\} \quad 4.3$$

If the applied voltage is dc, then different electrostatic forces can be formed by changing the gap shaping function, $g(x)$. Table 4.1 shows the total double-sided capacitance for different gap profiles that are evaluated using 4.1, and Table 4.2 presents electrostatic forces for different gap profiles. The force term in 4.7 consists of a voltage controlled constant times displacement i.e.,

$F(x) = \gamma V^2 x$, which acts like a linear spring force ($F(x) = kx$). Comb capacitors governed by 4.7 and 4.8 can be used to tune the frequency up and down, respectively. Combs governed by 4.9 introduce a cubic hardening force that is used to tune the softening nonlinearity in this work.

Table 4.1: Total capacitance for different gap profiles.

Gap profile	Electrostatic force	
$g(x) = \frac{g_0}{1 + x/x_{01}}$	$C(x) = \frac{2N\epsilon h}{g_0} \left(2x_{ov} + \frac{x_{ov}^2 + x^2}{x_{01}} \right)$	4.4
$g(x) = \frac{g_0}{1 - x/x_{01}}$	$C(x) = \frac{2N\epsilon h}{g_0} \left(2x_{ov} - \frac{x_{ov}^2 + x^2}{x_{01}} \right)$	4.5
$g(x) = \frac{g_0}{1 - x^3/x_{03}}$	$C(x) = \frac{2N\epsilon h}{g_0} \left(2x_{ov} + \frac{-2x_{ov}^4 - 12x_{ov}^2 x^2 - 2x^4}{4x_{03}} \right) V^2$	4.6

Table 4.2: Electrostatic forces for different gap profiles.

Gap profile	Electrostatic force	Finger Layout	
$g(x) = \frac{g_0}{1 + x/x_{01}}$	$F(x) = \frac{2N\epsilon h}{g_0} \frac{x}{x_{01}} V^2$		4.7
$g(x) = \frac{g_0}{1 - x/x_{01}}$	$F(x) = -\frac{2N\epsilon h}{g_0} \frac{x}{x_{01}} V^2$		4.8
$g(x) = \frac{g_0}{1 - x^3/x_{03}}$	$F(x) = -\frac{2N\epsilon h}{g_0} \left(\frac{3x_{ov}^2 x}{x_{03}} + \frac{x^3}{x_{03}} \right) V^2$		4.9

4.1.1 Shaped frequency tuning combs

Figure 4.3.a shows the frequency tuning comb topology used to tune the frequency with the corresponding SEM image in Figure 4.3.b. The tip of the finger is truncated to a 2 μm width to

satisfy the minimum width constraint of the design. As the combs engage, the rate of increase for the total capacitance increases due to the gap profile resulting in a positive dC/dx that increases in value with x . Figure 4.4 presents the calculated and simulated total capacitance for the shaped frequency tuning combs shown in Figure 4.3. The calculation does not take into account the fringe fields, leading to the difference between FEA and calculation. Figure 4.5 shows the position derivative (dC/dx) for the simulated total capacitance for the shaped frequency tuning combs. It is linear with respect to comb engagement as expected to tune the frequency.

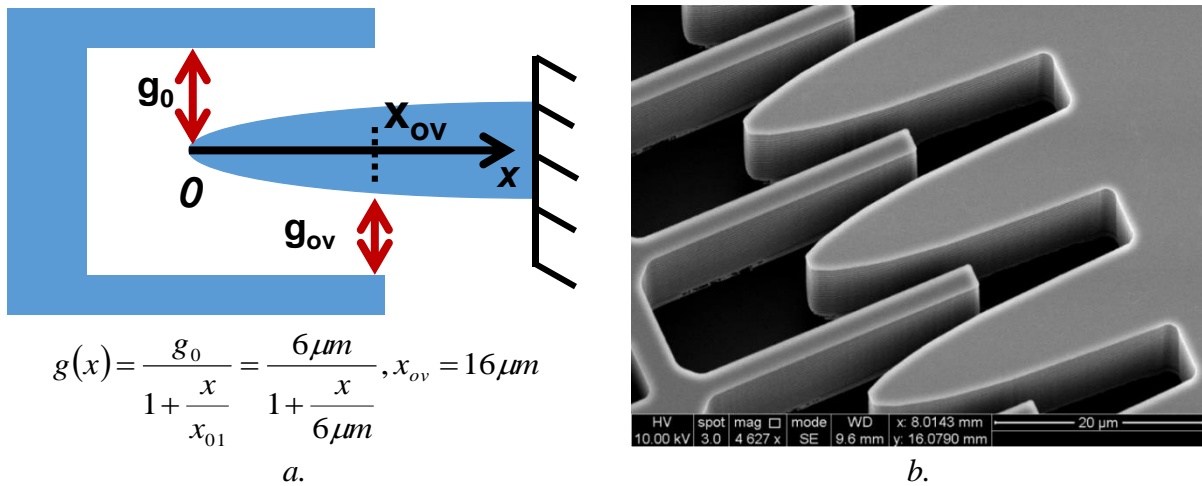


Figure 4.3: A gap profile for the shaped frequency tuning (a), and an SEM of the fingers (b).

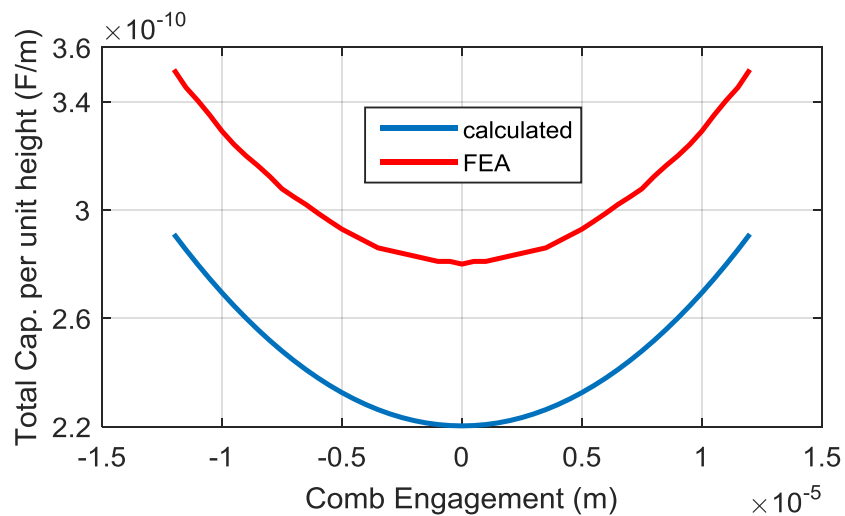


Figure 4.4: Calculated and simulated total capacitance for the shaped frequency tuning fingers shown in Figure 4.3.

The shaped frequency tuning combs in Figure 4.3 are successfully used to tune the x and y resonance frequencies of the gyroscope. Figure 4.6 shows a typical measured tuning curve for the shaped frequency tuning fingers. The tuning voltage is applied to mode 2 and 140 Hz resonance frequency difference has been tuned with 50 V. The efficiency of the shaped comb fingers, which is defined as $dC/dX/(comb\ area)$, directly relies on the initial gap (g_0) and gap coefficient (x_{01}); the minimum gap requirements must still be met at x_{ov} . The current design for the SOI-MEMS process was made for a minimum gap of 2 μm . Having a process with a smaller minimum gap design rule would improve the efficiency of the tuning.

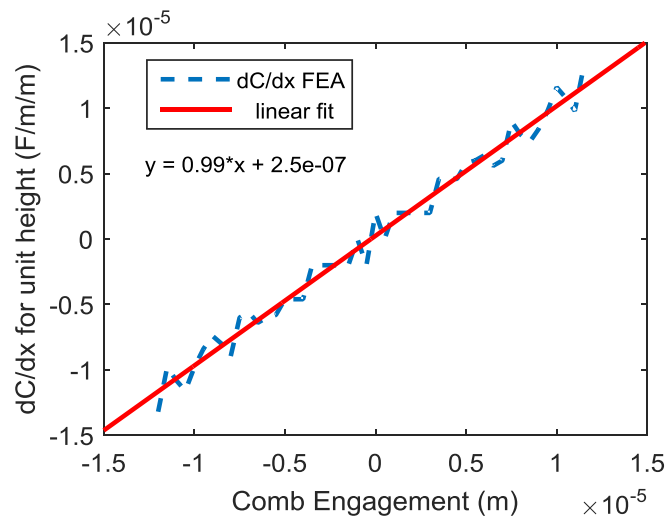


Figure 4.5: Derivative (dC/dx) of the simulated capacitance for shaped frequency tuning combs.

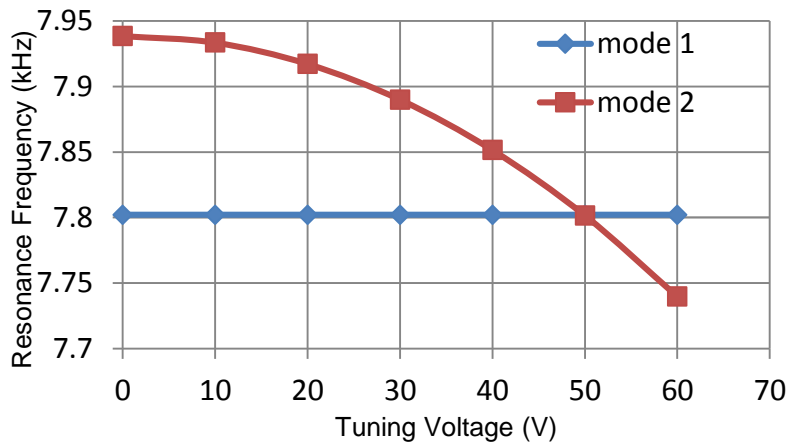


Figure 4.6: Measured tuning curve for the shaped frequency tuning combs.

One major concern about the shaped combs is the accuracy of the gap after fabrication. Since the generated force directly relies on the gap shape, an analysis has been done for a fixed offset in the gap shape for the shaped frequency tuning fingers. Assuming there is a uniform undercut, a , the fabricated gap turns out to be

$$g(x) = \frac{g_0}{1 + x/x_{01}} + a \quad 4.10$$

Then by inserting 4.10 into 4.3,

$$F(x) = NV^2 \epsilon h \left[\frac{1}{\frac{g_0}{1 + \frac{x_{ov} + x}{x_{01}}} + a} - \frac{1}{\frac{g_0}{1 + \frac{x_{ov} - x}{x_{01}}} + a} \right] \quad 4.11$$

After some algebra,

$$F(x) = NV^2 \epsilon h \times \frac{2g_0 x_{01} x}{g_0^2 x_{01}^2 + 2ag_0 x_{01}(x_{01} + x_{ov}) + a^2(x_{01}^2 + 2x_{01}x_{ov} + x_{ov}^2 - x^2)} \quad 4.12$$

The denominator of 4.12 contains displacement (x), which may lead to nonlinearity problems; however, for typical values of $x_{01} = 6 \mu\text{m}$, $x_{ov} = 16 \mu\text{m}$, maximum displacement $x = 10 \mu\text{m}$, and assuming relatively small undercut $a = 0.1$ to $0.2 \mu\text{m}$, the contribution of the x^2 term would be three orders of magnitude smaller than the $g_0^2 x_{01}^2$ term in the denominator. The rest of the denominator is all constants. So a fixed gap offset just leads to a decrease in the tuning efficiency, and it does not cause major operation problems.

4.1.2 Frequency tuning by changing overlap

Instead of changing the gap profile, an electrostatic force can also be created by changing the overlap area of the straight fingers [84]. Figure 4.7 explains the idea, the finger length on one side is tapered with a constant length which modifies the capacitance as the combs move in y direction.

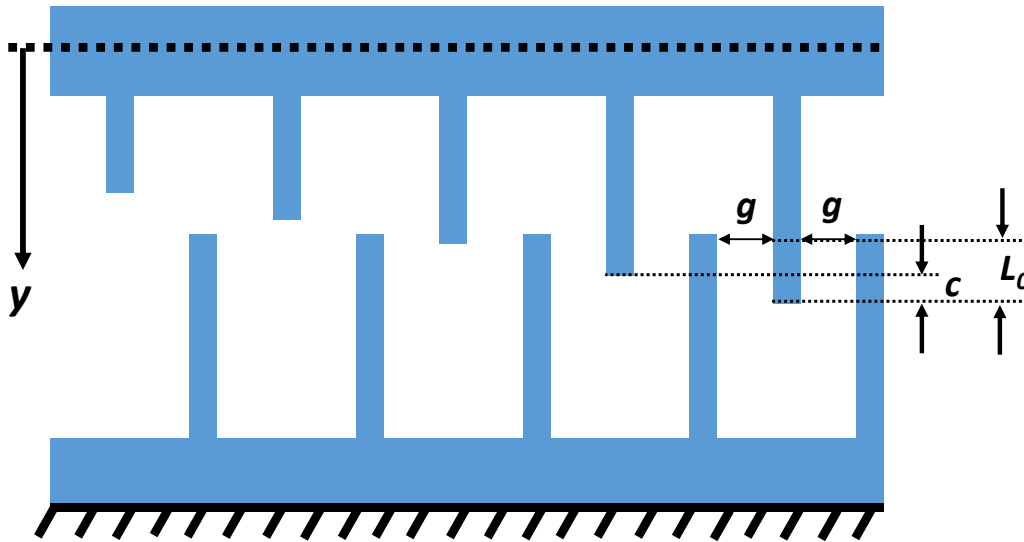


Figure 4.7: Frequency tuning by changing the overlap.

The efficiency of these fingers directly relies on the gap (g) and the finger tapering length (c), since the capacitance increases in every c displacement. The smaller the c the larger the capacitance change per unit comb engagement. The design constraint is the fingers should have an initial comb engagement (L_0) and for the largest and smallest displacement there should still be fingers that are engaging or disengaging. The choice of c depends on the layout area and the maximum displacement. So dC/dx of these fingers assuming symmetric placement on the layout is

$$\frac{dC(x)}{dx} = 2 \frac{\epsilon h |x|}{gc} \quad 4.13$$

Similar to the frequency tuning fingers, an electrostatic model of these linearly tapered fingers has been formed in COMSOL. Figure 4.8 shows the total double sided capacitance with respect to

comb engagement for a linear finger tapering length of $0.4 \mu\text{m}$. A 2nd order polynomial fits well to the simulated capacitance. The derivative of the total capacitance with respect to displacement (dC/dx) is presented in Figure 4.9. A linear slope is observed confirming the utility of these fingers for frequency tuning.

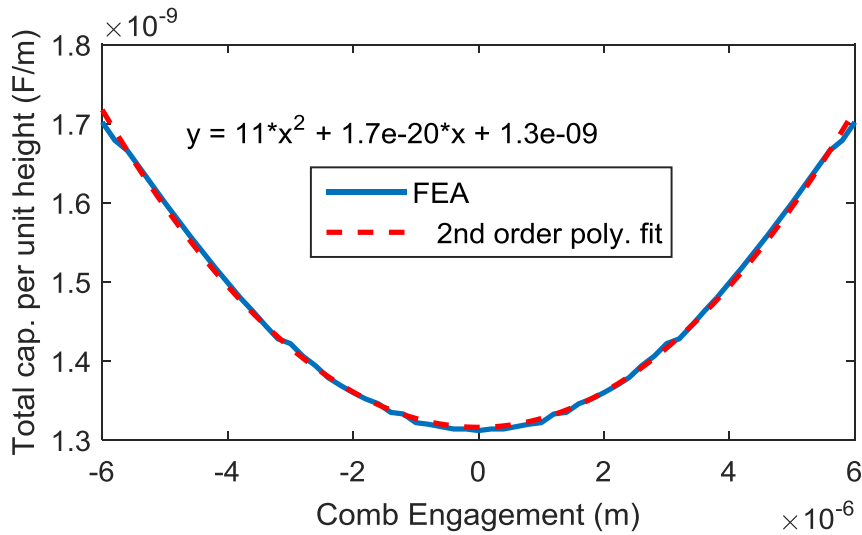


Figure 4.8: Simulated total capacitance for a finger tapering of $c=0.4\mu\text{m}$.

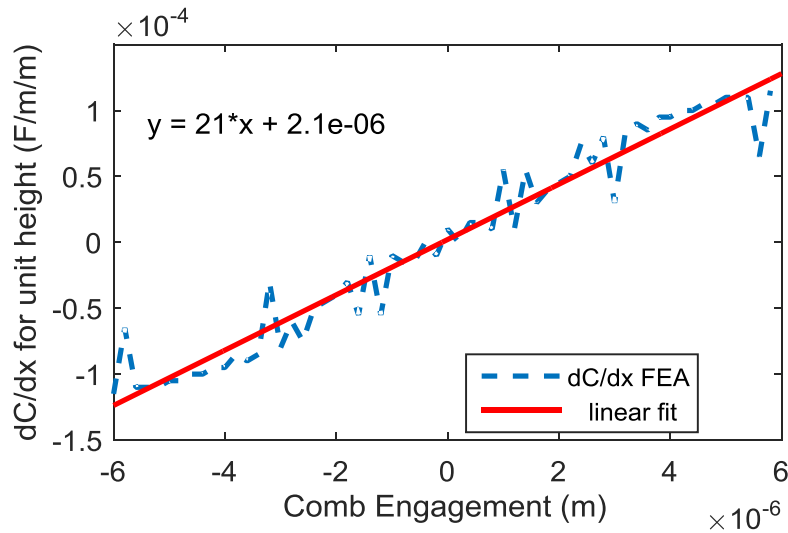


Figure 4.9: Derivative (dC/dx) of the simulated capacitance for the total capacitance shown in Figure 4.8.

Table 4.3 provides a comparison between shaped and linearly tapered fingers in the same layout area. They provide similar amount of tuning. Gyroscopes with linearly tapered frequency tuning

fingers have also been designed and fabricated in addition to the gyroscopes with shaped frequency tuning combs. But due to time limitations only gyroscopes with shaped combs have been tested.

Table 4.3: Comparison of shaped and linearly tapered fingers in the same layout area.

Shaped Combs		Linearly tapered combs	
Thickness, h	15 μm	Thickness, h	15 μm
Gap, g_0	6 μm	Gap, g	2.5 μm
Gap change coeff., x_{01}	8.5 μm	Tapering length, c	0.4 μm
Number of fingers, N_1	400	Number of fingers, N_2	8
$\frac{dC}{dx} = \epsilon h \frac{2x}{g_0 x_{01}} N_1$	20.8×10^{-4} F/m	$\frac{dC}{dx} = \epsilon h \frac{2x}{g_0 a} N_2$	21.2×10^{-4} F/m

4.2 Shaped combs for nonlinearity tuning

The gyroscope studied in this work exhibits softening nonlinearity at high displacements and this thesis proposes a shaped comb that cancels this softening nonlinearity by generating a hardening force. The hardening nonlinearity in the gyroscope is highly suppressed with the folded beam suspension and stress free die mounting with nanofoil covered in section 3.2.1. The softening nonlinearity in the gyroscope is originated from the usually neglected finger-tip to truss capacitances in the comb fingers. This second-order effect is verified with a Simulink system simulation that includes the finger-tip to truss capacitances. A parallel-plate capacitor model is used to extract the finger-tip to truss capacitances. Figure 4.10 presents the up and down frequency sweeps in Simulink including the tip capacitances for 35 V dc on the proof mass, 23 V dc frequency tune and various ac drive voltages. These values are a typical operating point for the gyroscope. Up and down sweeps are plotted with solid and dashed lines, respectively. The simulations were run by applying an ac chirp to capture the up and down sweep characteristics. The Simulink model

is the same as Figure 2.18 with the PLL replaced with the ac chirp signal. As the displacement increases, the resonance curve bends towards left and hysteresis increases confirming the softening nonlinearity. The finger-tip to truss distance is $15\ \mu\text{m}$ in these simulations, nonlinearity becomes dominant around $7\ \mu\text{m}$ displacement.

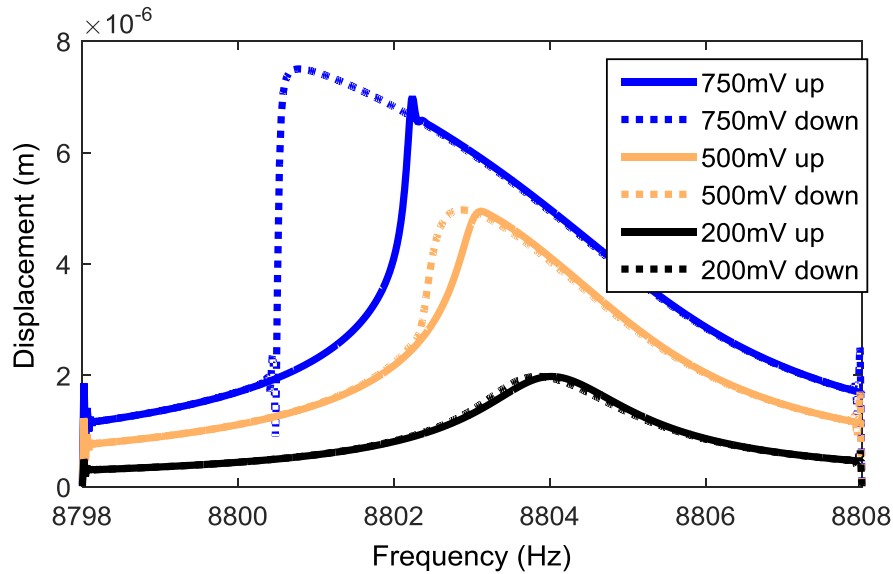
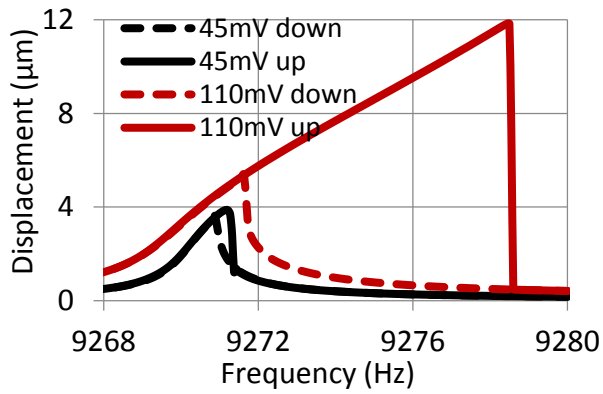
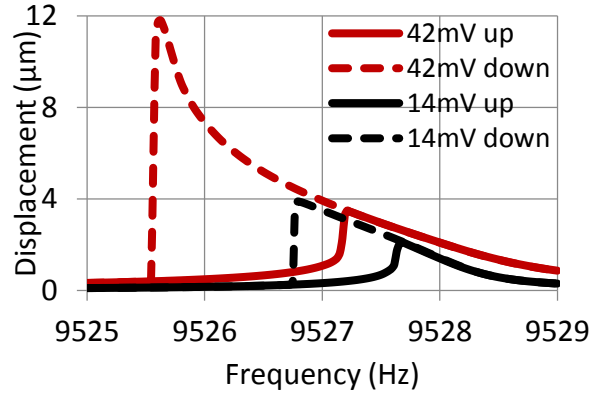


Figure 4.10: Up and down frequency sweeps in Simulink including the tip capacitances for 35 V dc on the proof mass, 23 V frequency tune and various ac drive amplitudes.

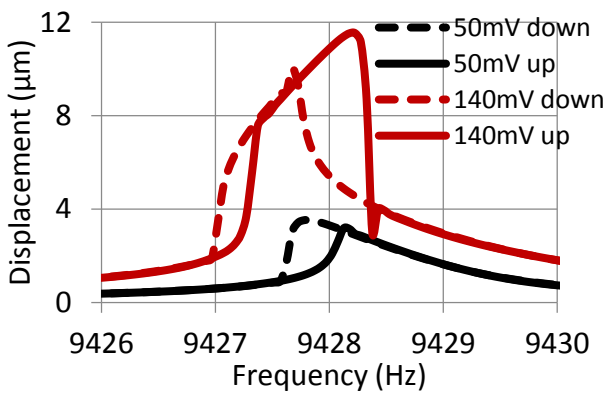
The nonlinearity of the device also depends on the spring stress affected by orientation of the device in the package, the die mount adhesive, and the mounting effectiveness across the die. Figure 4.11 presents the experimental frequency sweeps for the two modes for a straight mounted (a.1-3) and 45° mounted (b.1-3) gyroscope. The sweeps are carried out under a proof mass voltage of 40 V. Both of the dies use epoxy as the die adhesive and are tested in a vacuum chamber around 30 mTorr pressure. A significant hardening on the mode 1 of the straight mounted gyroscope is observed where the mode orientation is shown in Figure 4.11.a.3. Softening nonlinearity is observed for mode 2 for small displacements, and both softening and hardening nonlinearities are observed for high displacements. This is due to the fact that the DIP40 is a long rectangle and stress is asymmetric between the x and y directions.



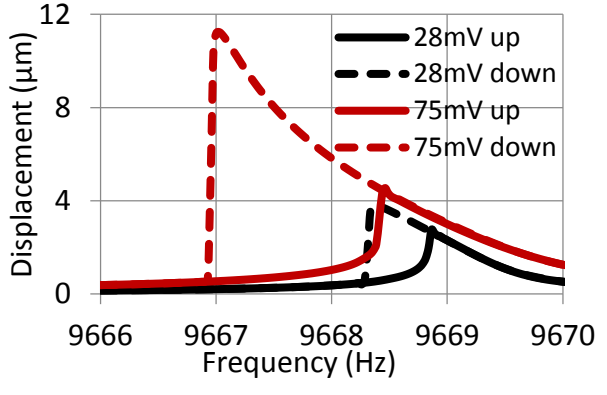
a.1 (mode 1)



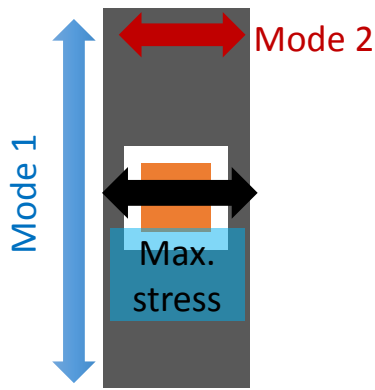
b.1 (mode 1)



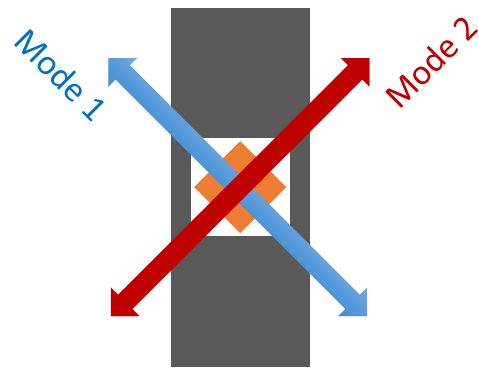
a.2 (mode 2)



b.2 (mode 2)



a.3



b.3

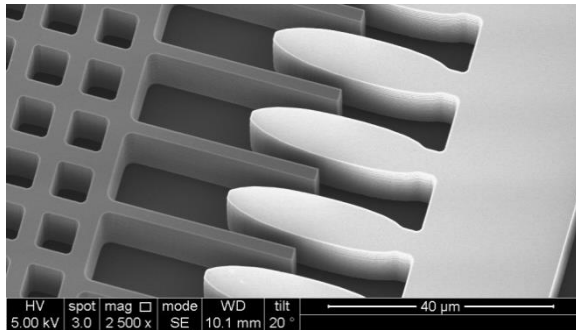
Figure 4.11: Experimental frequency sweeps for the two modes for a straight mounted device (a.1-3), and for a 45° mounted device (b.1-3).

The die mount epoxy has a glass transition temperature of 80°C [85] at which it transitions from a rigid state to flexible state. So once the epoxy is cured, due to the TCE difference between ceramic DIP40 and silicon MEMS die, mode 1 springs experience more stress compared to the mode 2

springs leading to hardening. However, 45° mounting relieves and distributes the stress equally between the two principle axes, leading to a softening nonlinearity in both axes as shown in Figure 4.11.b.1-3.

4.2.1 1st generation Nonlinearity Tuning Fingers

Two different types of hardening fingers have been developed throughout course of this thesis. The first generation fingers were implemented in the 2nd generation gyroscope design and have an oval shape with frequency and nonlinearity tuning in their profile as shown in 4.14 and Figure 4.12. Figure 4.13 shows the experimental frequency sweep results for different dc tuning potentials on the first generation nonlinearity tuning fingers [86]. The fingers are supposed to introduce hardening, but in the measurements they do not contribute enough hardening. It has been found and verified by the finite element analysis (FEA) that the (x/x_{01}) term in 4.14 causes a reduction in the cubic terms in the final force expression.



$$g(x) = \frac{g_0}{1 + \frac{x}{x_{01}} - \frac{x^3}{x_{03}}} \quad 4.14$$

Figure 4.12: SEM image of the first generation nonlinearity tuning fingers, the finer shape includes frequency and nonlinearity tuning at the same time.

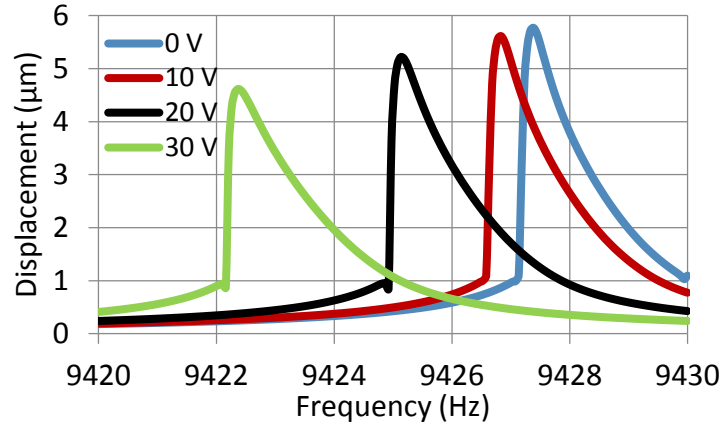


Figure 4.13: Experimental frequency sweeps for different dc tuning potentials on the first generation nonlinearity tuning fingers.

Figure 4.14 and Figure 4.15 show the simulated total double sided capacitance and dC/dx for the finger profile in 4.14 for $g_0 = 6.5\mu\text{m}$, $x_{01} = 6\mu\text{m}$, and $x_{03} = 7500\mu\text{m}^3$. The derivative dC/dx is almost a flat curve without a significant cubic dependence. The effect of x/x_{01} and x^3/x_{03} are opposite of each other, which leads to an almost flat total capacitance. This problem is solved by removing the linear tuning coefficient in the 2nd generation nonlinearity tuning fingers.

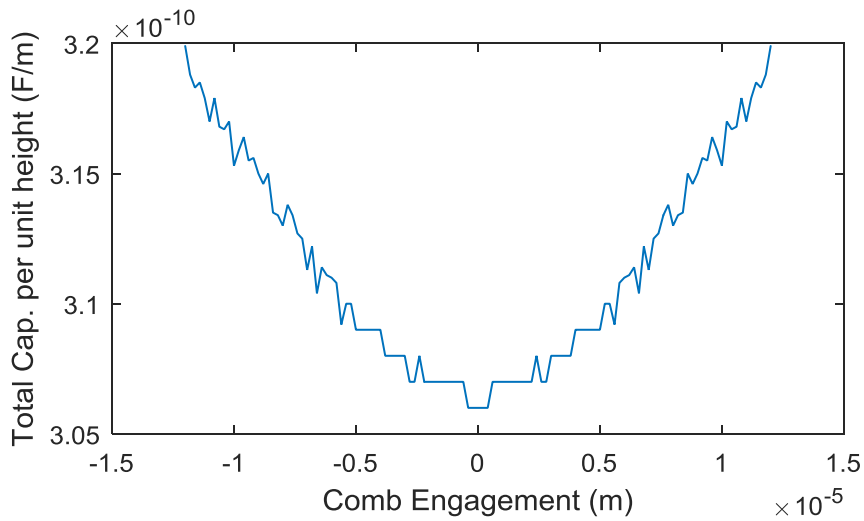


Figure 4.14: Total double sided simulated capacitance for the finger profile in 4.14 for $g_0 = 6.5\mu\text{m}$, $x_{01} = 6\mu\text{m}$, and $x_{03} = 7500\mu\text{m}^3$.

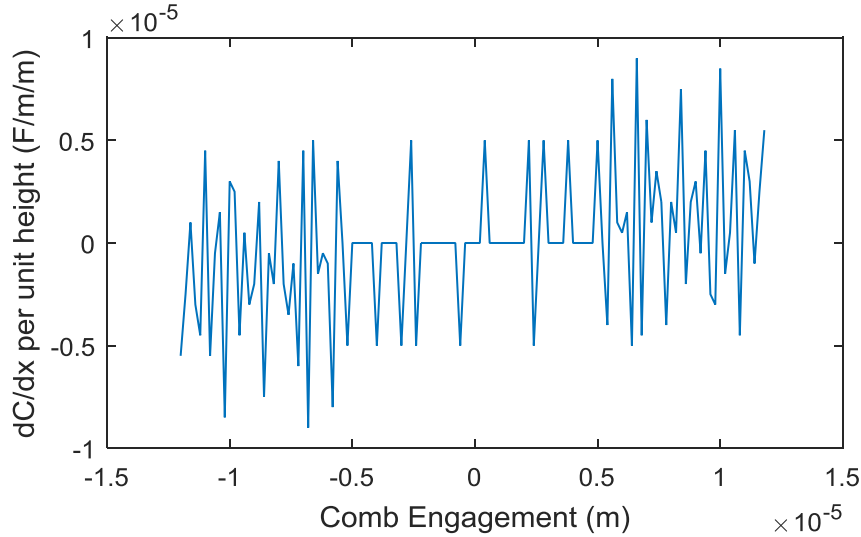


Figure 4.15: dC/dx for the total double sided capacitance shown above in Figure 4.14.

4.2.2 2nd generation Nonlinearity Tuning Fingers [87]

Figure 4.16 shows the second generation cubic nonlinearity tuning finger gap profile and the fabricated device SEM image that is designed to cancel the softening nonlinearity. These fingers were implemented in the 3rd generation gyroscope design. The linear frequency tuning term (x/x_{01}) is removed in this design. The gap increases cubically as the combs engage as opposed to the frequency tuning fingers in which the gap decreases as the combs engage. This increasing cubic gap profile leads to a cubic hardening force that is used to cancel the softening nonlinearity of the gyroscope. The biggest design challenge with the nonlinearity tuning fingers is obtaining a sharp change for the target range of displacements. The cubic term grows very fast as the displacement increases leading to impractical gaps. Zero overlap is a solution to this design challenge. The initial overlap of the fingers is set to zero ($x_{ov}=0$) allowing decreasing the cubic gap coefficient (x_{03}) to have a larger cubic dependence. The middle portion of the stator is also hollowed out to minimize the softening force generated by the tip to truss capacitance. Zero overlap also increases the finger-tip to anchor distance effectively reducing this softening force. Figure 4.17 and Figure 4.18 illustrate the FEA results for the simulated total double sided capacitance and dC/dx

of the second generation nonlinearity tuning fingers, respectively. The dC/dx shows both cubic and linear displacement dependence, the linear dependence results in frequency tuning and occurs as a result of the residual tip to truss capacitances. The effect of the squared term is not seen since the response is dominated by the linear coefficient at small displacements and by the cubic coefficients at high displacements.

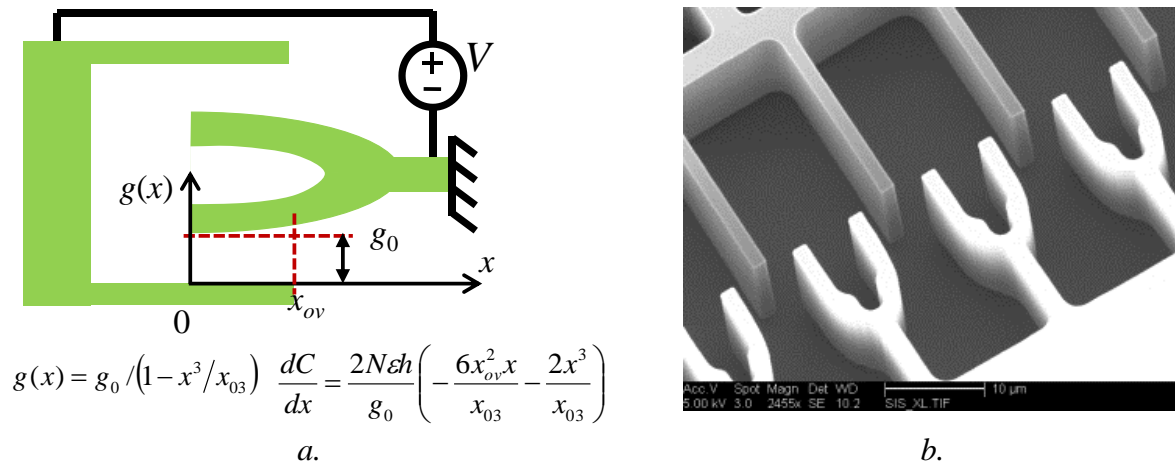


Figure 4.16: (a) The cubic nonlinearity tuning finger gap profile and (b) SEM of the fingers.

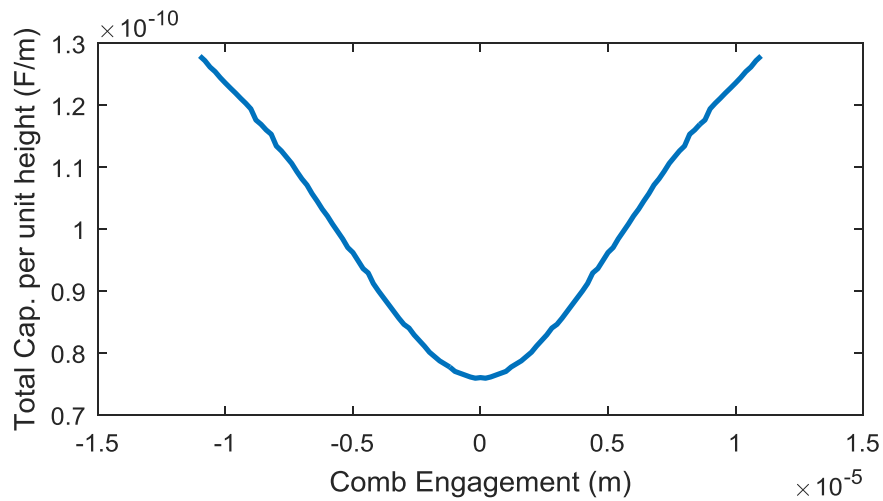


Figure 4.17: Simulated total double sided capacitance for the 2nd generation nonlinearity finger in Figure 4.16 with $g_0 = 2 \mu\text{m}$, and $x_{03} = 2500 \mu\text{m}^3$.

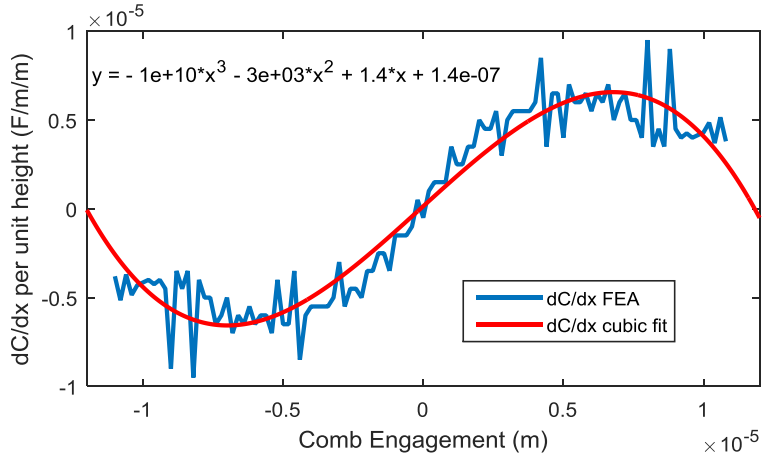


Figure 4.18: dC/dx for the total capacitance shown above in Figure 4.17.

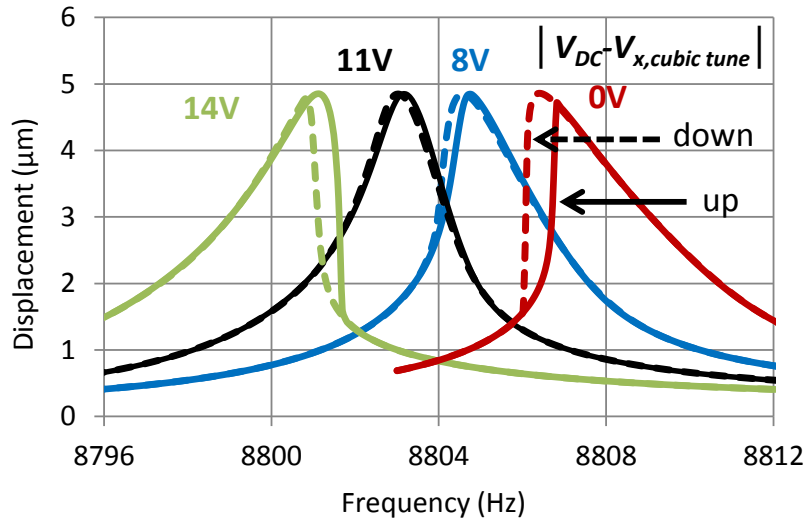


Figure 4.19: Measured up and down sweeps with increasing cubic tune potential for 600 mV ac for 15 μm finger-tip to anchor spacing.

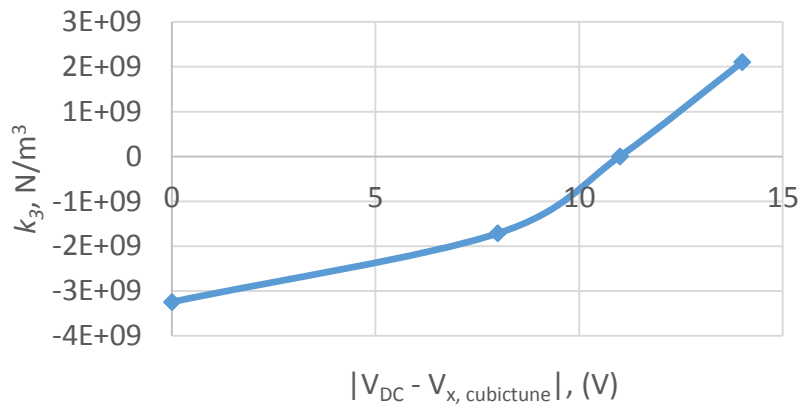


Figure 4.20: Extracted cubic nonlinearity coefficient vs. applied voltage, the coefficients are derived using the curves in Figure 4.19.

Figure 4.19 presents the measured up and down frequency sweeps for typical operation conditions of 600 mV AC, 35 V proof mass (V_{DC}), and 25 V frequency tune potential ($|V_{DC}-V_{freq.tune}|$) with increasing cubic tune potential ($|V_{DC}-V_{cubic.tune}|$). The initial softening nonlinearity gradually turns into a hardening nonlinearity with increased cubic tune potential, verifying the finger operation. An almost linear response without hysteresis is obtained at 11 V cubic tune potential. The slight frequency tuning is visible as predicted by the 2-D FEA as shown in Figure 4.18. Figure 4.20 shows the cubic nonlinearity coefficients for the frequency sweeps in Figure 4.19. The coefficients (k_3) are extracted by overlaying the measured results and the theoretical solutions. k_3 is negative when the nonlinearity is softening and positive when it turns into hardening. The tested gyroscope is in-house vacuum packaged as explained in the previous chapter. The gyroscope has a Q of 4750, limited by the residual gas pressure after sealing.

Figure 4.21 shows the measured up and down frequency sweeps for increased ac driving voltage of 900 mV resulting in higher displacements compared to Figure 4.19. The hysteresis is mostly removed by the hardening compensation but a completely linear response cannot be obtained. The gyroscope behaves as if it has two bifurcations. This is believed to be a result of a higher order term, i.e., the 5th harmonic, being more dominant in the softening force with increasing displacement. The nonlinearity tuning finger only independently controls the 3rd order nonlinearity and so does not completely cancel out the softening. Finger-tip to anchor spacing is 15 μm for this device, and the higher order harmonics can be suppressed by increasing the spacing for higher linear drive displacements.

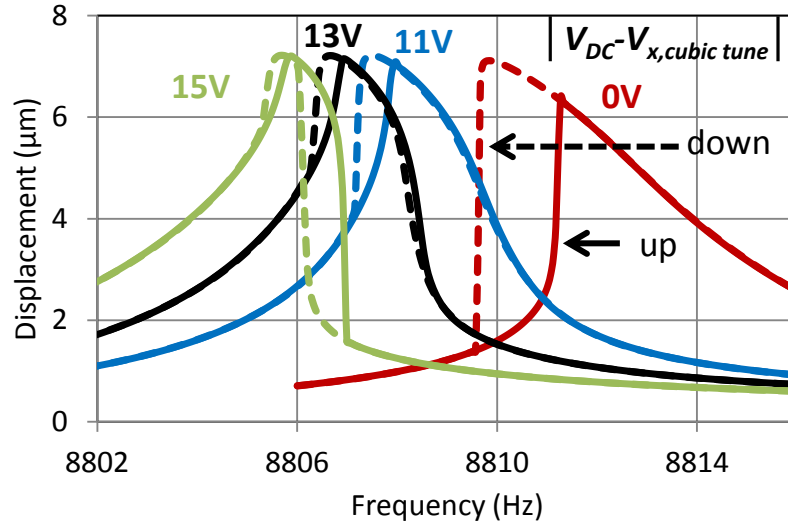


Figure 4.21: Measured up and down sweeps with increasing cubic tune potential for 900 mV ac for 15 μm finger-tip to anchor spacing.

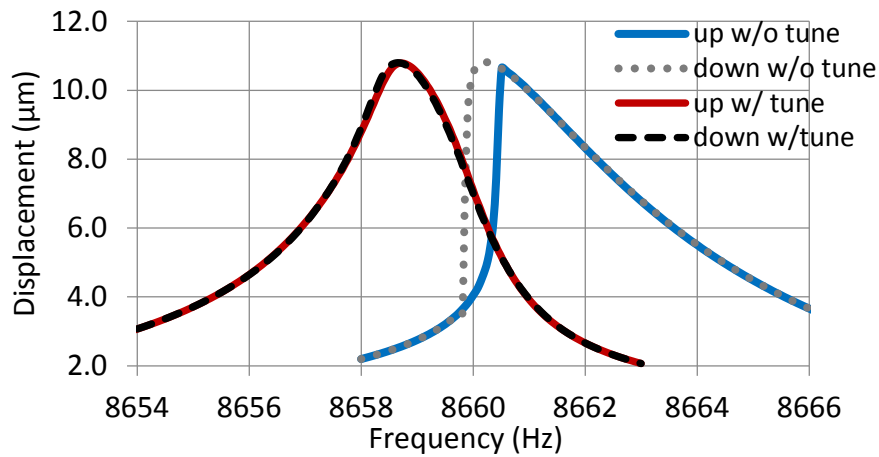


Figure 4.22: Measured up and down frequency sweeps for 10.7 μm drive displacement with and without nonlinearity tuning for 20 μm finger-tip to anchor spacing for 40 V dc proof mass, 600 mV ac drive, and 0 V frequency tuning potential. The nonlinearity is set for 10.5 V dc potential to tune the cubic nonlinearity.

Gyroscopes with two different finger-tip to anchor spacing have been designed, i.e., 15 μm and 20 μm . Figure 4.19 and Figure 4.21 report the measurement results for a device with 15 μm finger-tip to anchor spacing. Figure 4.22 presents the measured up and down frequency sweeps for 10.7 μm drive displacement with and without nonlinearity tuning for a gyroscope with 20 μm finger-tip to anchor spacing for 40 V dc proof mass, 600 mV ac drive, and 0 V frequency tuning potential. The nonlinearity is tuned for 10.5 V cubic tune dc potential. Increasing the finger-tip

to anchor spacing suppresses the 5th order softening harmonic and allows for higher linear displacements. This specific gyroscope has a Q of 4000.

4.2.3 Simulink Simulations with Nonlinearity Tuning

A Simulink model for the drive mode of the SOI-MEMS gyroscope including the PLL has been formed to understand the Amplitude-frequency ($A-f$) effects in closed-loop operation. The Simulink model presented in Figure 2.18 was used. The output voltage of the PLL was swept for different values of introduced cubic hardening and the final settling frequency of the PLL was recorded. Figure 4.23 shows the Simulink simulation results for the settling point of the PLL with respect to an arbitrary set point vs. PLL output voltage for various values of introduced cubic hardening. The legend from 0X to 9X represents the amount of the introduced hardening; the 1X step corresponds to $5.4 \times 10^9 \text{ N/m}^3$. Initially, without any nonlinearity tuning (0X), the PLL settling point shifts to lower frequencies with increasing input voltage due to intrinsic softening behavior. Also for high levels of introduced hardening (9X), the PLL settling point always shifts to higher frequencies due to hardening. At intermediate nonlinearity tuning (4X to 7X), the resonant behavior transitions from hardening to softening with increase in V_{PLL} , i.e., increase in displacement. If the gyroscope drive mode is operated in one of these zero-slope transition regions, then $df/dV_{PLL} \approx 0$ that minimizes the $A-f$ effect and uncharacterized drive-sense frequency mismatches. Operating at this point is expected to improve the long term stability of the gyroscope.

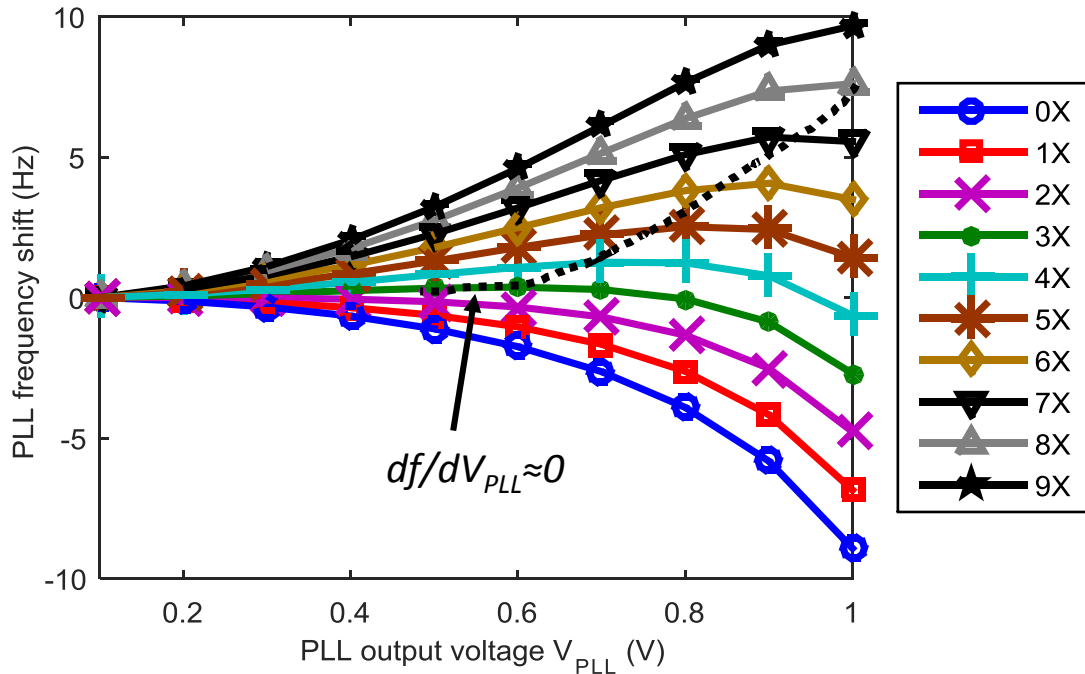


Figure 4.23: Simulink simulations for PLL settling point vs PLL output voltage for various hardening levels.

The PLL behavior while settling into the resonance (0°) phase is also investigated in the Simulink simulations. Figure 4.24.a shows the theoretical amplitude and phase solutions for up (solid) and down (dashed) sweeps. Figure 4.24.b shows the Simulink simulations in which the PLL quiescent frequency is set to a higher frequency than the resonance frequency (upper figure) and a lower frequency than the resonance frequency (lower figure). The resonance frequency is defined as the frequency where the phase is 0° (labeled as “3” in the figure). The resonance frequency is around 8794 Hz for this case. If the PLL quiescent frequency is higher (8804 Hz), then PLL follows the red arrows on the down sweep curve (from point 4, to 2, to 3) and locks to the 0° phase. If PLL quiescent is set to a lower frequency (8793 Hz), then PLL first follows the up sweep curve, starts from point 1 and arrives point 2, since theoretically it never sees 0° phase during the transition. Then PLL moves from point 2 to 3 on the down sweep curve locking into the 0° phase. In both cases the PLL locks into the same frequency that is verified by the Simulink simulations, since the

frequency for 0° phase is unique as shown in [48]. So, drive nonlinearities do not constitute a problem for the control loops.

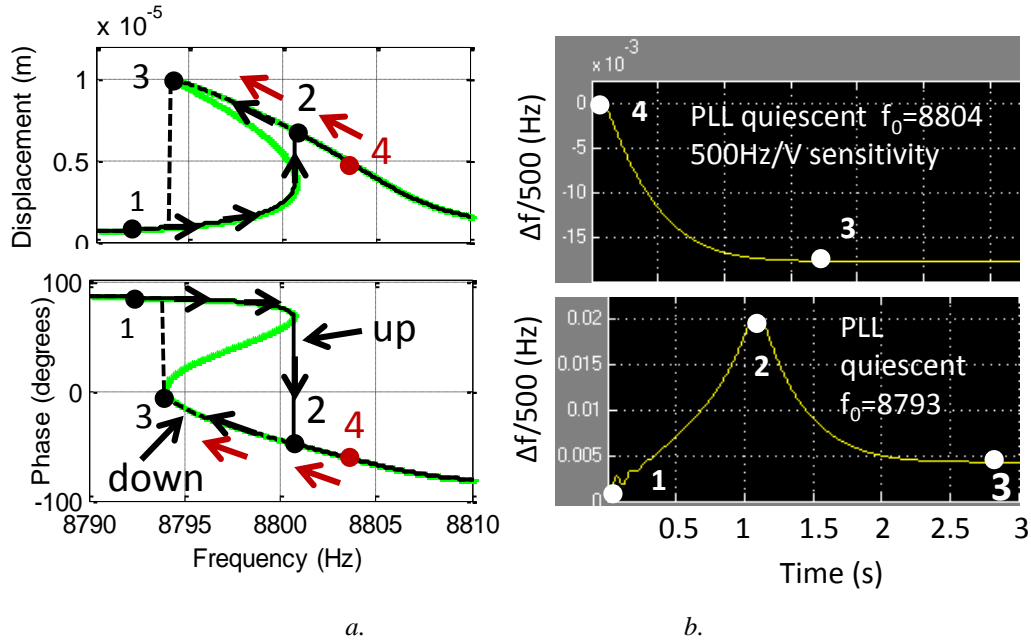


Figure 4.24: Theoretical amplitude and phase solutions for the up (solid) and down (dashed) sweeps (a), PLL frequency when the quiescent frequency is higher than the resonance (upper figure), and lower than the resonance (lower figure) (b).

4.2.4 Allan Deviation Results with and without Nonlinearity Tuning

Various Allan deviation experimental tests were performed for different drive displacements with and without nonlinearity tuning to understand the effect of nonlinearity on the performance. The gyroscope is operated at closed-loop drive with a PLL, and amplitude stabilization, and open-loop sense with 35 Hz mismatch. The tested gyroscope has a Q of 4000, finger-tip to anchor spacing of $20 \mu\text{m}$ allowing for higher linear displacements compared to the gyroscope with $15 \mu\text{m}$ spacing. The gyroscope is operated with $10.7 \mu\text{m}$ nonlinear displacement with and without nonlinearity tuning, the curves are shown in Figure 4.22. The hysteresis is clearly removed with the nonlinearity tuning. Figure 4.25 presents the Allan deviation test results for $2.8 \mu\text{m}$ small linear displacement, $5.6 \mu\text{m}$ slightly nonlinear displacement, and $10.7 \mu\text{m}$ displacement with and without

nonlinearity tuning. ARW scales with the increasing drive displacement as expected. However, bias instability does not improve for 10.7 μm nonlinear displacement. But when the nonlinearity is tuned bias instability also improves for the high displacement. Bias instability does not exactly scale with displacement as ARW, however nonlinearity cancellation provides an improvement. The relatively high ARW in these experiments originates from the electronics as verified by tests at $V_{\text{PM}} = 0$ V. Later, it was found that the noise source is one of the high voltage resistors.

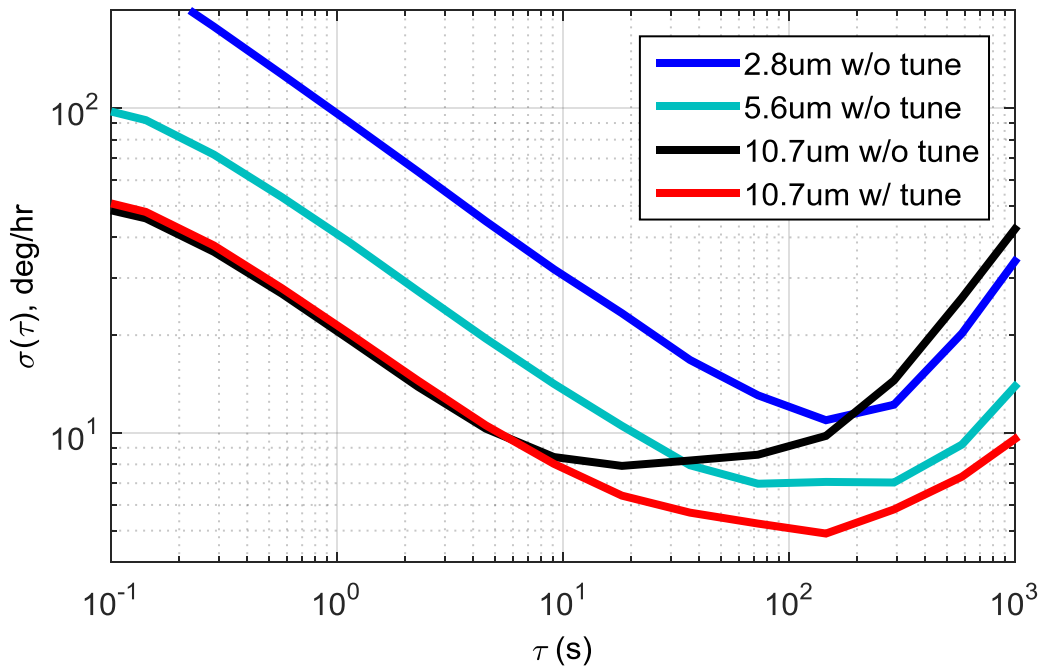


Figure 4.25: Measured Allan deviation test results with varying drive displacements with and without nonlinearity tuning.

Cancellation of the softening nonlinearity with a shaped finger design that introduces a dc voltage controlled cubic hardening has been successfully demonstrated. The tested gyroscope exhibits softening nonlinearity due to relatively stress-free nanofoil mount and folded springs. The nonlinearity tuning fingers completely linearizes the softening up to an amplitude 1/2 of the fingertip to anchor spacing. Beyond this displacement, double bifurcations occur as a result of the higher harmonics of the softening force. The drive oscillation is stable with the nonlinearities but

the oscillation frequency depends on the drive amplitude for large amplitudes. The proposed nonlinearity tuning method greatly suppresses this A - f effect on the drive mode leading to improvements in bias instability as well as in ARW.

4.3 Test Results on Quality Factor and Proof Mass Potential Relation

Quality factor (Q) is defined as the energy stored in a system divided by the energy dissipated per radian of vibration cycle [88], and is a measure of the dissipative losses for a system. Q is one of the important parameters for a MEMS gyroscope since it directly affects the thermal noise limit of the gyroscope. Matching the Q of the drive and sense modes eliminates one of the major drift sources for a whole angle gyroscope [89]. In this respect, methods to tune Q electrostatically will lead to a performance increase in whole angle gyroscopes. Having control over Q is also useful since it allows the designer to change the Q depending on the requirements. Q of a gyroscope can be tuned by electrical velocity feedback [90], at the cost of additional control circuits. However, understanding the nature of Q and losses of the gyroscope may lead to easier Q tuning. One focus of this thesis is to investigate the effects of electrical losses on Q and their potential usage on Q tuning. We have noticed a Q - V_{PM} dependence during the experiments of the 2nd generation devices, and this section provides details and modeling about those experiments. The presented results below are published in MEMS2014 [86].

4.3.1 Electrical Model of a Resonator

The gyroscope studied in this thesis includes electrostatic drive and sense. The gyroscope consists of two coupled resonators (modes) that are modeled as separate resonators. Figure 4.26 shows the equivalent electrical model for one mode.

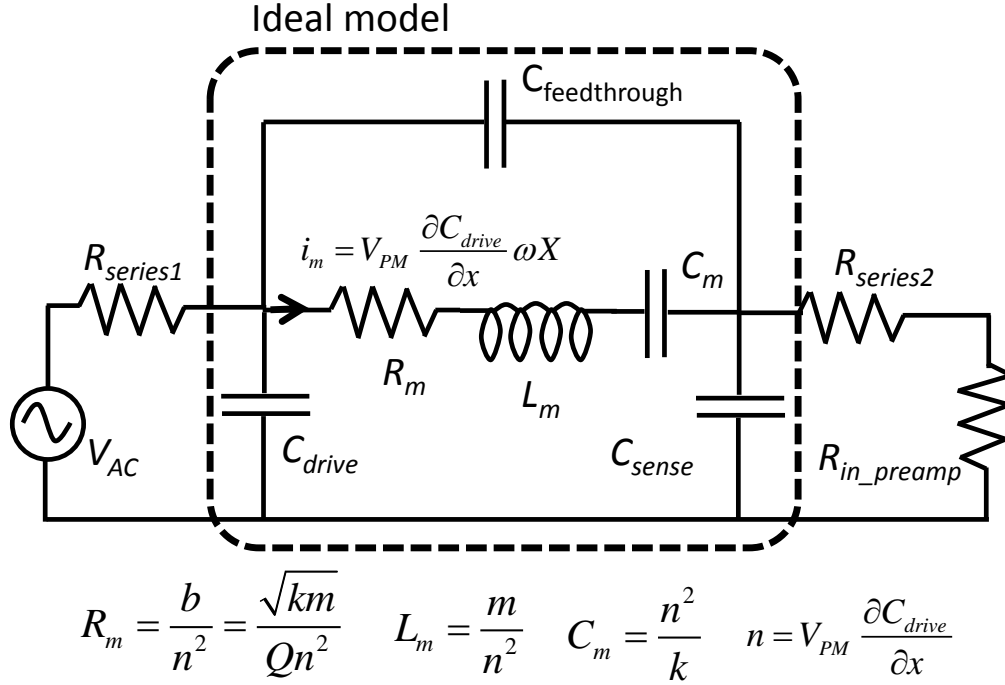


Figure 4.26: Equivalent electrical model for one mode of the gyroscope.

R_m , L_m , C_m , and i_m represent the motional resistance, inductance, capacitance, and current, respectively. $C_{feedthrough}$ represents the feedthrough capacitance from the drive to sense electrodes. C_{drive} and C_{sense} are the drive and sense electrodes, respectively. V_{PM} is the applied dc polarization voltage for driving and sensing. $R_{series1}$ and $R_{series2}$ are added resistors to the model to account for the electrical interconnect losses from the physical electrode to the transimpedance amplifier. The motional current output of the gyroscope is converted into voltage by a transimpedance amplifier that has ideally zero input impedance. However, due to the finite gain of the op-amp, the circuit has a non-zero input impedance that is represented by R_{in_preamp} . The design variables m , k , and b represent the physical mass, spring constant, and damping of the resonator respectively.

Q does not depend on the V_{PM} in the ideal circuit, assuming damping (b) is constant. $R_{series1}$, $R_{series2}$, and R_{in_preamp} are added to the ideal electrical equivalent model in Figure 4.26 to observe the change of Q with changing V_{PM} . When V_{PM} is changed, R_m , L_m , and C_m changes accordingly but $R_{series1}$,

$R_{series2}$, and R_{in_preamp} stay constant. As a result, a change in the quality factor is expected since the equivalent motional resistance does not exactly scale with V_{PM} . As V_{PM} decreases, R_m increases and the effect of $R_{series1}$ and $R_{series2}$ on Q decreases, so decreasing V_{PM} increases the Q . Assuming C_{drive} , C_{sense} , and $C_{feedthrough}$ have negligible impedance around the gyroscope resonance frequency the equivalent Q is

$$Q_{effective} \approx \frac{1}{R_m + R_{series1} + R_{series2} + R_{in_pre_amp}} \sqrt{\frac{L_m}{C_m}} \quad 4.15$$

The same phenomena can also be explained physically; as V_{PM} increases so does the motional current, and the power losses on the $R_{series1,2}$ (I^2R) increase resulting in a decrease in Q . Table 4.4 shows the typical values of the equivalent circuit parameters for the gyroscope tested in this study.

Table 4.4: Typical values of the equivalent circuit parameters for the gyroscope tested in this thesis.

V_{PM}	10 V	b	2.7×10^{-8} N-s/m
dC/dx	1.45×10^{-8} F/m	R_m	1.3 M Ω
m	3.15×10^{-8} kg	L_m	1.5 MH
k	114.6 N/m	C_m	0.18 fF
Q	70,000 (16 mTorr)	$C_{drive}=C_{sense}$	0.3 pF

4.3.2 Test Results on Q

Figure 4.27 shows the positions of the straight fingers (shaped frequency and nonlinearity tuning combs are not shown) with the calculated side-to-side device resistances for the 2nd generation gyroscope. There are three sets of straight fingers on each side that can be reached separately that are outer quad (blue), outer middle (orange), and inner fingers (green). The rotor is made from one layer of conducting silicon with a resistivity of 0.001 Ω -cm, and it can be reached from four different spring anchor locations (V_{PM1-4}).

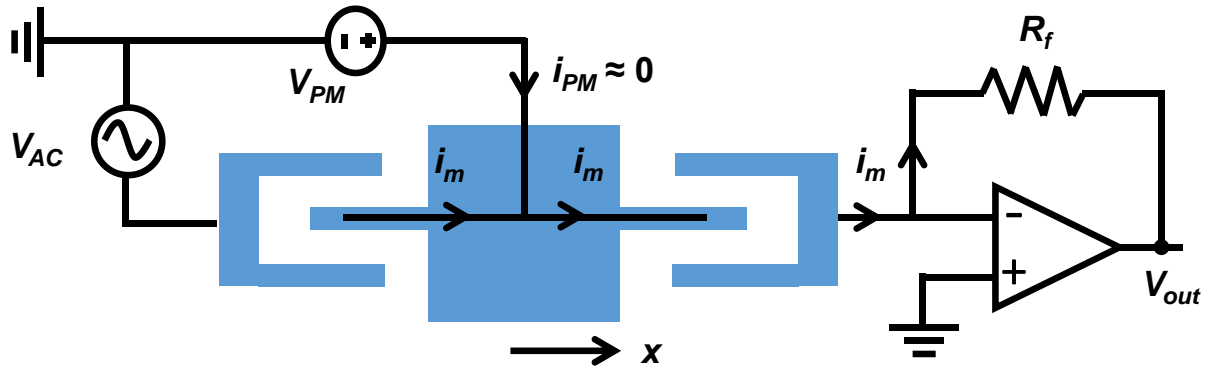


Figure 4.28: Resonance test-bench schematic: dc voltage V_{PM} is applied to the rotor and V_{AC} is applied through the stator fingers.

Figure 4.29 presents the Q of one mode of the gyroscope when tested from outer and inner combs for different V_{PM} . Both modes exhibit similar Q - V_{PM} characteristics, as V_{PM} increases Q goes down. The tests were done at a constant pressure of 16 mTorr to fix the air damping. Only one set of the fingers is used in each set of experiments. For example, the gyro is driven from one side using the inner fingers and the gyroscope's current is sensed using the inner fingers on the other side. All the other stator fingers are connected to V_{PM} to assure they do not contribute any force or current. Q of the gyroscope changes by 14% when inner fingers are used and changes by 32% when outer quad fingers are used in a V_{PM} range of 10 V to 40 V. The motional resistance of the device decreases with increasing V_{PM} but it is still hundreds of kilohms for 40 V, which is much larger than the silicon interconnect resistances shown in Figure 4.27. Although the interconnect resistances are not enough to cause such a Q change for our model, the motional current flows through a smaller resistance for the inner fingers compared to outer fingers. V_{PM} connection is made through V_{PM2} . The Q change with varying V_{PM} is repeatable and has been observed in several devices at constant pressure and at constant small (linear) amplitude. Figure 4.30 shows the Q - V_{PM} curves for three different devices tested from the outer quad and outer mid. fingers. All of them exhibit similar Q - V_{PM} characteristics, but the 3rd device goes to a higher Q because of the lower pressure. As the pressure is reduced, electrical damping becomes more dominant on Q since

the air damping is suppressed. In addition, the devices exhibit less Q - V_{PM} change if the inner fingers are used as demonstrated in Figure 4.29. A similar Q - V_{PM} change can also be seen in [91].

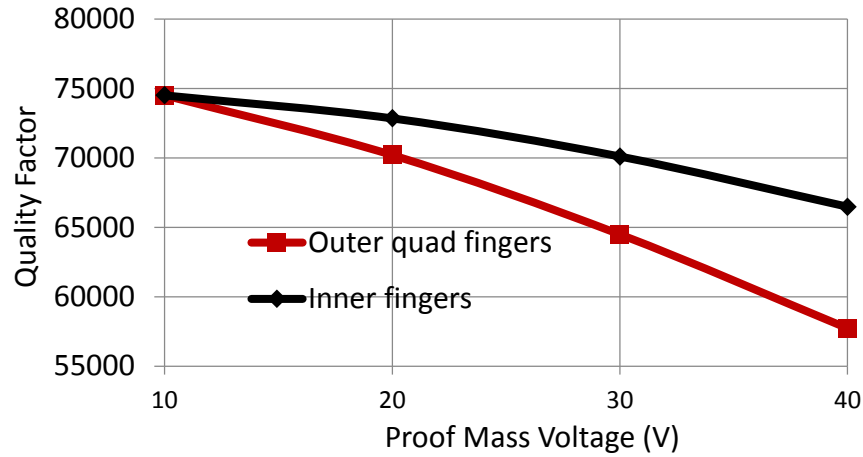


Figure 4.29: Q of one mode of the gyroscope when tested from outer and inner combs for different V_{PM} .

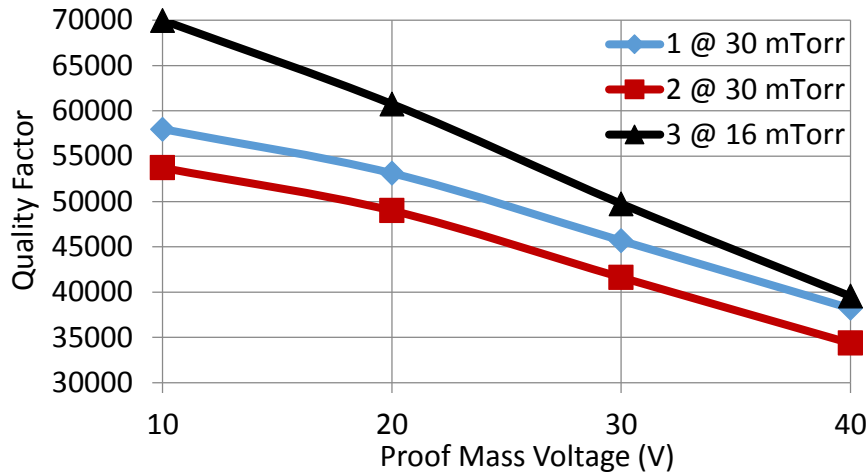


Figure 4.30: Q - V_{PM} curves for three different devices, exhibiting similar behavior.

Figure 4.31 shows the proposed layout structure to solve the not well understood Q - V_{PM} relation. The major source of the problem is thought to be the motional current flowing on the proof mass causing heat losses although not exactly consistent with our model. So instead of driving the device from one side and sensing on the other side as in Figure 4.28, if the fingers are placed side by side and differentially driven and sensed then the resistance seen by the current flow is highly

suppressed. The same design idea can be applied to the frequency and nonlinearity tuning fingers. In the 3rd generation SOI-MEMS gyroscope design this approach has been followed and Q - V_{PM} change is suppressed. The SOI-MEMS gyroscope is a mm sized device, Q - V_{PM} effects will be less for smaller sized devices since the resistance seen by the motional current will be less. The imbalanced driving and sensing as in Figure 4.28 on the other hand can be used for Q tuning.

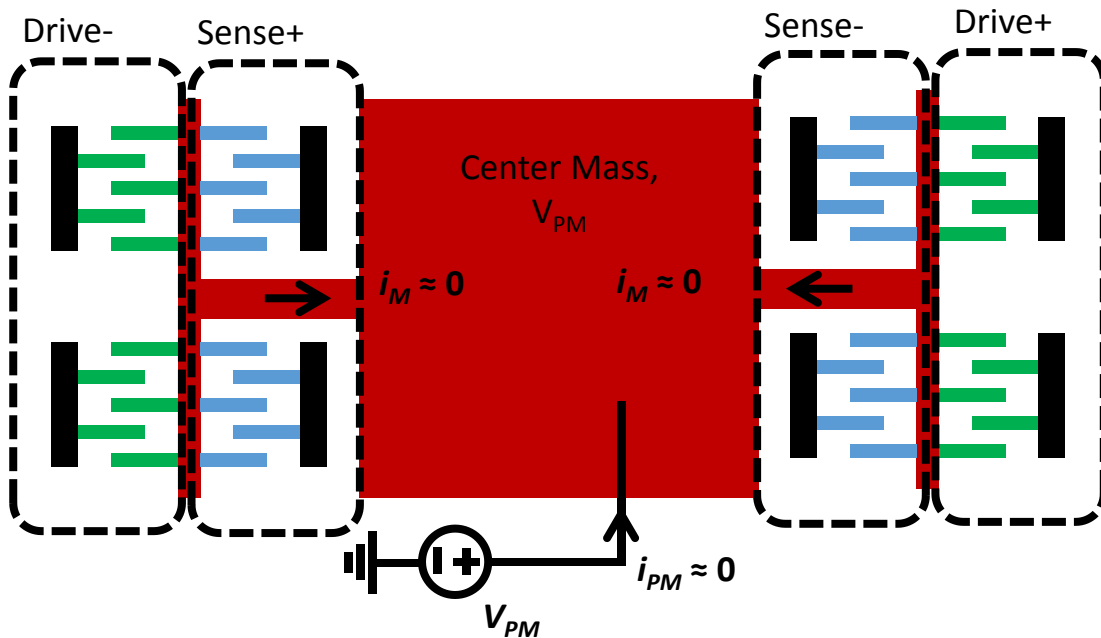


Figure 4.31: Proposed design for the gyroscope, drive and sense fingers are located side by side so no current flows on the proof mass.

4.4 Summary

This section focused on tuning of frequency, nonlinearity and quality factor. We designed the gap of the fingers to generate the required force for frequency and nonlinearity tuning. A linear ($1/x$) gap profile was used for frequency tuning and a cubic ($1/x^3$) gap profile was used for nonlinearity tuning. Frequency tuning using the finger overlap was also introduced. SOI-MEMS gyroscope exhibits softening nonlinearity due to biasing and stress free die mount. The nonlinearity tuning fingers introduce a dc voltage controlled cubic hardening to cancel out the softening nonlinearity. These fingers effectively cancel the softening up to 50% of the gap, after that higher order

nonlinearities come into play. The drive mode oscillations are still stable with nonlinearities but we think due to $A-f$ effect the bias instability performance is deteriorated. We experimentally showed the bias instability improvement at high drive displacement ($> 10 \mu\text{m}$) with nonlinearity cancellation.

Another way to minimize the softening nonlinearity problem in the gyroscope is increasing the finger-tip to truss distance. While this would solve the problem, there are fourteen combs across the gyroscope, so increasing finger-tip to truss distance would increase the gyroscope size in one dimension by $140 \mu\text{m}$. The layout efficiency would be lower. In addition, an extra degree of control is obtained with the nonlinearity tuning fingers.

A Q change with changing proof mass potential was observed during the experiments. There is a direct relation between the rate of change of Q and the current path on the proof mass. We think by designing a structure in which the ac current path is minimal $Q-V_{PM}$ change can be suppressed. This design philosophy was applied to the 3rd generation SOI gyroscope design and $Q-V_{PM}$ change was suppressed.

Chapter 5 On-chip Compensation Approach and Measurement Results

The main motivation of this thesis is understanding and compensating stress effects on the gyroscope ZRO. This chapter presents experimental results on stress testing. The studies were initiated by examining the stress and temperature effects on gyroscope resonance frequencies. First, temperature was used to induce stress on the device and then three-point and four-point bending testbeds were used to look at pure stress effects on the frequencies. Released stress sensors are developed with the 3rd generation SOI-MEMS gyroscope enabling exploration of the ZRO versus stress. Experimental results on stress-ZRO and stress-SF relations for open-loop operation were collected. Next, an ovenized stress testbed that locks into the on-chip temperature with an external heater was built to enable focus on effects of stress in the absence of temperature changes. Stress compensation significantly suppresses long-term drift resulting in 9°/hr angle random walk and 1°/hr bias instability at 10,000 s (around 3 hr) averaging time, which is a seven times improvement over the uncompensated gyroscope output.

5.1 Temperature Driven Stress Effects on Frequency

The results reported in this section are published in [92]. The initial studies focused on understanding the stress effects on gyroscope resonance frequencies. A testbed was used in which an on-chip silicon heater was used to create temperature driven stress on the gyroscope. The simulation methodology uses coupled FEA simulations explained in section 2.1.1. A 500 μm -thick glass substrate was inserted between the die and the package as in Figure 2.1 to thermally isolate the gyroscope so that the heaters create thermally induced stress gradients. Heating efficiency without the glass would be low since the silicon and package are both thermally

conductive, and the thickness of the SOI oxide layer ($2\ \mu\text{m}$) is small enough that it inadequately isolates the device from the rest of the die and from the package. Figure 5.1 shows the cross section and top view of the tested gyroscope after the gyroscope is mounted on the package, and explains how the device is heated. When the heater is activated, heat energy goes through the SOI oxide and creates a temperature gradient in the handle layer, which is then transferred back to the device through the anchors.

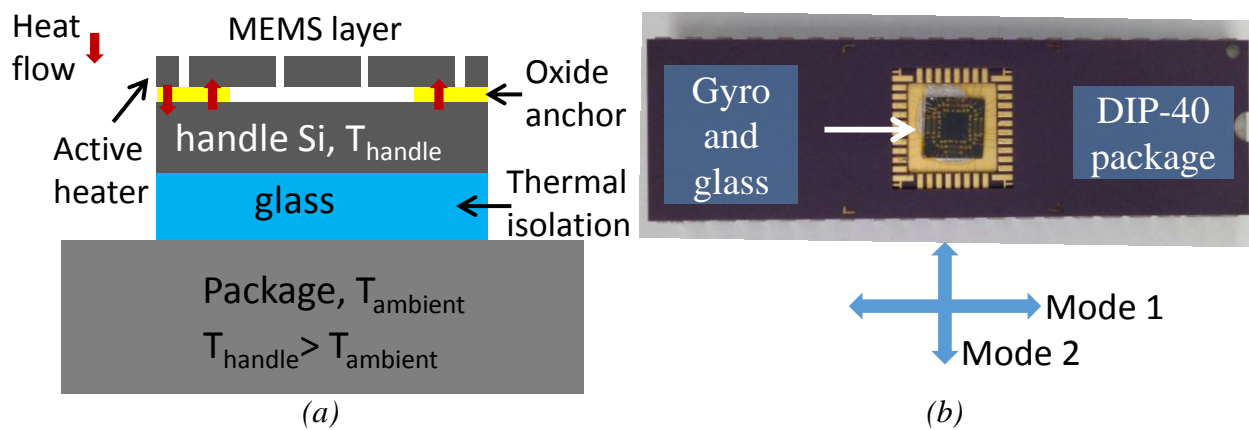


Figure 5.1: Cross section (a) and top view (b) of the test setup to observe the temperature induced stress effects on frequency. Glass thermally isolates the die.

The tests are performed by applying power to the on-chip silicon heater and observing the resonance frequency changes of the two vibratory modes of the gyroscope. Figure 5.2 and Figure 5.3 present the measured resonance frequency sweeps for Mode 1 and Mode 2 as defined in Figure 5.1.b for different heater power levels. These tests are performed in a vacuum chamber at 50 mTorr pressure. Figure 5.4 compares the frequency shifts with respect to zero heater power frequency between the FEA simulations (section 2.1.1) and measurements for different heater power levels. The simulations were done for two different cases, just by taking into account the $-60\ \text{ppm/K}$ temperature dependence of Young's modulus (E) denoted by "simulation only E ", and by taking into account the change of E with temperature and the stress through temperature induced anchor displacements denoted by "simulation $E + \text{stress}$ " in Figure 5.4. The frequencies decrease

more with the stress-induced anchor displacements included due to the stiffness change of the springs. So the effect of stress on resonance frequencies is comparable to that of temperature.

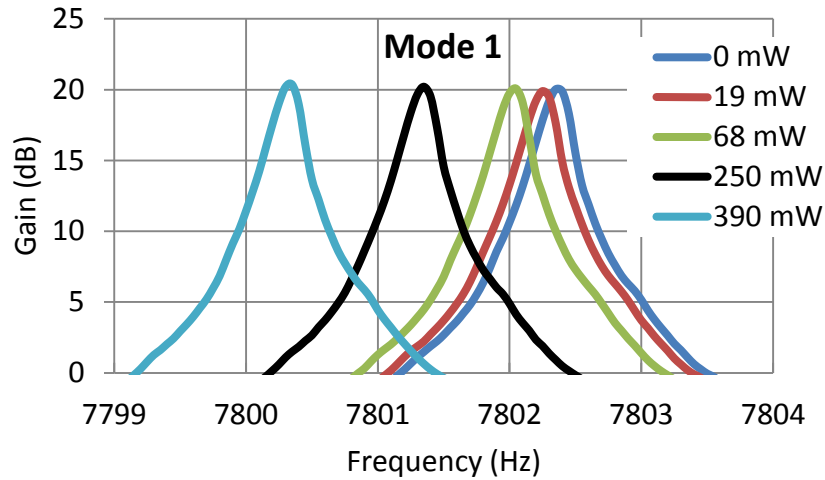


Figure 5.2: Measured frequency sweeps for different power levels for Mode 1.

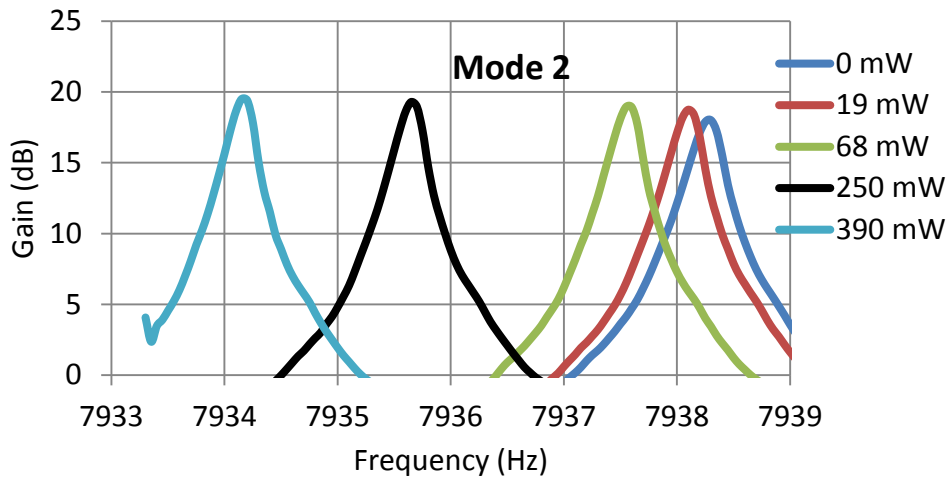


Figure 5.3: Measured frequency sweeps for different power levels for Mode 2.

The simulations and measurements agree for Mode 2; however, there is a mismatch between the measurements and simulations for Mode 1. Several experiments have been carried out on different samples and a regular pattern in which Mode 2 is consistent and Mode 1 is inconsistent with the simulations. The simulations yield identical results for Mode 1 and Mode 2. The location of the springs with respect to the package is important in terms of understanding the discrepancy between the two modes.

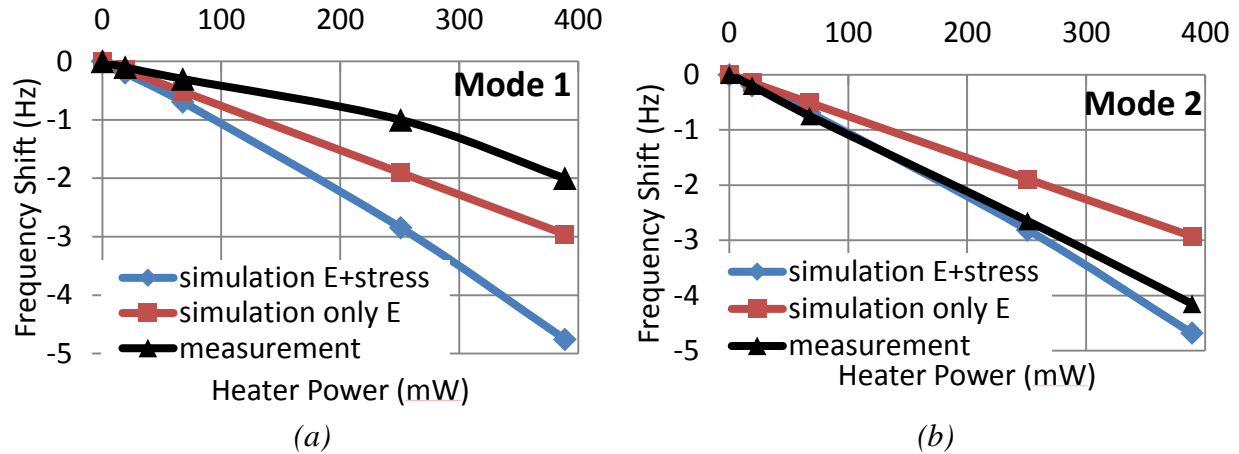


Figure 5.4: Comparison of simulated and measured frequency shifts for Mode 1 (a) and Mode 2 (b).

Figure 5.5.a shows the positioning of the springs. Mode 1 springs experience longitudinal anchor displacements along the short edge of the package. The gyroscope was mounted with an epoxy [85] and baked at 150°C. TCE of the ceramic DIP40 (6 ppm/°C) is two times the TCE of Si (3 ppm/°C), and once the epoxy is cured, compressive stress is exerted on the gyroscope. The amount of compressive stress is related with the glass transition temperature of the epoxy that is 80°C for our case. The epoxies are flexible above their glass transition temperatures. Since the DIP40 is a long rectangle, the compressive stress is concentrated on the narrow side leading to pre-stress on Mode 1 springs. Figure 5.5.b shows the expected frequency shifts with and without temperature under compressive and tensile stress. Due to pre-stress, Mode 1 springs start from point A, and Mode 2 springs start around f_0 , leading to the different measured behavior. Figure 5.5.c shows a measurement in which Mode 1 exhibits first an increase with the heater power and then it starts decreasing that is consistent with Figure 5.5.b.

The asymmetry of the DIP40 creates directionally different stresses on the modes of the gyroscope. To test this theory, a gyroscope was mounted with a 45° angle with respect to the package edge, and the resonance tests were repeated. Figure 5.6 shows the frequency shift vs. heater power for

the 45° mounted gyro. The frequency shift for the two modes are almost the same in this case and very close to simulation, which validates that the way the die is mounted on the package is important especially for asymmetric packages.

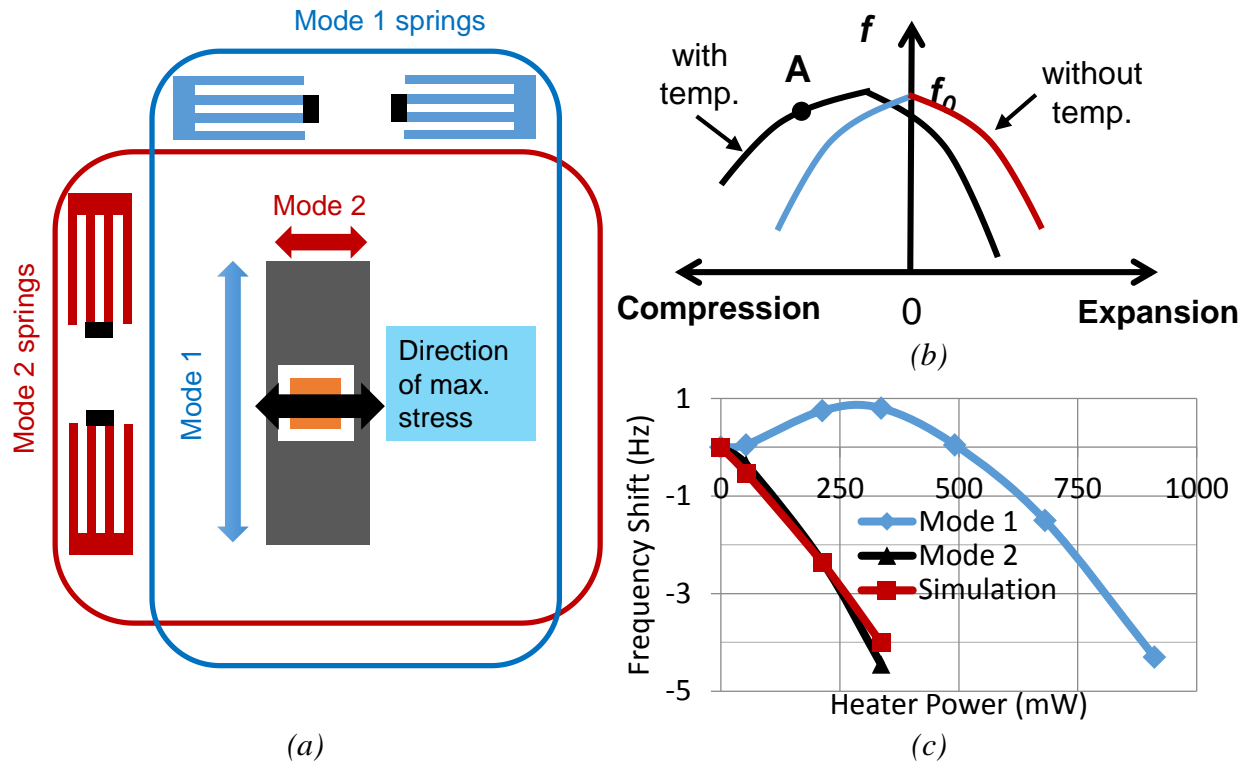


Figure 5.5: Location of the Mode 1 and Mode 2 spring with respect to the DIP40 (a), expected frequency shifts with and without temperature under compressive and tensile stress (b), measurement with increased heater power on Mode 1 (c).

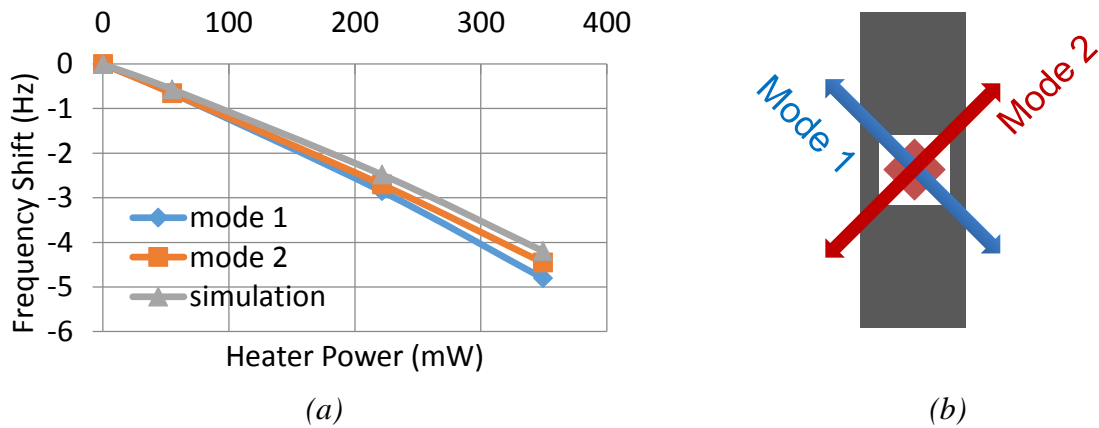


Figure 5.6: Measurement and simulation results for a 45° mounted gyroscope (a). Cartoon of a 45° mounted gyroscope with respect to DIP40 (b).

5.2 Pure Stress Effects on Frequency

The results reported in this section are published in [93]. The main motivation of this thesis is to understand the stress effects on the gyroscope, and towards that end three-point and four-point bending testbeds based on ASTM standards [94] have been developed to understand the pure stress effects on gyroscope frequencies.

5.2.1 Test Results with Three-Point Bending Testbed

Figure 5.7 illustrates the idea of the three-point bending stress testbed. The metal block between the PCB and hardwood base acts as a pivot. Turning $\frac{1}{4}$ "-20TPI (threads per inch) bolts on the sides of the package induces bending stress on the package with an edge deflection of 1.27 mm/turn that is transferred to the gyroscope by the die attach epoxy. Figure 5.8 shows the actual implementation of the stress testbed. The washers and the bolt are marked during the tests, and the package edge displacement is calculated by counting the turns of the bolts. A tubular vacuum setup that is explained in Section 3.2 is used during the experiments.

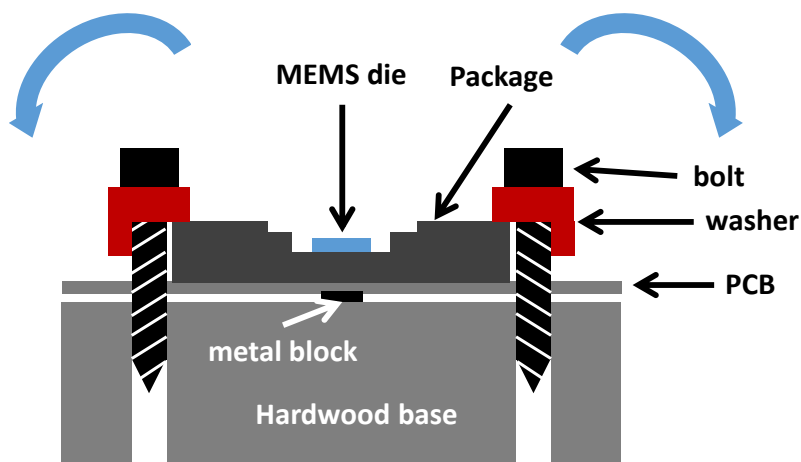


Figure 5.7: Three-point bending stress testbed, metal block between the PCB and hardwood acts as a pivot.

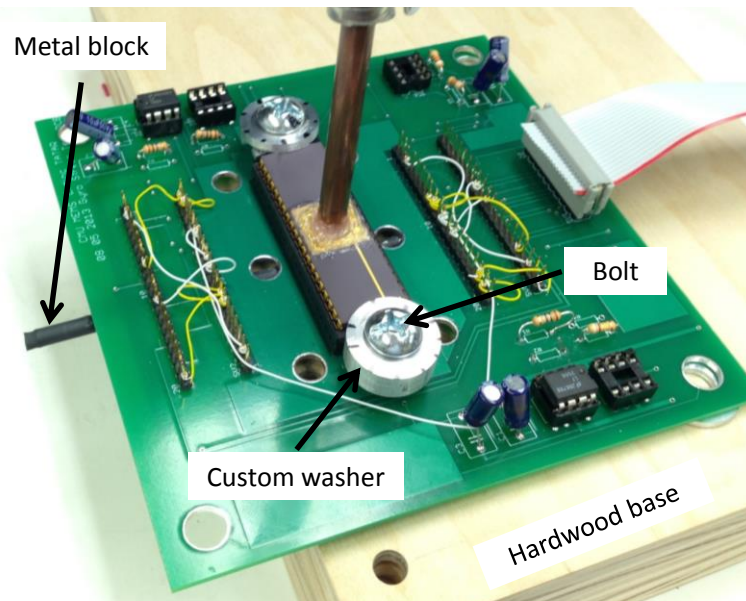


Figure 5.8: Actual implementation of the three-point bending testbed. A tubular vacuum system is used.

The gyroscope in the three-point bending stress testbed did not have any mechanism to directly measure stress. Package edge displacement caused by turning the bolts is therefore used to provide input data to the simulations for comparison with experiment. A simulation procedure similar to [92] is followed. First, a mechanical finite-element simulation of the package and die with forces applied to the package edges is run to obtain the gyroscope anchor displacements. Then, obtained anchor displacements are used as boundary conditions for the gyroscope eigenfrequency finite element simulations that find the resonance frequencies under several stress conditions.

Two gyroscopes with different orientations with respect to the package recess have been tested and simulated with the three-point stress testbed to investigate the effect of stress on the gyroscope's resonance frequency. Figure 5.9.a shows the simulated shape of the package with bending stress applied for a die aligned to the package recess. The simulated stress on the gyroscope to package edge displacement sensitivity is 2 MPa / 10 μm . Figure 5.9.b and c presents the simulated and measured frequency shifts vs. package edge displacements for mode x and y , respectively. The experiments have been repeated three times and the error bounds represent the

measured ranges. The uncertainty in mode y (Figure 5.9.c) seems more compared to the uncertainty in mode x (Figure 5.9.b) because the scale in Figure 5.9.c is smaller. The measured frequency shift for mode x is significantly larger than that of mode y . This is expected since three-point bending mostly creates longitudinal stress in the direction of mode x springs. The trend of the simulations and measurements agree except for large edge displacements on mode y . The possible reasons for the mismatch between the simulations and measurements are non-perfect transfer of the stress by the die attach epoxy, possible error between the modeled and actual package properties, and unwanted movements of the package with respect to the metal block during stress application.

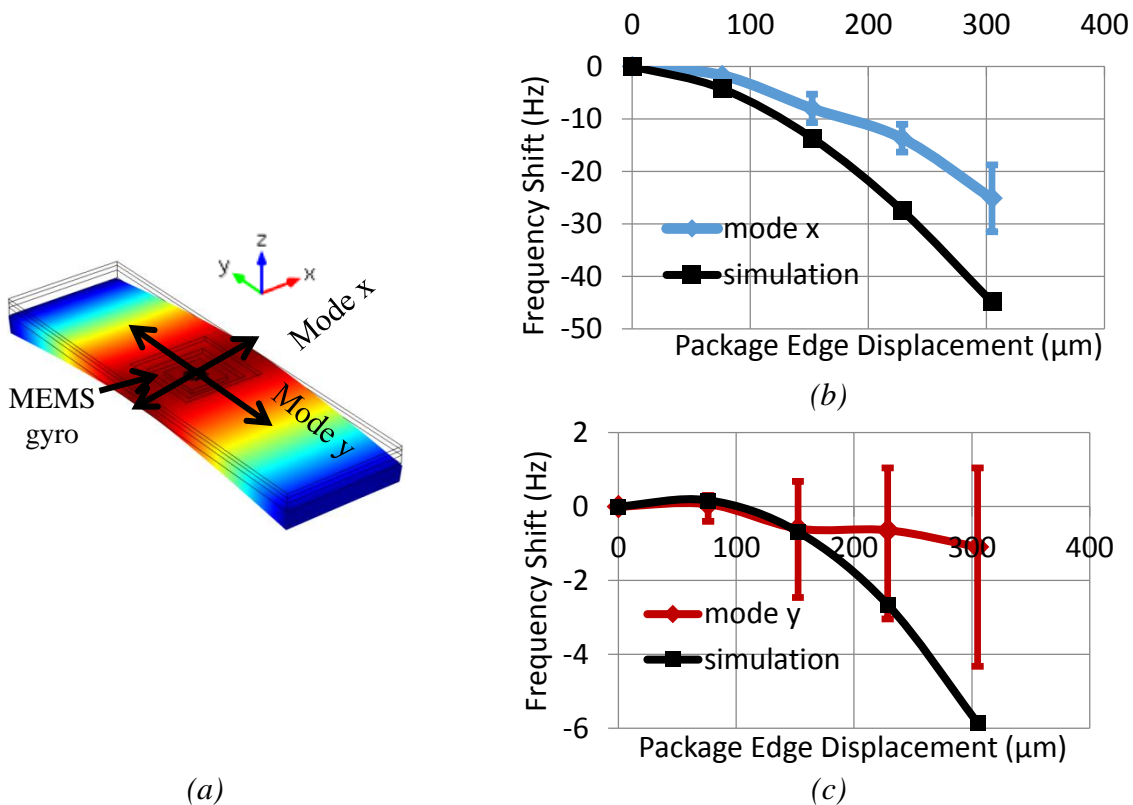


Figure 5.9: Simulated shape of the package with stress applied to the package edges (a). Simulated and measured frequency shifts with respect to the package edge displacement for mode x (b), and mode y (c). The gyroscope is mounted straight with respect to the package.

Figure 5.10.a shows the simulated shape of the package under stress for a die mounted 45° with the package recess, and Figure 5.10.b presents the simulated and measured frequency shifts for mode x and y . The simulation results in identical frequency shifts for both of the modes, because mode x and y experience the same anchor displacements due to 45° mounting with respect to the package recess. The measurement mismatch between mode x and y in Figure 5.10.b is believed to be caused by deviations from the 45° orientation that is likely since the die is mounted manually, and due to the imperfect bending stress (the die and the package may not exactly bending from the center) .

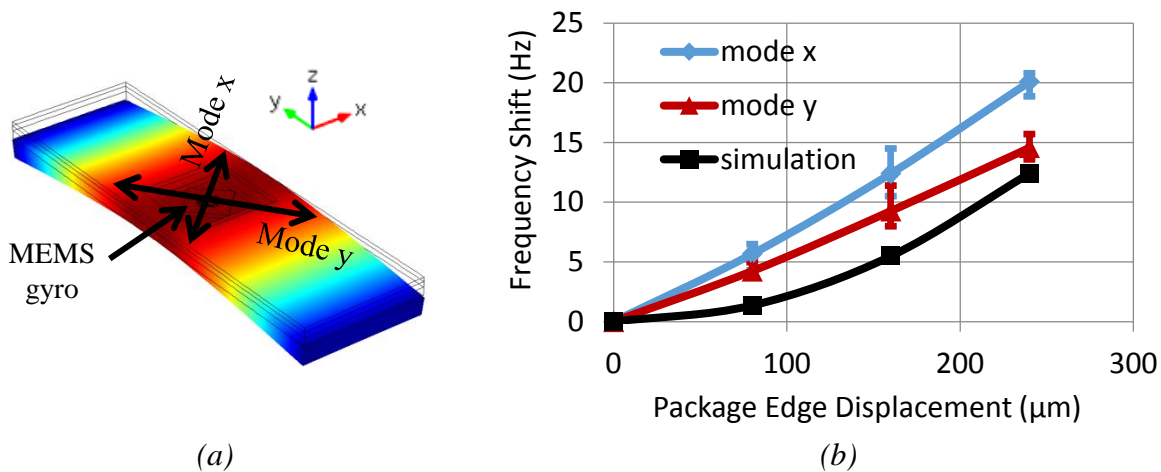


Figure 5.10: Simulated shape of the package with external stress applied to the package edges (a). Simulated and measured frequency shifts with respect to package edge displacement for mode x and mode y (b). The gyroscope is mounted 45° with respect to package recess.

Comparing Figure 5.9.b and c to Figure 5.10.b shows that a 45° mounted gyroscope has less frequency mismatch between the modes, and the frequencies increase with stress. In contrast, gyroscope dies aligned to the package recess see decreases in gyroscope frequencies. The frequency shifts are due to the changes in the flexure stiffness as a result of the applied stress. The gyroscope studied in this work uses folded flexures, and Figure 5.11 and Figure 5.12 show finite element results of folded flexures for the displacement (a) and y-axis stress (b) with longitudinal and transverse anchor displacements, respectively. Longitudinal anchor displacements induce

opposite stress on the inner and outer beams as explained in Section 2.1.1 and sees in Figure 5.11.b, and decrease the spring constant. However, transverse anchor displacements as in Figure 5.12.b stretch the beams creating a similar and tensile stress in all of the single beams. As a result, transverse anchor displacement increases the spring constant hence the resonance frequency. The orientation of the springs is shown in Figure 5.5.a, each mode's springs are aligned in the other mode's direction.

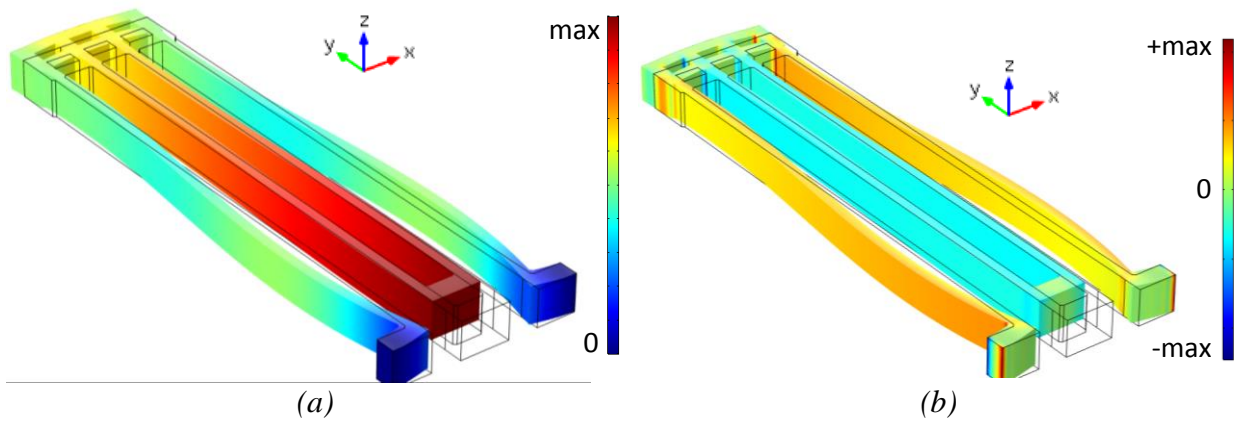


Figure 5.11: The displacement map (a) and y-axis stress map (b) of the folded flexures for a +y longitudinal anchor displacement.

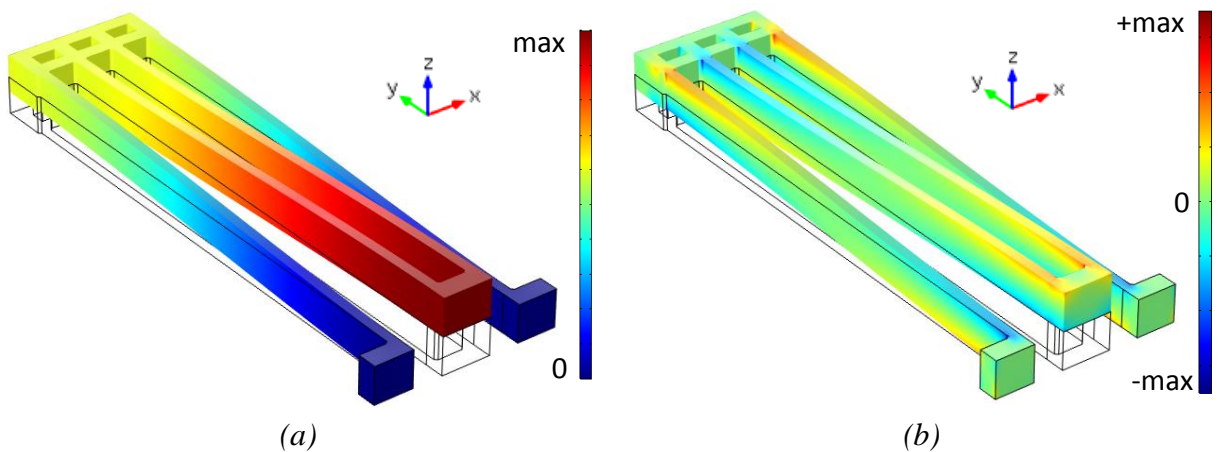


Figure 5.12: The displacement map (a) and y-axis stress map (b) of the folded flexures for a +z transverse anchor displacement.

The main difference between the straight and 45° mounting is the stress on the gyroscope anchors. 45° mounting results in transverse anchor displacements that increase the resonance frequency.

However, straight mounting leads to longitudinal anchor displacements dominating for mode x (Figure 5.9.b) and a balance between longitudinal and transverse anchor displacements for mode y (Figure 5.9.c).

5.2.2 Test Results with Four-Point Bending Testbed

Compared to a three-point bending test, a four-point bending test creates a more uniform stress on the die that is more similar to temperature induced stress so we moved to the four-point bending testbed in the later experiments. Figure 5.13 shows the four-point bending test concept adapted from the ASTM standards [94]. Custom machined aluminum (Al) fixtures and off-the-shelf steel cylinders are used to form the testbed. The ceramic DIP40 and the PCB are sandwiched in between four steel cylinders. The steel cylinders assure point contact. Applying a load on the top Al fixture creates an almost uniform compressive stress on the MEMS gyroscope.

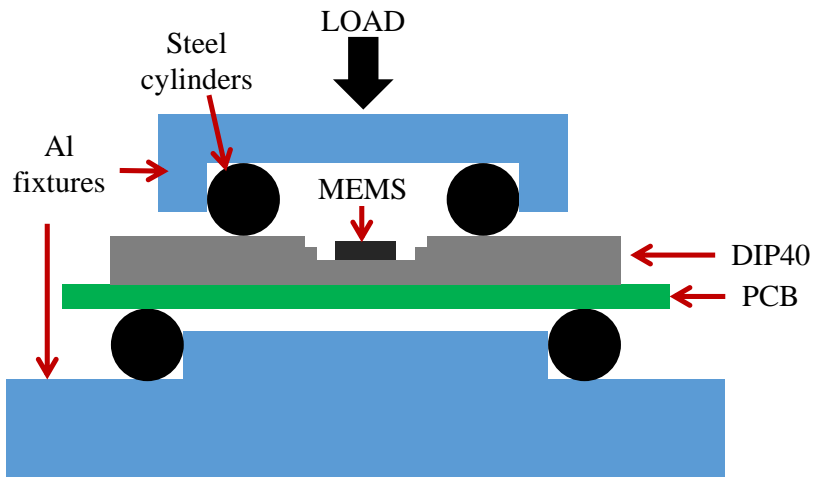


Figure 5.13: Four-point bending testbed, applying a load on the top Al fixture creates almost a uniform stress on the MEMS gyroscope.

Figure 5.15.a shows the implementation of the four-point bending stress testbed. This approach has been implemented using a custom vacuum chamber. A custom made rod that passes through a hermetic feedthrough couples the external load to the gyroscope within the chamber. The gyroscope and a PCB with the preamplifiers are in the vacuum chamber. The load is applied by

adding weights. The maximum applied load is 30 pounds (133.5 N) during the tests. The gyroscope includes Si piezoresistors on each side and Figure 5.14 shows the $\Delta R/R$ of these piezoresistors from a calibration run for a 45° mounted device. These piezoresistors exist in the 2nd generation SOI gyroscope design and sensitive to temperature. Since the calibration run was done in less than 5 minutes for each piezoresistor, temperature sensitivity was suppressed. The load sensitivity is calculated using the equations for $\langle 111 \rangle$ silicon in [95]. We assumed a p-type silicon with a doping of 5×10^{19} to calculate the piezoresistive coefficients. The coefficients are $\pi_{11} = 30.36 \text{ TPa}^{-1}$, $\pi_1 = -5.06 \text{ TPa}^{-1}$, and $\pi_{44} = 636.64 \text{ TPa}^{-1}$. The resistors 1 and 3 are aligned with the y axis, and resistors 2 and 4 are aligned with the x axis. The calculated load sensitivity is $-2.13 \text{ MPa}/10\text{N}$ for the x direction and $-1.36 \text{ MPa}/10\text{N}$ for the y direction. The stress is compressive as expected. The packaging stress can be as high as 50 MPa [60], so the applied weights are in the practical regime.

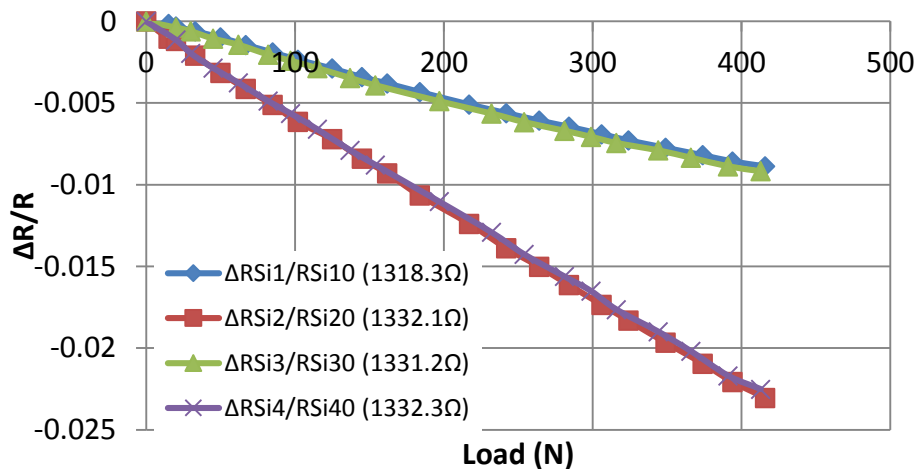


Figure 5.14: $\Delta R/R$ for the four silicon piezoresistors located on each side of the gyroscope during the calibration run.

Figure 5.15.b presents the simulated and measured frequency shift vs. load curves for both modes for a 45° degree mounted gyroscope that is mounted with epoxy. The modes are defined as in Figure 5.10.a. The error bars show the range of three repeated measurements. Compressive

longitudinal stress in the simulations lead to a decrease in the resonance frequencies with increased load. Simulated frequency shifts are the same for each mode due to 45° mounting.

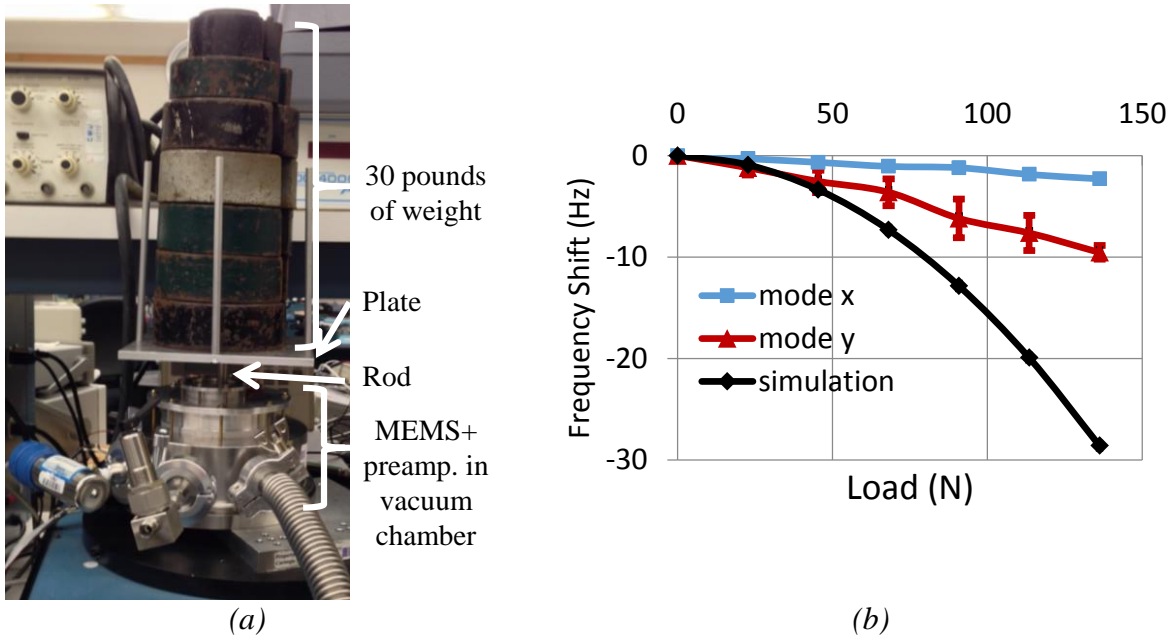


Figure 5.15: Actual implementation of the four-point bending test (a), and the measurement and simulation results for mode x and y (b).

The difference between the measured frequency shifts between the modes is believed to be a result of deviations from 45° mounting, centering of the MEMS die to the package, and alignment and centering of the four-point testbed. Although a different sample, the stress in the x and y directions is also different in the calibration run due to the mentioned possible error sources. These may cause the dominant anchor displacement for mode x and y to be different leading to different frequency behaviors. There is also a difference between the simulations and measurements. The simulations assume perfectly rigid connection between the MEMS dies and the package, and the four-point bending test is applied directly to the ceramic DIP40. However, during the implementation of the four-point bending test, the load is applied to a stack consisting of DIP40, zero insertion force (ZIF) socket, and the PCB. As a result, the anchor displacements and hence the frequency shifts are smaller compared to the simulations for the same load due to the more

rigid stack. Die attach epoxy also does not make a perfectly rigid connection, as another reason for the frequency shifts to be smaller compared to the simulations. Both the rigid stack and imperfect die attach could have been simulated but skipped due to time limitations. The stress sensor outputs were not particularly useful since the measurements took relatively long time in the order of half an hour, and the temperature changes dominated their outputs. The same type of tests was repeated in the 3rd generation SOI-MEMS gyroscope with temperature insensitive stress sensors that helped on the understanding of the frequency changes.

Figure 5.16 shows the simulated frequency shifts for the two modes of the gyroscope for different angles between the package recess and the MEMS gyroscope in a four-point bending testbed. A 45° angle between the package recess and the MEMS gyroscope yields identical frequency shifts for the two modes. As the angle deviates from 45° a split between the frequency shifts occur as a result of uneven stress distribution.

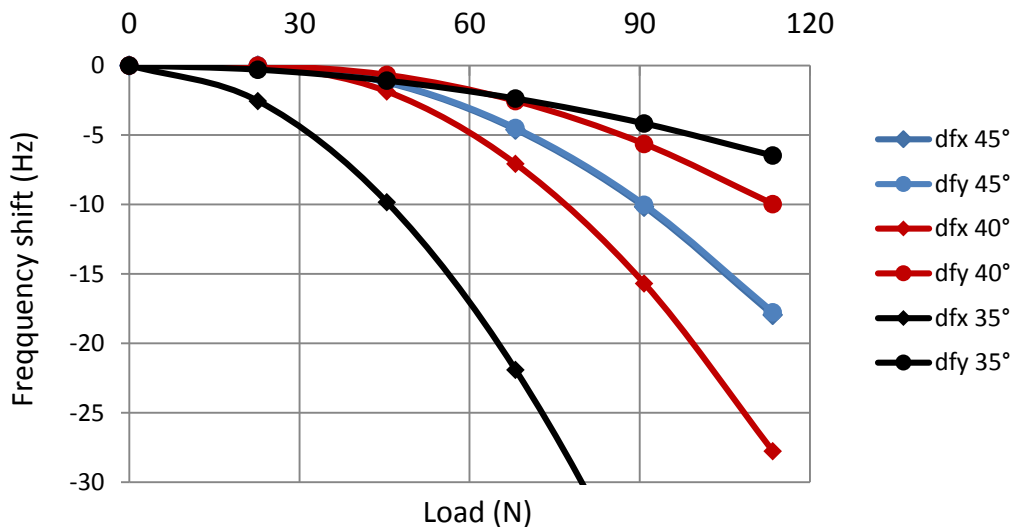


Figure 5.16: Simulated frequency shifts for the two modes of the gyroscope for different angles between the package recess and the MEMS gyroscope.

5.3 Environmental Sensors in the SOI-MEMS Gyroscope

The results presented in Section 5.1 and 5.2 show the environmental effects on the gyroscope; however, they lack the on-chip environmental sensors that are required for compensation and more accurate characterization. So, stress and temperature sensors have been designed in the third generation SOI MEMS gyroscope. Figure 5.17 shows the SEM image of the third generation SOI-MEMS gyroscope with the stress sensors highlighted.

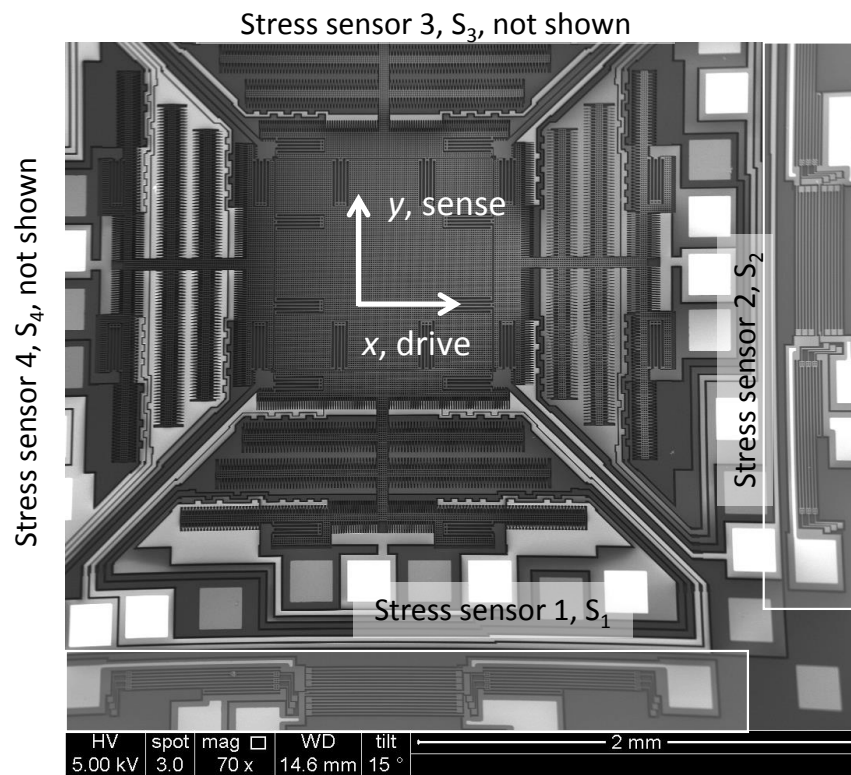


Figure 5.17: SEM image of the third generation SOI-MEMS gyroscope with stress sensor locations highlighted

The gyroscope design includes four on-chip piezoresistive stress sensors located on each side of the square perimeter of the gyroscope footprint. The piezoresistors are defined in the highly doped SOI device layer. Each stress sensor comprises four SOI resistors in a Wheatstone bridge to cancel out the temperature dependent resistance changes as shown in Figure 5.18.a. The stability of V_{DD} in the bridge directly determines the output stability; in initial work, the stress sensors are biased

around V_{PM} to prevent stiction, but that approach requires sequentially turning on the power supplies. Later, an RC biasing network was used to bias the gyroscope; details of this are explained in Section 1.7. The 5 V supply is implemented by a bandgap reference, which is more stable than the power supply and can work with any supply voltage larger than 5.5 V. The Analog Devices ADR445BRZ was used in this study [96]. Each bridge measures the stress component in its longitudinal direction while rejecting temperature effects. The stress and temperature sensitive piezoresistors $R_{stress1}$ and $R_{stress2}$, shown in Figure 5.18.b, are fixed-fixed released beams connected electrically in series to increase the nominal resistance. The temperature sensitive (and stress insensitive) resistors $R_{nostress1}$ and $R_{nostress2}$, shown in Figure 5.18.c, are released beams equal in electrical length to $R_{stress1}$ and $R_{stress2}$ and that are effectively free-free mechanically. $R_{nostress}$ has only two support anchors that are aligned on the same side of the beams so that $R_{nostress}$ does not capture any longitudinal stress. Each beam is 5 μm wide, 600 μm long, and 15 μm thick, so compliant tethers constrain the ends of the $R_{nostress}$ beams to prevent pinning and stiction to the substrate. The nominal resistance value is $R_0 = 1.7 \text{ k}\Omega \pm 2\%$.

The voltage output of the Wheatstone bridge is

$$\Delta V_i \approx -\frac{\Delta R}{2R_0} V_{DD} \quad 5.1$$

$$\frac{\Delta R}{R_0} = \varepsilon_i \times GF \quad 5.2$$

where i is the index of the bridge ($i = 1$ to 4), ΔR is the resistance change due to stress, V_{DD} is the bridge supply voltage (5V for our case), ε_i is the strain along the axis of the piezoresistors, and GF is the gauge factor of silicon. Strain and stress are linearly related by the Young's modulus. The GF for highly doped p-type silicon is 60 [97]. The sensitivity of the Wheatstone bridge to stress

is -1.13 GPa/V calculated from 5.1 and 5.2. The Wheatstone bridge produces a positive voltage for compressive stress since $R_{stress1,2}$ decreases with compression.

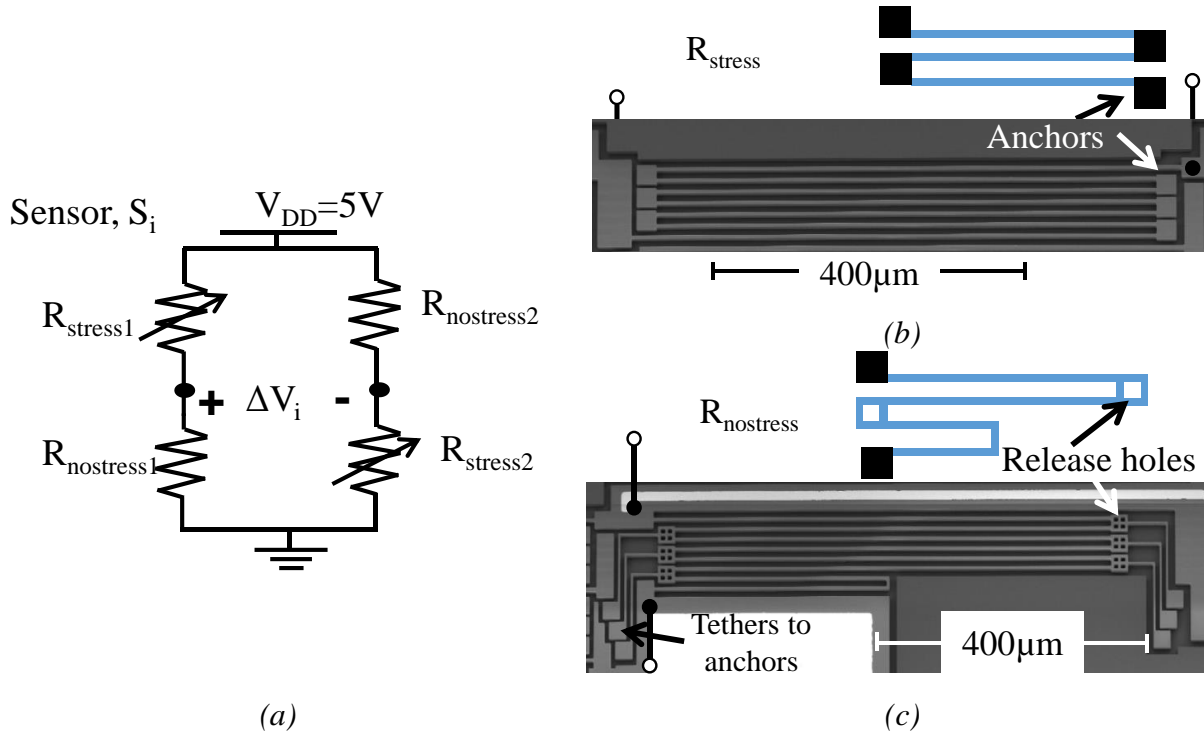


Figure 5.18: Wheatstone bridge stress sensor configuration to cancel temperature effects (a), stress and temperature sensitive released SOI piezoresistor, R_{stress} (b), temperature sensitive released SOI resistor, $R_{nostress}$ (c).

The resistors were characterized from 30°C to 80°C in an oven, with results given in Figure 5.19. The gyroscope sample is mounted with vacuum grease to suppress the stress effects and just to observe the temperature response on the two resistors. Both kinds of resistors identically respond to temperature changes, to the precision of the measurement, with a positive TCR of 1.6×10^{-3} .

Mechanical characterization used a four-point bending testbed and a 45° nanofoil mounted sample in an Instron machine that applies a controlled load, with results given in Figure 5.20. The DIP40 is placed directly under the bending load, which results in compressive stress in the die. The fixed-fixed beam piezoresistors ($R_{stress1,2}$) respond to the externally applied stress, while the free-free beam resistors ($R_{nostress1}$ and $R_{nostress2}$) have nearly zero stress coefficient of resistance (SCR),

$SCR_{stress}/SCR_{nostress} > 92$. In addition to their use in the Wheatstone bridge, $R_{nostress1}$ and $R_{nostress2}$ can be used as a temperature sensor with known TCR in the presence of external stress. The Wheatstone bridge outputs from different stress sensors were also recorded during the four-point bending tests. Figure 5.21 presents these test results for sensors S_3 and S_4 . They measure the longitudinal stress in the two principal orthogonal directions. Their sensitivity is different, and this is believed to be as a result of non-ideal die mount, i.e., the interfacial area between the MEMS die and the package is not 100% attached. Section 5.7 presents images from the nanofoil mounted devices where the die bonding is not 100%. Deviations from the 45° mount also lead to sensitivity differences between the stress sensors.

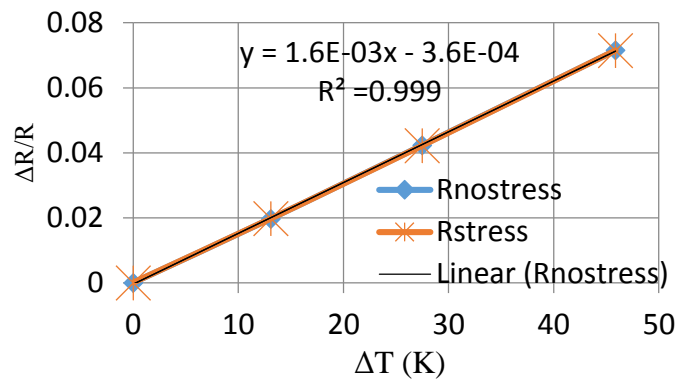


Figure 5.19: $\Delta R/R$ for $R_{nostress}$ and R_{stress} over temperature.

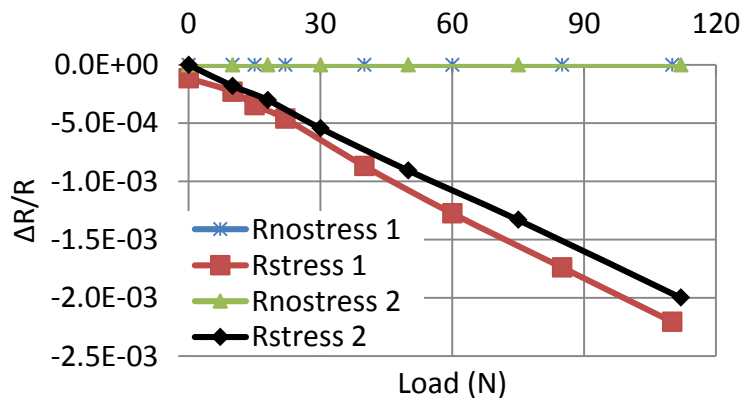


Figure 5.20: $\Delta R/R$ for $R_{nostress}$ and R_{stress} under a four-point compressive bending test.

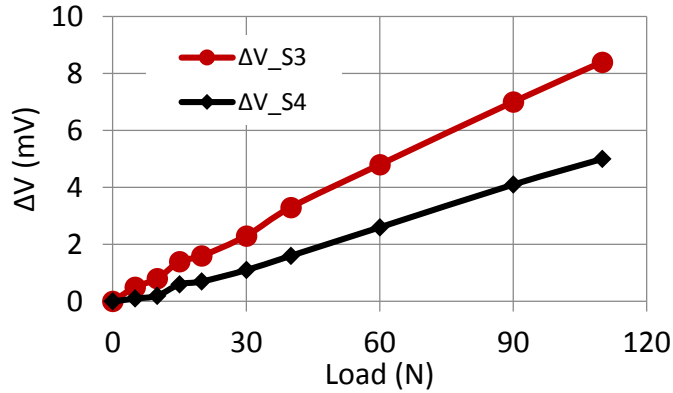


Figure 5.21: Wheatstone bridge outputs for S_3 and S_4 showing different sensitivities due to the die mount.

5.4 Stress Effects on ZRO and SF for Open-Loop Sense Mode

The results reported in this section are published in [98]. The initial stress test experiments for characterization of the ZRO and SF were run on a gyroscope with open-loop sense mode. The drive mode is closed loop with a phase locked loop (PLL) and amplitude control. The sense mode frequency is higher than the drive mode frequency ($f_{drive} < f_{sense}$) with 18 Hz mismatch. The tested gyroscope is in-house vacuum packaged and has a Q of 6,000. The open-loop bandwidth of the sense mode is around $(9 \text{ kHz}/6000) = 1.5 \text{ Hz}$, so 18 Hz mismatch is chosen to ensure that drive and sense phases satisfy mismatch condition and maximum motional current output is obtained from the sense mode.

Figure 5.22 shows the four-point bending stress testbed used during the experiments along with the photograph of the vacuum packaged gyroscope. The gyroscope PCB is sandwiched in-between the steel cylinders that are held by the aluminum fixtures. Adding weights on top of the setup creates compressive bending stress on the gyroscope, changing its characteristics. The goal of this test is finding the coefficients between the gyroscope ZRO, SF and stress sensor outputs.

The weights (“load” in Figure 5.22) on the gyroscope are incremented with 5 lbs steps up to 15 lbs during the tests. At each step, gyroscope ZRO, stress on both axes and temperature (with a

temperature sensing resistor) are recorded for 6 minutes, followed by a SF test on the rate table at $\pm 5^\circ/\text{s}$ and $\pm 10^\circ/\text{s}$ to compute the rate referred ZRO. Stress sensors 1 and 2 (S_1 and S_2 in Figure 5.17) are used capture the strain in the sense and drive axes, respectively. The stress testbed was set up on the rate table for continuous testing. The primary drift source in the experiments is believed to be the external stress since the measured on-chip temperature (using one of the temperature resistors) variation was less than 0.02°C .

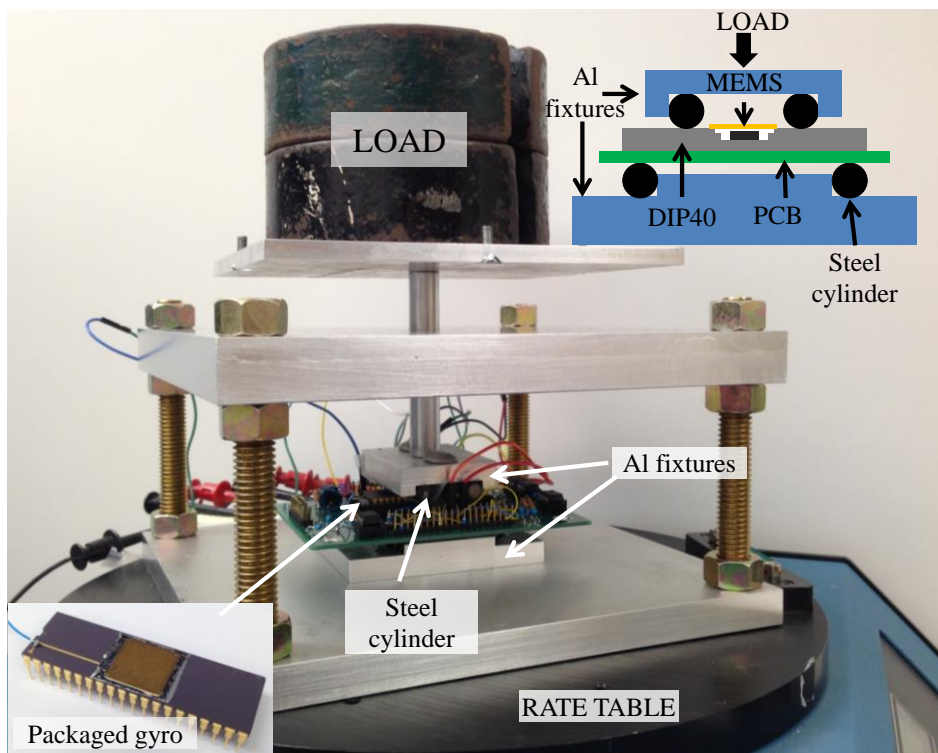


Figure 5.22: Four-point bending stress testbed used to test the vacuum packaged gyroscope on the rate table. Adding weights on the setup creates compressive bending stress.

Figure 5.23 shows the orientation of the die which is 45° with respect to the package and the transformation matrix that relates the measured stress and gyroscope parameters at constant temperature. The x axis is the drive mode and the y axis is the sense mode. The coefficients are obtained by linear least squares error fitting. This matrix is a step towards full model-based stress compensation. Each performance parameter has a dominant stress coefficient and a minor stress

coefficient that is at least five times less sensitive. The dominant stress term for each gyroscope parameter is highlighted. The gyroscope is mounted 45° with respect to the package to result in nominally equal package-induced stress on both modes.

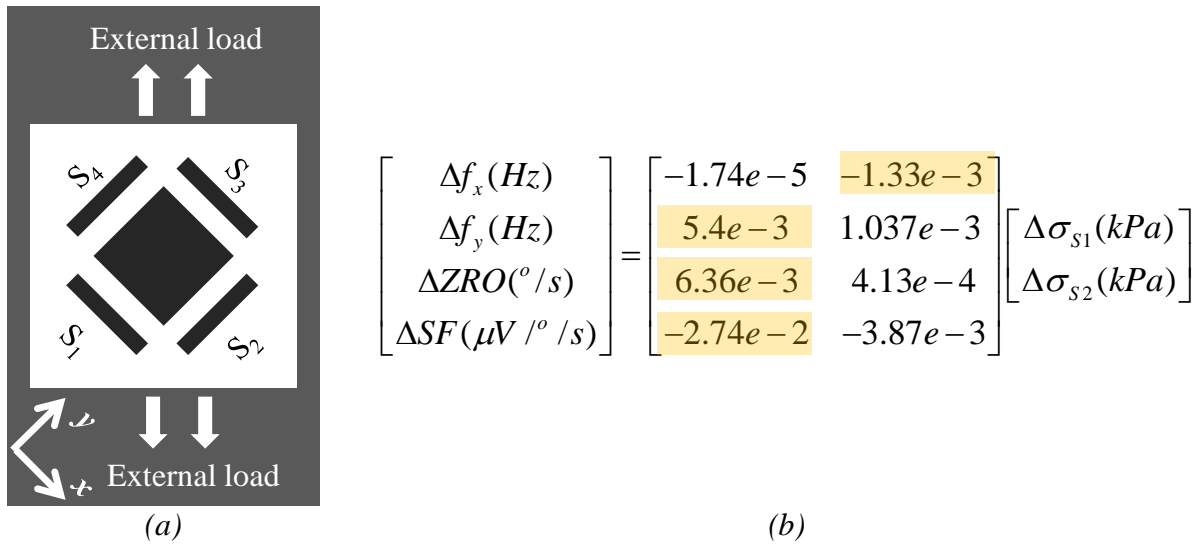


Figure 5.23: 45° die mount (a). Transformation matrix between stress and gyroscope parameters (b), each parameter is dominated by a single stress component.

Figure 5.24.a and b show the resonance frequency shift vs. dominant stress for drive and sense modes, respectively. The frequency shifts were obtained by open-loop frequency sweeps while the gyroscope is not working. The stress sensor outputs provide an approximately linear estimation of the resonance frequency shifts from the baseline. The stress is negative since the four-point bending test exerts compressive stress on the die. Drive and sense frequencies primarily shift with stress along their respective orthogonal axis since their flexural spring constant is primarily affected by longitudinal stress [92]. Both mode frequencies have a repeatable relationship with compressive stress; however, the sign of drive frequency response is counterintuitive. A decrease in the resonance frequency is expected with compressive stress. Although the 45° mounting equalizes the stress, the drive mode is believed to be pre-stressed due to the possible variation in

the nanofoil die bonding. The relatively low stress (< 1 MPa) applied during the tests is not sufficient for the drive frequency to start decreasing.

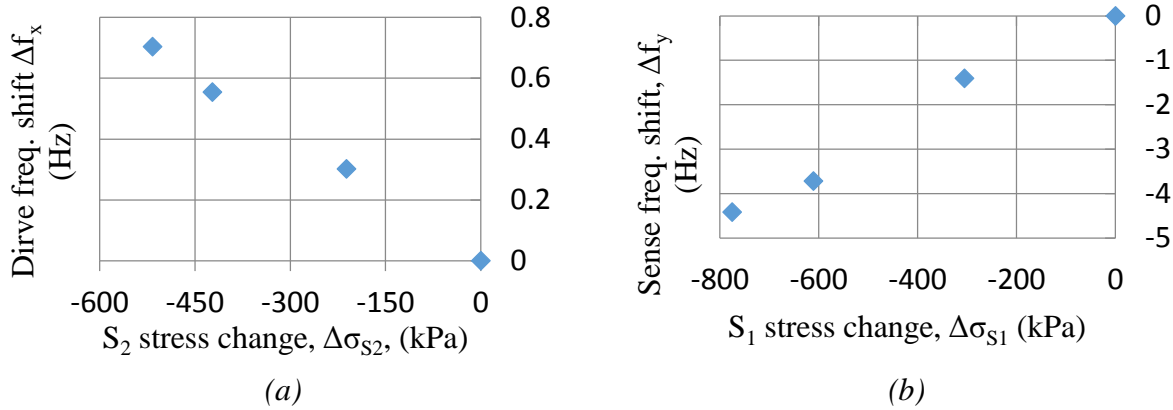


Figure 5.24: Drive mode frequency shift vs. stress sensor S_2 (a), and sense mode frequency shift vs. stress sensor S_1 (b), both of the shifts are linear with stress.

Figure 5.25 presents the SF test results as a function of the dominant sense mode stress (S_1) showing the increase with increasing stress. Since $f_{drive} < f_{sense}$ and the sense resonance frequency decrease is larger than drive frequency increase, reduced mismatch leads to increasing SF in open-loop operation.

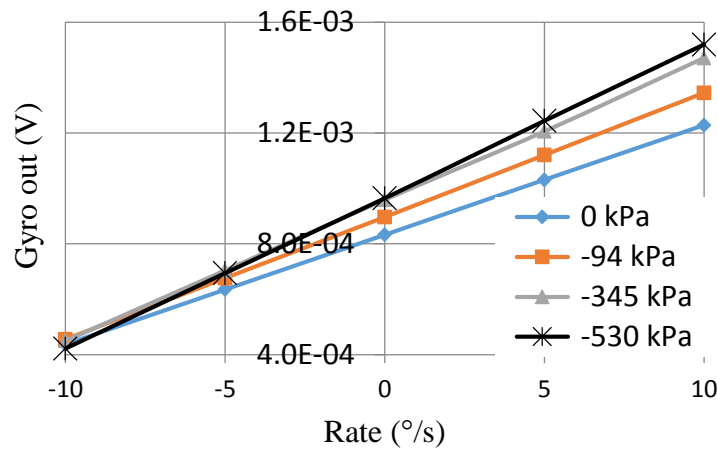


Figure 5.25: Scale factor test results for different stress levels on sense mode stress sensor (S_1).

Figure 5.26 shows the rate-referred ZRO change vs. the sense-axis stress. The ZRO shift is believed to be originating from drive and sense comb gap mismatches. A drive comb gap

mismatch generates an in-phase force on the sense mode that is indistinguishable from the Coriolis force, and leaks to the rate output because of the finite drive-axis spring constant of the sense-axis springs as explained in section 2.1.2. A sense comb mismatch on the other hand, increases the SF since an imbalance in the combs results in higher capacitive sensitivity. However mixed MEMS-electronics simulation results show $8^\circ/\text{hr}$ ZRO shift for the maximum stress point that is presented in Figure 2.15. As seen in those simulation results %s ZRO shifts are possible with stress if there is feedthrough that leads to quadrature leakage to the sense mode zero rate output. So relatively large %s level ZRO shifts shown in Figure 5.26 are believed to be a result of the feedthrough capacitances. The effect of feedthrough has been reduced later, by moving to a more carefully designed PCB and fully differential driving and sensing configuration.

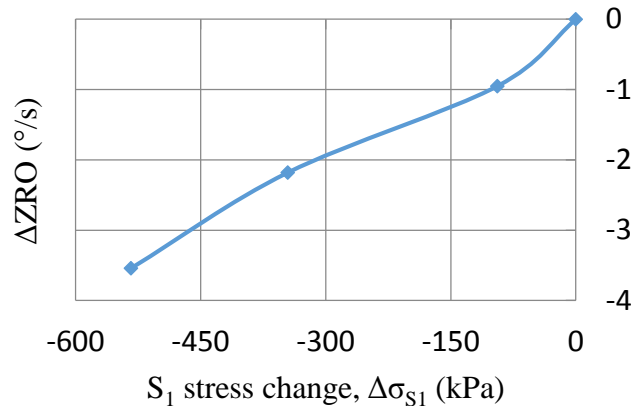


Figure 5.26: Zero rate output (ZRO) vs sense-axis stress (S_1).

After the matrix coefficients are obtained, the logical next step is to explore output compensation. However, the stress sensors on the tested die failed due to electrostatic pull down to the substrate and subsequent short circuit. The $600\ \mu\text{m}$ -long, $5\ \mu\text{m}$ -wide, $15\ \mu\text{m}$ -thick stress sensor beams are suspended over the $2\ \mu\text{m}$ SOI gap. Therefore, special attention must be paid to prevent electrostatic pull-down from the high dc potential (V_{PM} , 20 V to 40 V dc) on the SOI substrate that is biased at the same potential as the proof mass. The problem is solved by biasing one side of the

bridge to V_{PM} and the other side to $V_{PM} - 5V$, and powering the $V_{PM} - 5V$ source after V_{PM} . However, we moved to an RC biasing network (explained in Section 1.7) later that grounds the SOI handle layer and does not require sequential turn on of the supply voltages.

An Allan deviation test was run to observe the performance level of the SOI-MEMS gyroscope. The uncompensated Allan deviation graph in Figure 5.27 shows the performance of a SOI-MEMS gyroscope with a bias instability of $6.1^\circ/\text{hr}$ and angle random walk (ARW) of $46.6^\circ/\text{hr}/\sqrt{\text{Hz}}$. The gyroscope was operated at 50 Hz mismatch with closed-loop sense and quadrature cancellation in this test. As will be shown in the following sections, stress compensation highly suppresses the long term drift.

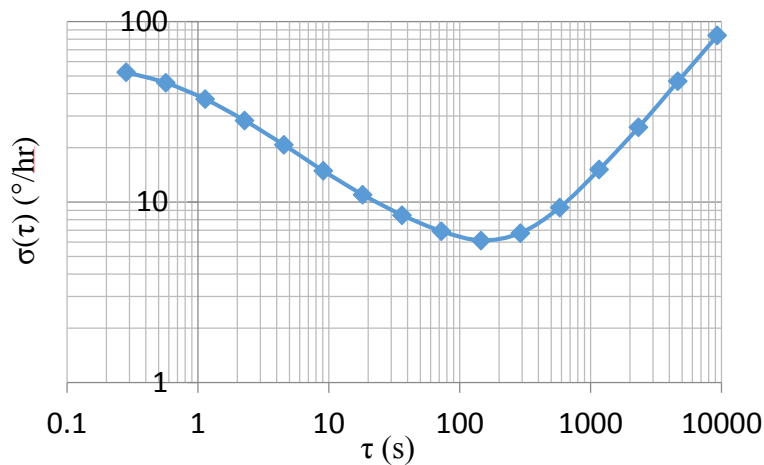


Figure 5.27: Uncompensated Allan deviation test results of a SOI-MEMS gyroscope.

5.5 Test Results on Stress and Temperature Compensation at Ambient Temperature

An experiment was run with closed-loop drive and sense modes at 25 Hz mismatch while recording ZRO, drive, and sense-axis stress, and temperature. Stress sensors are biased around V_{PM} in this experiment. The temperature is measured by recording the resistance of one of the temperature

sensing resistors. Figure 5.28 presents the results. The room temperature goes through a 1.5 K cycle. The ZRO and stress sensor outputs also go through a cycle, however even though the temperature goes back to its starting point, ZRO and stress sensor outputs return to a different value than their starting point.

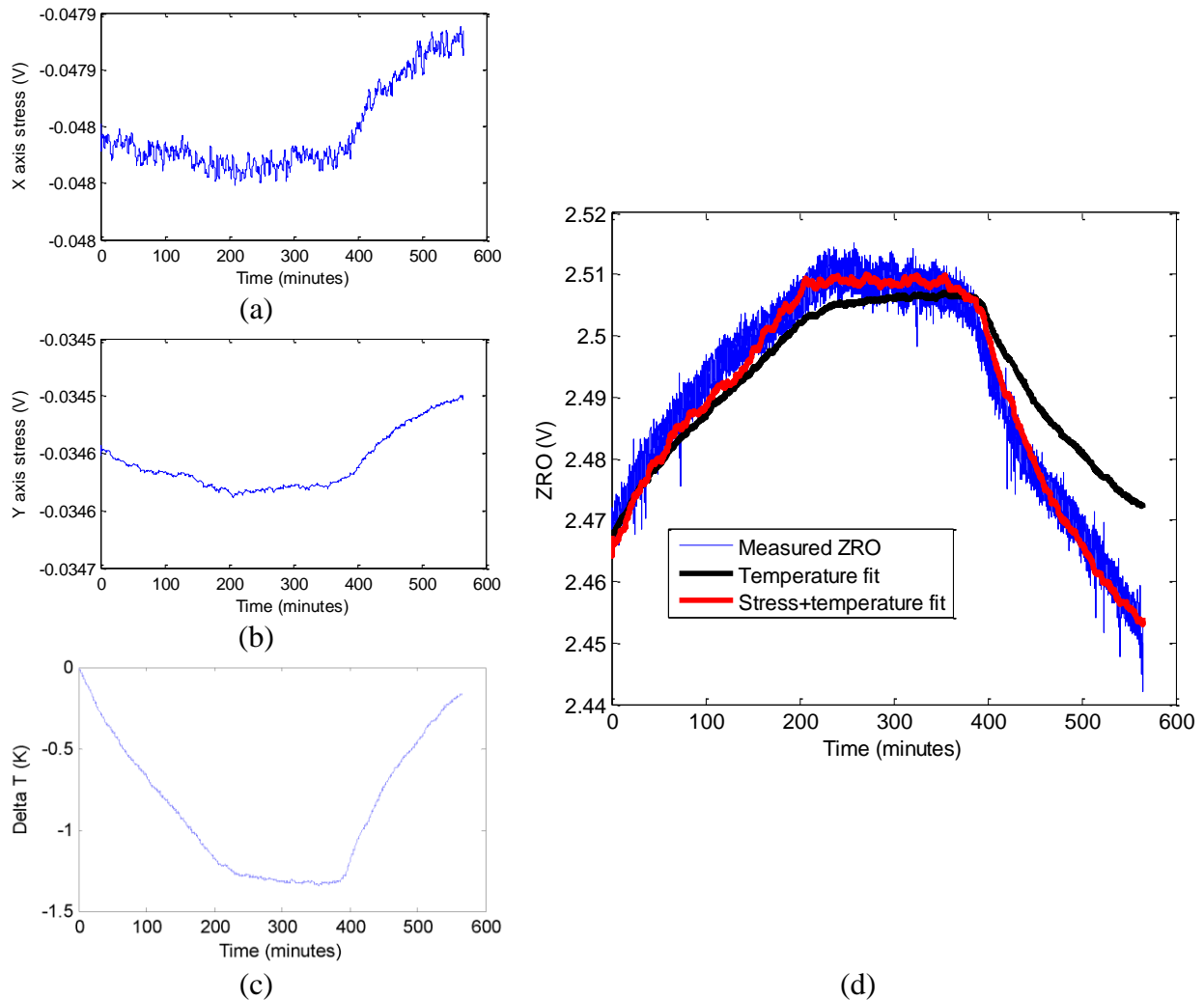


Figure 5.28: *x axis stress (a), y axis stress (b), temperature (c), and uncompensated ZRO with just temperature fitting and stress and temperature fitting (d).*

Figure 5.28.d shows the uncompensated ZRO and temperature fit, and stress and temperature fit. A least squares linear fitting has been applied assuming either ZRO is a function of just temperature or ZRO is a function of stress and temperature. Since stress sensor outputs follow ZRO closer a better fit is obtained when stress and temperature are used together. There was a grounding issue

with the x axis stress sensor that resulted in noisier measurements. For that reason, only the y axis stress sensor has been used during the fitting.

Figure 5.29 presents the Allan deviation analysis of the uncompensated, temperature compensated, and stress and temperature compensated ZRO. The compensated ZRO is obtained by subtracting the fitted ZRO from the uncompensated ZRO. Consistent with Figure 5.28.d, stress and temperature compensation yields a long term stability improvement of two times compared to temperature compensated ZRO and a seven times improvement compared to uncompensated ZRO. These compensation results show the potential benefit of stress compensation in improving long term stability.

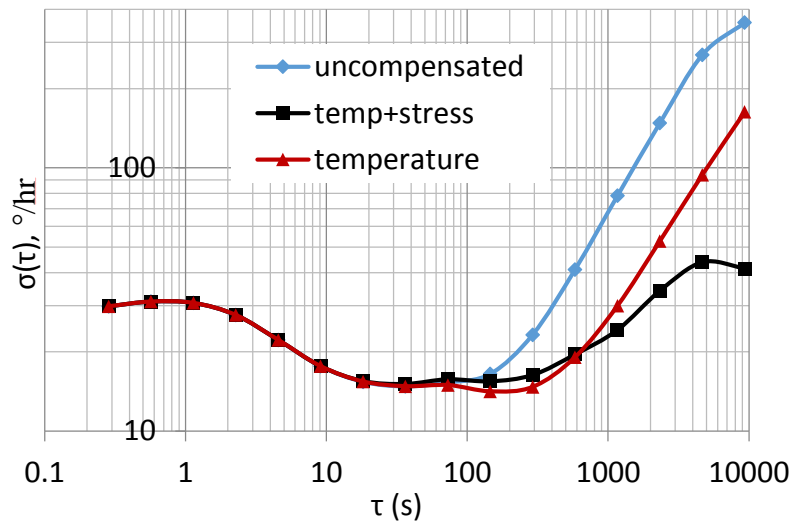


Figure 5.29: Allan deviation test results for the uncompensated, temperature compensated, and stress and temperature compensated ZRO.

5.6 Gyroscope Test Results with the Ovenized Testbed

Temperature fluctuations inherently change the stress acting on the gyroscope microstructure due to the TCE mismatch of the MEMS die and the package. To first order, these TCE stress effects are accounted for through conventional temperature compensation. However, external stress effects that are not correlated with on-chip temperature will remain. Results presented in

Figure 5.28 constitute an example for the case where stress compensation improves the effectiveness of the temperature compensation. To better understand the stress-only effects and suppress the temperature induced drifts, the gyroscope is ovenized using an external heater and temperature controller, as shown in Figure 5.30. The gyroscope is mounted with 45° orientation with respect to DIP40 for symmetric stress coupling to the die. A plunger connected to the second-level packaged heater block is loaded with adjustable weight to apply external compressive stress to the gyroscope die. This system is similar to a four-point bending test; the printed circuit board (PCB) leads act as outer anchors and adding load creates compressive stress on the MEMS gyroscope.

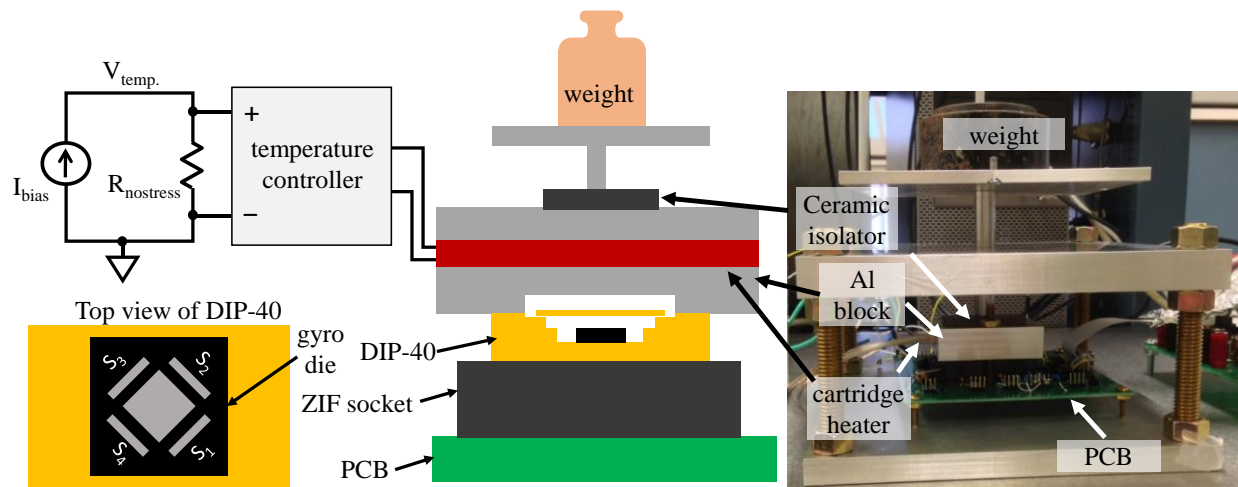


Figure 5.30: Ovenized gyroscope stress testbed. Adding weight creates compressive stress on the die.

A machined aluminum block that houses a cartridge heater is bolted to the testbed PCB to heat the gyroscope. Proportional-integral-derivative (PID) control parameters are tuned to compensate for the thermal lag due to the relatively large oven thermal time constant of around 30 minutes. Ceramic isolators thermally isolate the heater block from the aluminum rod that transfers the stress for the external stress application in order to keep the system thermal time constant independent

of the applied weight. The temperature was controlled at 27°C within $\pm 0.02^\circ\text{C}$ precision during the experiments. The tests were performed with and without external stress application.

One of the $R_{no\text{stress}}$ temperature sensing resistors on the S_4 side is biased with a constant current source and the voltage output is used as the servo input for the temperature controller. The drive resonance frequency can also be used as a temperature sensor [7], but using the stress-free on-chip temperature sensor allows observation of the stress effects on drive resonance frequency since stress and temperature are measured independently in our testbed. The Wheatstone bridge stress sensors on the other three sides (S_{1-3}) record die stress. The three stress sensor outputs are recorded with three multimeters controlled by a LabVIEW program.

The PCB electronics include the low noise transimpedance amplifiers in the differential x -axis and y -axis signal chains and the instrumentation amplifiers for additional gain and differential-to-single-ended conversion. The drift of the stress sensors directly relies on the quality of the 5 V V_{DD} supply, which is generated by a bandgap reference on the PCB [96]. Elsewhere on the PCB, voltage regulators supply power to the electronics, and buffers isolate the MEMS outputs and the ac output of the lock-in amplifier that drives the gyroscope. The details of the PCB is provided in Appendix D.

The gyroscope is operated in a fully closed-loop configuration. We used the architecture in the IEEE standard 1431-2004 that is explained in Section 2.2.1. A phase locked loop (PLL) and an amplitude control loop act on the drive mode to lock into the resonance and fix the drive displacement, respectively. The drive displacement is set to 1.3 μm during the experiments, to maintain capacitive linearity with displacement. Quadrature cancellation and force rebalance loops null the sense displacement. Both of these loops use ac signals to null the displacement, with applied signals that are 90° out of phase. Special attention has been paid to minimize the

feedthrough capacitance both on the PCB and from the die wirebonding so that ac quadrature cancellation does not introduce considerable feedthrough current. The motional current to feedthrough current ratio is kept above 60 dB during matched mode operation. Matched mode operation helps to suppress the feedthrough effects since less voltage is needed to null a specific displacement at matched mode to run the quadrature cancellation and force rebalance loops.

The tested gyroscope is in-house vacuum packaged and it has a quality factor of 18,000. The initial 80 Hz mismatch between the two vibratory modes is matched manually by changing the frequency tuning voltage on the sense mode first. The closed-loop sense mode provides enough bandwidth (20 Hz) to the gyroscope during the operation. The bandwidth provided by the closed-loop operation suppresses the drifts of drive and sense resonance frequencies during testing that is in the order of mHz. Preamplified outputs are fed into a digital Zurich Instruments HF2LI lock-in amplifier, and all of the demodulation and control loops are implemented digitally in the lock-in amplifier.

5.6.1 Test Results with External Stress

The results of an external stress test are plotted in Figure 5.31, showing the changes with respect to $t = 0$ in the uncompensated and compensated gyroscope ZRO, drive frequency, and environmental sensor outputs. The initial values are $9.2^\circ/\text{s}$ for ZRO, 300 K for temperature, 8790.9 Hz for frequency, 80.3 mV for S_2 , 87.8 mV for S_1 , and 86.8 mV for S_3 . A two-pound weight was applied and removed at 35 min intervals to demonstrate the significance of external stress effects on ZRO. Stress sensors S_1 and S_3 capture the die stress along the sense axis and stress sensor S_2 captures the die stress along the drive axis.

The temperature change is less than 40 mK. There is a correlated lowering of temperature from the addition of weight, as expected by the change in heat conductance. Adding weight creates a compressive stress on the gyroscope reducing the nominal resistance of the stress sensing resistors. This leads to an increase in the stress sensor outputs according to the Wheatstone bridge configuration in Figure 5.18, S_3 exhibits the highest sensitivity to applied stress measuring a change of -34 kPa/lb; S_2 exhibits a medium sensitivity measuring a change of -6.2 kPa/lb; and S_1 exhibits a small, almost insignificant sensitivity.

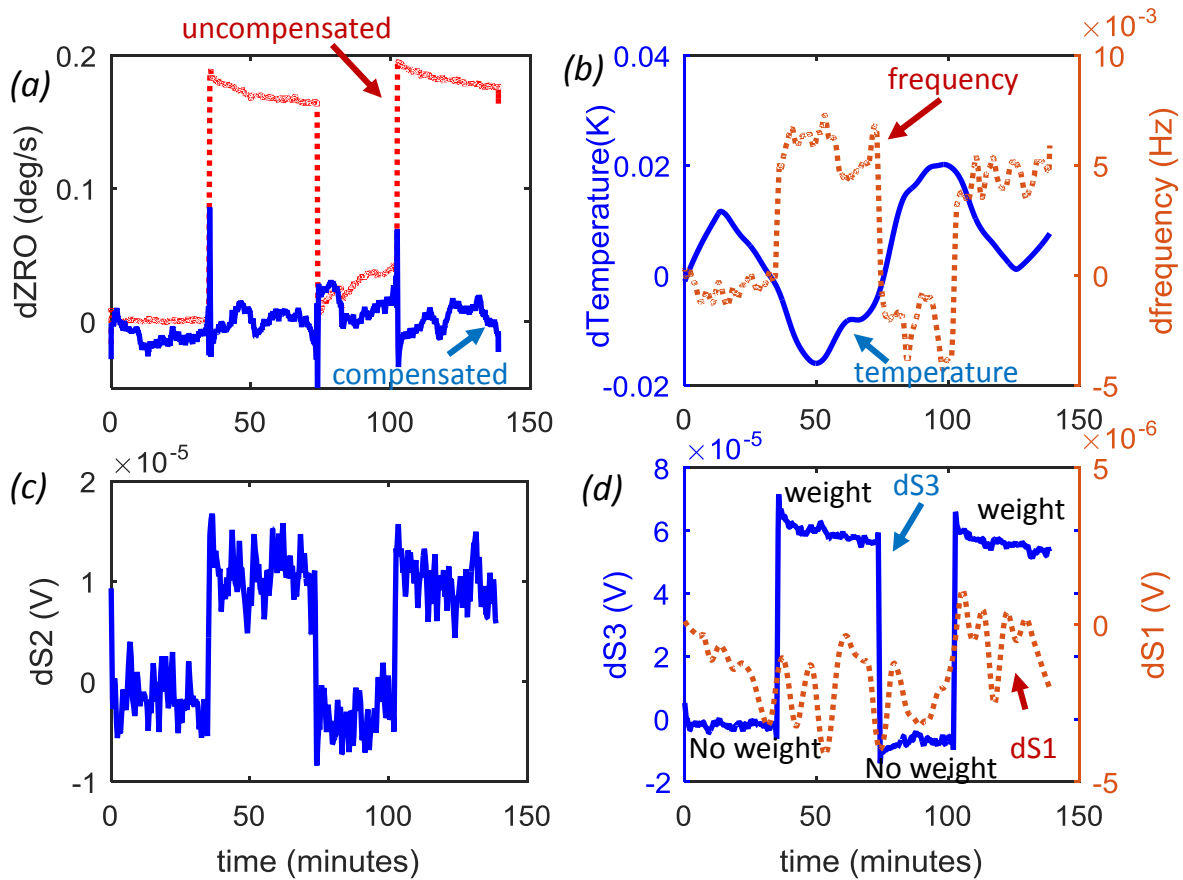


Figure 5.31: External stress test results. Changes in uncompensated and compensated gyroscope ZRO (a), drive frequency and on-chip resistive temperature sensor (b), drive-axis stress sensor S_2 (c), and sense-axis stress sensors S_1 and S_3 (d).

The sensitivities are calculated by using eqs. 5.1 and 5.2 and the measurements in Figure 5.31. Although the die is mounted 45° for even stress distribution, the measurements suggest an

asymmetric stress distribution on the die. We hypothesize that this is due to non-uniform die attachment where the die bonding varies across the chip area, leading to asymmetric stress coupling to the die. The correlation between S_3 and uncompensated ZRO is strong, with a sensitivity of $-9^\circ/\text{hr}/\text{kPa}$. The drive frequency is also affected by stress with approximate sensitivity of -73 ppb per kPa stress in the drive axis measured by S_2 , given the resonance frequency is 8.8 kHz.

The environmental sensor outputs are passed through a digital moving average smoothing filter (MATLAB function “smooth”) with 50 points for S_1 and S_3 and 1000 points for S_2 to suppress measurement noise of the multimeters. S_2 is filtered more since it exhibits low signal to noise ratio, and remains relatively unchanged with stress. The environmental sensor data is sampled every 1.67s during the measurements. A linear least squares error fitting algorithm between the gyroscope ZRO and the three filtered stress sensor measurements and the filtered temperature sensor measurement determines the environmental sensor sensitivity coefficients. Subtracting the weighted environmental sensor outputs from the raw gyroscope output yields the compensated gyroscope ZRO. Allan deviation of the gyroscope ZRO for the uncompensated, temperature compensated, stress compensated, and temperature and stress compensated cases are compared in Figure 5.32. Temperature compensation provides a slight improvement in the long term due to the residual thermal effect of the weight as observed in the temperature measurements in Figure 5.31. However, stress and temperature compensation and stress compensation yields almost identical results up to 300 s. Stress and temperature compensation together results in almost an order of magnitude improvement after 300 s.

A second external stress test experiment was carried out. The testbed is shown in Figure 5.33. Instead of applying and removing a weight as in Figure 5.30, a 175 gram copper weight was moved

from right to left back and forth every 30 minutes to observe the ZRO relation to external stress. The temperature control is not shown for simplicity, the testbed is identical to the first external stress test (in Figure 5.30) in terms of temperature control and recording the stress sensor outputs. Figure 5.34 presents the results of this second external stress test with changes with respect to the operating point at $t = 0$ in uncompensated and compensated gyroscope ZRO, along with the outputs from the drive frequency and on-chip resistive temperature sensor, from the drive-axis stress sensor S_2 , and from the sense-axis stress sensors S_1 and S_3 .

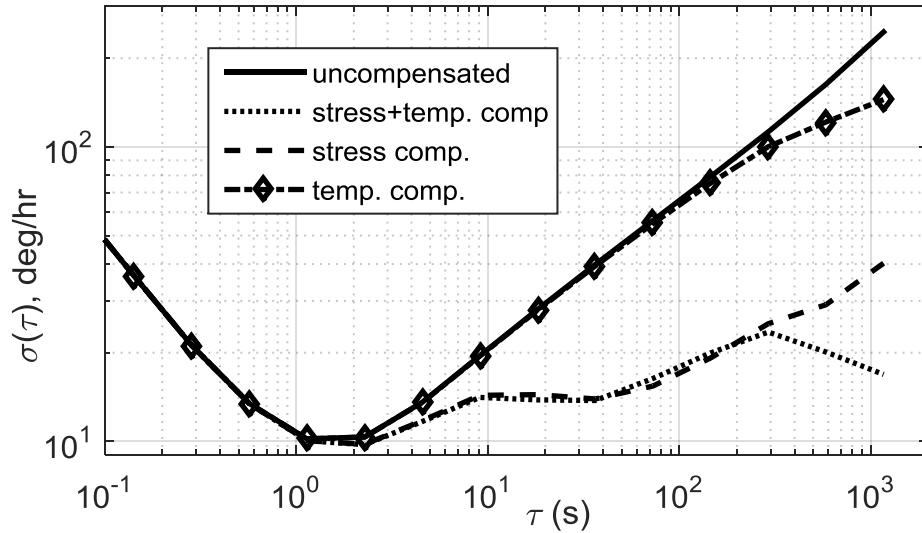


Figure 5.32: Allan deviation of the gyroscope ZRO for uncompensated, temperature compensated, stress compensated, and stress and temperature compensated cases.

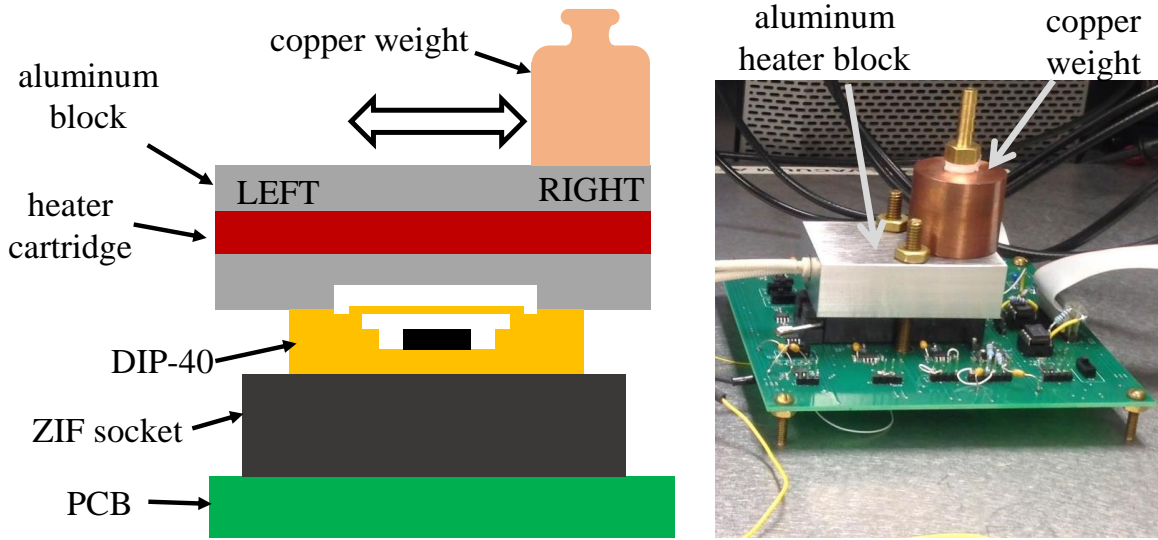


Figure 5.33: Second external stress test where a copper weight is moved from left to right for stress modulation. Temperature control not shown.

Since the copper weight was always kept on the aluminum block, the temperature remained within a 40 mK range during the experiment. As expected, the temperature and frequency are correlated due to the negative temperature dependence of the silicon Young's modulus. However, the frequency under oven control is stable to within 1 ppm, with the drive resonance frequency at 8.8 kHz. Even though the total weight on the gyroscope is always constant, changing the location of the copper weight creates $\%$ s level ZRO shift underlying the importance of stress compensation. A direct correlation between ZRO and S_3 is evident in Figure 5.34. The sensitivities and the sensitivity differences of the stress sensors are similar to the previous external stress test. S_1 and S_2 are not as sensitive as S_3 , suggesting an uneven stress distribution even though the gyroscope die is mounted 45° with respect to the package to distribute the package stress symmetrically on the die. This is believed to be a result of non-idealities in the die attachment.

The sensitivity of the stress sensors is -1.13 GPa/V , so the external stress formed by the applied weight leads to a ZRO to stress sensitivity of $17.6^\circ/\text{hr/kPa}$ based on the S_3 data that is different than the $-9^\circ/\text{hr/kPa}$ sensitivity obtained in the previous stress test. This behavior is believed to be

due to the fact that we have only one active stress sensor, so all different stress components are not measured. The stress formed by adding the two-pound weight versus sliding the copper weight is different, but there are not enough stress sensing degrees of freedom to capture the difference.

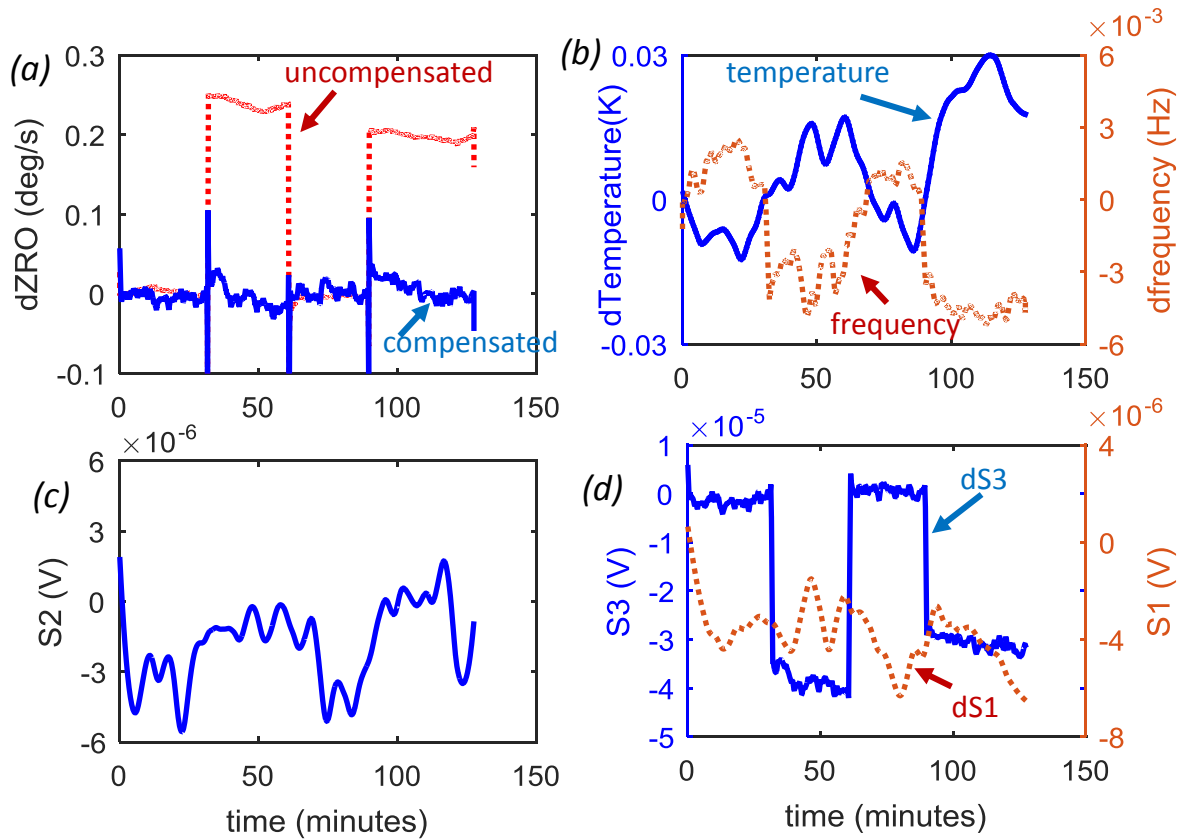


Figure 5.34: Result of second external stress test. Changes in uncompensated and compensated gyroscope ZRO (a), and outputs from the drive frequency and on-chip resistive temperature sensor (b), drive-axis stress sensor S_2 (c), and sense-axis stress sensors S_1 and S_3 (d).

The compensation coefficients are calculated with the linear least squares fitting, and Allan deviation plots in Figure 5.35 compare the uncompensated gyroscope ZRO with the stress only, temperature only, and joint stress and temperature compensated ZRO. Stress-only compensation and joint stress and temperature compensation yield very similar results with an order of magnitude improvement in the long term stability when compared to the uncompensated and the temperature-only compensated cases. Temperature-only compensation does not improve the long term stability since the device is ovenized.

The two external stress test results show that non-temperature induced external stress may lead to $\%/\text{s}$ level ZRO shifts and stress compensation can highly suppress the long term gyroscope drift. Two different experiments have been carried out to investigate the source of stress induced ZRO shifts. The first test includes open-loop frequency sweeps while the copper weight is on the right and left in Figure 5.33. However, open-loop frequency sweeps on the matched drive and sense modes do not give an accurate assessment on the resonance frequencies due to the high quadrature coupling between the modes. Therefore, the sense mode is intentionally detuned from the drive mode for open-loop frequency sweeps to be able to measure the resonance peak location accurately. Figure 5.36 and Figure 5.37 show the measured resonance frequency sweeps for the drive and detuned sense mode when the copper weight is at the right and left positions above the gyroscope.

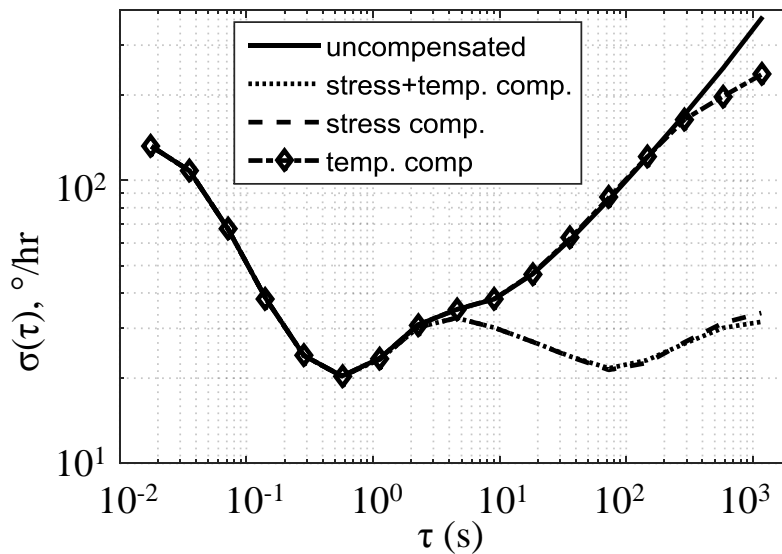


Figure 5.35: Allan deviation plots for uncompensated and stress, temperature, and stress and temperature compensated data.

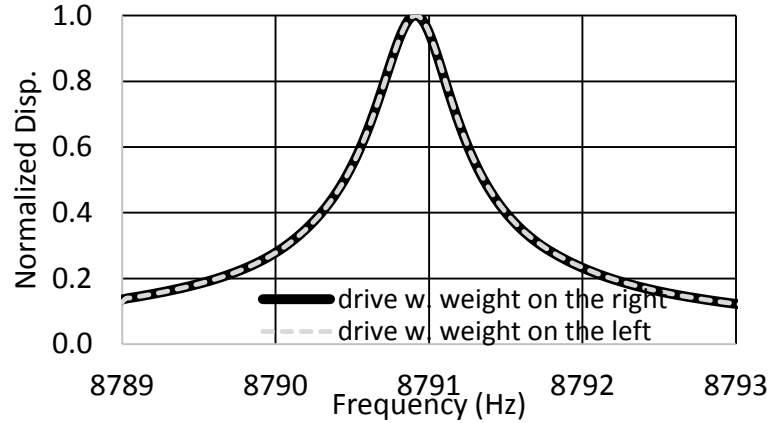


Figure 5.36: Open-loop frequency sweeps for the drive mode when the copper weight is on the right and left.

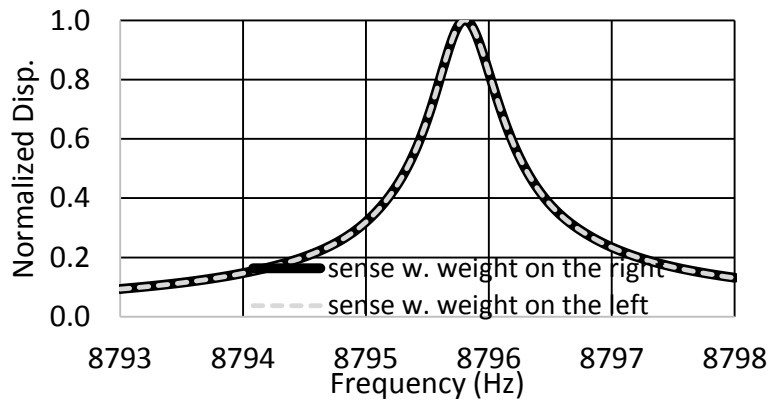


Figure 5.37: Open-loop frequency sweep for the intentionally detuned sense mode when the copper weight is on the right and left.

Next, to investigate the effect of frequency mismatch on ZRO, the frequency tuning voltage on the sense mode was intentionally changed to provide a mismatch with the drive mode, and the resulting ZRO was recorded. The results are presented in Figure 5.38. The correlated ZRO change is well less than $0.01^{\circ}/s$ for induced mismatch up to ± 0.8 Hz. The relative insensitivity of ZRO to frequency is achieved as a result of closed-loop sense-mode operation. The $0.2^{\circ}/s$ ZRO shift with external stress is more than an order of magnitude greater than that measured from modal frequency mismatch which is in the order of mHz according to Figure 5.36 and Figure 5.37. So modal frequency drifts do not explain the stress-ZRO relation. The main reason behind the long-term ZRO drift is believed to be the drive and sense comb-finger gap asymmetry created from

anchor motion due to stress. Drive gap asymmetry creates a force in the sense direction that is indistinguishable from the Coriolis force [39]. Sense gap asymmetries on the other hand change the sensitivity of the gyroscope that affects the ZRO.

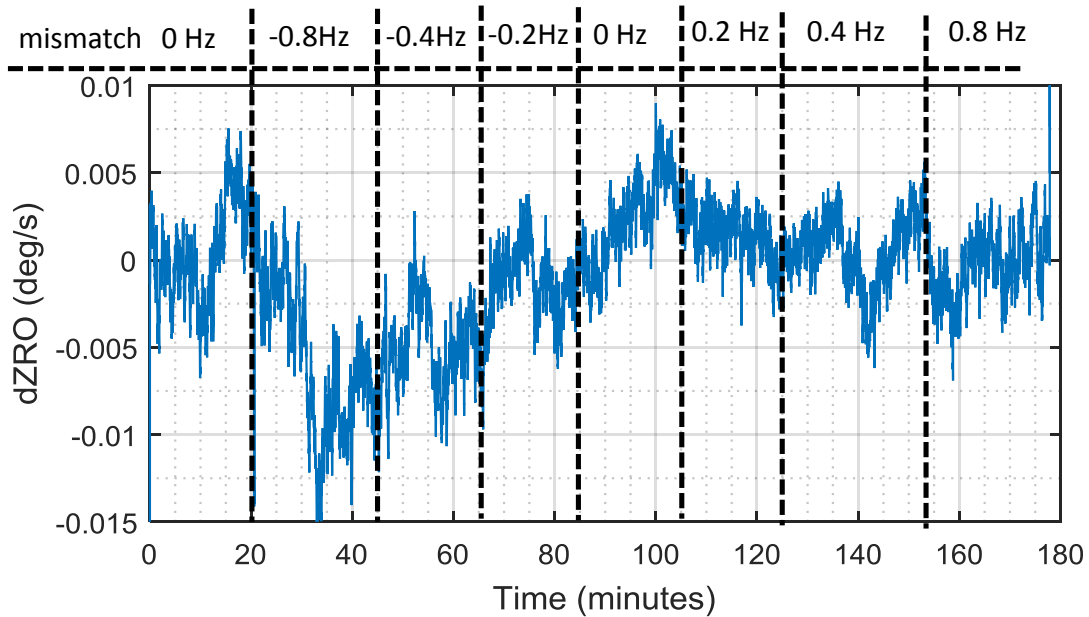


Figure 5.38: ZRO of the ovenized gyroscope for different values of frequency mismatch between the drive and sense modes.

5.6.2 Allan Deviation Results without External Stress

Several Allan deviation tests were performed at constant oven-controlled temperature and without external stress to assess the practical utility of the on-chip stress compensation. Each test was run 10 to 12 hours to capture the long term drift behavior of the SOI-MEMS gyroscope. Figure 5.39 presents the results from a sample run. It shows the changes with respect to $t = 0$ in uncompensated and compensated gyroscope ZRO, drive frequency, and the environmental sensor outputs. Even though the gyroscope is ovenized to a temperature stability of less than 40 mK, the gyroscope still exhibits a clear drift when uncompensated. State-of-the-art ovenized gyroscopes exhibit similar drift trends [24]. The resonant frequency and temperature are correlated to the first order; the

correlation coefficient is negative due to the -60 ppm/K temperature dependence of silicon Young's modulus.

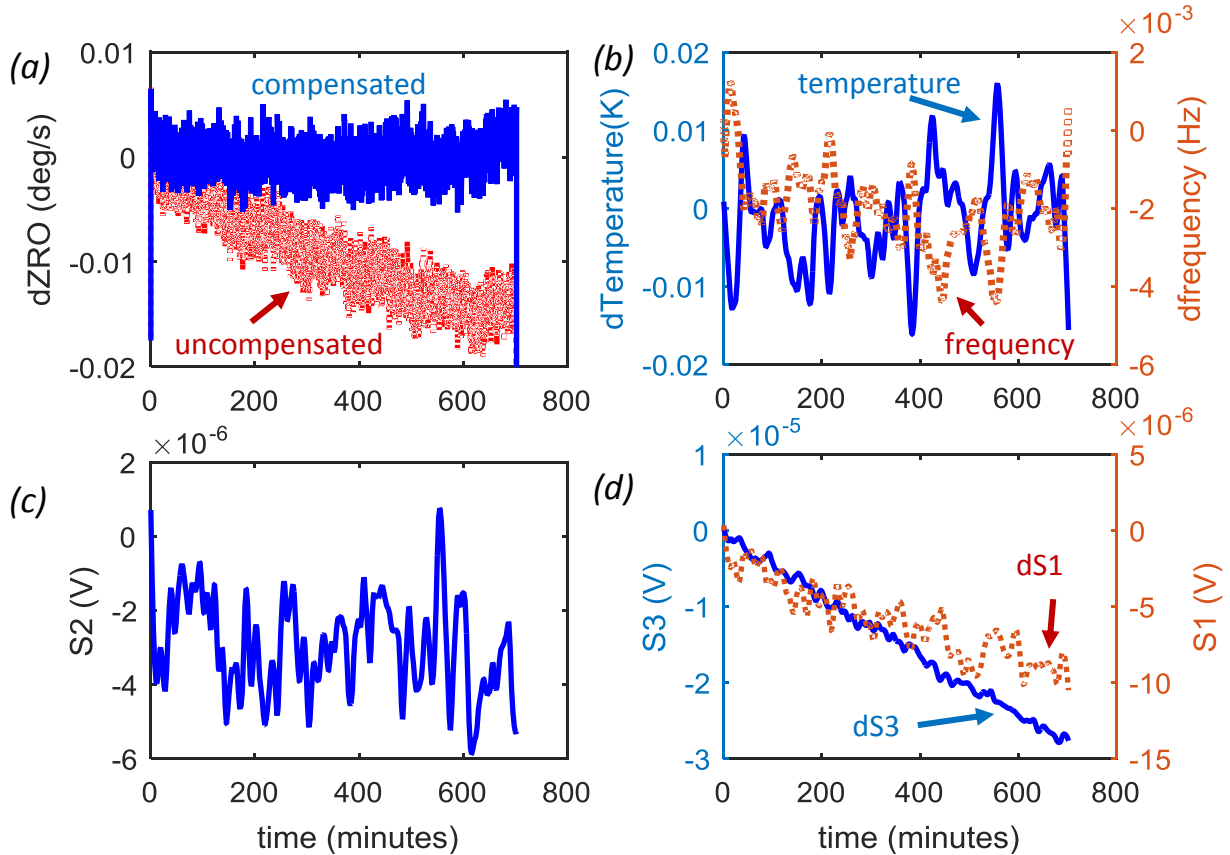


Figure 5.39: Long term measurement data for a test without external stress. Changes in uncompensated and compensated ZRO (a), and outputs from the drive frequency and on-chip resistive temperature sensor (b), from the drive-axis stress sensor S_2 (c), and from the sense-axis stress sensors S_1 and S_3 (d).

A couple of reasons for the source of the stress drift come to mind. First, the gyroscope is ovenized from the top surface and the bottom of the DIP40 is exposed to room temperature. Therefore, the changes in the room temperature may induce a varying stress on the gyroscope. The second source may be effects from the zero insertion force socket (ZIF); the gyroscope is mounted using a ZIF socket that clamps the DIP40 using a levered spring mechanism. This spring force on the DIP40 leads may drift with time that changes the stress on the gyroscope. And finally, the PCB, ZIF socket, ceramic DIP40 and surrounding materials may age with time leading to a stress change.

The S_1 and S_3 stress sensor outputs correlate to the change of the uncompensated ZRO over time. The S_3 stress sensor sensitivity to ZRO is $-1.9^\circ/\text{hr}/\text{kPa}$, which is different than the $-9^\circ/\text{hr}/\text{kPa}$ and $17.6^\circ/\text{hr}/\text{kPa}$ sensitivity measured from the stress tests shown in Figure 5.31 and Figure 5.34. These sensitivities are extracted by using the Wheatstone bridge equations 5.1 and 5.2, and the measurement results by assuming ZRO shift is only due to S_3 . The difference is believed to arise because the stress components originating from the application of the external load are different in each of the tests, and stress just from three regions can be measured.

The compensation coefficients are calculated through linear fitting, and Table 5.1 presents the individual compensation coefficients for the three tests and the average of the coefficients. As the most sensitive sensor, the output of S_3 dominates the compensation factors. The effect of S_3 is more than the compensation coefficient, since it also generates more signal compared to S_1 and S_2 . This is believed to be due to the non-uniform die bonding, and Section 5.7 provides details on the die bonding. The compensated ZRO in Figure 5.39.a greatly reduces long term drift compared to the uncompensated ZRO. Figure 5.40 shows the corresponding Allan deviation of gyroscope ZRO for the uncompensated, stress compensated, and stress and temperature compensated cases. Stress compensation and stress and temperature compensation results in very similar results with seven times improvement in the long term stability. This is expected since the device without any weights on it is better ovenized than the external stress test. Since temperature compensation does not contribute by a considerable amount, temperature compensation is not included in Table 5.1. The gyroscope angle random walk (ARW) is $9^\circ/\text{hr}$ and it is dominated by the thermomechanical noise of the mechanical structure. Open-loop noise measurements and closed-loop noise calculations in Section 2.3 suggest an ARW of $5^\circ/\text{hr}$. The closed-loop system is believed to be contributing this additional noise, and requires more attention in the future. Stress compensation

removes the rate random walk, and an angle random walk slope is obtained even at 10,000 s (~3 hrs) averaging time. The gyroscope stability is an order of magnitude better than the tests with external stress shown in Figure 5.32 and Figure 5.35, since it is more likely that the applied weights cause additional stress drifts other than the measured stress. The unmeasured stress components due to limited stress sensor degrees of freedom are believed to lead to the performance degradation.

Table 5.1: Individual compensation coefficients of the three individual coefficients and their average.

	S_1 (V/V)	S_2 (V/V)	S_3 (V/V)
test #1	363	16.4	163.7
test #2	-93.7	122.6	179.5
test #3	41.5	67.1	168.7
Average	103.6	68.7	170.6

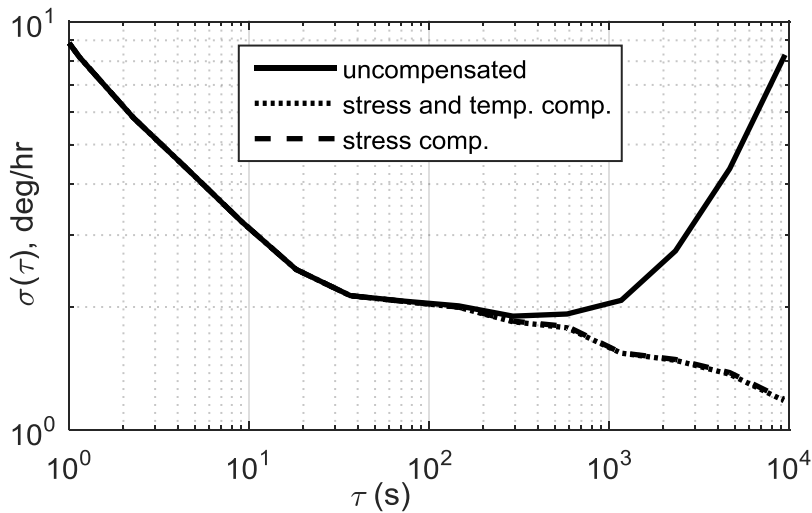


Figure 5.40: Allan deviation of the gyroscope ZRO for the uncompensated, temperature compensated, and stress and temperature compensated cases.

The stability of the compensation coefficients over time is a major concern for practical use. The ZRO test from Figure 5.40 (“test #1”) was repeated two more times to assess the repeatability of the coefficients. Figure 5.41 to Figure 5.43 show the Allan deviation from the three tests using various compensation coefficients. The compensation has been done just using the stress sensor

outputs. Optimized custom coefficients that give the best result are extracted from each test's own data. Averaged coefficients are computed as the average of the three sets of optimized coefficients shown in Table 5.1. The averaged and optimized coefficients, which include stress compensation, perform similarly to reduce the long term drift, with at most a $2\times$ penalty in the longest-term drift performance when using averaged coefficients.

The averaged compensation performs better than the optimized compensation between integration times of 100 s to 1000 s in Figure 5.41; this is due to the fact that the optimized coefficients are optimized for the overall data. The optimized compensation results in a better overall compensation compared to the averaged compensation. There is also an abrupt drop in the Allan deviation curve in Figure 5.42 around 4000 s. Each test is 12 hours long (43,200 s), and as the integration time increases, the confidence of Allan deviation decreases. So it is more likely to see abrupt changes in the Allan deviation for longer integration times.

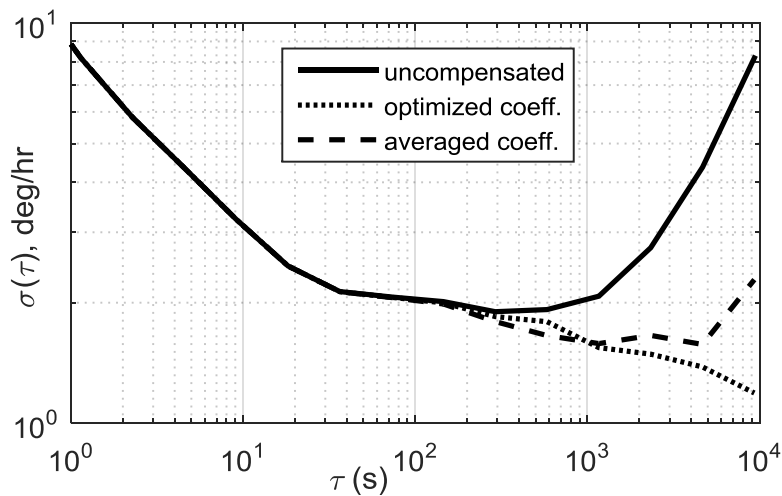


Figure 5.41: Allan deviation results for uncompensated and compensated ZRO for test #1.

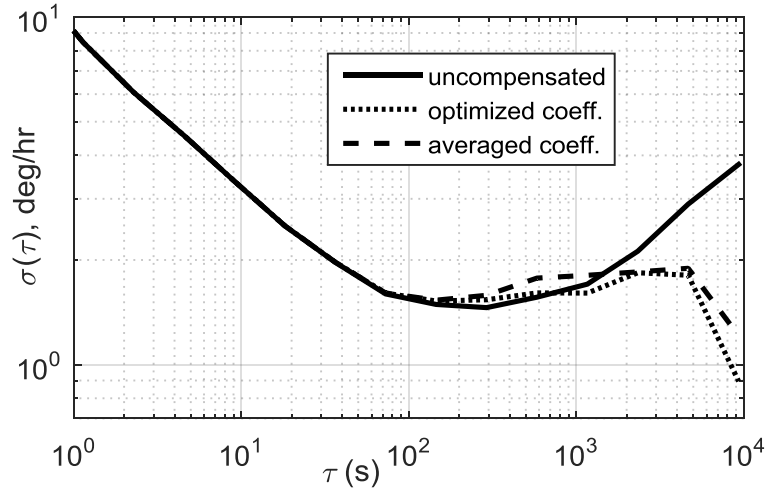


Figure 5.42: Allan deviation for uncompensated ZRO and compensated ZRO for test #2.

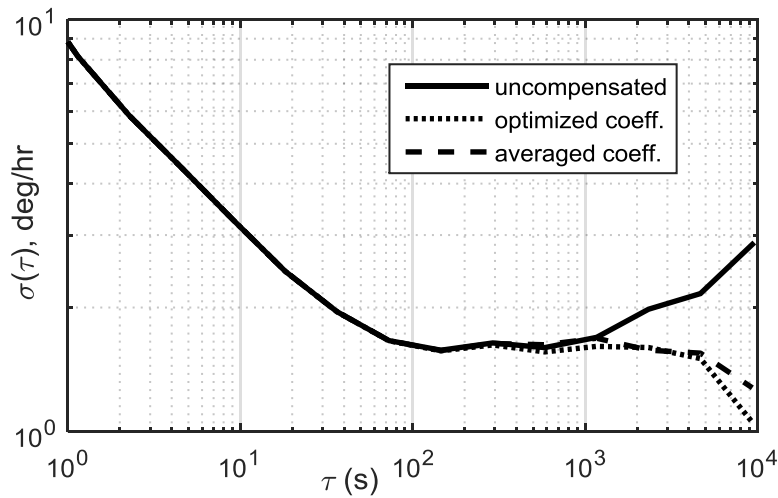


Figure 5.43: Allan deviation for uncompensated ZRO and compensated ZRO for test #3.

The raw ZRO (the starting point of the tests in Figure 5.41 through Figure 5.43) vs. stress sensor outputs was also analyzed. Figure 5.44 presents the uncompensated and compensated raw ZRO for the three tests. The Allan deviation tests were started with 24 hour intervals in between, so plotting the raw ZRO indicates a long term stability of the gyroscope on the order of days. The average compensation coefficients in Table 5.1 are used for the compensation. A five times improvement is obtained in the long term stability of the ZRO compared to the uncompensated ZRO.

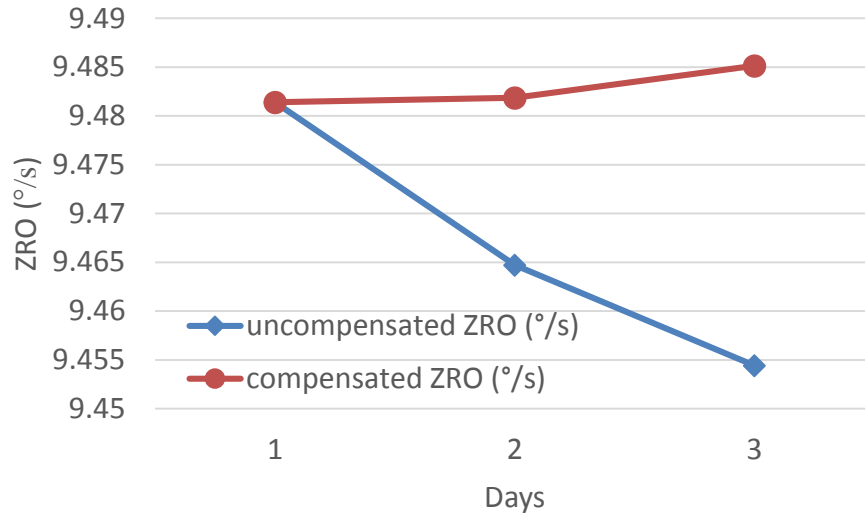


Figure 5.44: Uncompensated and compensated raw ZRO for the three Allan deviation tests in Figure 5.41 through Figure 5.43. The average compensation coefficients in Table 5.1 is used.

5.7 Discussion on Die Bonding and Stress Sensors

The presented test results in section 5.6 shows that one of the stress sensors (S_3) is sensitive to stress, however S_1 and S_2 exhibit almost no sensitivity to applied stress. This brings up the question of whether S_1 and S_2 are functional sensors or there isn't much stress in S_1 and S_2 region. An experiment was conducted to investigate this issue in which the stress and temperature changed together, and Figure 5.45 presents the environmental sensor outputs. After the temperature is settled on the gyroscope in Figure 5.33 without any external stress, the copper weight is added on top. Since the thermal mass increased, temperature initially went down by almost 2 K and then settled back to its original value due to temperature control. S_3 shows a stress sensitivity; however, S_1 and S_2 follow the temperature. Changing the temperature leads to an inevitable stress change due to the TCE difference. The ceramic package has a higher TCE, so once the temperature is reduced, there will be compressive stress that should lead to an increase in the stress sensor outputs according to the Wheatstone bridge configuration in Figure 5.18. The temperature increase should lead to a decrease in the stress sensor outputs. But an opposite trend in S_1 and S_2 is observed.

Positive and negative sides of the Wheatstone bridge were recorded to understand the stress sensor characteristics; the two terminals yielded similar results to measuring the direct output of the bridge.

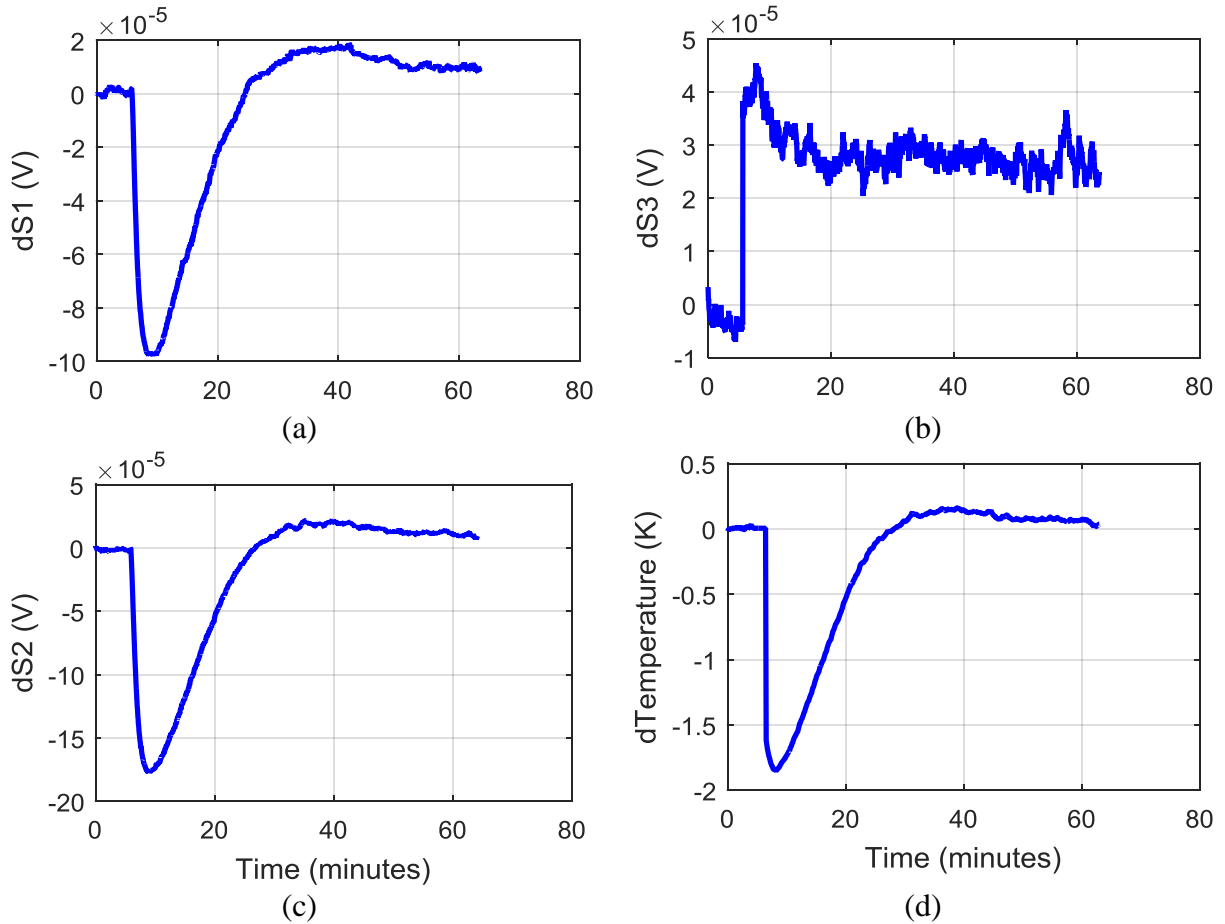


Figure 5.45: Response of the environmental sensors when copper weight is added on top the gyroscope in Figure 5.33.

Another gyroscope was tested in order to have more data on the stress sensor response. The tested gyroscope is not vacuum packaged; the environmental sensor outputs were recorded at atmospheric pressure. Figure 5.46 shows the environmental sensor outputs at constant temperature when the copper weight is moved from left to right and vice versa using the testbed in Figure 5.33. A clear and similar response can be seen on S_2 and S_3 outputs, S_1 does not respond to stress. Figure 5.47 presents the environmental stress outputs in response to a 4.5 K temperature change.

They change negatively with temperature as expected, S_2 and S_3 responses are similar with almost four times the S_1 response. The nature of the stress sensor outputs depends on the specific samples, and die mount plays an important role in this lack of replicability.

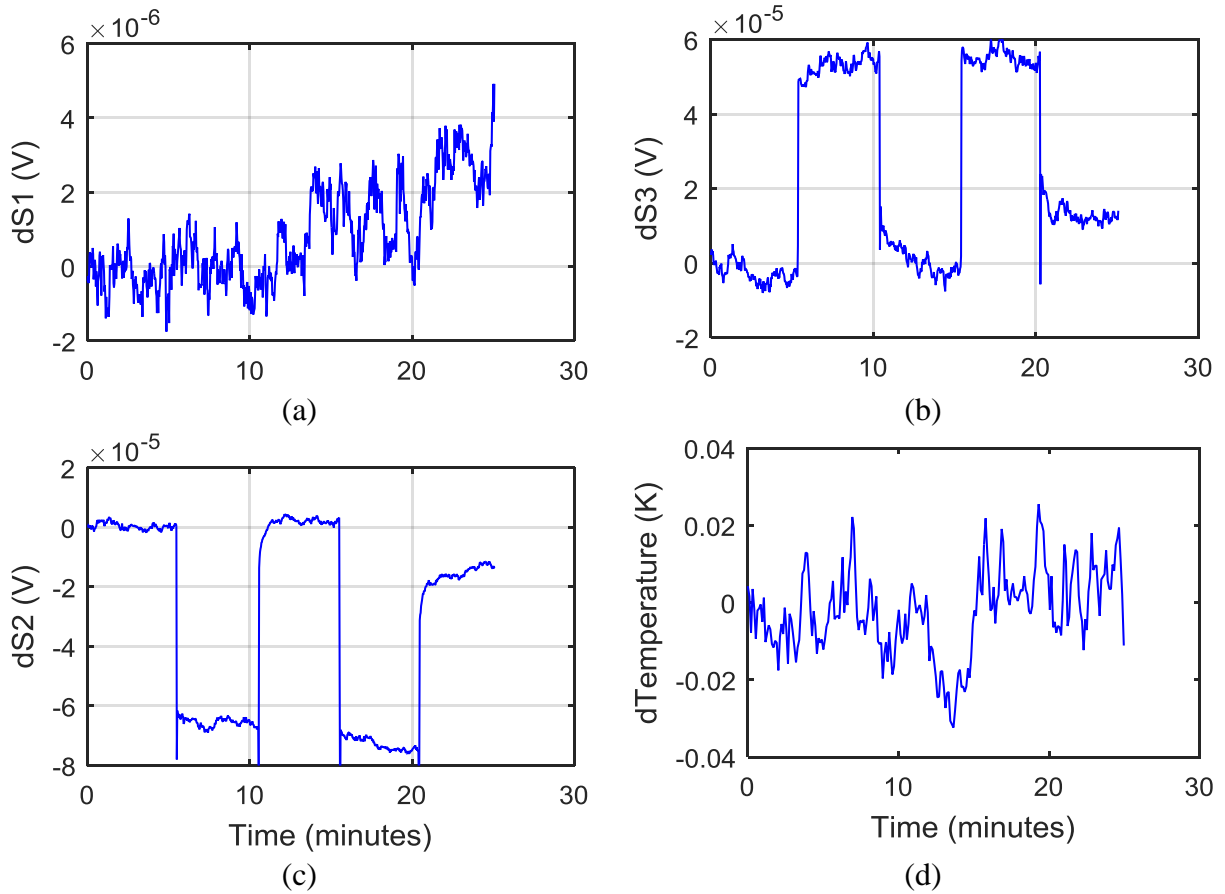


Figure 5.46: Environmental sensor outputs of a different gyroscope at fixed temperature when the copper weight is moved from left to right and vice versa.

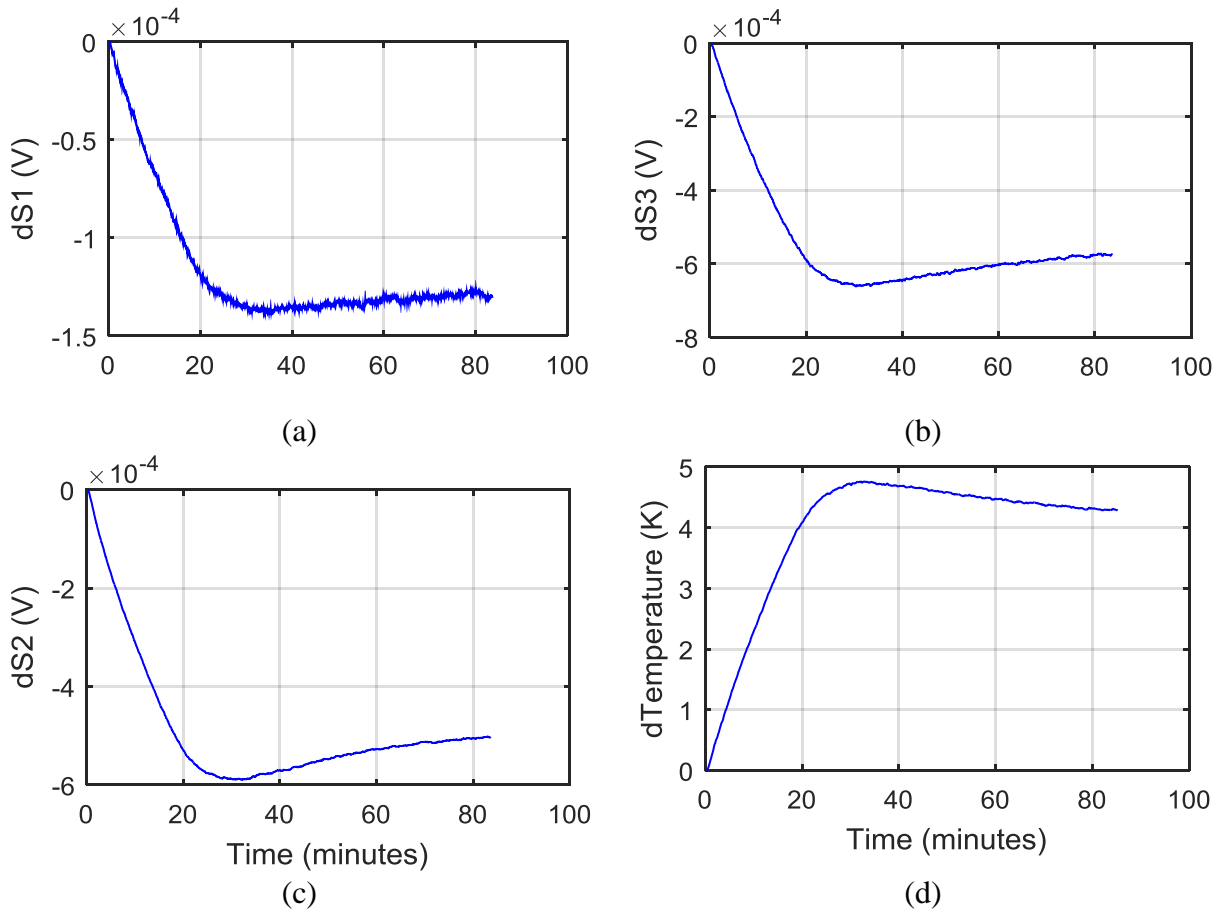


Figure 5.47: Environmental sensor outputs of a different gyroscope in response to a temperature change.



Figure 5.48: Backside view of the gyroscope after it is demounted from the DIP40.

We demounted the tested gyroscope from the package by heating it up to the tin melting temperature. Figure 5.48 presents the backside view. As seen from the solder wetting on the backside gold, the die mount is not uniform and is only from one side. This non-uniform die bonding may lead to the different stress sensor responses that are observed.

Different die bonding experiments on multiple samples were carried out. Figure 5.49.a shows the manual nanofoil activation that has been done in all of the samples. In this technique, nanofoil is activated by shorting two wires using the setup in Figure 3.4. Since the nanofoil is activated only from one side, it may lead to bonding on one side of the chip as in Figure 5.48. So as a different alternative, the nanofoil is wirebonded from the four corners and activation was achieved by applying the voltage and ground diagonally as shown in Figure 5.49.b; the same setup in Figure 3.4 was used. The nanofoil activates, but all the wirebonds break since they cannot handle the amount of the activation current. Figure 5.50 shows the backsides of the multiple chips that were activated manually and by using wirebonds. The samples with the wirebonded activation shows less die bonding compared to the manually activated samples. The manual activation results in a variety of bonding areas, from 15% to 20% to almost full bonding. The low bonding area in the wirebonded activation is believed to be due to the fact that wirebonds cannot handle the activation current. This may lead to an activation that is not predictable. A good die bonding can be obtained with nanofoil and manual activation. There are two reasons that can be listed for the samples with less die attachment area for the manual activation. The first and more likely reason is the flatness of the die mount tool and of the bottom piece in the die mounting set up in Figure 3.4. If the top and bottom pieces are not parallel, this may lead to uneven pressure distribution on the nanofoil. The second reason is the cleanliness of the gold on the bottom of the chips. Some of the chips are stored in gelpaks, and the gel may leave residues preventing the successful die bonding. Unfortunately, the initial location of the chips was not recorded, so the particular chips in the tests that come from the gelpak are not known.

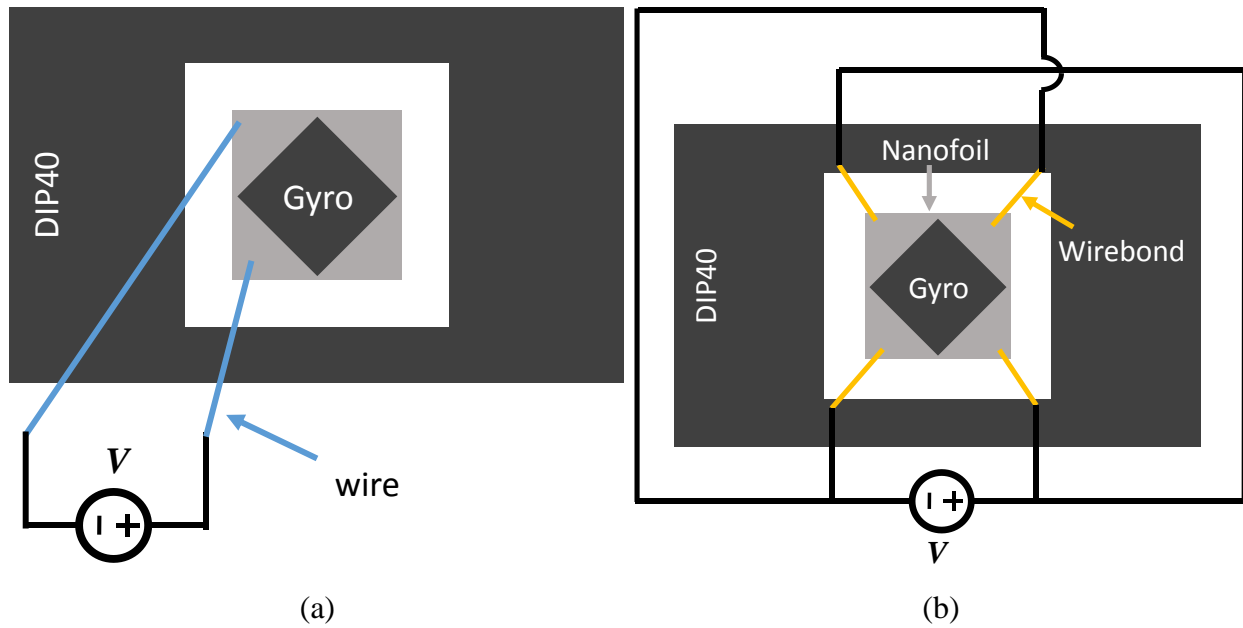


Figure 5.49: (a) Manual nanofoil activation from one side, and (b) balanced nanofoil activation from corners using wirebonding.

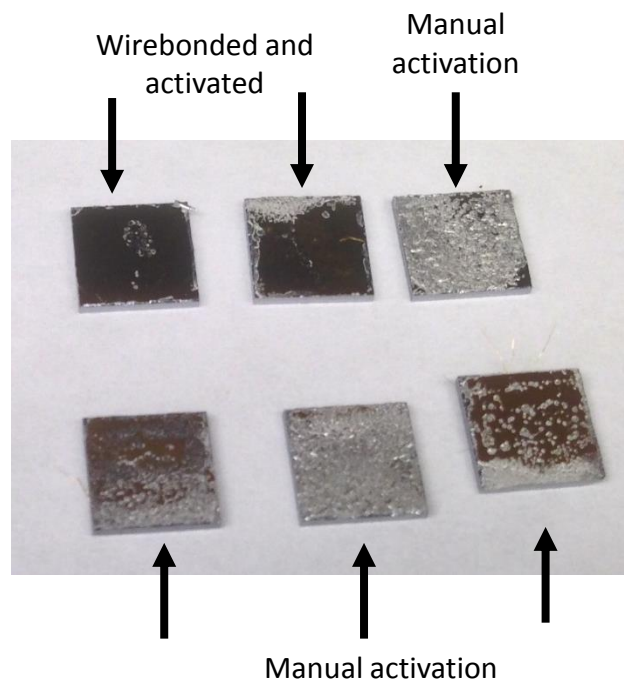


Figure 5.50: Backside images of the manual activated and wirebond activated samples.

The nominal resistance of the released resistors in the stress sensors are $1.7 \text{ k}\Omega$ and they are biased from a 5 V power supply. So 1.5 mA current flows through each branch of the Wheatstone bridge. Since the gyroscope is vacuum packaged, the heating of these released resistors is different due to

their design. Figure 5.51 shows the simulated temperature distribution of the stress sensors in vacuum for a 5 V power supply, and Figure 5.52 presents a zoomed view of Figure 5.51 to show the temperature difference between the two types of resistors. The stress and temperature sensitive resistor (R_{stress}) is anchored from each end; however, the temperature sensitive resistor (R_{nostress}) is anchored through tethers. This makes their thermal response different, and this leads to an almost 10 K temperature difference in between the resistors in vacuum for the 5 V supply, as shown in Figure 5.52. The temperature difference leads to an offset at the stress sensor outputs. The power dissipated in the resistances is proportional to V_{DD}^2 , which is directly proportional to the temperature difference between R_{stress} and R_{nostress} , and the sensitivity of the stress sensors is proportional to V_{DD} . So the offset at the stress sensor outputs is expected to depend on V_{DD}^3 . Every 1 K temperature difference creates 12.5 mV offset at the stress sensor outputs, and the average measured stress sensor offset changes between 80 to 110 mV, which is consistent with the simulated temperature difference. One way of reducing the offset is decreasing the power supply voltage at the expense of reduced sensitivity.

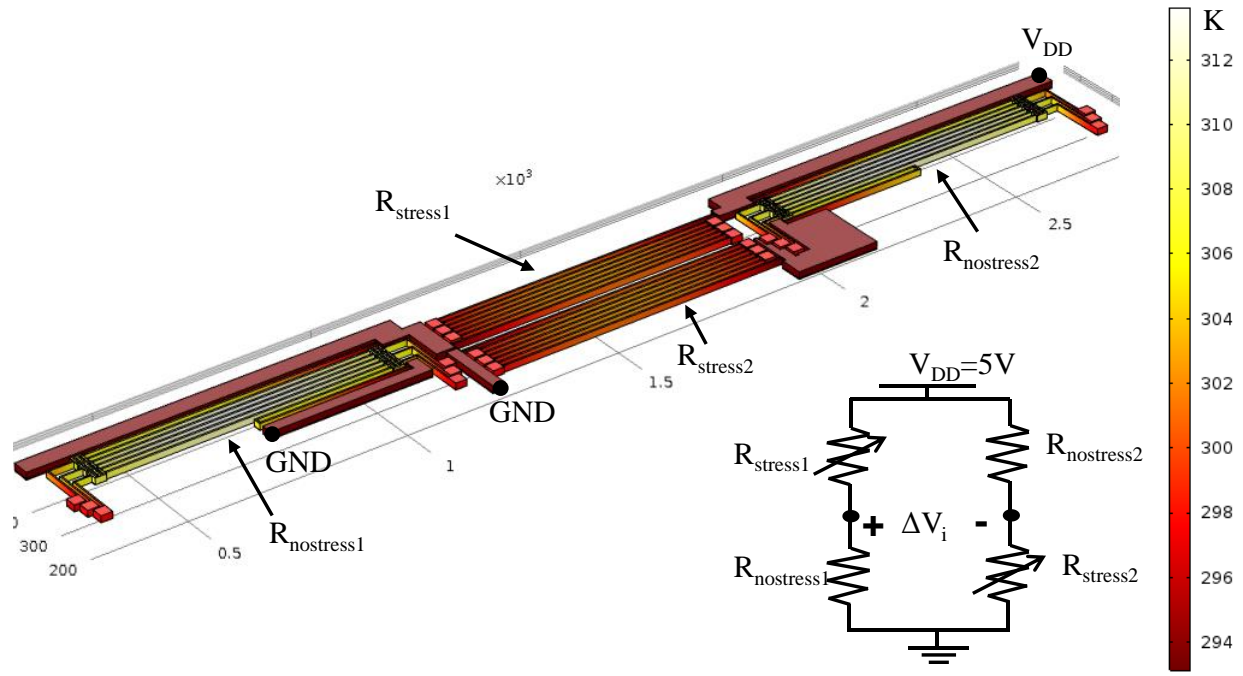


Figure 5.51: The simulated temperature distribution of the stress sensors in vacuum for 5 V V_{DD} .

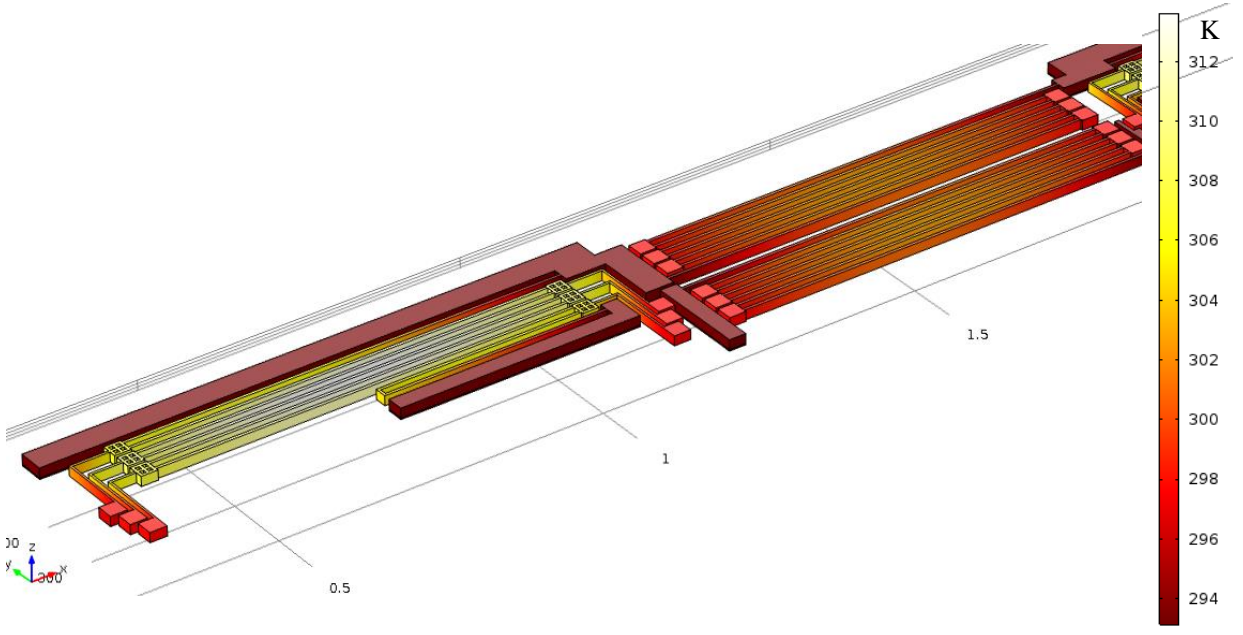


Figure 5.52: Zoomed view of Figure 5.51 to show the temperature difference between $R_{nostress}$ and R_{stress} .

5.8 Summary

This chapter provided the core experimental data on the environmental stress and temperature effects on the gyroscope performance, and showed that the long term gyroscope drift can be significantly suppressed with the stress compensation. The measured temperature induced stress effects on gyroscope frequencies were elucidated and compared with the simulations. The gyroscope resonance frequency changes due to the -60 ppm/K temperature dependence of Young's modulus and anchor displacements. Due to the long rectangle shape of the DIP40, packaging stress is concentrated on the short edge during curing of the die mount epoxy. Mounting the MEMS die 45° with respect to the package distributes the packaging stress equally on the two modes of the gyroscope. The stress effects on the gyroscope resonance frequencies were measured using three-point and four-point bending stress testbeds. Longitudinal anchor displacements lead to a decrease in the resonance frequencies since the inner and outer beams see opposite stress in the folded flexure, however transverse anchor displacements lead to an increase in the resonance frequencies since both the inner and outer beams see tensile stress.

Very long-term gyroscope drift can be suppressed up to seven times with on-chip stress compensation in a mode-matched closed-loop ovenized gyroscope, as demonstrated by experiment. On-chip stress sensors comprise stress and temperature sensitive fixed-fixed beams and temperature sensitive folded flexures connected in a Wheatstone bridge configuration to cancel the temperature effects. The uncompensated gyroscope exhibits long-term drift even though the gyroscope is oven controlled at 27°C with temperature stability of better than 0.04°C . Using only temperature control does not completely eliminate the long-term drift since the temperature is already fixed. The inclusion of on-chip stress compensation provides significant improvement to long-term drift. Our test results, using a small number of released SOI resistors

in a Wheatstone bridge as on-chip stress sensors, demonstrate that on-chip stress sensing — with even very limited measurement capability and degrees of freedom — provides up to seven times improvement in long term drift. Averaged stress compensation coefficients through a linear least squares fitting algorithm result in successful ZRO compensation, suggesting that the compensation approach will translate to practical use. Allan deviation results indicate that the compensated ZRO still exhibits an angle-random-walk slope even at 10,000 s (~3 hr) averaging time. These promising results suggest that on-chip stress measurement with greater degrees of freedom will provide an even more robust approach to compensate for residual long term instability.

Chapter 6 Conclusions and Future Work

6.1 Conclusions

As the MEMS gyroscope performance is improving continuously, the performance hit to a point where environmental stress and temperature changes play an important role on the gyroscope stability. The current trend in the literature is focusing on temperature compensation [6]-[9] or die mounting with minimal stress [15]-[18] to improve the long term stability. But there will always be an inevitable residual stress on the MEMS die due to the TCE mismatch between the MEMS die and the package in addition to the external stress that is not captured by temperature sensing. Constant temperature testing of one of the state -of-the-art gyroscopes in an oven still exhibits long term drift [24] showing that just temperature compensation is not sufficient to fully remove the long term drift. This thesis shows that long term gyroscope drift can be highly suppressed with on-chip stress compensation, for the first time to our knowledge.

In addition to stress, this thesis work developed tuning of the nonlinearities. High drive displacement improves the signal to noise ratio of a gyroscope but it comes with hardening or softening nonlinearities in the amplitude-frequency relation. This work proposes tuning of the softening nonlinearity by introducing a dc voltage controlled hardening nonlinearity through cubically shaped comb fingers.

Simulation methodologies merging FEA and circuit simulation were developed to investigate the effects of temperature and stress on gyroscope resonance frequencies, ZRO and SF. The fundamental principle behind the simulations is obtaining the anchor displacements by using the accuracy of FEA. Anchor displacements are the key factor to understand the stress effects on the gyroscope since the interaction of the device with its environment is established through the

anchors. The detailed model of the package and MEMS gyroscope anchors (without the actual mechanical structure since its mechanical effect is negligible) is simulated in FEA with the stress sources first, and anchor displacements are obtained. The anchor displacements are used as the boundary conditions for the eigenfrequency simulations that give the stress-resonance frequency relation. The anchor displacements are also inserted into the mixed MEMS-electronics circuit simulation including the detailed electromechanical model of the gyroscope and front-end electronics. The NODAS MEMS behavioral models allow simulation of the whole gyroscope system and obtain ZRO and SF changes with stress. The simulations showed $3.2^\circ/\text{hr}$ ZRO shift per 10 nm gap mismatch. Including the drive feedthrough in the simulations led to quadrature feedthrough originated ZRO shift of $3^\circ/\text{s}$ for 1 MPa stress, compared to the $8^\circ/\text{hr}$ ZRO without feedthrough. This shows the importance of feedthrough minimization.

Closed-loop drive with amplitude and frequency control, and closed-loop sense with quadrature and rate control adapted from the IEEE standards [62] was employed during the gyroscope operation. The control loops are first simulated in SIMULINK for the PID controller parameter selection. The gyroscope is operated in matched mode without active frequency control, and a 20 Hz closed-loop sense bandwidth suppressed the uncharacterized drive and sense frequency mismatches. Different closed-loop mode matching techniques were explored, but best stability was obtained without the frequency control loops. The closed-loop matched mode operation suppresses the feedthrough effects since the motional current output of the gyroscope is maximized when the modes are matched. The gyroscope and front-end amplifiers are located on a PCB, and all the control loops are implemented in a digital lock-in amplifier. Noise analysis of the sense mode at matched mode revealed that the gyroscope is thermomechanical noise limited.

The gyroscope is in-house fabricated with the SOI-MEMS process and in-house vacuum packaged. The SOI-MEMS process consist of two masks; the first mask is the pad patterning and the second mask is for the DRIE of the structural layer. The main process contribution of this thesis is the optimization of the DRIE recipe by slowing down the etch rate to reduce the unwanted silicon shorts due to notching. The in-house developed vacuum packaging system uses metal lids with thin film Ti/Au getters attached to a ceramic DIP40. The gyroscope is mounted stress free into the DIP40 with Nanofilm. A specific vacuum chamber was developed for first heating only the metal lid for getter activation at high temperature (400°C), and then moving the package towards the lid, and achieving the vacuum seal with a low temperature Indium preform at 200°C. The vacuum packaging has been successfully applied to several devices with the highest vacuum of 50 mTorr.

Shaped combs were designed for tuning the frequency and nonlinearity of the gyroscope. Instead of having a fixed gap, the electrostatic gaps are changed as a function of finger engagement with a shaping function for the desired force displacement characteristics. As opposed to the parallel-plate capacitors, shaped combs do not have a theoretical displacement limitation and allow the design of three-fold symmetric gyroscopes with interchangeable drive and sense axes. The main tuning contribution of this thesis is the introduction of nonlinearity tuning fingers that implement cubic hardening force through their gap profile. Experimental validation was accomplished in tuning the softening nonlinearity with the use of the cubic hardening fingers. Allan deviation analysis on the open-loop gyroscope output shows that a 1.5 times improvement of the long-term gyroscope stability can be obtained with nonlinearity tuning compared to the untuned case. Although the drive displacement is fixed with a control loop in a gyroscope, small fluctuations around the set point lead to uncharacterized frequency mismatches due to the Amplitude-frequency ($A-f$) effect, and nonlinearity tuning highly suppresses this effect. In addition, quality factor (Q)

changes with the proof mass voltage (V_{PM}) changes were observed in the 1st and 2nd generation gyroscope designs. The amount of Q - V_{PM} change is directly proportional to the path length that the motional current flows on the proof mass, so the path of the motional current on the proof mass was minimized by designing differential fingers in the 3rd generation gyroscope design.

The environmental temperature and stress vs. gyroscope performance simulations were validated with experiments. Different test setups have been used. The first setup induces stress on the gyroscope using an on-chip silicon heater. The resonance frequencies shift due to the -60 ppm temperature dependence of Young's modulus and anchor displacements. Longitudinal anchor displacements lead to a decrease in the resonance frequencies since the inner and outer beams experience opposite stress in a folded beam. The orientation of the MEMS die with respect to the package cavity also affects the resonance frequencies; since the DIP40 is a long rectangle, the stress is concentrated on the short edge. Mounting the die 45° with respect to the package cavity distributes the stress equally on the two gyroscope modes.

Three-point and four-point bending testbeds were built to investigate the stress effects on gyroscope resonance frequencies. The applied stress in the bending testbed translates into anchor displacements modifying the spring constants, and the resonance frequencies shift. Longitudinal anchor displacements lead to a resonance frequency decrease since the inner and outer beams experience opposite stress in the folded flexures, however transverse anchor displacements lead to a resonance frequency increase since both the inner and outer beams experience tensile stress. The measured results are consistent with the simulations.

The on-chip stress sensors consist of temperature and stress sensitive released fixed-fixed beams, and temperature sensitive folded beams. Connecting these two resistors in a Wheatstone bridge cancels out the temperature effects. The on-chip stress sensors are located on the four sides of the

SOI-MEMS gyroscope and each one measures the principle stress along its direction. The gyroscope was ovenized at 27°C to focus purely on the stress effects. Allan deviation tests have been performed on the mode matched gyroscope with closed-loop drive and sense in the ovenized testbed with and without external stress. Although the temperature of the gyroscope is fixed, the gyroscope ZRO still exhibited a drift. The same trend was observed at the stress sensor outputs. The compensation coefficients were obtained by running a linear least square error fitting in between the ZRO and stress sensor output. The stress compensation significantly suppresses the long term drift resulting in $9^\circ/\text{hr}/\sqrt{\text{Hz}}$ angle random walk and $1^\circ/\text{hr}$ bias instability at 10,000 s (around 3 hr) averaging time in a test without external stress, which is a seven times improvement over the uncompensated gyroscope output. The repeated tests resulted in similar compensation coefficients showing the promise of stress compensation. Different stress sensitivities of ZRO were obtained, $-1.9^\circ/\text{hr}/\text{kPa}$ without external stress, $-9^\circ/\text{hr}/\text{kPa}$ and $17.6^\circ/\text{hr}/\text{kPa}$ sensitivity for the two different stress tests. The difference is believed to be due to the limited number of stress sensors on the die, only one stress sensor clearly responded to stress. The comb gap mismatches are responsible for the ZRO shift; it was experimentally verified that the resonance frequency mismatch of the drive and sense modes cannot lead to measured ZRO shifts.

The stress compensation was successfully demonstrated on the SOI-MEMS gyroscope with a limited number of stress sensors. Only one of the stress sensors responded to stress, and this is believed to be due to die bonding. Examining the bonding area of multiple dies showed a variation on the bonding area. Even with a single stress sensor, significant improvement was obtained on gyroscope drift, so by adding more stress sensors an even better and more repeatable and general compensation is expected to be obtained.

Table 6.1 shows a comparison of the state-of-the-art commercial and research gyroscopes with the gyroscope studied in this work. The Invensense ICM-30630 is a gyroscope for the smart phone and consumer market, and is included in the table for comparison. Bias instability data is not provided in the datasheet. A figure of merit is introduced to compare the performances of the gyroscopes:

$$FOM = \frac{\sqrt{\frac{ARW \times bias}{\sqrt{\tau}}}}{\sqrt{die_area}} \quad 6.1$$

where ARW is angle random walk and τ is the integration time for the bias instability point. Since ARW sets the starting point for the bias instability, ARW and bias instability are correlated. The square root of their product takes into account that correlation. Dividing the bias instability ARW product by the square root of the integration time sets the unit to $^{\circ}/hr$ in the numerator. The unit for the FOM is $^{\circ}/hr/m$. According to 6.1, the smaller the FOM, the higher performance the gyroscope has when normalized to the size of the device area (i.e., roughly proportional to the proof mass). But the layout area is not specified for some of the gyroscopes in Table 6.1. Only the numerator of 6.1 is used as FOM for that reason in Table 6.1.

All of the gyroscopes except the gyroscope in this work exhibit long term drift, indicated by the rate random walk in Table 6.1. This feature is a strong motivation for the stress compensation. The ARW of the gyroscope in this thesis is small compared to the other research gyroscopes because it is in some cases smaller in size and it uses comb fingers to sense the output current and they generate less output current compared to the parallel plate capacitors. However, the gyroscope in this thesis has the best long term stability, and provides a comparable FOM to the state of the art thanks to the stress compensation. The FOM with the die area included will be

even better for our gyroscope since the reported mechanical device areas for Silicon Sensing and HRL gyroscope are significantly bigger.

Table 6.1: Comparison of the state of the art commercial and research gyroscopes with the gyroscope studied in this work.

Gyroscope	ARW (°/hr/√Hz)	Bias Inst. (°/hr)	τ for the bias inst. (s)	Rate Random Walk (Yes/No)	Mech. Device Area	FOM (°/hr)
Sensoror STIM210 [8]	9	0.5	1500	Yes	-	2.64
Analog Devices ADIS1636 [9]	10	4	1000	Yes	-	8.71
Silicon Sensing CRS09-02 [99]	2	0.5	300	Yes	6mm diameter	1.86
Honeywell [24]	0.18	0.02	1080	Yes	-	0.08
HRL DRG [101]	0.2	0.03	500	Yes	8mm diameter	0.13
Invensense ICM- 30630 [100]	57.6	-	-	Yes	-	-
This work	9	1.1	10000	No	2.6mmx 2.6mm	2.44

Temperature is the major drift source for the MEMS gyroscopes, however the studies in the literature show that it does not completely solve the long term drift problem. In this work, stress compensation is shown to have the potential to suppress the long-term stability significantly. The current performance is limited by the thermomechanical noise of the gyroscope, and can be improved by either improving the vacuum packaging system or increasing the mass of the device with a thicker SOI-device layer, or with a larger device.

6.2 Future Work

The suggested future work consists of short term and long term parts. The short term part includes the design modifications on the current system to improve the performance. The stress sensors were designed as 640 μm long silicon resistors with a target nominal resistance of 1 $\text{k}\Omega$ assuming the resistivity of SOI device layer is 0.001 $\Omega\text{-cm}$ to 0.005 $\Omega\text{-cm}$. The resistances turned out to be 1.7 $\text{k}\Omega$. The resistivity of the SOI wafers can be measured before the design and potentially shorter resistances can be designed that would be more tolerant to stiction.

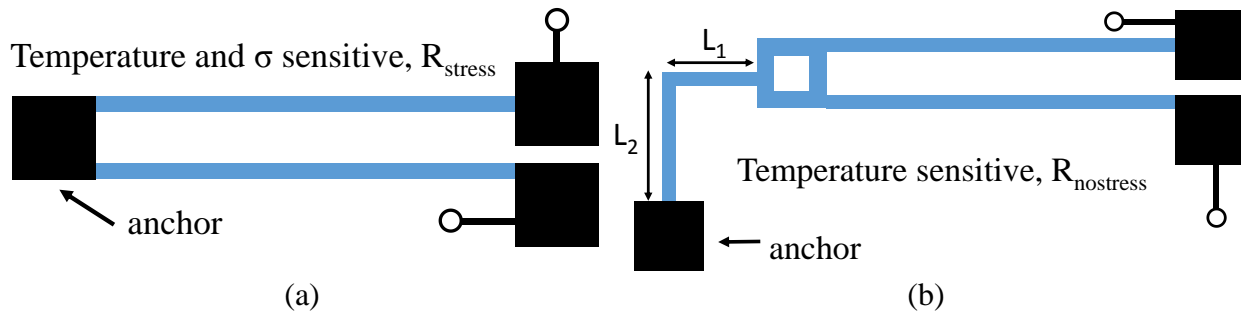


Figure 6.1: The current design for R_{stress} (a) and R_{nostress} (a).

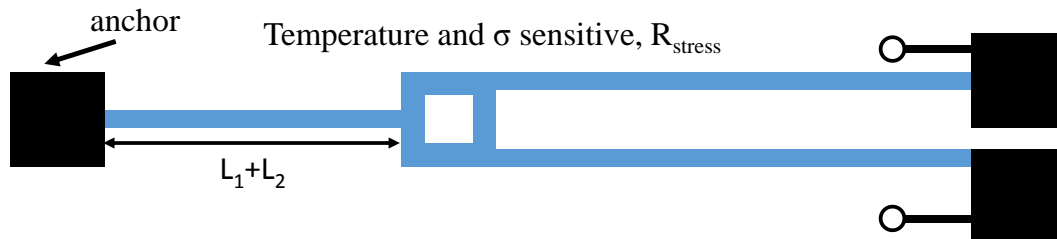


Figure 6.2: The proposed design for R_{stress} for thermal matching to R_{nostress} .

Since the thermal characteristics of the stress and temperature sensitive and temperature sensitive resistors are different in the current design, they heat differently in vacuum and a power supply dependent offset is observed at the output. Figure 6.1 shows the current design for the temperature and stress sensitive resistor R_{stress} , and temperature sensitive resistor R_{nostress} . A proposed future modification to the design keeps R_{nostress} resistor the same and designs the R_{stress} resistor as shown in Figure 6.2. A straight beam is used in R_{stress} instead of a crab-leg beam in R_{nostress} so that R_{stress}

and R_{nostress} are equivalent in terms of thermal path, however R_{stress} is much more rigid in the longitudinal direction. The total length of the crab leg beam is equal to the length of the straight beam in R_{stress} . This design update also improves the matching of their nominal resistances. Since the two resistors will be thermally matched, their response time to environmental temperature changes will be identical providing a further enhancement on the compensation.

The current compensation algorithm is open loop, i.e., the coefficients are obtained and then compensation is performed. As a closed-loop stress compensation approach, actuators can be placed on the proof mass that servo on the environmental sensor outputs and try to null the stress by counter reaction.

The nanofoil die attachment process needs to be optimized in order to have repeatable more than 90% die bonding area. The first item to check is the flatness of the vacuum tool that holds the chip in place and applies the bonding pressure, and the flatness of the bottom aluminum block that supports the DIP40 during nanofoil bonding. The effect of gelpak on the cleanliness of the backside gold should also be investigated. Increasing the pressure during die bonding can also be investigated as an alternative. An oxygen plasma cleaning on the backside of the dies before the bonding may also improve the bonding. The gyroscopes can be loaded into the oxygen plasma upside down on a clean polished silicon wafer.

The die mounting and packaging stress can be characterized using stress sensors. One can have an array of stress sensors on a standard SOI die (without the gyroscope) and take stress measurements on a probe station before the die mounting. These measurements can then be repeated after the die mounting and different die adhesives (nanofoil/solder preform) and different die attachment areas can be evaluated. This kind of research would be an important contribution to the literature since stress on the device is a direct function of the die mount.

Further characterization of the vacuum packaging system would be useful. Although the vacuum sealing is performed less than 1 μ Torr pressure, the estimated pressure inside the cavity is around 50 mTorr. A quality factor of 50,000 was obtained for the main gyroscope sample, corresponding to around 20 mTorr pressure during the final runs with a 1.5 μ m thick getter (this is a second generation getter, the results reported in Section 3 are with a 1 μ m thick getter). This points out that lower pressures can be obtained with further research on outgassing and gettering. The first recommended experiment is doing a vacuum packaging without getter. This would give information on the quality of the in-house sputtered Ti/Au getter. A sample can be mounted using a solder preform that is known not to outgas and that would give information on the outgassing characteristics of the nanofoil. In addition, samples can be outgassed at higher temperatures ($> 150^{\circ}\text{C}$) to observe the effect on final package pressure.

The combination of nonlinearity compensation and stress compensation could not be done because of the sample failure. Combining the two compensations at closed-loop matched mode operation would improve the angle random walk and bias instability at the same time. If closed-loop control is needed on the nonlinearity tuning, the vibration amplitude can be slightly perturbed and the resonance frequency can be checked. The controller looks for a cubic nonlinearity tuning potential where the resonance frequency does not change with the oscillation amplitude.

This study showed the importance of stress compensation with limited number of stress sensors. In the ideal case, a stress sensor under each anchor is needed to fully compensate the stress. An integrated CMOS-MEMS gyroscope in the long term can validate this hypothesis. Small stress and temperature sensors can be designed in CMOS that can enable multiple stress sensors in a small area. Each stress sensor occupies 3 mm by 0.5 mm area in the SOI-MEMS technology and this cannot be shrunk by an order of magnitude due to the pads and nominal resistance

requirements. CMOS-MEMS gyroscopes have been designed, but unfortunately the environmental sensors did not work. Special attention should be paid to the design of the CMOS stress sensors as they are as important as the gyroscope. On the other hand, CMOS-MEMS might have different problems due to its inherent dielectric metal cross section such as charging [102].

As further steps to improve the drift performance, future studies may focus on adsorption of the gases inside the vacuum cavity, which affects the mass, or on dielectric charging on the oxide interface, or on aging of material properties.

Appendices

A. Details of the SOI-MEMS Process

SOI-MEMS Process

Purpose	Process Detail	Time
Cleaning	SOI wafers come with both sides polished so it might be difficult to understand which side is the device side. Once the wafer manufacturers thin the device side to the desired thickness and do CMP, a step on the edge of the wafer is formed. So the side that you can see the step height on the wafer edge is the device layer of the SOI wafer. Place the SOI wafer into 4" cassette of the wafer washer and squeeze acetone and IPA	
	Wash the wafer in the wafer washer	1 cycle
Removing surface oxide	Immerse the wafer in the cleanroom BHF Check the hydrophobicity to verify that the oxide is removed	2 min.
	Wash the wafer with DI and dry, prepare the sputtering chamber before BHF, transfer the wafer as fast as you can. The goal is minimizing the surface oxidation.	
Cr/Au sputtering in Perkin Elmer 6J (5nm/400nm)	Cr and Ti targets are switched, so talk to the cleanroom staff about the Cr target. Wait till the high vacuum is reached (< 1 μ Torr)	
	Sputter at 5 mTorr pressure, 25 sccm flow	
	Presputter Cr at 100 W to clean the oxide on Cr source	10 min
	Sputter Cr at 50 W (~5 nm)	45s
	Presputter Au at 50 W	1 min
	Sputter Au at 50 W (~100 nm)	2 min
	Wait for cool down	3 min
	Presputter Au at 50 W	30s
	Sputter Au at 50 W	2 min
	Repeat this presputtering sputtering cycle Au for a total of 4 times, the target is 8 mins total Au sputtering	

Photolithography for pad metallization	Deposit HMDS in the HMDS oven with recipe #2, 2 min HMDS vapor	
	Spin AZ4210, 6 s @ 600 rpm, 30 s @ 4000 rpm	
	Soft bake at 95°C	2 min
	Use the pad mask and expose in MA6 with vacuum contact, check the contact pressure should be larger than 0.6 bar, at 5 mW/cm ² power	70 s
	Develop in 1:3 AZ 400K developer, keep developing until all the field is clear. Have two beakers one for developer one for DI, finally wash the wafer with DI gun.	1.2-1.5 min
	Wash the wafer in wafer washer	1 cycle
	Oxygen plasma in IPC Barrel Etcher for descum at 100 W, clean the residual PR from development	2 min
Hard bake to harden PR mask	In one of the ovens at 110°C, resist should be sloped, time specified includes the warm up	30 min
Au/Cr wet etch	Au wet etch, etchant provided by the cleanroom, check etch rate on the bottle. First etch for 150 s rinse dry and check.	180-190 s
	Rinse with DI, dry (wafer washer can be used), verify the yellow Au color is gone	
	Cr wet etch, etchant provided by the cleanroom, check etch rate on the bottle, total etch time < 30 s. Watch for the Cr color to disappear during etching.	25s
	Rinse with DI, dry (wafer washer can be used), verify the Cr is gone	
	Au etch in case Au has diffused into Cr	15 s
	Rinse with DI, dry, and load the wafer into wafer washer for final cleaning	
	Over-etching 10-20% is useful because any metal residue on the surface acts as a mask in the DRIE step and leads to grassing	
Piranha cleaning	1:1 H ₂ SO ₄ :H ₂ O ₂ (400 mL : 400 mL), in one of the 800 mL-1 L beakers. Add H ₂ O ₂ last. Use one of the 4" wafer holders, and immerse the wafer into piranha device side looking down so that any particle lands on the bottom. PR stripper in cleanroom is generally very dirty and does not remove hardbaked and metal etchant seen PR well.	20 min

	Piranha and HF attacks Ti so if Ti is used for adhesion piranha and more importantly HF cannot be used.	
	Wash the wafer with DI gun and use wafer washer again. Check the PR is gone and there are no metal residues. Wait for the Piranha to cool before disposing into the sink. Consult to cleanroom stuff about disposal in case Piranha disposal procedure has changed.	
	If the PR is not gone do not use ultrasonic power as it generally peels the Au metallization from the Cr undercut regions and may cause metal particle problem across the wafer.	
Photolithography for structural layer	Deposit HMDS in the HMDS oven with recipe #2, 2 min HMDS vapor	
	Spin AZ4210, 6 s @ 600 rpm, 30 s @ 4000 rpm	
	Soft bake at 95 °C	2 min
	Use the structure mask and expose in MA6 with vacuum contact, check the contact pressure should be larger than 0.6 bar, at 5 mW/cm ² power. Alignment to the pad mask is required align to the plus signs on the pad mask. Exposure time is very sensitive optimize on dummy wafers first.	39 s
	Develop in 1:3 AZ 400K developer, keep developing until all the dissolved red PR cloud is clear. Have two beakers one for developer one for DI, finally wash the wafer with DI gun.	0.8-0.9 min
	Extensively observe the sample under optical microscope, look at center and edges and take measurements. Because there are pads (0.4 μm thick) on the wafer the mask does not touch the wafer surface completely that leads to scattering of UV light. So the gaps would be 0.3-0.5 μm wider.	
	Wash the wafer in the wafer washer once you verify that the development is complete.	1 cycle
Structural layer Si DRIE	Talk to cleanroom staff to turn on the gases for DRIE. Also tell them to change the platen temperature to 15°C because normally platen is kept at 19°C. The recipe is under folder “dylan”. The recipe is : Etch: time: 12 s; pressure: manual 58%, 21 mTorr; gas: 130 sccm SF ₆ , 13 sccm O ₂ , power: 600 W coil, 12 W platen both at 13.56 MHz	40 cycles, 14min 40s

	<p>Passivation: time: 10 s; pressure: manual 58%, 12 mTorr; gas: 85 sccm C₄F₈, power: 600 W coil, 0 W platen both at 13.56 MHz</p> <p>40 cycles, 14 min 40 s (may change slightly)</p> <p>Inspect the wafer, there is not a clear way of understanding the etch frontline but make sure everything looks the same from the center to the edge.</p>	
	<p>Oxygen plasma in the DRIE, the purpose is removing most of the PR and DRIE polymer. Exposing gold to DRIE chamber is not allowed, so make sure there is still PR after the oxygen plasma. Use recipe “polyrem” or “rempoly” whichever does not have the platen power. We want to have an isotropic etch.</p>	2 min
Piranha Cleaning	<p>1:1 H₂SO₄:H₂O₂ (400 mL : 400 mL), in one of the 800 mL-1 L beakers. Add H₂O₂ last. Use one of the 4” wafer holders, and immerse the wafer into piranha device side looking down so that any particle lands on the bottom. Repeat piranha with fresh chemicals 2 times until the wafer is clean.</p>	2x20min
	<p>Wash the wafer with DI gun and use wafer washer again. Check the PR is gone and there are no metal residues. Wait for the Piranha to cool before disposing into the sink. Consult to cleanroom stuff about disposal in case Piranha disposal procedure has changed.</p>	
	<p>If the wafer is not clean repeat piranha do not use ultrasonic power since it destroys the fragile mechanical structures.</p>	
Removing surface oxide and Sputtering Cr/Au	<p>Repeat the removing surface oxide and Cr/Au sputtering steps on the backside of the wafer. This Cr/Au metallization will be used to solder the MEMS die to the ceramic DIP. Wafer holders of e-beam evaporator can be used to load the SOI wafer while loading the SOI wafer upside down into sputtering chamber.</p>	
Dicing Protection	<p>Cover the surface of the wafer with a high viscosity PR (AZ4610). No HMDS required. Spin it at 600 rpm for 30 s to make it even. Get a hot plate and increase the temperature with 80°C/hr to 60°C in half an hour and bake it at 60°C for half an hour. The purpose is not fully baking the resist just to make it hard enough to stay on the wafer surface. If you bake it too much it is more difficult to later remove it.</p>	
Dicing	<p>Ask the cleanroom to dice the wafer into 5 mm by 5 mm pieces. The wafer already has the dicing lanes with metallization.</p>	

Die Release Process

PR cleaning	<p>Use 3 baths of acetone and 2 baths of IPA</p> <p>Load the selected dies into the chip basket and always keep them in the chip basket, it is easier for processing and safer for the chips.</p> <p>The first bath of acetone is very short (30-40 s), the purpose is leaving the particles in the first bath. Immediately move the basket to the 2nd acetone bath and keep it there for 5 minutes. Move the basket to the 3rd acetone bath and keep it there for 5 additional minutes to clean the PR.</p> <p>Next 2 baths of IPA with a total period of 5 minutes. 2 baths of DI water bath 5 minutes each.</p>	
Piranha cleaning	<p>1:1 H₂SO₄:H₂O₂ (200 mL : 200 mL), in one of the 600mL beakers. Add H₂O₂ last. Very gently immerse the basket into the solution. Do not immerse more than 10 dies at once, leave enough clearance between the dies. The dies inevitably go on top of each other, a Teflon fixture can be designed to prevent this. Piranha can be repeated depending on the cleanliness of the dies.</p>	20 min
	3 baths of DI water	3x5min
	<p>Inspect random dies after drying and make sure they are clean. The dies don't need to be fully dry for BHF release, but should be mostly dry.</p>	
BHF release	<p>Immerse the basket (the basket should be teflon) into the BHF provided by cleanroom and every 10 minutes give it a little agitation by slowly turning or shaking it. The etch rate of the BHF is 1µm/10min.</p>	45-50 min
	<p style="text-align: center;">3 baths of DI water</p> <p>From now on the devices are released so they should not be removed from the liquid.</p>	3x5min
Critical point drying	3 baths of IPA, the goal is removing all the DI water.	3x7min
	<p>Check the weights of the fill and cool CO₂ tanks before starting the process, if they are low notify the cleanroom staff for the tank change.</p> <p>Clean critical point dryer (CPD) with IPA. Use the 4" CPD basket put one of the 4" O-rings under the wafer. Use one of the Teflon rings to fill the chamber, and fill the chamber with IPA. Set the purge timer to 5 (25 minutes). Move the chip basket from IPA beaker to the IPA filled CPD chamber</p>	

	and quickly transfer the dies. Tighten the nuts according to the CPD manual, and follow the manual.	
--	---	--

B. Details of Vacuum Packaging

Getter Deposition Process

The first process in the vacuum packaging is the preparation of metal lids with getters. Ti/Au getter material is sputtered on the metal lids using an aluminum shadow mask as shown in Figure 3.6. We will provide the details of the getter deposition process and pre-cleaning in the table below.

	The lids come with Au/Sn eutectic solder attached to them since it requires 300 to 320°C melting temperature they are not compatible with our process. Unfortunately, Spectrum Semiconductor, the company I purchased the lids, does not sell metal lids without solder. Au/Sn solder is tack welded to the lid. Gently remove Au/Sn solder with sharp tweezers, complete removal is not possible some solder remains at the tack weld points but it is okay. This process requires wearing gloves to keep the lids clean for soldering.	
	We will deposit the getter on the other side of the lid where Au/Sn solder has never touched. We will call that side as the clean side, and Au/Sn solder side as the back side. So from now on make sure the clean side always looks up.	
Organic cleaning	Up to 25 lids can be processed at once, 25 is the limit of the shadow mask. Fill IPA in a petri dish, and first squeeze IPA on the lids and put them in IPA bath one by one.	5 min
	Get a hot plate and set it to 70°C, remove the lids from IPA first put them on a wiper to remove the IPA on the back side and transfer them to hot plate while clean side is facing up. This process dries the IPA, if you immerse the lids into DI water each of them should be dried with nitrogen gun, which is difficult and time consuming. This technique also keeps the lids cleaner since they are not touched that much.	
	Load the lids into a petri dish and do a 200 W oxygen plasma cleaning in IPC Barrel Etcher. In 300 W the sample heats too quick and the concern is you burn the organic residues before chemically removing them.	5 min

Sputtering Ti/Au in Perkin Elmer 6J (1.5 $\mu\text{m}/30\text{ nm}$)	Place the lids into the shadow mask with the clean side facing up and tighten the bolts evenly. The shadow mask has recesses for the lids so that alignment is easy.	
	We will deposit 1 to 1.5 μm titanium. Depending on the data in the log sheet, the deposition rate for titanium varies between 4.3 nm/min to 6.66 nm/min for 50W power, 5 mTorr pressure and 25 sccm argon flow. So we assume 5.5 nm/min, for 1 μm titanium 181 minutes of sputtering is needed. To increase the deposition rate we increased the power to 75 W which will increase the deposition rate by 50%. Not to overheat the target we will sputter 30 minutes and wait for 15 minutes. We recommend booking the sputter for a day and pumping overnight for a high pressure (low, e.g. 10^{-7} Torrs). This high pressure also reduces the risk of getter saturation during deposition.	
	Cr and Ti targets are switched, so talk to the cleanroom staff about the Ti target. Load the samples one day before and pump overnight. Base pressure should be low e.g., 10^{-7} Torr. I did getter deposition at 1.2×10^{-6} Torr and it also turns out to be okay, but the lower the base pressure the better.	
	Sputter at 5 mTorr pressure, 25 sccm flow	
	Presputter Cr at 100 W to clean the oxide on Cr source	10 min
	Sputter Ti at 75 W power	30 min
	Wait for the target to cool down	15 min
	Presputter Cr at 100 W to clean the oxide on Cr source	5 min
	Sputter Ti at 75 W power	30 min
	Repeat this presputtering/sputtering/waiting for a total of 6 times. The total sputtering time is 180 minutes.	
	Presputter Au at 50 W	1 min
	Sputter Au at 50 W (~30 nm) The deposition rate for gold is consistent with different users: 50 nm/min at 50 W, 5 mTorr, and 25 sccm Ar flow.	36 s

Vacuum Packaging Process

- 1.** If the chamber has not been used for a long time (months). Bake the chamber overnight at 400°C while it is empty with the pumps on. This will clean the chamber and expedite the pump down time during packaging.
- 2.** After the sample is mounted and wirebonded verify the operation of the device. To check that none of the wirebonds is above the DIP40 ceiling, first do a manual inspection from the side of the package after wirebonding. If you see a height then fix it because if the wirebonds touch to the metal lid, this will cause a short problem after vacuum packaging. I soldered wire wrapping wire to one of the metal lids for the electrical connection. I place the metal lid on the package and apply a small weight (10g) to keep the lid in place. Then I check whether there are any shorts between the metal lid and wirebonds using a multimeter before vacuum packaging. Wire wrapping wire is very compliant and does not create torque on the lid.
- 3.** Place the sample in the vacuum chamber for outgassing on the walls of the heated die aligner. Pump down the chamber and start increasing the temperature slowly. Do not set it to the desired temperature directly since the temperature overshoot may cause your die mount solder to melt. The melting of the die mount solder is important for our case since we want to keep the die mount stress free. I bake my samples at 150°C overnight (12 hours), my die mount solder is tin (melts at 230°C). In the final runs I am suspecting that 150°C melted or softened tin, so I suggest temperatures of 130°C and 140°C, if you are following my recipe. Otherwise if you do not care about die mount adhesive melting, you can bake at any temperature you want. The purpose of this step is to get rid of the adsorbed gases that may outgas later and the temperature of this step has a direct effect on the final

pressure inside the vacuum sealed cavity. Ideally this step should be done before the vacuum sealing without breaking the vacuum but our setup is not capable of this. And die mount indium solder hardens if baked for long hours, so that's why we will vent the chamber next and add our die mount solder. But we try to minimize the time that the sample is exposed to atmosphere by preparing everything first and then venting the chamber.

4. We will cut the solder preform and place it on the sample in this step. Figure 0.1 shows the tools needed to cut the solder preform. I recommend rinsing these tools with IPA before starting for organic cleaning. First cover the surface with aluminum foil bought from the cleanroom. Regular aluminum foil has residual oil on it that may contaminate the solder preform, we use clean aluminum foil for that reason.

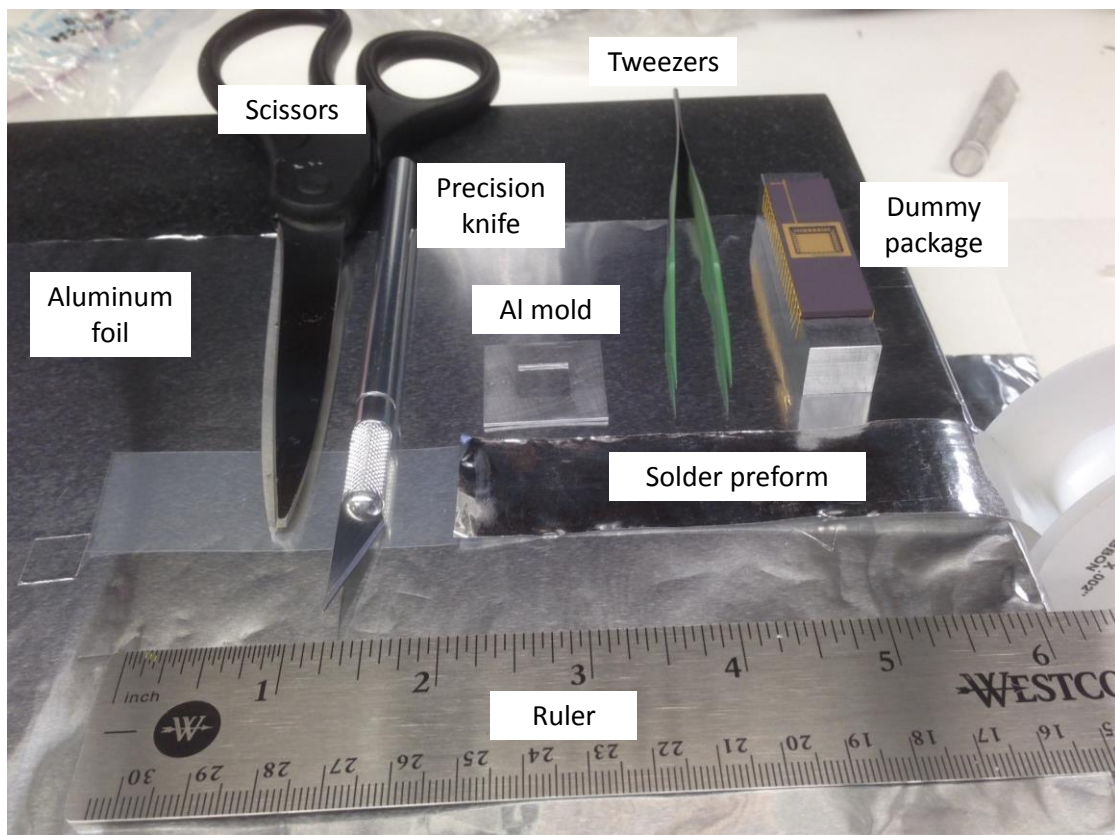


Figure 0.1: Tools needed to cut the solder preform.

The solder preforms come in the form of metal tapes with 1 mil (25 μm) thickness. I use two folds (50 μm) to assure good bonding. Using the ruler and precision knife mark 0.875” on the tape first and then cut the solder with scissors. Since indium is very soft using scissors for cutting is the easiest way. Cut two pieces and stack them on top of each other. The Al mold is shaped in the inner side to match the bonding ring on the DIP40. Place the Al mold on the cut solder preform and push firmly with your fingers, using the precision knife remove the inner side of the solder preform. Do this at once and make sure there are no residual solder pieces on the inner side. Since indium sticks on the precision knife I change the blade every time before I do this. Once the inner side removed I cut the outer side with scissors iteratively until one side is narrower than the width of the DIP40. During cutting hold the preform with tweezers but release the preform during the cutting otherwise indium bends. Once one side is narrower than DIP40, I don’t care about the other side much since it increases the chances of tearing the indium.

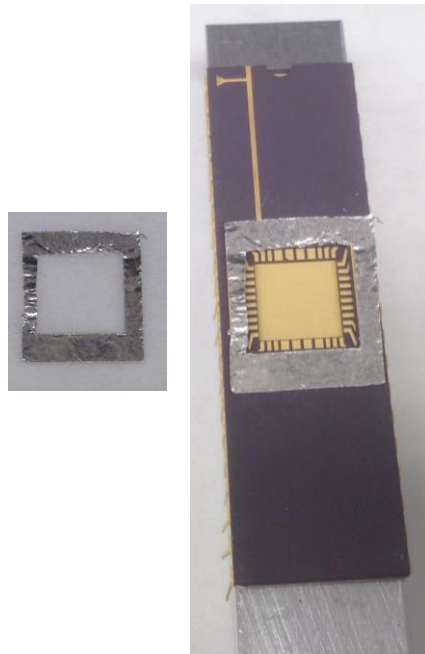


Figure 0.2: Standalone cut solder preform and solder preform on the dummy package.

Figure 0.2 shows the standalone cut solder preform and solder preform on the dummy package. You can measure how much you need to cut by putting the solder on the dummy package during the process. Meanwhile start the cooling in the vacuum chamber by decreasing the temperature set point to 0°C and turning on the cooling water. Always stop the pump after the cooling is complete and cooling water is turned off. Keeping the cooling water on in the atmosphere leads to condensation on the cooling pipes inside the vacuum chamber, and high vacuum cannot be obtained afterwards.

After the solder preform is cut into the frame shape and the sample is cooled in vacuum, vent the chamber. We should be as quick as we can to minimize the adsorption. Align the solder preform on the bonding ring of the DIP40 and push firmly with the Al mold on the solder preform after the alignment is complete. This will attach the indium preform to the DIP40, check the attachment by flipping the DIP40 upside down a couple of times.

5. Figure 0.3 shows inside of the vacuum chamber and the top piece that houses the package holder and shutter. Rinse the metal lid with IPA and place it in the middle recess on the die aligner in the vacuum chamber. Insert the DIP40 with the indium preform into the package holder. Check the alignment of the top package holder and bottom die aligner by moving the package towards the die aligner while making sure the top piece completely covers the vacuum O-ring. Do not make full contact between the DIP40 and the lid but keep the DIP40 in the die aligner, and start the pump. The vacuum will hold the top piece in place. Turn off the vacuum once the vacuum reaches to 200-300 Torr. Move the package holder up and down and verify that package holder slides into the die aligner smoothly. After the alignment verification turn on the pumps retract the package holder to

top and insert the shutter between the DIP40 and heated die aligner. Paper clips can be used to adjust the heights of the shutter and package holder and keep them in place.

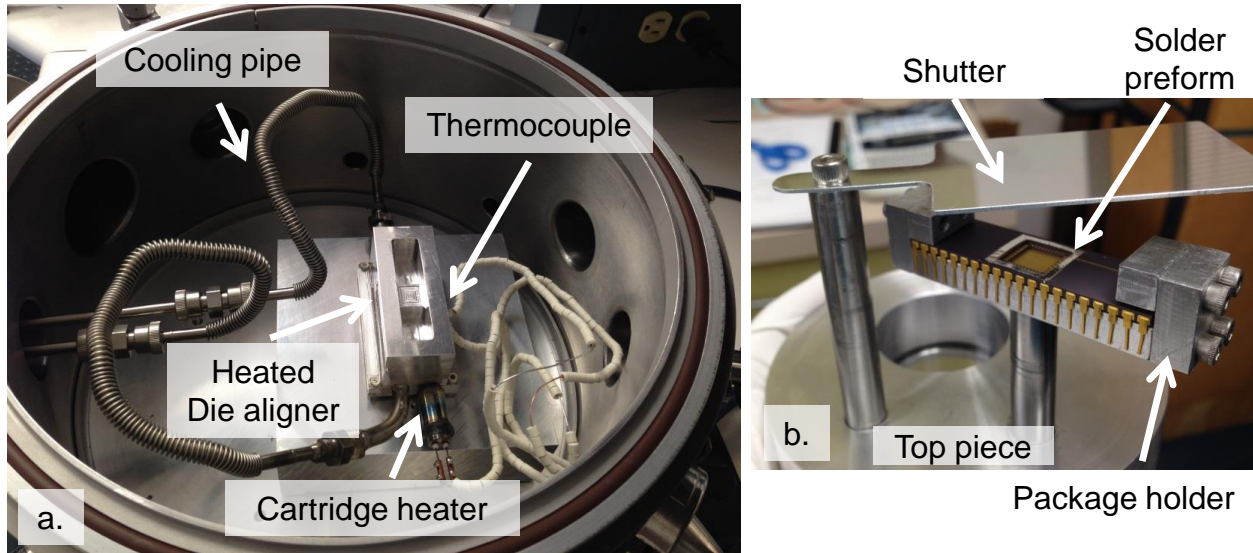


Figure 0.3: Inside of the vacuum chamber (a), and the top piece that houses the package holder and shutter.

6. Turn on the ion gauge when the roughing gauge cannot read. The ion gauge sometimes turns on, shows millitorr level pressure and shuts down automatically although the roughing gauge shows less than $100 \mu\text{Torr}$. Since we do not use the system all the time I think the ion gauge is contaminated during the unused times leading to this problem. Keep turning on the ion gauge, the read pressure by the ion gauge will drop, since it cleans itself as the current is applied each time. Degas can be used to clean the ion gauge but the pressure should be less than $50 \mu\text{Torr}$. Degas applies high current on the ion gauge filament for 2 minutes to clean the gauge. When microtorr level pressure is reached first set the temperature to 70°C , there will be a jump in the pressure due to initial outgassing of the heated die aligner but the pressure will recover. Then increase the temperature with $20\text{--}30^\circ\text{C}$ steps slowly while watching the pressure. Wait until the pressure is 1 to $2 \mu\text{Torr}$ before increasing the temperature. If the pressure at 150°C is less than $1 \mu\text{Torr}$ then keep

increasing the temperature up to 250°C. If not wait half an hour at 150°C for the pressure to settle and then increase the temperature to 250°C.

7. Wait at 250°C for half an hour. This has two purposes; first the lid goes through outgassing, second base pressure is reached. If the chamber is clean you should see a pressure in the low 10^{-7} Torr at the end of this half an hour.
8. Increase the temperature by 15°C in every 2 minutes, and once you reach 385°C start the timer for 20 minutes and increase the temperature to 400°C. Keep the temperature at 400°C. 400°C activates the getter. Increasing the temperature gradually assures that high vacuum conditions are preserved. The pressure will rise a little as you increase the temperature. The pressure should be less than 1 μ Torr not to saturate the getter after activation.
9. Since the getter is activated the remaining steps should be performed as soon as possible. At the end of 20 minutes set the temperature to 0°C (so that heater is off) and turn on the cooling water. Wait till the temperature reaches to 80-90°C, this should take 15-20 minutes.
10. Open the shutter, remove the paper clips for the package holder and merge the DIP40 and the lid. Apply 5 pounds on top of the package holder to apply pressure during vacuum sealing. Increase the temperature set point to 120°C, since the thermal load has increased there will be an excessive overshoot (almost 30°C). By taking into account this overshoot increase the temperature gradually. Temperature set point of 160-170°C should result in 200°C temperature. Increase the set point when the temperature increase rate slows down. For successful bonding 30-50°C above the melting point of the solder is recommended. Indium melting point is 157°C. Exceeding 200°C too much may lead to melting of the die

mount tin. So keep the temperature around 200°C for 2 minutes, and then turn on cooling water after setting the temperature to 0°C

11. When the temperature reaches less than 60°C remove the 5 pound weight form the package holder and retract the DIP40 from the heated die mount tool. Turn off the ion gauge and stop the pumps. It takes 10 minutes for the turbo pump to stop and then vent the chamber. Remove the vacuum packaged sample.

12. Leave the chamber under vacuum, pump down and turn off the pumps.

C. Integrated Gyroscope Designs in TSMC MEMS and Tower Jazz Process

Integrated gyroscope designs were developed for the TSMC-MEMS and Tower Jazz processes. The gyroscope structure is basically the same with the SOI-MEMS design but modifications were done based on the design rules of the specific process.

Integrated Gyroscope Design in TSMC MEMS Process

An integrated gyroscope with on-chip transimpedance amplifiers and stress and temperature sensors was designed for the TSMC-MEMS process [103]. A single crystal silicon wafer with the MEMS structures is bonded to a CMOS wafer in this process, connections between the MEMS and the circuits are made by the anchors on the CMOS wafer. Finally MEMS die is wafer level vacuum packaged. The device includes distributed piezoresistive stress sensors designed similar to [104] and proportional to absolute temperature (PTAT) sensors to measure the stress and temperature. Figure 0.4 presents the layout of the integrated TSMC MEMS gyroscope. The design includes four temperature sensors, and eight stress sensors distributed across the die area. Each stress sensor consists of one normal and one shear stress sensor. The mechanical structure is 2.4 mm by 2.4 mm.

Two versions of this layout were taped out, one with the on-chip transimpedance amplifier and environmental sensors (this chip is labeled as “CKT” on the corner), and one without the on-chip transimpedance amplifier and with the environmental sensors (this chip is labeled as “NO_CKT” on the corner). The transimpedance amplifier is an OPAMP with $5M\Omega$ resistance in the feedback path, chopper stabilization is used in the OPAMP to overcome the $1/f$ noise of the CMOS technology. We received a total of 350 of these chips, 175 CKT and 175 NO_CKT.

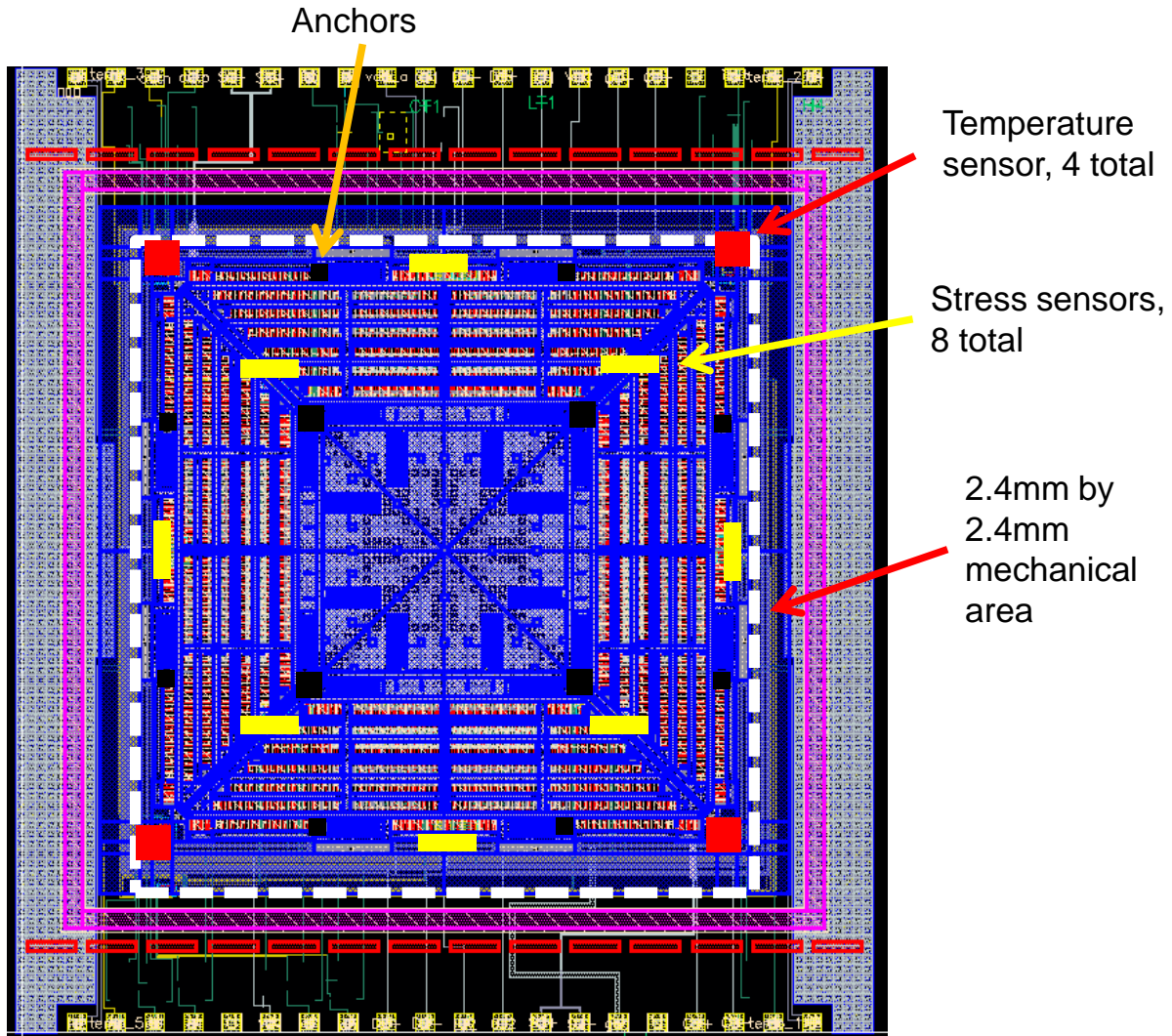


Figure 0.4: Layout of the integrated TSMC MEMS gyroscope.

Figure 0.5 presents the pad distribution for the NO_CKT TSMC-MEMS gyroscope. The design includes heater resistors under the anchors to induce thermal stress. There are four serially connected resistors on each corner. The ground connections are shorted on the layout, and access to each corner is achieved through Heater1-4 pads. The temperature sensors work all the time and the four temperature sensor outputs can be reached through Temp. 1-4 pads. The stress sensors need to be selected first through D0-D3 pins, and the negative and positive Wheatstone bridge outputs can be read from the “Out n” and “Out p” pads respectively. R1-2 pads rotate the power supply and ground connections of the Wheatstone bridges to get rid of the offset problem.

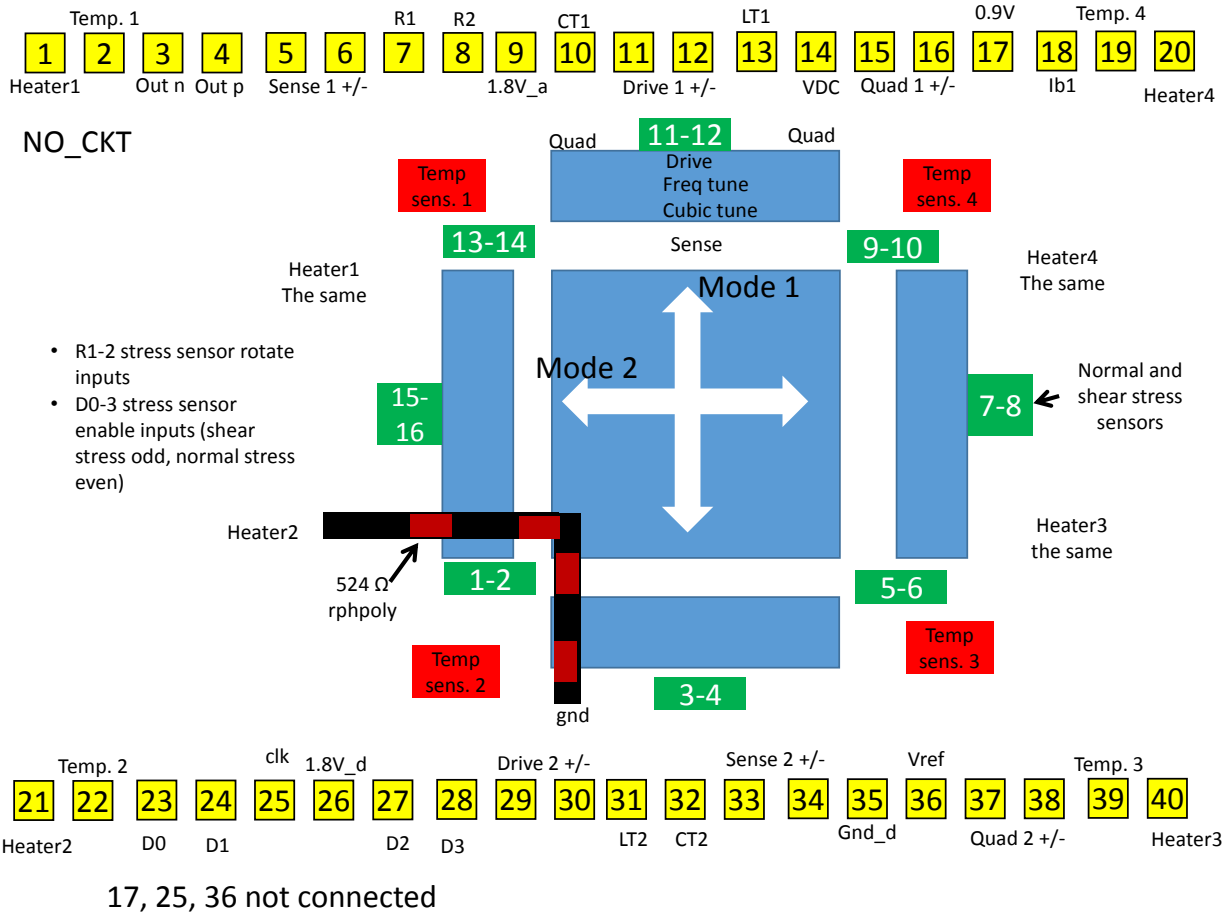


Figure 0.5: Pad map of the NO_CKT TSMC MEMS gyroscope.

The gyroscope modes are labeled as 1 and 2, and the gyroscope is driven and sensed differentially. Figure 0.6 shows the 1/8th of the TSMC MEMS gyroscope layout with the fingers labeled. The layout is symmetric. Sense 1+/- are the differential sensing straight comb fingers for mode 1, Drive 1+/- are the differential driving straight comb fingers for mode 1, Quad 1+/- are the differential straight comb fingers allocated for the ac quadrature cancellation for mode 1, VDC is the proof mass voltage, LT1 is the dc frequency-tuning voltage for mode 1, CT1 is the dc nonlinearity tuning voltage for mode 1. The same naming convention is followed for mode 2. Sense, Drive and Quad are the same fingers they can be used interchangeably. The rest of the connections are for the front end circuits and environmental sensors. 0.9V is the $V_{dd}/2$ voltage where $V_{dd}=1.8V$ for the transimpedance amplifier. Ib1 is the bias current for the PTATs. 1.8V_a

and 1.8V_d are the analog and digital 1.8V power supplies. 1.8V_a powers the temperature sensor and the front end circuits, and 1.8V_d powers the stress sensors. Clk is the clock for the front end chopper stabilization which can be provided from a function generator. Vref is the biasing voltage for the biasing of the low pass filter in the CKT die. There is one ground in the system that is Gnd_d. There is also a 100 kHz low pass filter in front of the transimpedance amplifier to filter out the high frequency noise.

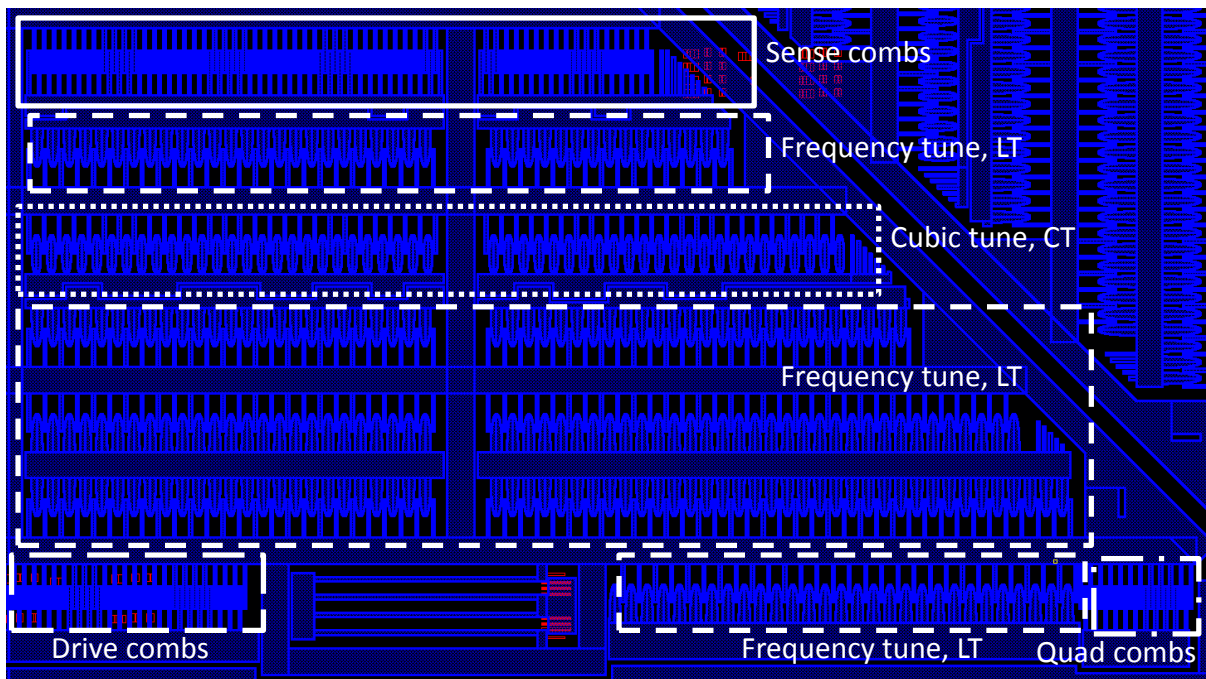


Figure 0.6: 1/8th of the TSMC-MEMS gyroscope layout with the fingers labeled.

CKT and NO_CKT dies share the same pad distribution. Sense 1+/- and Sense 2+/- straight combs are directly connected to the input of the on-chip transimpedance amplifiers and they go through a low pass filter. Sense 1 +/- and Sense 2+/- pads are voltage and they are the outputs of the low pass filter in the CKT die. Pad 17, 25, and 36 are needed in the CKT die and are not need to be connected in the NO_CKT die.

The taped out cells are in the tsmc018rf kit under the library “tsmc018_005” and the two different dies are CMU_die1_ckt, and CMU_die2_nockt. We tested five of the dies without the circuits (CMU_die2_nockt) and we were able to see only one functional device. An off-chip transimpedance amplifier was implemented on a bread board. The die was mounted with epoxy and 45° with respect to the package recess. Figure 0.7 presents the measured open-loop frequency sweeps for the two gyroscope modes. There is 300Hz frequency mismatch between the modes which may be out of the tuning range of the frequency tuning fingers and the quality factor is low (450). This low quality factor represents Torr level pressure and it is consistent with the results presented by TSMC [105].

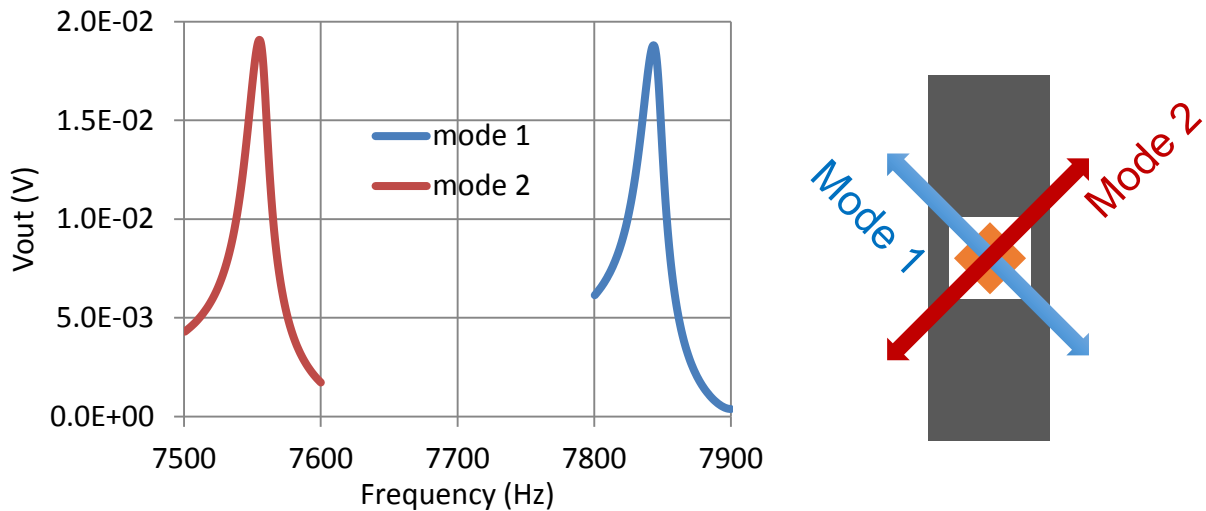


Figure 0.7: Measured resonance curves from one of the TSMC MEMS gyroscopes, the device is mounted 45° with respect to the package recess.

The operation of the environmental sensors were not verified. Further investigation is needed to figure out the reason why only single device worked out of the five tested devices. The cap is silicon and not transparent, removal of the cap and optical inspection would reveal the problem. There may be a stiction problem. The nonlinearity tuning fingers in the TSMC gyroscope are the

first generation nonlinearity tuning fingers covered in Section 4.2.1, and will not work. A design update is needed on the nonlinearity tuning fingers.

The low quality factor problem can be solved by opening a vent hole on the cap with focused ion beam and then following the vacuum packaging approach developed in this thesis. Figure 0.8 shows the proposed vacuum packaging approach to solve the low quality factor problem of the TSMC MEMS gyroscopes. A gold layer is deposited on the backside of the dies, and then mounted with nanofoil, and wirebonded. The venting hole is opened after verifying the functionality of the device. Next the vacuum packaging approach developed in Chapter 3 can be followed.

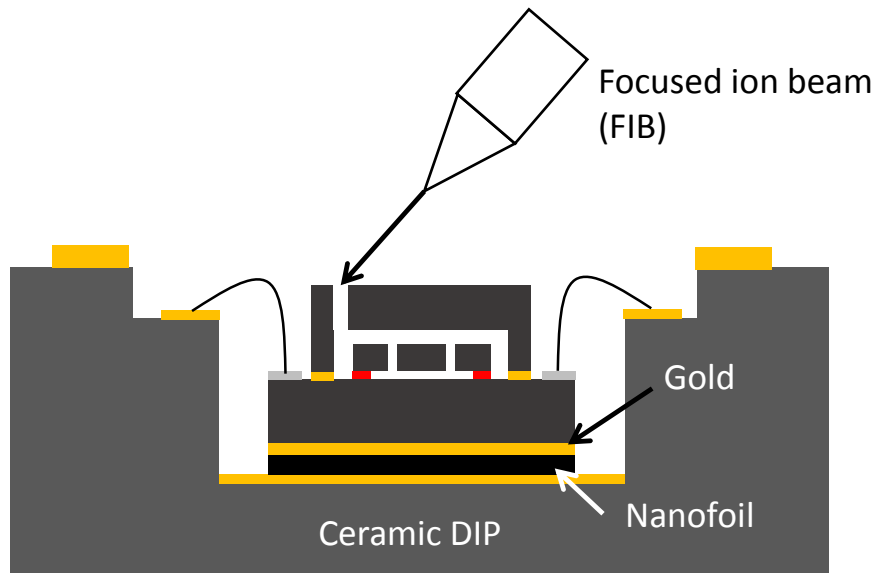


Figure 0.8: Proposed vacuum packaging approach to solve the low quality factor problem of the TSMC MEMS gyroscopes.

Integrated Gyroscope Design in Tower Jazz Process

Another integrated gyroscope was designed in TowerJazz 0.18 μ m technology. This gyroscope requires post processing in CMU with the Si-CMOS MEMS process [106]. MEMS masking layers are embedded in the CMOS metal layers. The MEMS die is first thinned and then bonded to a carrier. The MEMS structure is formed by etching away the oxide in the gaps with advanced oxide

etching (AOE), and the device is released with deep reactive etching (DRIE) on the substrate silicon. Figure 0.9 shows the layout of the gyroscope along with the locations of the environmental sensors and front end electronics. The charge amplifier front end and ADC is located on the proof mass to save space and minimize parasitics. The gyroscope has distributed thirteen shear and normal stress sensors and nine PTAT sensors. The gyroscope design includes two separate scan chains to program the gain of the front end and to select the desired environmental sensor output. All the environmental sensor outputs are connected to the same pad with switches and the desired switch is selected with the scan chain. Figure 0.10 shows the pad distribution for the Tower Jazz gyroscope. Yellow and white color distinguishes between the ac and dc signals, and black and red text distinguishes between the pads with and without ESD protection. This was a joint work with Ekin Yagmur Gonen, and detailed information about the front end, environmental sensors, and corresponding pads can be found in [107].

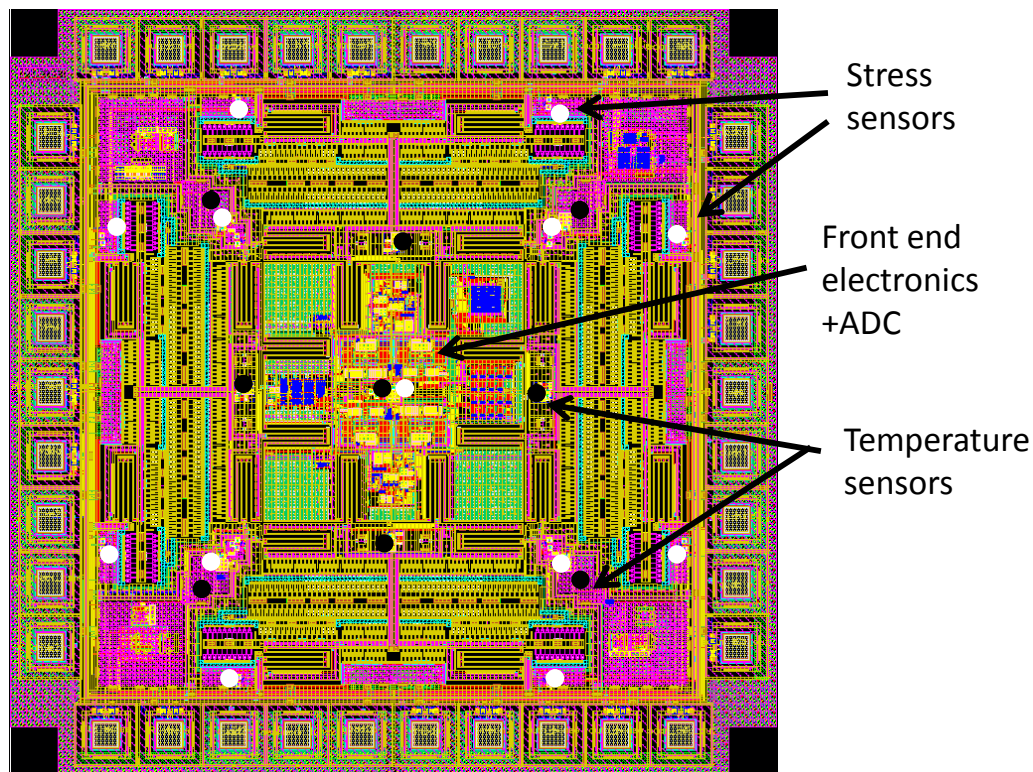


Figure 0.9: Layout of the integrated Tower Jazz gyroscope.

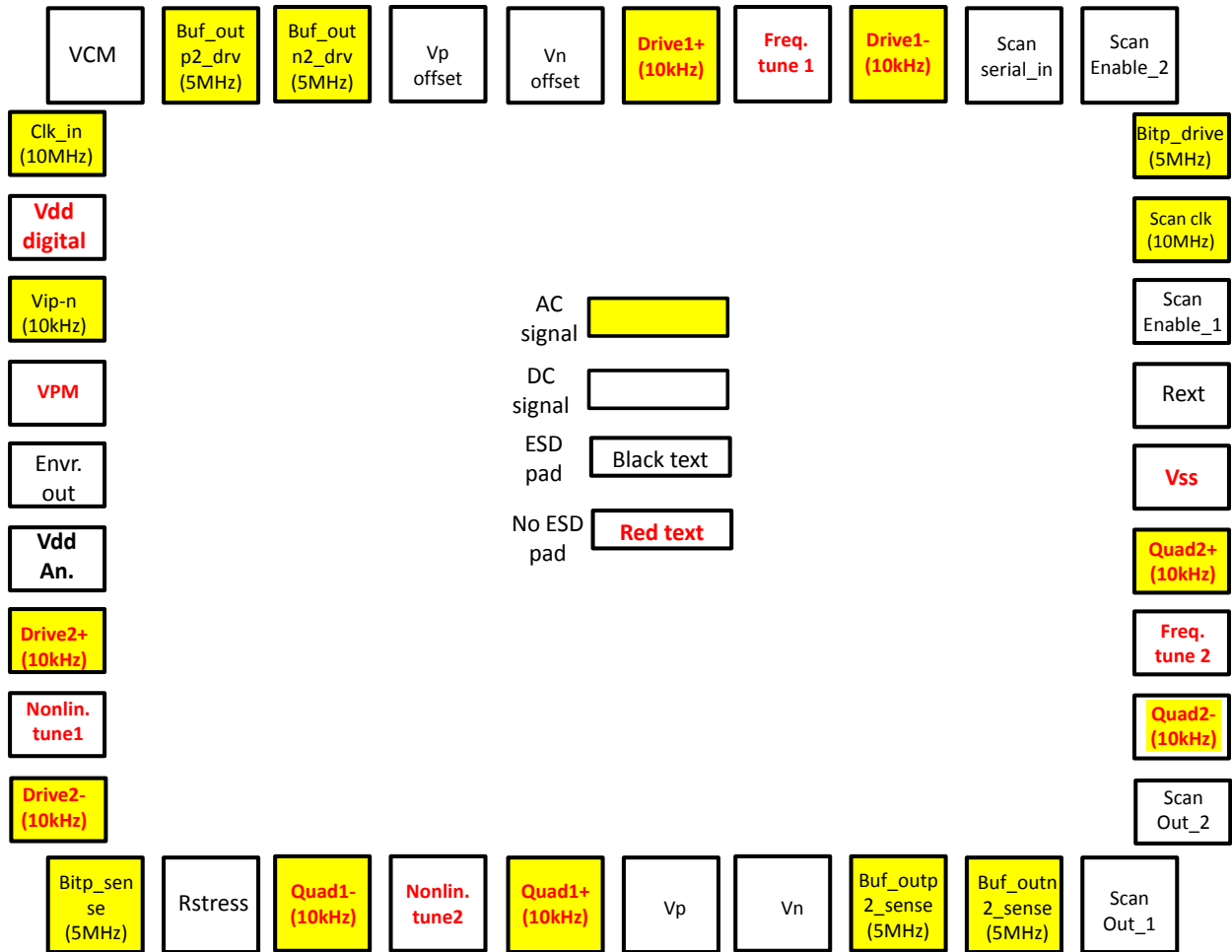


Figure 0.10: Pad distribution of the Tower Jazz gyroscope.

We will review the MEMS gyroscope pads. Figure 0.11 shows the layout image of the Tower Jazz gyroscope with the finger labels. The sense combs are connected to the input of the on-chip charge amplifier. Modes are labeled as 1, and 2. Frequency tuning fingers are connected to the “Freq. tune” pad and are used to tune the frequency mismatch between mode 1 and 2. This design includes the updated second generation nonlinearity tuning fingers, and “Nonlin. tune” pad is connected to those fingers. One side of the nonlinearity and frequency tuning fingers are connected to ground on the layout. Drive +/- and quadrature +/- fingers are the names of the straight combs on different side plates. These fingers are used to drive the gyroscope on the drive mode and used to cancel the rate and quadrature error on the sense mode. The corresponding pads are “Drive +/-

and Quad +/-“. One side of the Drive and Quad straight fingers are all shorted and connected to the “VPM” pad for applying dc polarization voltage.

We designed electrostatic discharge (ESD) protection bridges for the inputs of the on-chip charge amplifiers. The electrical connections coming from the sense combs are grounded while the routing is going to the charge amplifier inputs. This is to protect the charge amplifier inputs from the accumulated charge on the sense combs during plasma processing. Figure 0.12 shows one of these ESD protection bridges. These connections should be cut before testing the front end circuits. Otherwise the inputs are always shorted. Focused ion beam (FIB) or laser cutter can be used. There are a total of eight of these bridges and each bridge requires two cuts.

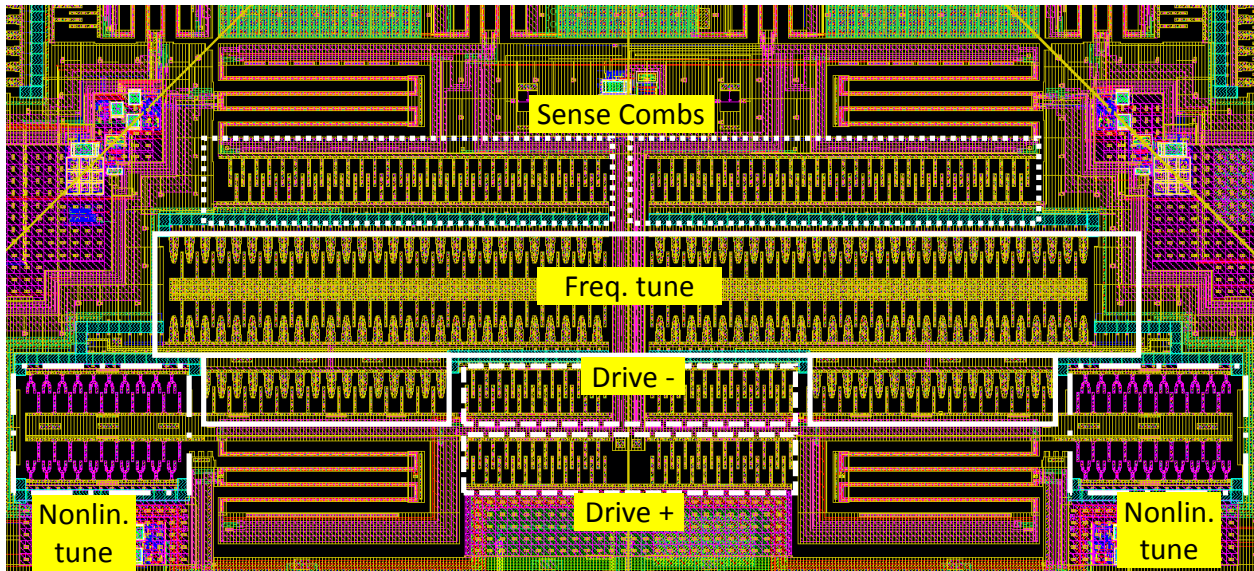


Figure 0.11: Layout image of the Tower Jazz gyroscope with the finger labels.

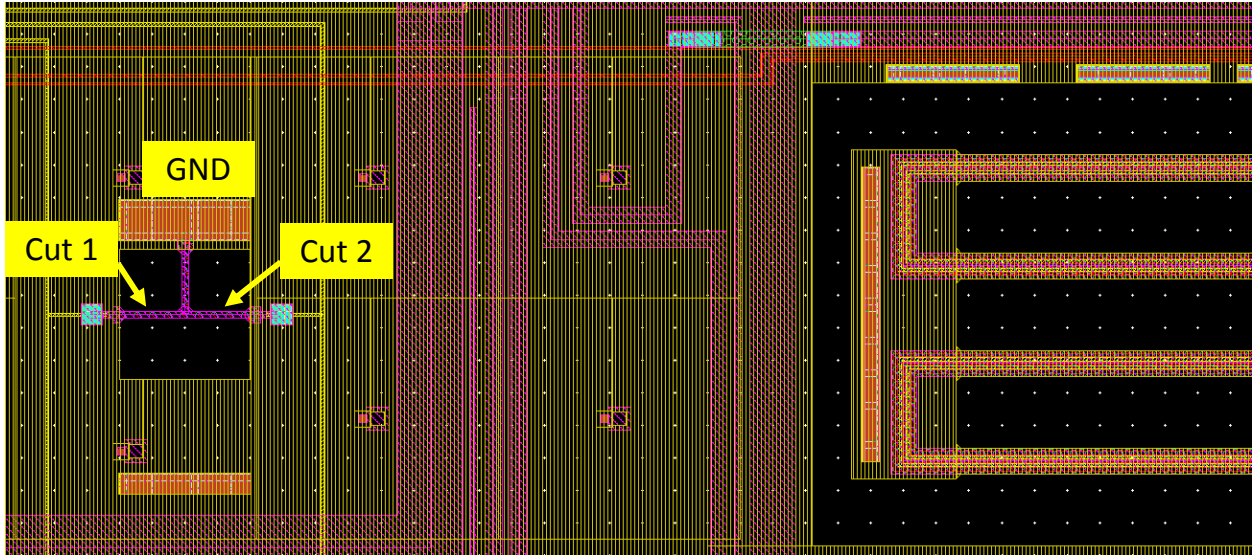


Figure 0.12: ESD protection bridges for the input of the charge amplifiers.

Figure 0.13 and Figure 0.14 show the 1/4th and 1/8th of the Tower Jazz gyroscope, respectively after we received them from the foundry. These chips are not processed and covered with passivation.

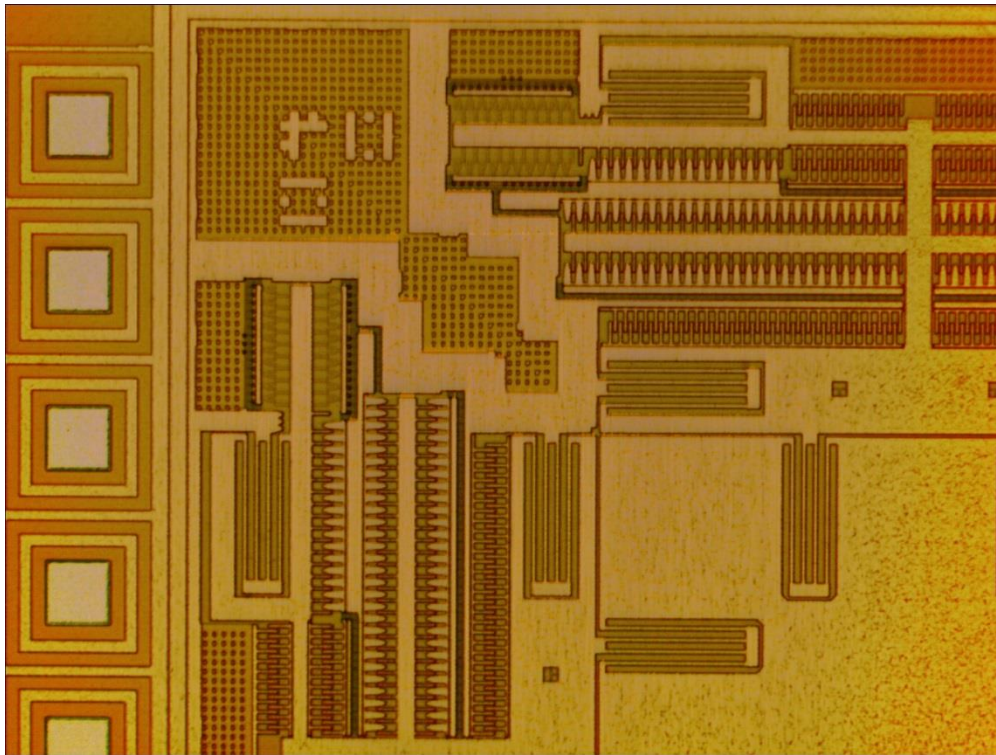


Figure 0.13: Optical image of the 1/4th of the Tower Jazz gyroscope.

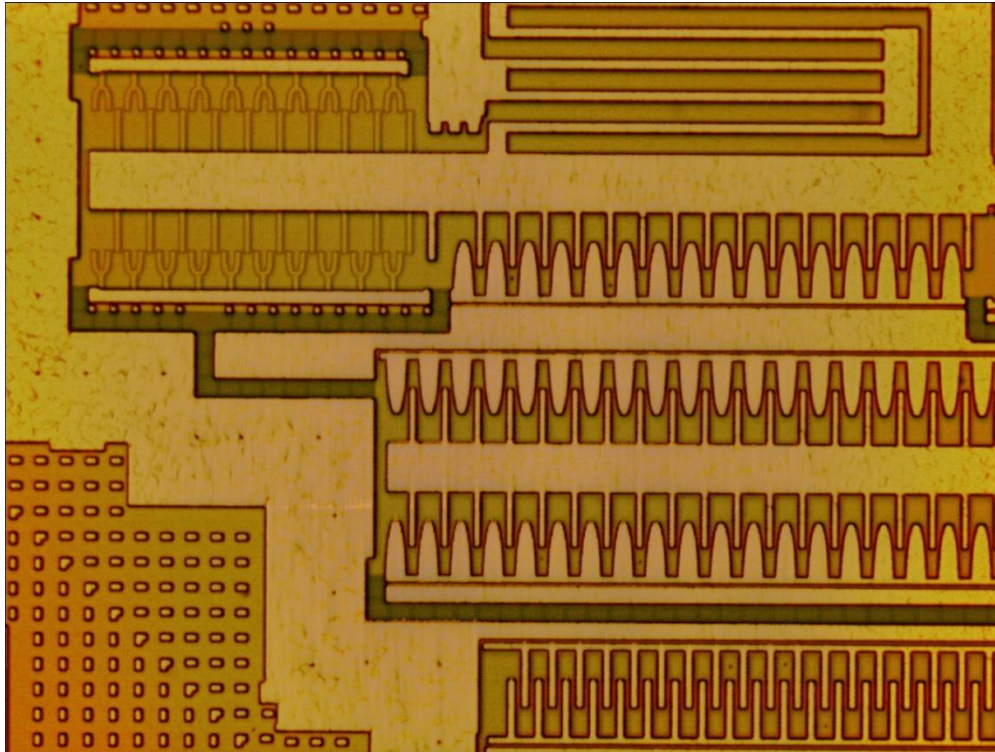


Figure 0.14: Optical image of the 1/8th of the Tower Jazz gyroscope.

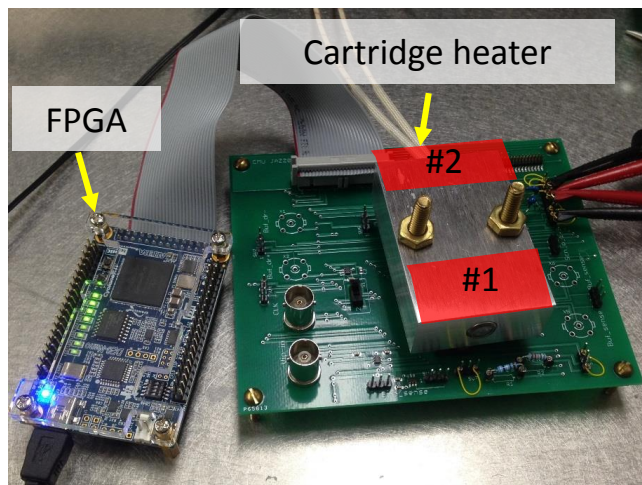


Figure 0.15: Testbed for the Tower Jazz gyroscope.

The functionality of the scan chains and the environmental sensors was tested on the Tower Jazz gyroscope. Figure 0.15 shows the testbed. An Altera DE0-NANO FPGA board [108] is used to generate the clock and control signals for the scan chains. The gyroscope chip is wirebonded to a DIP40 and temperature is changed our ovenization setup. The PCB includes voltage level converters, since our chip operates at 1.8V but FPGA operates at 3.3V.

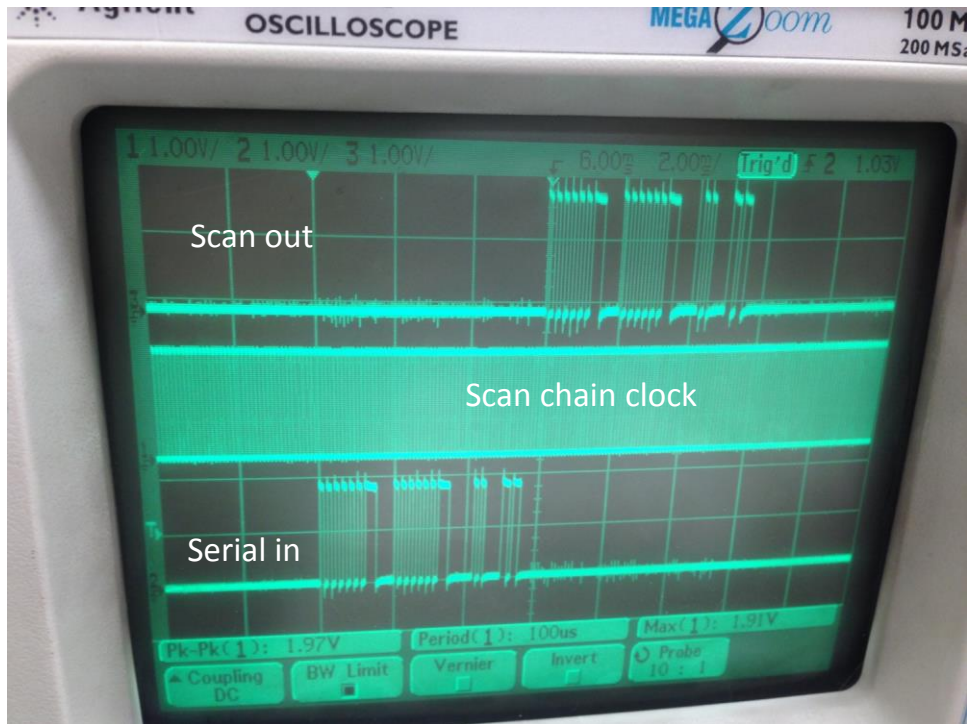


Figure 0.16: Scope screen shot for scan chain testing.

We started with the scan chain testing since almost everything is controlled with it. The scan chain enable is always kept high, and a serial bit sequence is inserted into the scan chain. The serial input should come out of the scan chain after N clock cycles where N is the number of bits in the scan chain. Figure 0.16 shows a scope screen shot with the serial out, scan chain clock, and serial in. The scan chain enable is always high in this test. Scan out and serial in are the same verifying the operation of the scan chain.

Environmental sensors were tested after the scan chain operation was verified. Figure 0.17 shows the measurement result, where the ambient temperature is measured by the SOI temperature resistor and CMOS temperature sensor. There is almost 1K peak to peak rms noise on the CMOS temperature sensor which is consistent with the 621 μV rms simulated noise [107]. This noise can be reduced by averaging since temperature is a slowly changing variable. But the average temperature sensor output noise still might not be enough for precision gyroscope compensation.

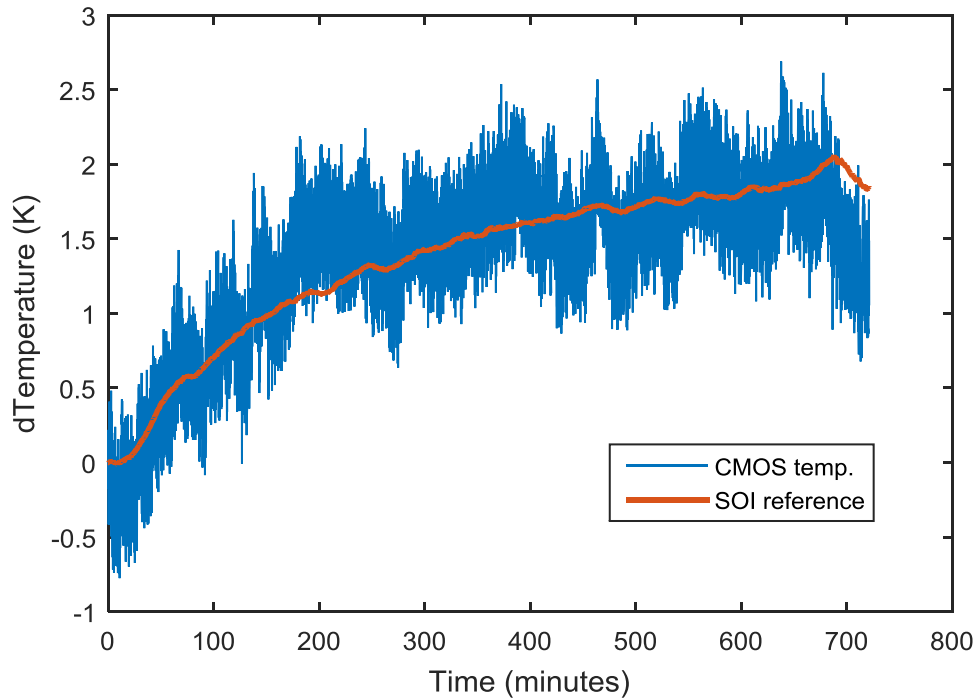


Figure 0.17: Comparison between the SOI temperature resistor and CMOS temperature sensor, both of them are measuring the ambient temperature.

The idea behind the Tower Jazz gyroscope design was having distributed environmental sensors on the gyroscope die and continuously reading all the sensor outputs. This requires FPGA programming where FPGA scans through all the sensors and saves the data. We couldn't reach to fully automated testing, we selected each environmental sensor manually and recorded the data with a multimeter in our tests. By using the setup in Figure 0.15 one temperature sensor is selected and a fixed heater power is applied to the chip for 70 minutes, the power was turned off, and the sample is left for cooling. This was repeated for three different temperature sensors. Figure 0.18 presents the test results. These temperature sensors were selected from across the device, i.e. one on one corner (temp. 1), one on the center (temp. 2), and one on the other corner (temp. 3). The results suggest a temperature gradient on the die, the heated aluminum in Figure 0.18 may have better thermal contact on one side than the other. However, we assumed the same scale factor for all of the stress sensors. In case the scale factor is different the interpretations might be wrong.

There was an offset problem on the temperature sensors, different sensor outputs at room temperature varied between 800mV-1V. The simulated room temperature is around 850mV.

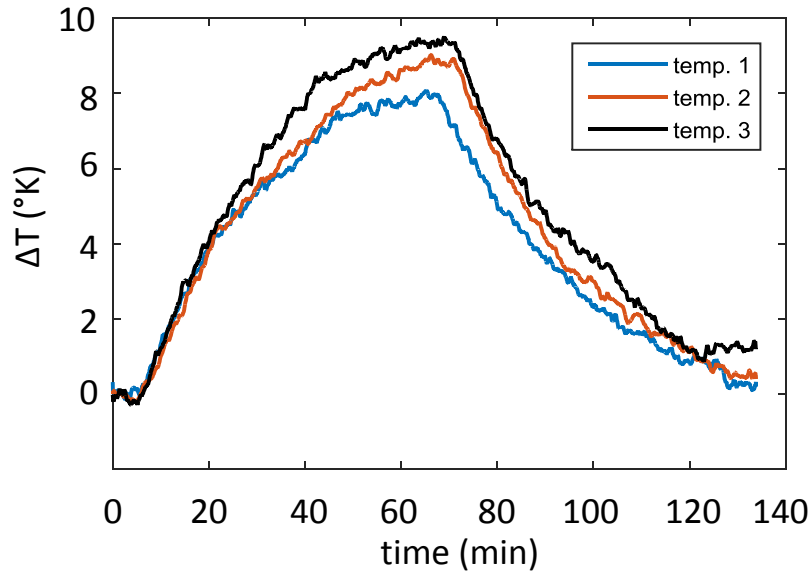


Figure 0.18: Temperature sensor measurement results from three different sensors.

We used the stress testbed in Figure 5.30 without ovenization to test the stress sensors. Figure 0.19 presents the test results from one of the normal stress sensors. We started by applying a two pounds weight and increasing it up to five pounds, although the noise is high the stress sensor responded. However once we removed the five pounds weight the output did not return to its nominal value, and adding and removing the five pounds did not affect the output. Several other sensors were tested and similar responses observed. It is difficult to comment on the functionality of the stress sensors with this data. The SOI stress sensors responded with a clear change in their outputs for the same stress. There is also a noise issue with the CMOS stress sensors. Further characterization is needed for the CMOS stress and temperature sensors. Programming the FPGA so that it scans through all the environmental sensors and saves the data continuously would help understanding the problem of the sensors. Once stress is applied for example, all the stress sensor outputs to the same stimulus can be seen. The same argument is correct for a temperature stimulus.

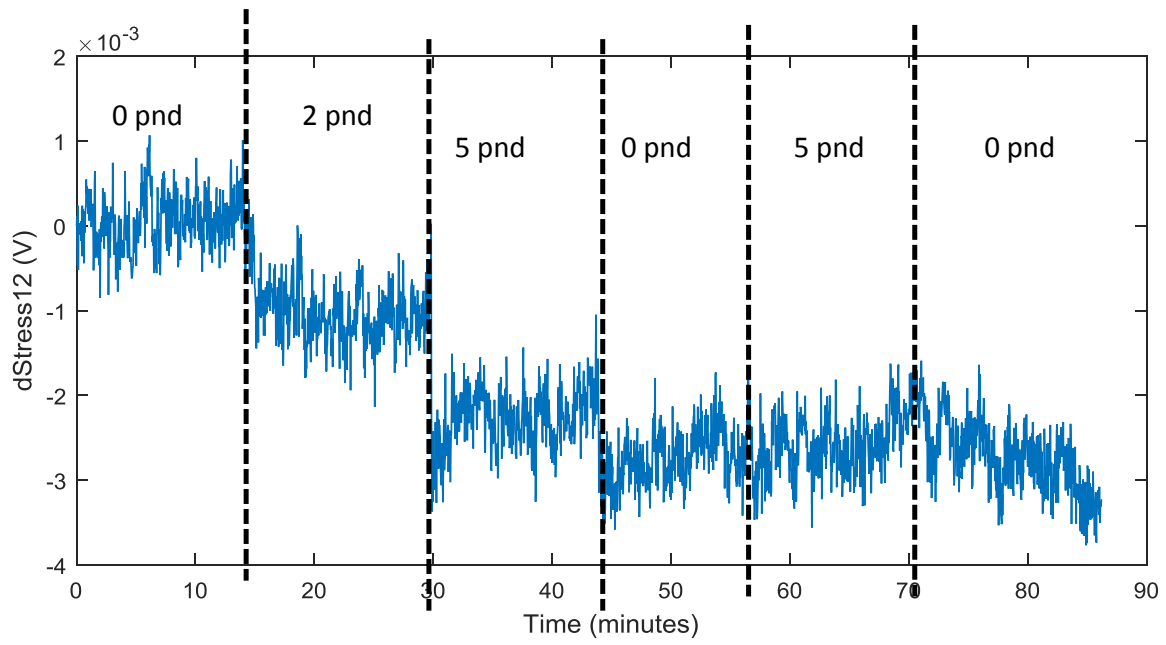


Figure 0.19: Test results from one of the normal stress sensors in a stress testbed.

D. Details of the Gyroscope PCB

The gyroscope PCB includes four transimpedance amplifiers that convert the current output to voltage, instrumentation amplifiers that convert the differential voltage outputs to single ended, and voltage buffers for sensing the gyroscope displacement. There are buffers and inverters on the drive side to generate differential drive for driving the gyroscope, force rebalance operation, and quadrature cancellation. Bandgap references generate the power supplies for the stress sensors. Although not used, there are instrumentation amplifiers to amplify the differential output of the stress sensors. There are voltage regulators for $\pm 2.5\text{V}$ for the power supply of the transimpedance amplifier OPAMPs. Figure 0.20 shows the photograph of the gyroscope PCB with the components labeled.

Table 0.1 provides the summary of the components. The connection to the external world, i.e. to the power supplies and Zurich Instruments lock in amplifier is achieved through a connection PCB. A ribbon cable connects the gyro PCB and the connection PCB. The connection PCB accepts banana and BNC cables that are selected via a switch. Table 0.2 presents the pin map of the connection PCB. Mode 1 is used as the sense mode and Mode 2 is used as the drive mode for the results reported in Section 5.6.

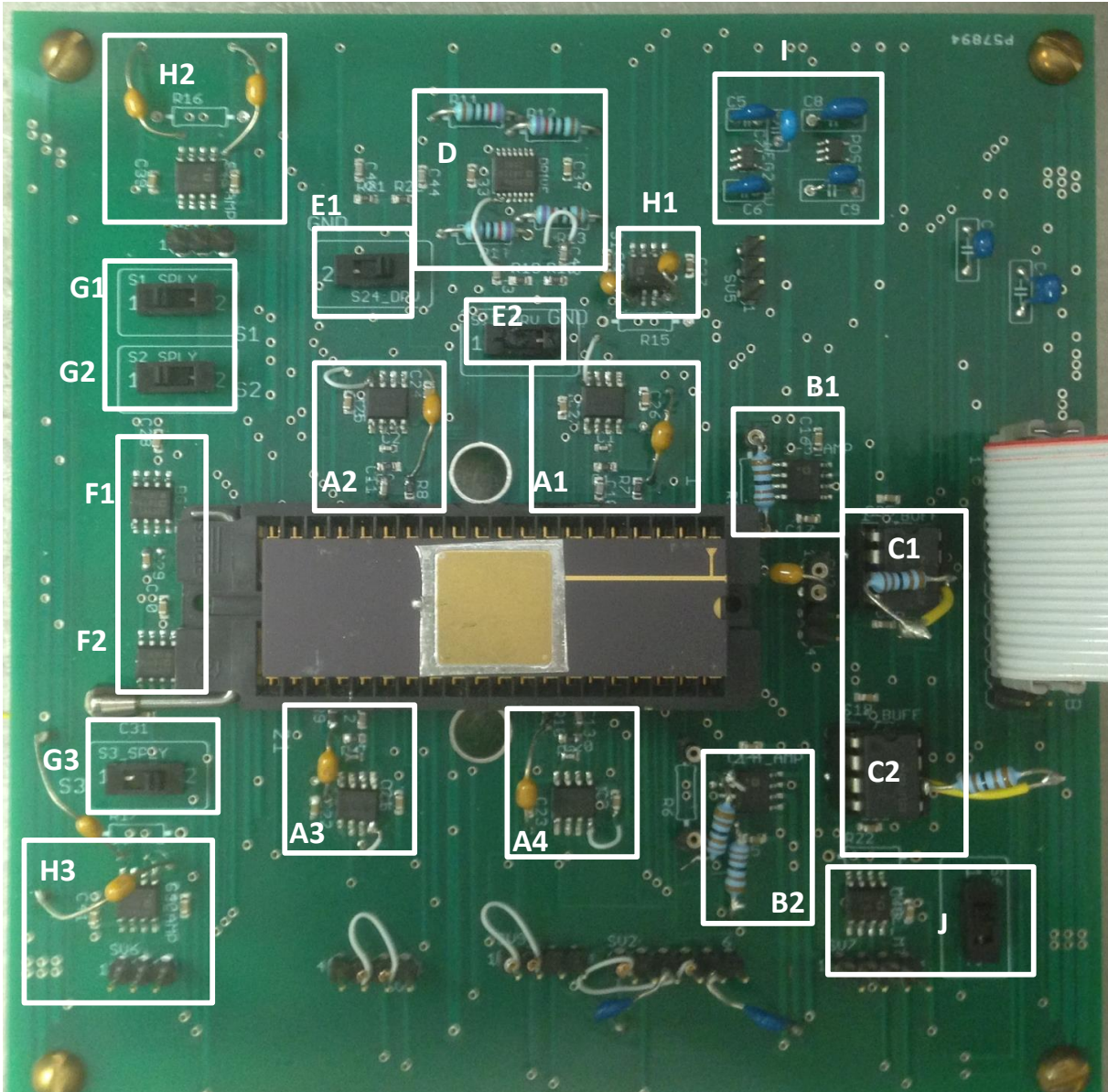


Figure 0.20: Photograph of the gyroscope PCB.

Table 0.1: Summary of the components.

Label	Component Summary
A1, A3	Differential transimpedance amplifiers for mode 1, implemented with MAX4475 OPAMP, and 5pF//500MΩ on the feedback
A2, A4	Differential transimpedance amplifiers for mode 2, implemented with MAX4475 OPAMP, and 5pF//500MΩ on the feedback
B1	Instrumentation for mode 1, output of A1 and A3 is converted to single ended, implemented with AD8421, has a gain of 10 with 1.1kΩ gain resistance
B2	Instrumentation for mode 2, output of A2 and A4 is converted to single ended, implemented with AD8421, has a gain of 1
C1	Output buffer for the output of B1, implemented with LF356
C2	Output buffer for the output of B2, implemented with LF356
D	Generates the differential ac driving signals for mode 1 and 2, implemented with a quad AD8648 OPAMP. The signals are inverted with a gain of -1 (using 10kΩ resistors), and buffered. Force rebalance and quadrature cancellation is achieved using a single output, lock in amplifier can add two 90° phase shifted signals inside.
E1-E2	Switches for the ac drive signals to switch between single sided and differential drive
F1-F2	Bandgap references for the supply of the stress sensors, implemented with ADR445. Two of them are used since their current sourcing capability is limited
G1-G3	Switches to turn on and off the power supplies for the stress sensors. Initially designed for S ₁ , S ₂ , S ₃ for stress sensing and S ₄ for temperature sensing. But currently S ₂ is used for temperature sensing and S ₄ is used for stress sensing
H1-H3	Designed for amplifying the stress sensor outputs and converting the differential signals to single ended. Currently not used, using a multimeter to measure the differential stress sensor outputs performed better. Implemented with AD8422BRZ
I	Voltage regulators to generate +/-2.5V for the transimpedance amplifier OPAMPs. Implemented with TPS76325 for +2.5V, and TPS72325 for 2.5V
J	Initially designed for mode matching but never used
	RC biasing of the stators is achieved by 500MΩ resistance and 5nF capacitance, refer to 1.7 for operation

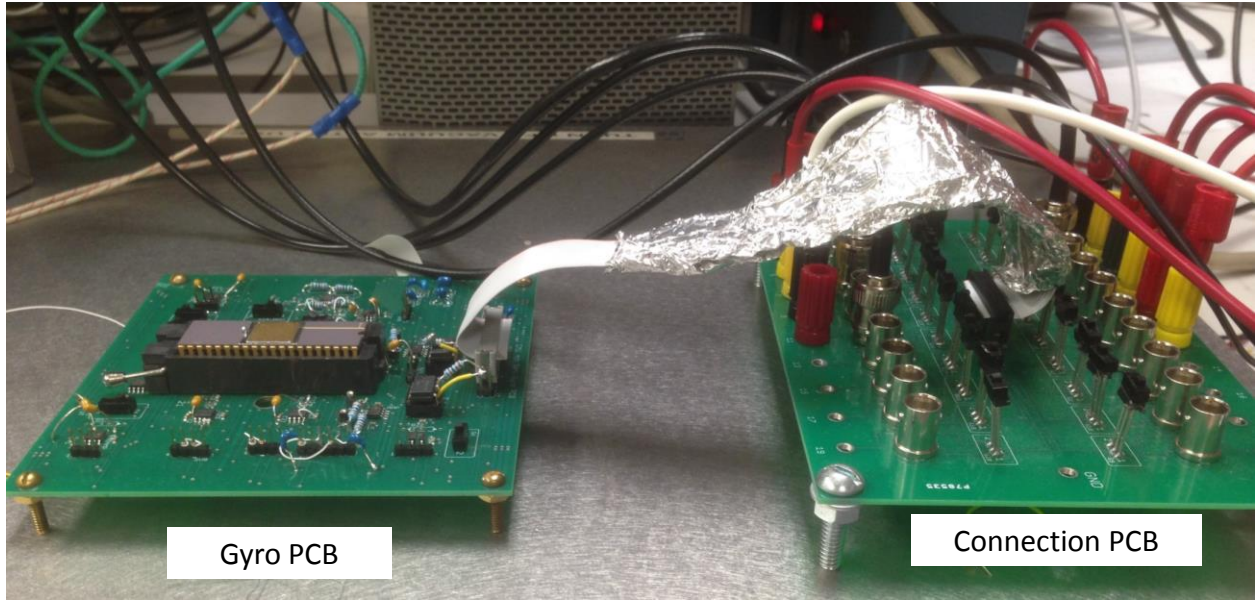


Figure 0.21: Photograph of the Gyro PCB and the Connection PCB.

Table 0.2: The pin map of the connection PCB

Pin #	Connection	Value if needed
1	Drive signal for mode 2, connected to output 2 of lock-in amplifier	
2	+ power supply for ICs	6V
3	Ground	
4	Drive signal for mode 1, connected to output 1 lock-in amplifier	
5	- power supply for ICs	-6V
6	Nonlinearity tuning voltage for mode 1	0V
7	Output voltage for mode 1, connected to input 1 of lock-in amplifier	
8	Proof mass voltage	35V
9	Frequency tuning voltage for mode 1	38.1V
10	Nonlinearity tuning voltage for mode 2	0V
11	Output voltage for mode 2, connected to input 2 of lock-in amplifier	
12	Frequency tuning voltage for mode 2	0V

References

- [1] J. Bernstein, S. Cho, T. King, A. Kourapenis, P. Maciel, and M. Weinberg, "A micromachined comb-drive tuning fork rate gyroscope," *Proceedings of MEMS1993*, Fort Lauderdale, FL, Feb. 7-10, 1993, pp. 143-148.
- [2] Yole Développement, "6 and 9-axis sensors consumer inertial combo sensors", Nov 2014.
- [3] Yole Développement, "High-end gyroscopes, accelerometers and IMUs for defense, Aerospace & industrial", Feb. 2015.
- [4] N. Yazdi, F. Ayazi, and K. Najafi, "Micromachined inertial sensors," *Proceedings of the IEEE*, vol. 86, no.8, pp. 1640-1659, August 1998.
- [5] N. El-Sheimy, H. Hou, and X. Niu, "Analysis and modeling of inertial sensors using Allan variance," *IEEE Transactions on Instrumentation and Measurement*, vol. 57, no.1, pp. 140-159, January 2008.
- [6] A. D. Challoner, H. H. Ge, and J. Y. Liu, "Boing disc resonator gyroscope", *Proceedings of PLANS2014*, Monterey, CA, May 5-8, 2014, pp. 504-514.
- [7] I. P. Prikhodko, A. A. Trusov, and A. M. Shkel, "Compensation of drifts in high-Q MEMS gyroscopes using temperature self-sensing," *Sensors and Actuators A: Physical*, vol. 201, pp. 517-524, October 2013.
- [8] (2015) STIM210 datasheet, Sensoror. Available online: <http://www.sensoror.com>.
- [9] (2015) ADIS16136 datasheet, Analog Devices. Available online: www.analog.com.
- [10] J. W. Joo, and S. H. Choa, "Deformation behavior of MEMS gyroscope sensor package subjected to temperature change," *IEEE Transactions on Comp. and Pack. Tech.*, vol. 30, no.2, pp. 346-354, June 2007.
- [11] S. H. Choa, "Reliability of MEMS packaging: vacuum maintenance and packaging induced stress," *Microsystem Technologies*, vol. 11, issue 11, pp. 1187-1196, October 2005.
- [12] X. Zhang, S. Park, and M. W. Judy, "Accurate assessment of packaging stress effects on MEMS sensors by measurement and sensor-package interaction simulations," *Journal of Microelectromechanical Systems*, vol. 16, no. 3, pp. 639-649, June 2007.
- [13] S. S. Walwadkar, and J. Cho, "Evaluation of die stress in MEMS packaging: Experimental and theoretical approaches," *IEEE Transactions on Component and Packaging Technologies*, vol. 29, no. 4, pp. 735-742, December 2006.
- [14] J. Song, Q. A. Huang, M. Li, and J. Y. Tang, "Effect of die-bonding process on MEMS device performance: System-level modeling and experimental verification," *Journal of Microelectromechanical Systems*, vol. 18, no. 8, pp. 274-286, April 2009

- [15] T. F. Marinis, J. W. Soucy, and D. S. Hanson, "Isolation of MEMS devices from package stress by use of compliant metal interposers," *Proceedings of Electronic Components and Technologies Conference*, San Diego, CA, 2006, pp. 1108-1117.
- [16] H. H. Ge, and A. D. Challoner, "Method of producing an isolator for a microelectromechanical (MEMS) die," *United States Patent*, US 8,322,028 B2, Dec. 4, 2012.
- [17] R. A. Belt, D. P. Mortenson, "Low-stress hermetic die attach," *United States Patent*, US 2008/0251866 A1, Oct. 16, 2008.
- [18] B. R. Simon, G. Sharma, S. A. Zotov, A. A. Trusov, and A. M. Shkel, "Intrinsic stress of eutectic Au/Sn die attachment and effect on mode-matched MEMS gyroscopes," *Proceedings of ISISS2014*, Laguna Beach, CA, Feb. 25-26, 2014, pp. 1-4.
- [19] H. J. Galle, and M. W. Judy, "MEMS device with stress relief structures," *United States Patent*, US 2014/0217521 A1, Aug. 7, 2014.
- [20] D. M. Rozelle, "The hemispherical resonator gyro: from wineglass to the planets," *Northrop Grumman*.
- [21] J. Y. Cho, and K. Najafi, "A high-Q all-fused silica solid-stem wineglass hemispherical resonator formed using micro blow torching and welding," *Proceedings of MEMS2015*, Estoril, Portugal, January 18-22, 2015, pp. 821-824.
- [22] D. Senkal, M. J. Ahamed, M. H. A. Ardakani, S. Askari, and A. M. Shkel, "Demonstration of 1 million Q-factor on microglassblown wineglass resonators with out-of-plane electrostatic transduction," *Journal of Microelectromechanical Systems*, vol. 24, no.1, pp. 29-37, February 2015.
- [23] Y. Lin, G. G. Li, A. C. McNeil, T. F. Miller, L. Z. Zhang, "MEMS device with central anchor for stress isolation," *United States Patent*, US 8,610,222 B2, Dec. 17, 2013.
- [24] B. Johnson, K. Christ, D. Endean, B. Mohr, R. Supino, H. French, and E. Cabuz, "Tuning fork MEMS gyroscope for precision northfinding," *Proceedings of Inertial Sensors and Systems 2015*, Karlsruhe, Germany, Sept. 22-23, 2015, pp. 1-10.
- [25] S. Nadig, S. Ardanuc, B. Clark, and A. Lal, "Dome-disc: diffractive optics metrology enabled dithering inertial sensor calibration," *Proceedings of MEMS204*, San Francisco, CA, January 26-30, 2014, pp. 608-611.
- [26] E. E. Aktakka, J. K. Woo, D. Egert, R. J. M. Gordenker, and K. Najafi, "A microactuation and sensing platform with active lockdown for *in situ* calibration of scale factor drifts in dual-axis gyroscopes," *IEEE/ASME Transactions on Mechatronics*, vol. 20, no. 2, pp. 934-943, April 2015.
- [27] (2015), Coriolis force. Available online. https://en.wikipedia.org/wiki/Coriolis_force.
- [28] (2016), Foucault pendulum. Available online. https://en.wikipedia.org/wiki/Foucault_pendulum.

- [29] M. Kline, "Frequency modulated gyroscopes," *PhD. Thesis*, Dept. of Electrical Engineering and Computer Science, University of California, Berkeley, 2013.
- [30] S. A. Zotov, A. A. Trusov, and A. M. Shkel, "High-range angular rate sensor based on mechanical frequency modulation," *Journal of Microelectromechanical Systems*, vol. 21, no.2, pp. 398-405, April 2012.
- [31] M. S. Kranz, and G. K. Fedder, "Micromechanical vibratory rate gyroscopes fabricated in conventional CMOS," *Proceedings of Symposium in Gyro Technology 1997*, Stuttgart, Germany, September 16-17, 1997, pp. 3.0-3.8.
- [32] E. Tatar, S. E. Alper, "Quadrature-error compensation and corresponding effects on the performance of fully decoupled MEMS gyroscopes," *Journal of Microelectromechanical Systems*, vol. 21, no.3, pp. 656-667, June 2012.
- [33] J. A. Geen, S. J. Sherman, J. F. Chang, S. R. Lewis, "Single-chip surface micromachined integrated gyroscope with 50°/hr Allan Deviation," *IEEE Journal of Solid State Circuits*, vol. 37, no. 12, pp. 1860-1866, December 2002.
- [34] M. W. Putty, "A micromachined vibrating ring gyroscope," *PhD. Thesis*, University of Michigan, Ann Arbor, 1995.
- [35] C. H. Ahn *at al.*, "On-chip ovenization of encapsulated disk resonator gyroscope," *Proceedings of TRANSDUCERS'15*, Anchorage, AK, June 21-25, 2015, pp. 39-43.
- [36] H. Johari, and F. Ayazi, "Capacitive bulk acoustic wave silicon disc gyroscopes," *Electron Devices Meeting*, San Francisco, CA, December 11-13, 2006, pp. 1-4.
- [37] S. E. Alper, and T. Akin, "A symmetric surface micromachined gyroscope with decoupled oscillation modes," *Sensors and Actuators A*, vol. 97-98, pp. 347-358, April 2002.
- [38] A. A. Trusov, A. R. Schofield, A. M. Shkel, "Gyroscope architecture with structurally forced anti-phase drive-mode and linearly coupled anti-phase sense mode," *Proceedings of TRANSDUCERS'09*, Denver, CO, June 21-25, 2009, pp. 660-663.
- [39] J. A. Geen, "Progress in integrated gyroscopes," *Proceedings of PLANS 2004*, April 26-29, 2004, pp. 1-6.
- [40] S. G. Saraswathy, J. Geen, J. Chang, "High performance gyro with fast start up time, high range, wide bandwidth, low noise and excellent vibration immunity," *Proceedings of PLANS 2012*, Myrtle Beach, SC, April 23-26, 2012, pp. 20-23.
- [41] A. A. Trusov, I. P. Prikhodko, S. A. Zotov, and A. M. Shkel, "Low-dissipation silicon tuning fork gyroscopes for rate and whole angle measurements," *IEEE Sensors Journal*, vol. 11, no. 11, pp. 2763-2770, November 2011.
- [42] Stephen D. Senturia, *Microsystem Design*, Kluwer Academic Publishing, 2001, pp. 561-567.

- [43] H. Xie, and G. K. Fedder, "Integrated microelectromechanical gyroscopes," *Journal of Aerospace Engineering*, vol. 16, no.2, pp.65-75, April 2003.
- [44] T. B. Gabrielson, "Mechanical-thermal noise in micromachined acoustic and vibration sensors," *IEEE Transactions on Electron Devices*, vol. 40, no.5, pp. 903-909, May 1993.
- [45] A. M. Elshurafa, K. Khirallah, H. H. Tawfik, A. Emira, A. K. S. Abdel Aziz, and S. M. Sedky, "Nonlinear dynamics of spring softening and hardening in folded-MEMS comb drive resonators," *Journal of Microelectromechanical Systems*, vol. 20, no.4, pp. 943-958, August 2011.
- [46] S. Shmulevich, and D. Elata, "Dynamically balanced folded-beam suspensions for resonators," *Journal of Microelectromechanical Systems*, available online.
- [47] H. Jeong, and S. K. Ha, "Dynamic analysis of a resonant comb-drive micro-actuator in linear and nonlinear regions," *Sensors and Actuators A*, vol. 125, pp. 59-68, 2005.
- [48] H. K. Lee, R. Melamud, S. Chandorkar, J. Salvia, S. Yoneoka, and T. W. Kenny, "Stable operation of MEMS oscillators far above the critical vibration amplitude in the nonlinear regime," *Journal of Microelectromechanical Systems*, vol. 20, no.6, pp.1228-1230, December 2011.
- [49] S. Nitzan, T-H. Su, C. Ahn, E. Ng, V. Hong, Y. Yang, T. Kenny, and D. A. Horsley, "Impact of gyroscope operation above the critical bifurcation threshold on scale factor and bias instability," *Proceedings of MEMS2014*, San Francisco, CA, January 26-30, 2014, pp. 749-752.
- [50] (2015), Duffing equation, Available online.
http://en.wikipedia.org/wiki/Duffing_equation.
- [51] J. J. Gagnepain, "Nonlinear properties of quartz crystal and quartz resonators," *Proceedings of Freq. Control Symposium*, Ft. Monmouth, NJ, May 1981, pp. 14-30.
- [52] M. Agarwal, "Optimal drive condition for nonlinearity reduction in electrostatic microresonators," *Applied Physics Letters*, 89, 214105, 2006.
- [53] E. Y. Gonen, "Design of a reconfigurable delta-sigma based capacitive CMOS front-end with temperature and stress sensors for a CMOS-MEMS gyroscope," *M.S. Thesis*, Dept. of Electrical and Computer Engineering, Carnegie Mellon University, 2014.
- [54] W. C. Tang, M. G. Lim, and R. T. Howe, "Electrostatic comb drive levitation and control method," *Journal of Microelectromechanical Systems*, vol. 1, no.4, pp.170-178, Dec. 1992.
- [55] T. Mukherjee, G. K. Fedder, D. Ramaswamy, and J. White, "Emerging simulation approaches for micromachined devices," *IEEE Transactions on Computer Aided Design of Integrated Circuits and Systems*, vol. 19, no. 12, pp 1572-1589, Dec. 2000.
- [56] M.A. Hopcroft, W.D. Nix, and T.W. Kenny, "What is the Young's modulus of silicon?," *Journal of Microelectromechanical Systems*, vol. 19, no. 2, pp. 229-238, April 2010.

- [57] E. Tatar, S.E. Alper, and T. Akin, "Quadrature error compensation and corresponding effects on the performance of fully decoupled MEMS gyroscopes," *Journal of Microelectromechanical Systems*, vol. 21, no. 3, pp. 656-667, June 2012.
- [58] G. K. Fedder and Q. Jing, "A hierarchical circuit-level design methodology for Microelectro-mechanical Systems," *IEEE Transactions on Circuits and Systems-II: Analog and Digital Signal Processing*, Vol. 46 (10), pp.1309-1315, October 1999.
- [59] Q. Jing, "Modeling and simulation for design of suspended MEMS," *Ph.D. Thesis*, Dept. of Electrical and Computer Engineering, Carnegie Mellon University, 2003.
- [60] S. S. Walwadkar, and J. Cho, "Evaluation of die stress in MEMS packaging: experimental and theoretical approaches," *IEEE Transactions on Component and Packaging Technologies*, vol. 29, no.4, pp. 735-742, Dec. 2007.
- [61] (2015) HF2LI Datasheet, available online, Zurich Instruments. <http://www.zhinst.com>.
- [62] IEEE Standard Specification Format Guide and Test Procedure for Coriolis Vibratory Gyros, IEE Std 1431-2004, 2004.
- [63] C. D. Ezekwe, B. E. Boser, "A mode-matching $\Sigma\Delta$ closed-loop vibratory gyroscope readout interface with a $0.004^\circ/\text{s}/\sqrt{\text{Hz}}$ noise floor over a 50 Hz band," *Journal of Solid-State Circuits*, vol. 43, no. 12, pp. 1860-1866, Dec. 2008.
- [64] F. Yesil, S. E. Alper, and T. Akin, "An automatic mode matching system for a high Q-factor MEMS gyroscope using a decoupled perturbation signal," *Proceedings of TRANSDUCERS'15*, Anchorage, AK, June 21-25, 2015, pp. 1148-1151.
- [65] H. Wu, "System architecture for mode-matching a MEMS gyroscope", M.E. Thesis, Dept. of Electrical Engineering and Computer Science, Massachusetts Institute of Technology, June 2009.
- [66] A. Sharma, M. F. Zaman, M. Zucher, and F. Ayazi, "A $0.1^\circ/\text{hr}$ bias drift electronically matched tuning fork microgyroscope", *Proceedings of MEMS2008*, Tucson, AZ, January 13-17, 2008, pp. 6-9.
- [67] (2015) MAX4475 datasheet, available online, Maxim Integrated. <http://datasheets.maximintegrated.com>.
- [68] (2015) AD8421 datasheet, available online, Analog Devices. <http://www.analog.com>.
- [69] (2015) LF356 data sheet, available online, Texas Instruments. <http://www.ti.com>.
- [70] D. Kim, and R. T. M'Closkey, "Spectral analysis of vibratory gyro noise," *IEEE Sensors Journal*, vol. 13, no. 11, pp. 4361-4374, November 2013.
- [71] (2016), STS Multiplex ICP RIE, available online, CMU Nanofab. <http://nanofab.ece.cmu.edu/equipment/machines/sts.html>.

- [72] C. Guo, E. Tatar, and G.K. Fedder, "Large- displacement parametric resonance using a shaped comb drive", *Proceeding of MEMS2013*, Taipei, Jan. 20-24, 2013, pp. 173-176.
- [73] J. Kim, D. Cho, and R. S. Muller, "Why is (111) silicon a better mechanical material for MEMS," *Proceedings of TRANSDUCERS'01*, Munich, Germany, June 10-14, 2001, pp. 662-665.
- [74] C.E. Franks, A. Shikata, and C.A. Baker, "Performance testing and results of the first Etec CORE-2564", *Proc. of SPIE 12th BACUS Symp. on Photomask Tech. and Mang.*, Vol. 1809, pp. 2-13, 1993.
- [75] F. Laermer, and A. Urban, "Challenges, developments and applications of silicon deep reactive ion etching," *Microelectronic Engineering*, vol. 67-68, pp. 349-355, 2003.
- [76] F. Laermer, and A. Urban, "Milestones in deep reactive ion etching," *Proceedings of TRANSDUCERS'05*, Seoul, Korea, June 5-9, 2005, pp.1118-1121.
- [77] A. R. Schofield, A. A. Trusov, "Versatile vacuum packaging for experimental study of resonant MEMS," *Proceedings of MEMS2010*, Hong Kong, Jan. 24-28, 2010, pp. 516-519.
- [78] (2015) Nanofilm, Indium Corporation. <http://www.indium.com/nanofilm>.
- [79] V. Chidambaram, X. Ling, and C. Bangtao, "Titanium-based getter solution for wafer-level MEMS vacuum packaging," *Journal of Electronic Materials*, vol.42, no.3, pp. 485-491, 2013.
- [80] (2015) SAES Getters, available online. <http://www.saesgetters.com/product-groups/getters>.
- [81] Langmuir (unit), available online. [http://en.wikipedia.org/wiki/Langmuir_\(unit\)](http://en.wikipedia.org/wiki/Langmuir_(unit))
- [82] B. D. Jensen, S. Mutlu, S. Miller, K. Kurabayashi, J. J. Allen, "Shaped comb fingers for tailored electromechanical restoring force," *Journal of Microelectromechanical Systems*, vol. 12, no. 3, pp. 373-383, June 2003.
- [83] S. E. Alper, K. Azgin, and T. Akin, "A high-performance silicon-on-insulator MEMS gyroscope operating at atmospheric pressure," *Sensors and Actuators A*, vol. 135, pp. 34-42, 2007.
- [84] S. Shmulevich, I. Hotzen, and D. Elata, "A perfect electrostatic anti-spring," *Proceedings of IEEE Sensors'13*, Baltimore, MD, Nov. 3-6, 2013, pp. 1-4.
- [85] (2016) H20E Epoxy data sheet, available online, Epotek. <http://www.epotek.com>.
- [86] E. Tatar, T. Mukherjee, and G.K. Fedder, "Tuning of nonlinearities and quality factor in a mode-matched gyroscope", *Proceeding of MEMS2014*, San Francisco, CA, Jan. 26-30, 2014, pp. 801-804.
- [87] E. Tatar, T. Mukherjee, and G.K. Fedder, "Nonlinearity tuning and its effects on the performance of a MEMS gyroscope", *Proceeding of TRANSDUCERS'15*, Anchorage, AK, June 21-25, 2015, pp. 1133-1136.

- [88] B. Kim *et al.*, “Temperature dependence of quality factor in MEMS resonators,” *Journal of Microelectromechanical Systems*, vol. 17, no. 3, pp. 755-766, June 2008.
- [89] I. P. Prikhodko, S. A. Zotov, A. A. Trusov, and A. M. Shkel, “Foucault pendulum on a chip: angle measuring silicon MEMS gyroscope”, *Proceeding of MEMS2011*, Cancun, Mexico, Jan. 23-27, 2011, pp. 161-164.
- [90] C. Jeong, S. Seok, B. Lee, H. Kim, and K. Chun, “A study on resonant frequency and Q factor tunings for MEMS vibratory gyroscopes,” *Journal of Micromechanics and Microengineering*, vol. 14, pp. 1530-1536, 2004.
- [91] D. K. Agrawal, J. Woodhouse, and A. A. Seshia, “Modeling nonlinearities in MEMS oscillators,” *IEEE Transactions on Ultrasonics, Ferroelectrics, and Frequency Control*, vol. 60, no.8, pp. 1646-1659, 2013.
- [92] E. Tatar, C. Z. Guo, T. Mukherjee, and G.K. Fedder, “Interaction effects of temperature and stress on matched-mode gyroscope frequencies”, *Proceeding of TRANSDUCERS’13*, Barcelona, Spain, June 16-20, 2013, pp. 2527-2530.
- [93] E. Tatar, C. Z. Guo, T. Mukherjee, and G.K. Fedder, “Effect of stress on matched-mode gyroscope frequencies”, *Proceeding of International Symposium on Inertial Sensors and Systems (ISISS) 2014*, Laguna Beach, CA, February 25-26, 2014, pp. 1-4.
- [94] Standard Test Method for Flexural Strength of Advanced Ceramics at Ambient Temperature, ASTM, C1161-13.
- [95] J. C. Suhling, and R. C. Jaeger, “Silicon piezoresistive stress sensors and their application in electronic packaging,” *IEEE Sensors Journal*, vol.1, no. 1, pp. 14-30, June 2001.
- [96] (2015) ADR445 datasheet, available online, Analog Devices.
<http://www.analog.com>.
- [97] Kulite Sensing, available online:
http://www.kulite.com/docs/transducer_handbook/section2.pdf.
- [98] E. Tatar, T. Mukherjee, and G.K. Fedder, “On-chip characterization of stress effects on gyroscope zero rate output and scale factor”, *Proceeding of MEMS2015*, Estoril, Portugal, January 18-22, 2015, pp. 813-816.
- [99] (2016) CRS09-02 datasheet, available online, Silicon Sensing.
<http://www.siliconsensing.com>.
- [100] (2016) ICM-30630 datasheet, available online, Invensense.
<http://www.invensense.com>.
- [101] R. L. Kubena, R. J. Joyce, and A. D. Challoner, “Correlation of frequency, temperature, and bias stability of a Si ring gyro ”, *Proceeding of Inertial2016*, Laguna Beach, CA, February 22-25, 2016, pp. 21-24.

- [102] K. L. Dorsey, "Dielectric charging in CMOS MEMS," *Ph.D. Thesis*, Dept. of Electrical and Computer Engineering, Carnegie Mellon University, 2013.
- [103] C. M. Liu *at al.*, "MEMS technology development and manufacturing in a CMOS foundry," *Proceeding of TRANSDUCERS2011*, Beijing, China, June 5-9, 2011, pp. 807-810.
- [104] P. Gieschke, B. Sbierski, and O. Paul, "CMOS-based piezo-FET stress sensors in wheatstone bridge configuration", *Proceedings of IEEE Sensors 2011*, Limerick, Ireland, October 28-31, 2011, pp. 93-96.
- [105] Y. Chet *at al.*, "Differential micro-pirani gauge for monitoring MEMS wafer-level package", *Proceedings of MEMS2015*, Estoril, Portugal, January 18-22, pp. 89-92.
- [106] Yu-Jen (Dylan) Fang, "Si-CMOS-MEMS technology for inertial sensors," *Ph.D. Thesis*, Dept. of Electrical and Computer Engineering, Carnegie Mellon University, 2012.
- [107] E. Y. Gonen, "Design of a reconfigurable delta-sigma based capacitive CMOS front-end with temperature and stress sensors for a CMOS-MEMS gyroscope," *M.S. Thesis*, Dept. of Electrical and Computer Engineering, Carnegie Mellon University, 2014.
- [108] (2016) Altera DE0-Nano datasheet, available online, Altera. <http://www.terasic.com>.